Vilim Štih

Signatures of motion processing and decisions in the larval zebrafish brain

Graduate School of
Systemic Neurosciences
LMU Munich

Dissertation der
Graduate School of Systemic Neurosciences der
Ludwig-Maximilians-Universität München

15th of December 2020

Supervisor:
Prof. Dr. Ruben Portugues

1st Reviewer:
Prof. Dr. Alexander Borst

2nd Reviewer:
Prof. Dr. Isaac Bianco

Date of defense: 25th of June 2021

Contents

Summary

This thesis traces the investigation of representations of whole field motion, a behaviorally highly relevant stimulus across species and contexts, in the brain of the larval zebrafish. The studies both cover the whole brain, as well as focus on specific brain structures (the cerebellum and the interpeduncular nucleus) and investigate processing of whole field motion in different contexts, in particular evidence accumulation and decision making.

In the first manuscript, we performed a comprehensive characterisation of sensory and motor responses in the whole granule cell population of the larval zebrafish cerebellum. We found responses to both neutral and behavior-eliciting stimuli (such as whole field motion), multimodality and dense, temporally-correlated activation of the population. The lack of sparseness and temporally-uniform activity were surprising in the context of prevailing theories of cerebellar function, however, the activity patterns we describe cover a rich range of sensorimotor signals that can support cerebellar learning.

The second manuscript presents an adaptation of the classical random-dot kinematogram stimulation paradigm to zebrafish, by using the stimulus to elicit an optomotor response. We have found that the optomotor behavior in this condition exhibits characteristic properties of evidence accumulation-based decision making: uncertainty-dependent latencies and error rates, as well as history dependence. By having this paradigm in larval zebrafish, we could examine neural correlates of perceptual decision making and evidence accumulation in the whole brain. We analyzed whole-brain recordings, finding signatures of different parts of the evidence-accumulation process distributed thought the brain. Responses with properties indicative of final stages of evidence accumulation - bidirectional modulation and long time constants - were localized in several midbrain structures, most prominently in nuclei raphe and the interpeduncular nucleus (IPN).

In the third manuscript we investigated the motion-response properties of the IPN, identified in the previous study as a possible nexus of motion information. We characterized its anatomy with confocal imaging, and using functional imaging in different transgenic lines discovered precise geometric patterning of the responses to different motion directions thought the structure. Complementing this data with a traced electron microscopy dataset we found structural correspondences that partly explain the spatial distribution of the responses, in particular potential axo-axonal inhibition.

Finally, we present Stytra, the software system for stimulation and behavioral tracking built to perform most of the studies included in the thesis, as well as many other studies in the lab. In addition to Stytra, I describe the associated open-source ecosystem we built alongside in the lab to acquire and analyse behavioral and imaging data.

Introduction

Processing and acting on motion information is a major task for nervous systems. The purpose of the brain is to produce behavior, and many behaviors are caused or influenced by environmental motion. These behaviors can range from the involuntary reflexes of the opotokinetic nystagmus to complex decision-making processes when estimating velocities of oneself and other participants in street traffic. Currently, it is not possible to study the full range of such behaviors in humans or other mammals at the level of the whole brain with cellular resolution. This has limited investigation to mostly small collections of cells in several predefined brain regions, therefore potentially missing large parts of the circuits. However, many aspects of these behaviors are also present in larval zebrafish, a vertebrate whose whole brain can be imaged at the cellular resolution and with genetic access to specific cell types. In this thesis, I will present several studies where we investigated motion processing in different circuits and contexts, and how they bring us closer to building a fuller picture of brain function through this lens.

The thesis is comprised of two sections: three studies on where and how the information about environmental motion is integrated in the fish brain and used to produce behavior, and the software infrastructure built along the way, to answer these and many more questions in systems neuroscience.

Systems neuroscience in larval zebrafish

The zebrafish, *Daniio Rerio*, is an organism with a long history of biological research. The transparency of the larval stage was an attractive feature for embryologists, as all the developmental stages can be continuously monitored under a microscope. This in turn has spurred the development of genetic tools, which in the last decade of the 20th century enabled neuroscientific studies in the organism. In particular, development of the Gal4-UAS system[1] has enabled targeted expression of proteins in different cell types and brain region defined genetically.

The development of functional calcium indicators - proteins which change their fluorescence when binding calcium[2] - have enabled large-scale optical approaches to physiological measurements. The potential changes across the membrane that accompany generation of action potentials open voltage-gated calcium channels and therefore increase local calcium concentration, making more of it available to bind to the indicators. Therefore, the fluorescence has a direct, although nonlinear, link

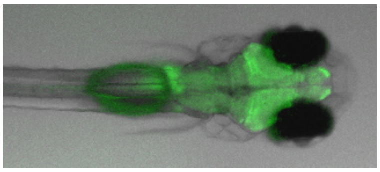

Figure 1: An epiflourescence image of a larval zebrafish expressing a green calcium indicator (GCaMP5G) pan-neuronally.

[1] Scott et al., "Targeting Neural Circuitry in Zebrafish Using GAL4 Enhancer Trapping".

[2] Rose et al., "Putting a Finishing Touch on GECIs".

to spiking activity[3]. These optical signals can be measured in the larval zebrafish brain with several kinds of microscopes, described in the next section.

The larval zebrafish exhibits a wide range of innate, but flexible and adaptable behaviors, ranging from the optomotor response[4], postural control[5], prey capture[6], escaping looming stimuli [7], rheo-[8], photo-[9], thigmo-[10], chemo-[11] and thermotaxis[12]. While performing each of these behaviors, the fish swim in discrete bouts, which makes the motor activity easy to segment and quantify. The bouts can be further classified in several types, and different stimulus situations engage different subsets of bout types[13]. While the work in this thesis relies mainly on the optomotor responses, the neural representations investigated are likely to be employed by the fish for other behaviors as well.

Functional brain imaging

The previously described developments in optical indicators progressed together with microscopy technologies, two of which we are employing for in-vivo brain imaging in larval zebrafish: two-photon and lightsheet microscopy. These two methods present different approaches of optically sectioning the sample perpendicular to the imaging plane.

In case of two-photon imaging[14], a pulsed infrared laser is focused on a point inside the sample, where the co-occurrence of two lower-energy photons within a very confined temporal period and spatial volume causes excitation equivalent to one photon of approximately twice higher energy. As this effect is proportional to the square of the light intensity, it is restricted to a very small region around the focal point. Therefore there is no illumination or scattering from the tissue below or above the focal plane. The focal point is scanned very rapidly by galvanometric mirrors while simultaneously collecting the photons emitted by the fluorescence with a photomultiplier tube (see Figure 2). The scanning and data acquisition are synchronized by using high sample-rate acquisition boards, so that every sample of the measured current from the photomultiplier tube is assigned a location known from the controlled position of the beam. With dedicated signal processing hardware (field-programmable gate arrays - FPGAs), it is possible to count individual photon events, resulting in some cases in higher signal-to-noise ratios, however in the experiments described here we used the photoelectric current integrated over the time bin assigned to one pixel. With current technology, it is not possible to scan the whole zebrafish brain at a high enough rate for volumetric imaging with cellular resolution. Two-photon whole-brain imaging studies therefore have to rely on protocols repeated across many imaging planes, and the data analyzed in a plane-wise fashion and combined to yield whole-brain characterizations[15]. This however limits the analysis of population activity to entities present in a single plane, and the experimental protocols to those that are short and elicit reliable responses when repeated tens to hundreds of times.

In contrast, lightsheet microscopy relies on illuminating the sample from the side by a focused laser beam, which is scanned at a high fre-

[3] Greenberg et al., “Accurate Action Potential Inference from a Calcium Sensor Protein through Biophysical Modeling”.

[4] Orger, Smear, et al., “Perception of Fourier and Non-Fourier Motion by Larval Zebrafish”.

[5] Ehrlich and Schoppik, “Control of Movement Initiation Underlies the Development of Balance”.

[6] Bianco, Kampff, and Engert, “Prey Capture Behavior Evoked by Simple Visual Stimuli in Larval Zebrafish”.

[7] Temizer et al., “A Visual Pathway for Looming-Evoked Escape in Larval Zebrafish”.

[8] Oteiza et al., “A Novel Mechanism for Mechanosensory-Based Rheotaxis in Larval Zebrafish”.

[9] Burgess, Schoch, and Granato, “Distinct Retinal Pathways Drive Spatial Orientation Behaviors in Zebrafish Navigation”.

[10] Schnörr et al., “Measuring Thigmotaxis in Larval Zebrafish”.

[11] Herrera et al., “Larval Zebrafish Use Olfactory Detection of Sodium and Chloride to Avoid Salt-Water”.

[12] Haesemeyer et al., “The Structure and Timescales of Heat Perception in Larval Zebrafish”.

[13] Marques et al., “Structure of the Zebrafish Locomotor Repertoire Revealed with Unsupervised Behavioral Clustering”.

[14] Denk, Strickler, and Webb, “Two-Photon Laser Scanning Fluorescence Microscopy”.

[15] Portugues, Feierstein, et al., “Whole-Brain Activity Maps Reveal Stereotyped, Distributed Networks for Visuomotor Behavior”.

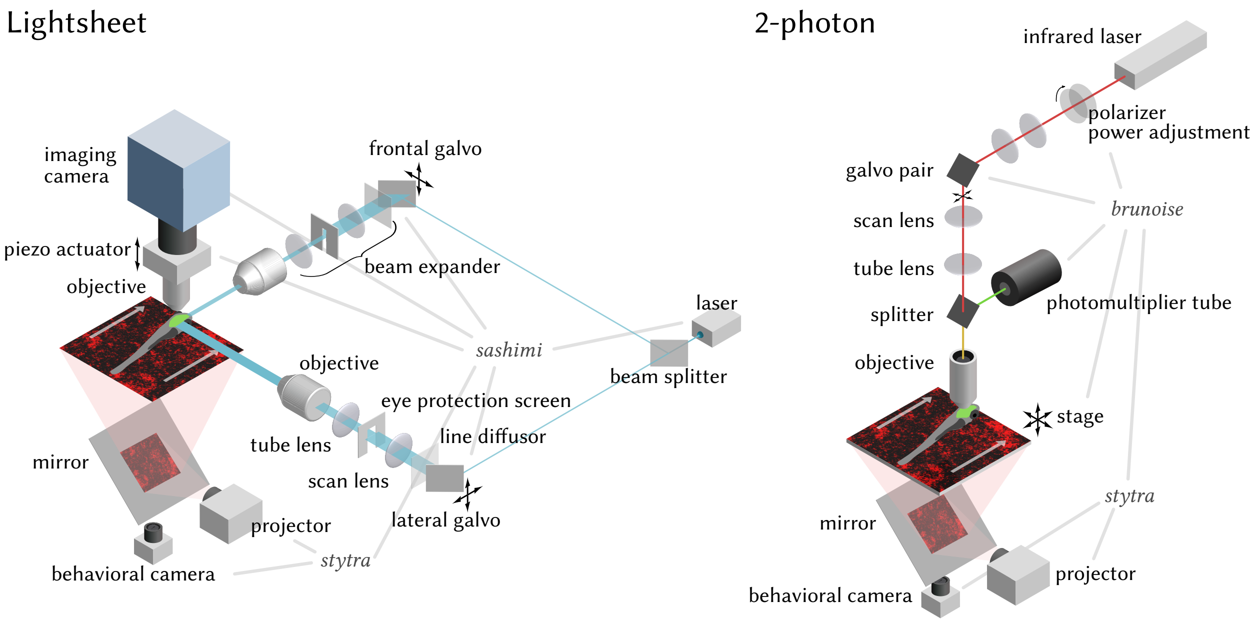

Figure 2: Schemata of the two microscopes, lightsheet and two-photon. The software packages for hardware control (described in the final section of the introduction) are *italic gray* and connected by gray lines to the components they control.

quency to produce a sheet of light[16]. The sheet of light can be in turn translated with an additional galvanometric mirror, at a slower rate, usually 1-10Hz. This illuminated plane is imaged by a high-sensitivity camera at a high framerate, synchronized with the translation of the illuminated plane and the camera objective, moved by a piezoelectric actuator (see Figure 2). Other lightsheet configurations, e.g. where the sheet is produced by a cylindrical lens[17], or where the sample is moved instead of the sheet of light, are common but less suitable for functional imaging. Lightsheet experiments result in a volumetric stack where the whole sample is recorded almost simultaneously. This opens up opportunities for whole-population activity analysis, such as looking at the dimensionality of the population response, what the dimensions of stimulus-related and unrelated activity are, whether the activity of the brain lies on a low-dimensional manifold spanning behavior-relevant variables[18], as well as dynamical systems-[19] and topology-based data analyses approaches[20].

In addition to two-photon and lightsheet imaging, volumetric whole brain imaging has also been achieved with lightfield imaging[21] (reconstructing the sources of light using a microlens array in front of the sensor and computational techniques) and HiLo microscopy [22] (using structured illumination to extract only the signal coming from the plane which is in focus). While these approaches can yield higher framerates, they are severely limited in the z-resolution and in the case of lightfield images, very computationally intensive to process.

The cerebellum in larval zebrafish

The cerebellum is a major brain region involved most prominently in motor control. In mammals it consists of a cerebellar cortex and deep cerebellar nuclei, whereas in zebrafish the role of the nuclei is taken by eurydendroid cells interspersed throughout the structure. Its regular and

[16] Keller et al., “Reconstruction of Zebrafish Early Embryonic Development by Scanned Light Sheet Microscopy”.

[17] Engelbrecht and Stelzer, “Resolution Enhancement in a Light-Sheet-Based Microscope (SPIM)”.

[18] Gallego, Perich, Naufel, et al., “Cortical Population Activity within a Preserved Neural Manifold Underlies Multiple Motor Behaviors”.

[19] Bruno, Frost, and Humphries, “A Spiral Attractor Network Drives Rhythmic Locomotion”.

[20] Giusti et al., “Clique Topology Reveals Intrinsic Geometric Structure in Neural Correlations”.

[21] Prevedel et al., “Simultaneous Whole-Animal 3D Imaging of Neuronal Activity Using Light-Field Microscopy”.

[22] Kim et al., “Pan-Neuronal Calcium Imaging with Cellular Resolution in Freely Swimming Zebrafish”.

intricate anatomy has drawn the attention of neuroscientists for over half a century, spurring the development of one of the first theories linking a neuroanatomical structure to a learning algorithm: the Marr-Albus-Ito family of models[23,24,25]. In these models, the cerebellum receives inputs through two channels: granule cells which provide a rich and sparse representation of the current state of the sensory world, and the climbing fibers of the inferior olive which deliver signals about motor or prediction errors. These signals converge onto Purkinje cells, large, almost-planar neurons which synapse with the parallel fibres of the granule cells and whose bodies are enveloped by climbing fibers (see Figure 3). A learning rule - long-term-depression - enables association between these two signal streams. Due to the very large number of granule cells (in mammals almost 50% of all the neurons in the brain), cerebellar theories posited that they transform the input signals into high-dimensional, sparse and decorrelated representations so that different contexts and conditions can be easily separated by the adjusting synaptic weights on the parallel fibers. While there are many variations of cerebellar learning theories, they tend to examine variations of one feature (connectivity, or plasticity rules[26]), while retaining the rest of the assumptions. However, the non-anatomical evidence for the different assumptions was sparse and incomplete, relying on single-cell recordings in few cell types for activity, and in-slice experiments for plasticity. Our studies of the zebrafish cerebellum, the first of which is presented in this thesis as *Manuscript 1*, attempt to fill some of these gaps, as in the zebrafish we have complete optical access to record the activity of the major cell types: granule, Purkinje and eurydendroid cells. The larval zebrafish display several adaptable motor behaviors [27], and the cerebellum is natural brain area to look for

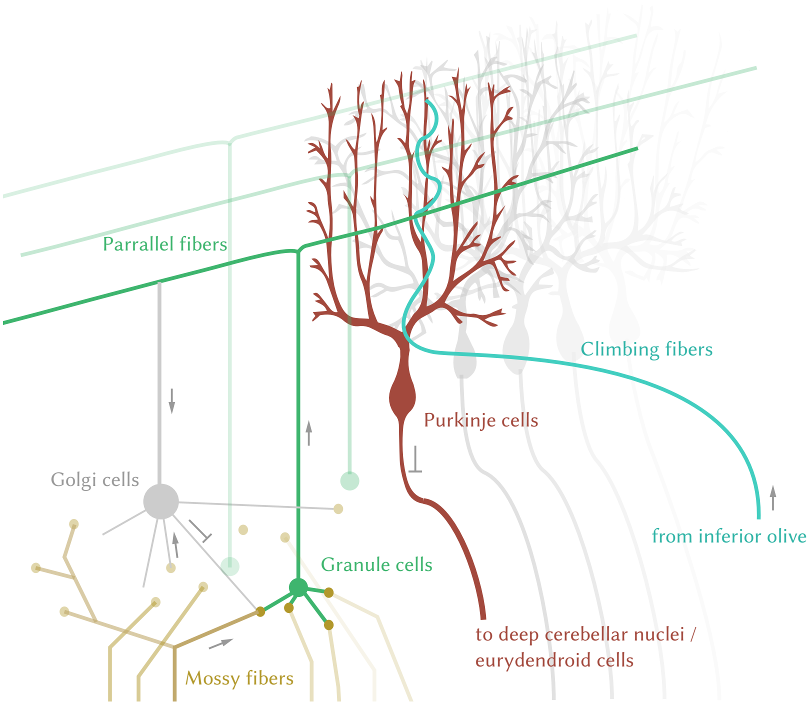

Figure 3: Schema of the cerebellar circuitry

[23] Marr and Thach, "A Theory of Cerebellar Cortex".

[24] Albus, "A Theory of Cerebellar Function".

[25] Ito, "Cerebellar Circuitry as a Neuronal Machine".

[26] Bouvier et al., "Cerebellar Learning Using Perturbations".

[27] Portugues and Engert, "Adaptive Locomotor Behavior in Larval Zebrafish".

signatures of control of these behaviors. In order to examine if the activity of cerebellar neurons contains information relevant for these behaviors, we started by examining the properties of granule cells. Until now, granule cells responses remain poorly studied, given the challenges of electrophysiology in such small cells. We investigated the presence of the theoretically-assumed granule-cell representation properties by using a rich, multimodal repertoire of stimuli: the optomotor-response evoking gratings, mild shocks, and whole-field flashes which usually do not cause behavior. We found several types of responses to this protocol, and most cells within each type were active together, showing no sparseness. Cells responding to a group of stimuli were confined to different parts of the cerebellum, with motion-excited groups mainly in the caudo-lateral part of the structure. Also, the luminance responses exhibited a degree of topographic organization. Additionally to the purely-sensory responses, we found motor and multimodally-responding granule cells. To investigate whether the granule cell representation has any effect on the behavior, we performed local bicuculine injections, disabling the inhibition within the cerebellum, which caused the fish to respond to all stimuli (including the flashes), and also caused similarly patterned activity in cells which previous to the injection did not show stimuli-related responses. Finally, using electrophysiological recordings, we have found that there is no temporal patterning in the probed granule cells while displaying whole-field flashes: all cells that had an excitatory response showed the same temporal profile after the flash onset, and similarly for the cells inhibited by luminance stimuli on flash offset (however on a limited number of recordings).

The optomotor response

Starting from the observation of the tendency of the zebrafish to align itself to the perceived direction of motion and swim along it[28] - the optomotor response (OMR) - a great variety of studies has been designed to exploit this behavior. Though simple in principle, the stimulus space and spectrum of behavioral outputs enables a investigating a diverse set of phenomena ranging from motion perception[29] to motor adaptation[30,31]. The optomotor response depends on whole-field stimuli in the red and green part of the visual spectrum and it is modulate by the spatial and temporal frequency of the stimulus[32]. For a wide range of speeds, the larvae match their swimming speed to the speed of the background motion, which they accomplish by modulating different (although co-varying) aspects of the behavior: employing different bout types, decreasing the inter-bout interval and changing the tail beat frequency[33]. In the case of forward motion with grating stimuli, the OMR can be modelled with an inhomogeneous Poisson process, where the rate is dependent on the velocity of the gratings, and there is no need for sensory integration to explain the behavior[34]. The aligning (turning) part of the optomotor response has been studied in detail in the study by Orger et al.[35], who quantified the dependence of the behavior on stimulus orientation in a freely-swimming assay. They found a very strong modulation of bout

[28] Orger, Smear, et al., "Perception of Fourier and Non-Fourier Motion by Larval Zebrafish".

[29] Yildizoglu et al., "A Neural Representation of Naturalistic Motion-Guided Behavior in the Zebrafish Brain".

[30] Portugues and Engert, "Adaptive Locomotor Behavior in Larval Zebrafish".

[31] Markov et al., "A Cerebellar Internal Model Calibrates a Feedback Controller Involved in Sensorimotor Control".

[32] Orger and Baier, "Channeling of Red and Green Cone Inputs to the Zebrafish Optomotor Response".

[33] Severi et al., "Neural Control and Modulation of Swimming Speed in the Larval Zebrafish".

[34] Portugues, Haesemeyer, et al., "Whole-Field Visual Motion Drives Swimming in Larval Zebrafish via a Stochastic Process".

[35] Orger, Kampff, et al., "Control of Visually Guided Behavior by Distinct Populations of Spinal Projection Neurons".

types (determined by the direction and distance of the bout) on stimulus direction, and identified spinal projection neurons that mediate turning. A more recent study[36] detailed the neural responses to both forward and side-wise motion, with a focus on binocular integration. Through an almost-whole-brain screen, they identified three areas of focus: the arborization field 6, the pretectum and the hindbrain. AF6 was analyzed as an area representative of those directly receiving optic flow, the pretectum one where binocular representations are present, and the hindbrain where the responses match closely the behavioral output. Using modeling, behaviorally-relevant modes of functional connectivity between different response types in these regions where found.

Regarding the properties of the visual stimuli causing the optomotor response, two recent publications from our group[37] [38] focused on forward swimming and turning respectively. In the first study, the swims were found to be triggered by a combination of whole-brain motion and a local light-to-dark transition, and the behavior was strongly modulated by the steepness of the transition. The signals corresponding to the two elements of the behavioral trigger (the light-to-dark transition and whole-field motion) were found to be widely distributed throughout the brain and often co-located. In the second study, *glider* stimuli were used to explore the turning response with different spatio-temporal correlation combinations occurring in natural environments, finding that the ratios of responses in pretectum are closely related to the behavioral response ratios.

Evidence accumulation

Most motor decisions need to be made in conditions of partial uncertainty about the world in which the animal acts. A classic model to study this aspect of decision making is the random-dot kinematogram task, where an animal is trained to indicate the direction of perceived motion. The coherence of this motion can be manipulated by the experimenter, which causes increases in latency and error rates. These behavioral outcomes are well predicted by evidence integration models, where the accumulation of evidence is modelled as integrating a biased, noisy process, and when the variable representing the integrated evidence reaches a threshold, a behavior is triggered[39].

In Manuscript 2, we present an adaptation of this paradigm to larval zebrafish. To successfully perform the optomotor response, zebrafish have to estimate the direction of the flow. This task can be made more difficult by manipulating the degree of uncertainty in the stimulus. When increasing this uncertainty we observe that the fish both make more errors, and take longer to initiate the behavior. The behavior displays additional properties indicating long-term influences of the stimulus and motor history: tuning in one direction is less likely if the previous stimulus or turn were in the opposite direction. All of these these properties are indicative of time-dependent decision making processes, which we proceed to investigate with whole-brain imaging. From the imaging data, regression-based analysis revealed widely-distributed correlates of main parts of

[36] Naumann et al., “From Whole-Brain Data to Functional Circuit Models”.

[37] Andreas M. Kist and Portugues, “Optomotor Swimming in Larval Zebrafish Is Driven by Global Whole-Field Visual Motion and Local Light-Dark Transitions”.

[38] Yildizoglu et al., “A Neural Representation of Naturalistic Motion-Guided Behavior in the Zebrafish Brain”.

[39] Gold and Shadlen, “The Neural Basis of Decision Making”.

the decision making process: motion-dependent, long-term integrating, bidirectionally modulated and motor event-correlated units. To further characterize these responses, we fitted a flexible parameterized model that can describe most sensory-related units within its parameter space. We reduced the parameters of the model to two main dimensions: whether the units are excited or inhibited by left or right motion, and a weighted time constant. Finally, informed by these investigations, we constructed a simple model from the same family as the one parametrizing the imaging to describe the behavior on a timescale of bout rates. Using these predicted rates as regressors, we looked for locations in the brain where the correlations would appear in prominent patterns. A particularly interesting area, with a windmill-like arrangement of the correlated and anti-correlated patches was the interpeduncular nucleus (IPN), a region in the ventral midbrain.

The interpeduncular nucleus exhibits structured optic flow-dependent activity

The properties of the IPN responses found in the previous study - a striking stimulus-direction-dependent geometric patterning, as well as bidirectionality of responses (a patch of tissue excited by motion in one direction and inhibited by motion in the opposite direction) - indicated a potentially important role of this structure in the spatial optomotor behavior. While the previously mentioned studies mainly deal with either turning or forward swimming in the context of the optomotor response, investigations combining the two and therefore covering the behavior for both turning and forward swimming have been more limited [40]. To tackle this question, we used a simple but well-controllable stimulus of motion in 8 cardinal directions, to probe where correlations to all displayed directions can be found and decoded. In addition to the previously well-described tectal and pre-tectal areas, parts of the forebrain, the nuclei raphe and the IPN showed responses tuned to all directions around the circle. Using different transgenic lines, we localised tuned responses in all parts of the structure, from different neuropil areas to the (mostly inhibitory) cell bodies. We combined this functional imaging data with detailed anatomy obtained through electron microscopy, which showed striking structural correspondences to the functionally-defined areas. Patches of similar tuning were consistent with the spanning trees of cells of the IPN, suggesting that the responses are shaped by axo-axonal inhibition.

Open source software in systems neuroscience

A systems neuroscience lab needs to acquire multiple kinds of high-dimensional data - behavior and physiology, while presenting animals with closed-loop stimulation paradigms. Both the behavioral and the imaging data needs to be processed and interpreted: the behavior segmented into units and quantified, the raw data from the imaging aligned, filtered and segmented into sources of activity (cells or processes), and both data sources need to be combined along with information about the

[40] Naumann et al., "From Whole-Brain Data to Functional Circuit Models".

stimulus paradigm to provide insights into neural processing. A significant amount of time in labs is spent developing systems enabling these processes. However, many of the requirements are shared between labs, resulting in a large duplication of efforts. The model of open-source software provides extensive tools and methodologies for both sharing and collaboration, showing a clear way forward. The first open-source package from the lab, Stytra, deals with behavioral acquisition and stimulation. In the meantime we have developed subsequent packages covering the remaining needs of the lab: Sashimi[41] and Brunoise[42] for imaging acquisition, and Bouter[43] Fimpy and Calcium for data analysis.

Stytra

One of the core components of systems neuroscience is the study of behavior. Most behavioral paradigms for larval zebrafish contain a combination of common components: tracking of fish position, tail and eyes, displaying a family of stimuli in various sensory modalities, linking the stimuli to behavior in a closed loop and synchronizing with imaging setups. At the point of writing Stytra, there was no comprehensive solution providing all of the required features, and custom programs were written per each experiment, in either the data-flow visual programming language LabView or as monolithic MATLAB or Python scripts. This made reproducing experiments on different setups and at other labs difficult, and caused significant duplication of efforts. We developed Stytra in a modular fashion, so that each of the common components can be used independently and combined in various ways, considering all the existing use cases: freely swimming experiments where stimuli are displayed in relation to the fish position, head-restrained experiments where there is a need for fast and precise tail tracking, imaging experiments where the start of the stimulation protocol has to be as close as possible in time to the acquisition of the first imaging frame. Also, automated data and metadata management has been built in the core of the framework, so all experiment-relevant parameters are stored in structured, common formats. Stytra uses several parallel processes: a main process that displays the user interface and coordinates the data transfer through other processes, camera and tracking processes and a microscope synchronization process. We have demonstrated how Stytra can be used to replicate behavioral experiments from literature. We also showed an example imaging experiment synchronized with Stytra showing how the recorded data enables easy analysis of behavioral, stimulation and imaging data together using a common zebrafish stimulation paradigm, delineating acute motor and sensory responses. Finally, we argue that compared to other open-source packages for behavioral tracking and stimulation Stytra covers a unique and comprehensive set of features.

Microscopy

Functional two-photon and lightsheet microscopy are comparatively recent neurophisiology paradigms with very limited ready-made hardware and software solutions. For the studies described in this thesis, as well as

---

[41] Asua, Štih, and Petrucco, *Portugueslab/Sashimi.*

[42] Štih, Paoli, and Asua, *Portugueslab/Brunoise.*

[43] Štih, Prat, et al., *Portugueslab/Bouter.*

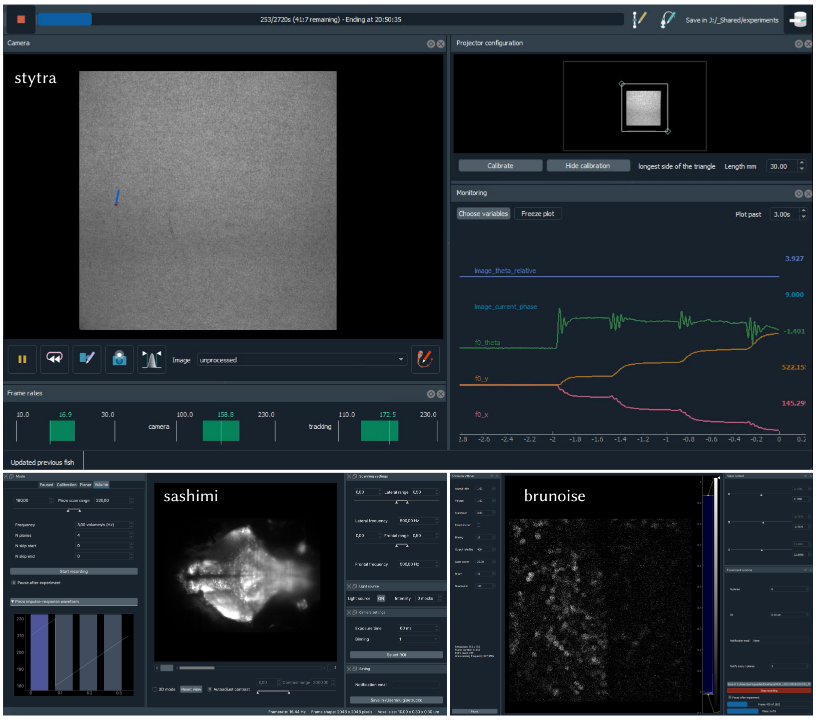

Figure 4: Screenshots of the data acquisition programs developed in the lab: Stytra, the behavior and stimulation program on top, and Sashimi (lightsheet) and Brunoise (two-photon) imaging acquisition programs below.

others from the group, custom setups were built. To control all parts of the instruments, acquire data and synchronize it with behavior and stimulus acquisition usually requires separate software tools, where separate programs are provided by the component manufacturers. To overcome this situation, we developed our own packages: Sashimi[44] (for the lightsheet microscope) and Brunoise[45] (for the two-photon microscope) handle all use cases in the lab and are easily extensible due to their modular nature (see Figure 2). Like Stryra, they are built out of multiple components running in different processes which communicate via message passing and shared memory (for bigger data arrays). The common architecture consists of processes for

- managing shared state and displays the user interface
- hardware control (input-output boards, camera)
- data preprocessing (reshaping, denoising)
- saving to disk
- coordinating the microscope acquisition with the stimulus presentation and tracking in Stytra

Additionally, there are parts that manage settings and dynamic imaging visualization. The common modules are implemented in the Scopecuisine package, which Sashimi and Brunoise depend on. Sashimi manages the synchronization of different hardware components: the scanning mirrors, the piezoelectric objective motor and the camera triggering, and provides a user friendly method of calibrating the system, which is necessary to adjust for each experiment. Additionally, it enables noise subtraction

[44] Asua, Štih, and Petrucco, *Portugues-lab/Sashimi*.

[45] Štih, Paoli, and Asua, *Portugues-lab/Brunoise*.

and a rich set of visualization options by embedding the open-source Napari viewer. Brunoise, the two-photon acquisition program, handles computation of optimal scanning parameters and patterns with user-specified image quality and framerate settings, and can be extended to provide additional features such as drift correction and laser ablation.

Data analysis

After acquisition, both behavioral and imaging data require preprocessing pipelines, to bring the high-volume input data to manageable size from which inferences about behavior and brain function can be made. For the behavioral data acquired through Stytra, we developed Bouter, a package that extracts summaries of tracked behavior. Bouter handles both common types of larval zebrafish experiments: head-restrained and freely-swimming, and extracts periods of swimming (bouts), computes different properties of the bouts and facilitates combining behavioral information with information about stimuli presented into structured tables. For some classes of stimuli, it provides a reconstruction of the displayed stimulus in fish-centered coordinates (for both freely-swimming and head-restrained experiments). With this package many common analyses (e.g. number and directionality of turns elicited by a particular stimulus) can be executed with only a few lines of code. For imaging data, to extract activity of single cells and contiguous parts of neuropil, several processing stages are necessary. First, a motion-correction step is needed to eliminate two kinds of motion artifacts: due to slow drift of the embedded samples and tail motion-introduced deformations. Several approaches to this problem are combined in the VolumeRegistration[46] package that handles both lightsheet and two-photon imaging scenarios. The package is an efficient reimplementation of the algorithms from the Suite2p calcium imaging analysis package[47] in the Julia programming language. In VolumeRegistration, the approach of Suite2p is extended to be agnostic to the data formats presented and the algorithms are generalized to work on volumetric data, for lightsheet imaging. The subsequent region-of-interest (ROI) extraction, based on local time-series correlations is implemented in packages Fimpy and Calcium. Calcium additionally supports local non-negative matrix factorization-based region extraction. Factorization is necessary to demix overlapping signals in neuropil or in lightsheet data, where there is significant light contamination from neighbouring regions. In Calcium, the parameters of the non-negative matrix factorization algorithms are additionally cross validated in different parts of the dataset, so that the data is described with the optimal number of sources and spatial sparsity.

[46] Štih, *Portugueslab/VolumeRegistration.Jl.*

[47] Pachitariu et al., “Suite2p”.

Manuscripts

Manuscript 1: Sensorimotor Representations in Cerebellar Granule Cells in Larval Zebrafish Are Dense, Spatially Organized, and Non-temporally Patterned

Laura D. Knogler, Daniil A. Markov, Elena I. Dragomir, **Vilim Štih**, Ruben Portugues

Published in: Current Biology - Volume 27, Issue 9, 8. May 2017

Current Biology

Article

Sensorimotor Representations in Cerebellar Granule Cells in Larval Zebrafish Are Dense, Spatially Organized, and Non-temporally Patterned

Graphical Abstract

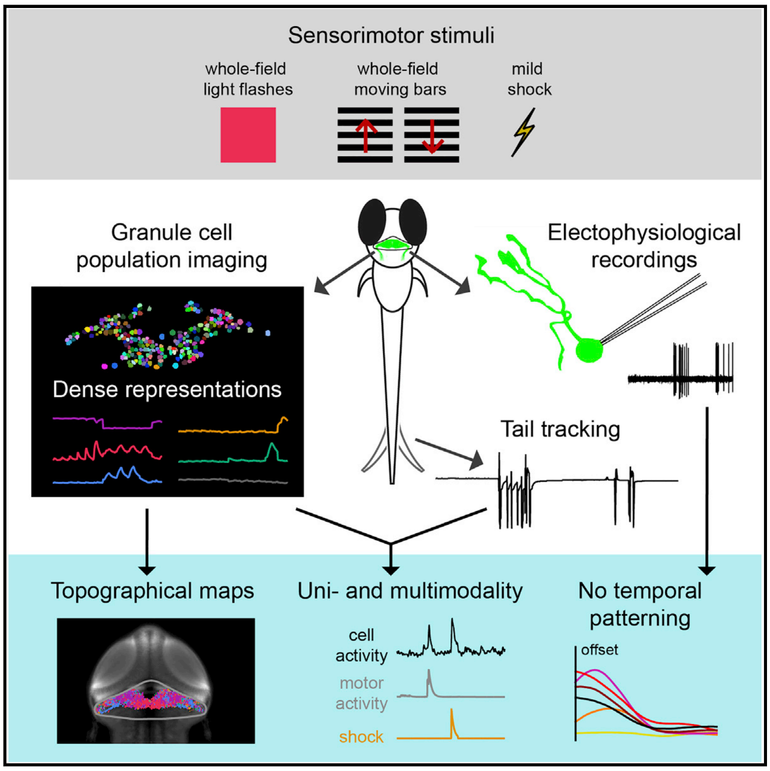

Highlights

- We image and record from cerebellar granule cells in behaving larval zebrafish
- Sensorimotor representations are dense and not temporally patterned
- We also find motor-related activity and multimodal sensorimotor representations
- Representations fall into a small number of anatomically clustered response types

Authors

Laura D. Knogler, Daniil A. Markov,
Elena I. Dragomir, Vilim Štih,
Ruben Portugues

Correspondence

rportugues@neuro.mpg.de

In Brief

Experimental evidence for the long-held theory that granule cells transform sensorimotor information into sparse, temporally patterned representations is lacking. Knogler et al. show that granule cells in behaving zebrafish in fact show dense, low-dimensional, non-temporally patterned activity that is anatomically clustered.

Knogler et al., 2017, Current Biology *27*, 1288–1302
May 8, 2017 © 2017 The Author(s). Published by Elsevier Ltd.
http://dx.doi.org/10.1016/j.cub.2017.03.029

Current Biology
Article

Sensorimotor Representations in Cerebellar Granule Cells in Larval Zebrafish Are Dense, Spatially Organized, and Non-temporally Patterned

Laura D. Knogler,[1] Daniil A. Markov,[1] Elena I. Dragomir,[1] Vilim Štih,[1] and Ruben Portugues[1,2,*]
[1]Max Planck Institute of Neurobiology, Sensorimotor Control Research Group, Am Klopferspitz 18, Martinsried 82152, Germany
[2]Lead Contact
*Correspondence: rportugues@neuro.mpg.de
http://dx.doi.org/10.1016/j.cub.2017.03.029

SUMMARY

A fundamental question in neurobiology is how animals integrate external sensory information from their environment with self-generated motor and sensory signals in order to guide motor behavior and adaptation. The cerebellum is a vertebrate hindbrain region where all of these signals converge and that has been implicated in the acquisition, coordination, and calibration of motor activity. Theories of cerebellar function postulate that granule cells encode a variety of sensorimotor signals in the cerebellar input layer. These models suggest that representations should be high-dimensional, sparse, and temporally patterned. However, in vivo physiological recordings addressing these points have been limited and in particular have been unable to measure the spatiotemporal dynamics of population-wide activity. In this study, we use both calcium imaging and electrophysiology in the awake larval zebrafish to investigate how cerebellar granule cells encode three types of sensory stimuli as well as stimulus-evoked motor behaviors. We find that a large fraction of all granule cells are active in response to these stimuli, such that representations are not sparse at the population level. We find instead that most responses belong to only one of a small number of distinct activity profiles, which are temporally homogeneous and anatomically clustered. We furthermore identify granule cells that are active during swimming behaviors and others that are multimodal for sensory and motor variables. When we pharmacologically change the threshold of a stimulus-evoked behavior, we observe correlated changes in these representations. Finally, electrophysiological data show no evidence for temporal patterning in the coding of different stimulus durations.

INTRODUCTION

The brain encodes the external world via sensory representations. It does so in a way that these activity patterns convey as much relevant information as possible for the actions that the organism must perform to maximize its chances of survival. The vertebrate cerebellum is believed to be a key player in these sensorimotor transformations and has been shown to be involved in multiple aspects of motor coordination, the calibration of reflexes, the acquisition of fine motor skills, and classical conditioning [1]. The input layer of the cerebellum consists of the cerebellar granule cells, the most numerous neurons in the brain of many vertebrates (including humans). Influential work [2, 3] motivated by anatomical [4], physiological [5], and theoretical arguments [6] has had a strong impact on models of cerebellar function.

These models postulate that granule cells provide an expansive recoding of their mossy fiber inputs into a sparse and high-dimensional representation that is recognized and learned by downstream Purkinje cells. These representations must be sparse not only in the space of possible stimuli but also in the temporal dimension, thus allowing a straightforward decoding of time since stimulus onset from their activity. This temporal patterning is believed to underlie the acquisition of appropriately timed cerebellar-dependent conditioned responses [7] (but see [8]).

Monitoring the physiology of granule cells via electrophysiological recordings is difficult and has most often been carried out in anesthetized rodents [9–11]. Together with anatomical studies mapping mossy fiber inputs to the granule cell layer [12, 13], there is growing evidence to show that multimodal inputs are integrated in single granule cells such that they can function as a coincidence detector to recognize complex stimuli (but see [14, 15]). In addition, recent work has also reported motor signals in granule cells of behaving mice [16, 17], thus opening the door to addressing issues involving efference copy signals and internal models that have been intensely studied in theoretical work during the last decades [18].

The larval zebrafish cerebellum, like that of all teleosts, shares the basic structure of its mammalian counterpart yet contains fewer cells by many orders of magnitude. Nonetheless, by just 5 days post-fertilization (dpf), anatomical studies show that the majority of Purkinje cells and granule cells are present in a ratio of approximately 1:20 and have formed the classic three-layered configuration [19–21]. Purkinje cells are active from 4 dpf [22, 23], a developmental time point that coincides with the onset of the ability of the zebrafish larva to maintain its balance in the water and perform maneuvers to hunt food and escape predation [24]. This mirrors the timeline seen in the developing rat where

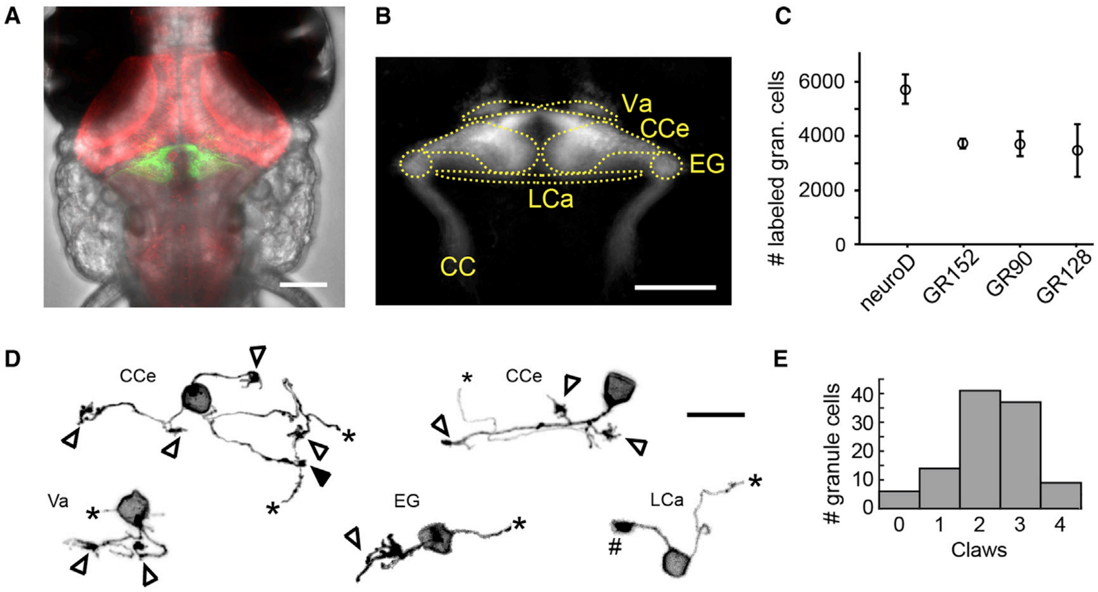

Figure 1. Characterization of the Larval Zebrafish Cerebellum and Its Granule Cell Population

(A) Composite confocal stack showing the head of a 7-dpf transgenic larval zebrafish in bright-field expressing GCaMP6f pan-neuronally (in red) and mCherry in a large population of granule cells (in green). The scale bar represents 100 μm.

(B) Schematic showing the anatomical lobes of the zebrafish cerebellum. CC, crista cerebellaris; CCe, corpus cerebella; EG, eminentia granularis; LCa, lobus caudalis cerebelli; Va, valvula cerebelli. The scale bar represents 100 μm.

(C) Quantification of the number of granule cells labeled in each of the four transgenic zebrafish lines used in this study (n = 3, 6, 5, and 2 fish, respectively). Data are represented as mean ± SEM.

(D) Example labeled granule cells from different regions of the cerebellum with zero, one, two, three, or four dendritic claws. Open arrowheads indicate dendritic claws, black arrowheads indicate dendritic branches without claws, pound indicates putative growth cone, and the truncated parallel fiber axons for all cells are marked with asterisks. The scale bar represents 10 μm. See Figure S1 for additional morphology of granule cells.

(E) Histogram showing the distribution of dendritic claw number in granule cells at 6 or 7 dpf (range = 0–4 claws; n = 107 granule cells from 86 fish).

See also Figure S1.

the appearance of postural and motor behaviors coincides with the rapid growth of Purkinje cell dendrites from postnatal days 9 to 18 [25]. Purkinje cells show visually evoked responses by 6 or 7 dpf from mossy fibers inputs via the parallel fibers of granule cells, and by this stage, multiple climbing fiber inputs have already been eliminated [22, 26]. Imaging, optogenetic, and lesion experiments in the larval zebrafish reveal that cerebellar neurons are active and indeed necessary during swimming [27], oculomotor tracking [27, 28], motor adaptation [29], and associative learning [30]. The anatomical and functional maturity of cerebellar circuits in the 6–8 dpf zebrafish therefore appear roughly equivalent to the 2- to 3-week-old rodent cerebellum [25, 31].

The compact size of the zebrafish cerebellum, optical transparency of the tissue, and availability of genetic driver lines to target cerebellar neuron subpopulations provides a unique opportunity to investigate how granule cells encode sensorimotor information. In this study, we harness these possibilities to optically monitor activity in genetically identified granule cells in awake, sensing animals as they are presented with sensory stimuli while simultaneously recording their behavior. Our experiments allow us to study the response properties of the population as a whole and address issues, such as the dimensionality and the sparseness of sensorimotor representations in these neurons. We uncover the anatomical mapping of functional responses across and within sensory modalities. We complement our calcium-imaging experiments with high-temporal-resolution electrophysiological recordings that allow us to investigate whether timing is explicitly encoded in single-cell granule cell activity.

RESULTS

Anatomical Organization of the Zebrafish Cerebellum

The cell types and anatomical organization of the larval zebrafish cerebellum are homologous to the mammalian cerebellum yet offer a more tractable circuit due to the lower number of cells [20]. In larval zebrafish, the cerebellum is located in the dorsal ~200 μm of the brain just caudal to the optic tectum (Figure 1A) and is therefore accessible for imaging and electrophysiology.

We took advantage of several transgenic gal4 driver lines generated by Takeuchi et al. [32], whose pattern of expression within the zebrafish cerebellum is limited exclusively to granule cells and their parallel fibers (Figure S1), as shown by previous immunohistochemical and anatomical characterization [32]. The zebrafish cerebellum consists of three lobes: the valvula cerebelli (Va; anterior lobe), the corpus cerebelli (CCe), and the caudolateral lobe, which is further subdivided into the eminentia granularis (EG) and the lobus caudalis cerebelli (LCa) (Figure 1B) [20].

These different transgenic lines have overlapping but nonidentical expression patterns that differed in the density of labeling as well as the lobe specificity [32], allowing us to obtain maximal coverage for population imaging and also target individual granule cells for electrophysiology (Figures S1D and S1E). We performed automated segmentation to identify and quantify granule cell somata across the four transgenic lines used in this study to label granule cells (Figure 1C; n = 16 fish). These methods suggest that there are at least 6,000 granule cells in the larval zebrafish cerebellum, a population approximately 20 times larger than the number of Purkinje cells [21]. This system therefore provides a large yet tractable population with which to investigate sparseness and dimensionality.

Zebrafish Granule Cells Have Stereotypical Dendritic Claws and Parallel Fiber Projections

Granule cells across species typically have only three to seven dendrites that each receives excitatory input from a single mossy fiber bouton [4, 33]. The dendrites of granule cells are highly elaborated and appear as claws, each of which makes many thousands of synaptic contacts with a single incoming mossy fiber bouton within a structure known as the glomerulus. This limited number of dendritic claws, and thus synaptic connectivity, has been highlighted by modeling studies as the best configuration for a feedforward network modeled on the granule cell layer given the trade-off between sparseness and information transmission [34]. Studies examining the early developmental stages of the zebrafish cerebellum have shown that granule cell differentiation and migration occur rapidly in the early larva cerebellar during 2–4 dpf [19, 20]. From these studies, we know that a large population of granule cells are established in the three-layered structure of the zebrafish cerebellum by 6 dpf and have fully extended their axons, although the detailed anatomy of these cells, in particular their dendritic morphology and whether or not claws are present, is unknown.

We obtained mosaic expression of a fluorescent reporter construct to visualize the morphology of single granule cells in different regions of the cerebellum (see Supplemental Experimental Procedures). This allowed us to examine how parallel fiber projections and dendritic morphologies varied across granule cells located in different areas of the granule cell layer.

High-resolution imaging of single granule cells showed that those present in the CCe, Va, and EG consistently had between one and four distinct claws (Figures 1D and 1E; mean ± SD = 2.3 ± 1; n = 107 cells from 86 fish; Figure S1A). The number and morphology of dendritic claws was stable from 6 or 7 dpf to 11 or 12 dpf (no change in claw number in 15/16 cells from 14 fish; paired sign test p = 0.32) and persisted to 20–22 dpf (Figure S1C; n = 2). Labeled granule cells from the LCa had very few claws in 6 or 7 dpf larvae (4/5 with zero claws) but did show protrusions resembling axonal growth cones, which could be related to their relative immaturity compared to granule cells in other regions (Figure S1A) [19]. Nonetheless, the majority of granule cells possess the hallmark dendritic claws of mammalian granule cells and, as such, could be capable of receiving and integrating multiple mossy fiber inputs in the input layer of the cerebellar circuit.

As in mammalian cerebella, the parallel fibers extend longitudinally across the mediolateral axis of the cerebellum and are organized in a sheet (Figure S1A). Our results reveal five distinct parallel fiber projection types (Figure S1A) that correspond to somata location, thus refining our knowledge of the axonal projection map from previous studies [19, 20]. All parallel fibers span the cerebellum in a longitudinal (mediolateral) orientation with the distance covered dependent to a large extent on the width of the cerebellum as it increases along the rostral to caudal axis. Notably, only a subpopulation of labeled granule cells had parallel fibers that project to the crista cerebellaris (CC) of the dorsal hindbrain (Figure S1A; n = 9/26 cells), which corresponds to the vestibulocerebellum in zebrafish [19]. This suggests that granule cells with projections to the CC might be enriched for carrying information crucial for vestibulomotor integration, such as motor efference copies. The different dendritic morphologies and parallel fiber projections therefore suggest regional specializations that may link with the functional role of these cells in different sensorimotor processes.

Granule Cell Representations Are Dense across the Population

Granule cells are believed to re-encode mossy fiber signals arriving in the cerebellum in a sparse, higher dimensional representation. However, it has never before been possible to measure sparseness experimentally across the entire granule cell population due to the large size of the mammalian cerebellum. Functional imaging of local populations of putative granule cells from a known motor region of the cerebellum in the awake, behaving mouse revealed motor-correlated activity in the majority of these cells [16], providing evidence for dense granule cell representations in this cerebellar subregion. We therefore took advantage of the compact and optically accessible larval zebrafish cerebellum in order to test the hypothesis that granule cell representations are sparse at the population level, across the entire cerebellum.

We presented three types of sensory stimuli to awake larval zebrafish with genetically encoded calcium indicators expressed in cerebellar granule cells and used a two-photon microscope to image the responses (Figures 2A and 2B; Movie S1). We imaged every fish throughout the entire volume of the cerebellum. The sensory stimuli consisted of the following: (1) a whole-field red flash of six different durations, (2) a black and red grating that moved forward at one of three speeds (3, 10, and 30 mm/s) or in reverse at 10 mm/s, and (3) a mild electric stimulus delivered to the bath (Figure 2A). Experiments on transgenic lines expressing calcium indicators pan-neuronally revealed that these stimuli activated visual processing regions and the cerebellum quite specifically (Movie S2). In a subset of these experiments, tail movements were recorded simultaneously with neuronal activity in order to measure behavioral responsiveness to stimuli. Neither the whole-field flashes nor the reverse motion gratings elicited any behavioral response (Figure 4A). It is known, however, that larval zebrafish show light-mediated turning [35] and startle responses [36], which indicates that small changes in luminance are an ethologically relevant stimulus for the animal. The forward gratings elicited forward swimming, a behavior known as the optomotor response, whereas the electric shock was titrated to elicit a short motor response in approximately half of trials.

These imaging experiments in the awake zebrafish revealed dense (non-sparse) activation of the entire granule cell layer in response to the simple stimuli we presented (Figure 2B). In a given imaging plane, anatomical segmentation revealed several

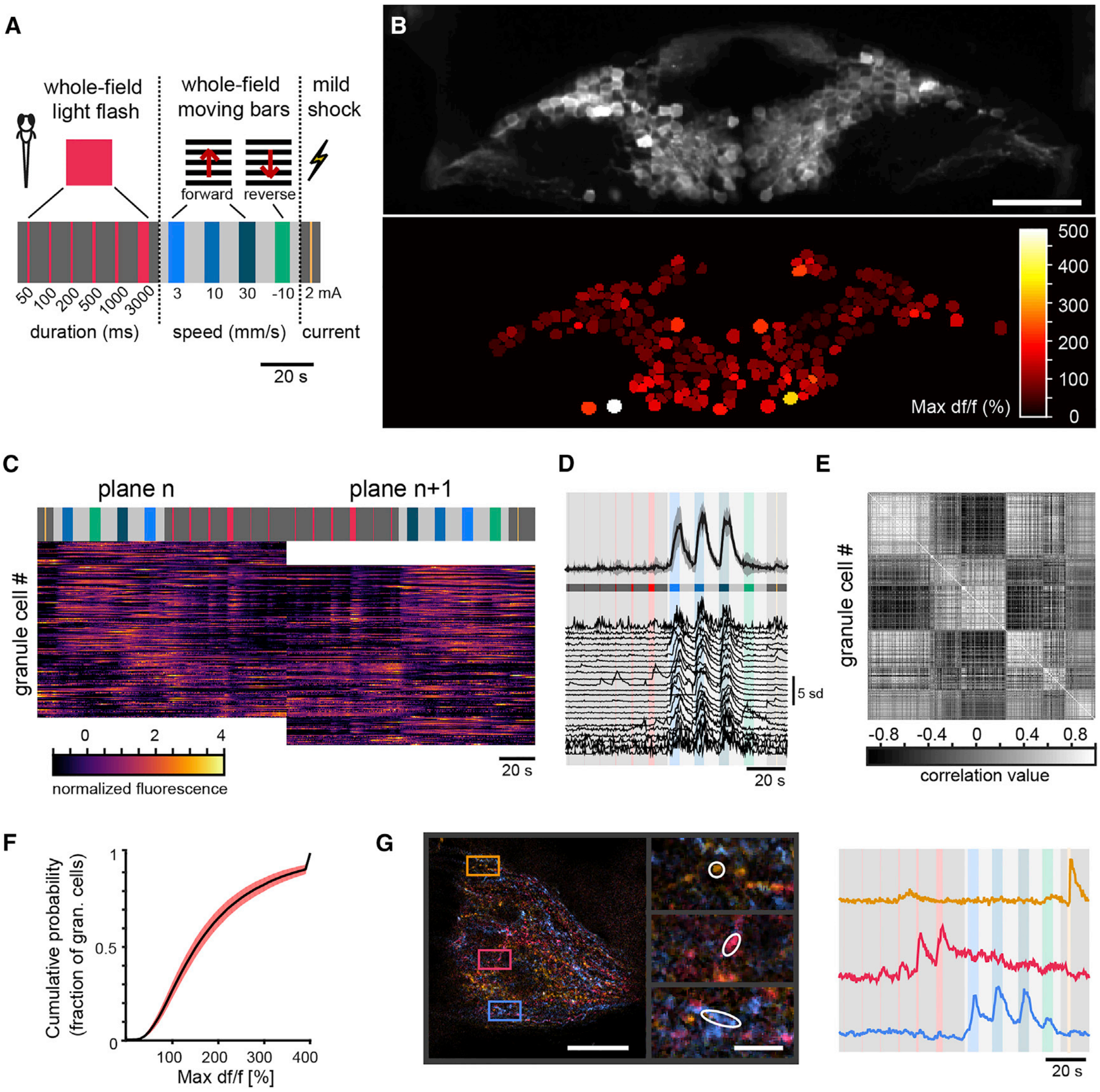

Figure 2. Representations in Granule Cells Are Non-sparse

(A) Stimulus paradigm presented to the larvae. Whole-field flashes were of 50, 100, 200, 500, 1,000, and 3,000 ms durations. Moving gratings were presented for 5 s at three caudo-rostral speeds (3, 10, and 30 mm/s) and one rostro-caudal speed (−10 mm/s). Average luminance across whole-field gratings was half as bright as the red flashes but brighter than the background luminance (shown here as dark gray). A mild (2 mA) electric shock lasting 10–25 ms was also delivered. These stimuli were presented in a randomized order in the experiments but are reshuffled to this order in later panels.

(B) Top: anatomical image of one imaging plane through the granule cell layer (scale bar, 50 μm). Bottom: heatmap of the maximum df/f signal (as a percent) for all anatomically segmented neurons in this plane shows dense activation of these neurons. See Figure S2 for anatomical segmentation.

(C) All of the granule cells extracted from two subsequent imaging planes (1 μm apart). In most cases, the same granule cell could be imaged in multiple planes.

(D) Upper trace: example average granule cell response to the stimuli presented with SD (shaded region). Lower traces: z scored activity traces from this same cell collected across multiple planes.

(E) All 252 granule cell responses appearing in plane n+1 from (C) were clustered using k means into seven response types, and the reorganized correlation matrix is shown. Most granule cells exhibit some stimulus-locked response as evidenced by the high degree of structure in the correlation matrix.

(F) Histogram showing the mean (across 16 fish) cumulative distribution of maximum df/f for all (not just active) granule cells. The shaded region denotes the SE. On average, over 50% of granule cells had a maximum df/f above 150%.

(G) Left: pseudocolored image of a single plane of parallel fibers from the right cerebellar hemisphere showing the difference between fluorescence during a particular stimulus frame and the average fluorescence. Blue, forward moving fast gratings; red, 3 s flash stimulus; yellow, shock stimulus. The scale bar represents 25 μm. Insets show higher magnification of regions of interest (ROIs) containing putative presynaptic puncta from parallel fibers (position indicated by the boxes at left) responsive to different stimuli. The scale bar represents 5 μm. Right: the activity traces from these circled ROIs at left show responses that match with the activity seen in granule cell somata (e.g., compare lower blue trace to trace in D).

See also Figure S2 and Movies S1, S2, and S3.

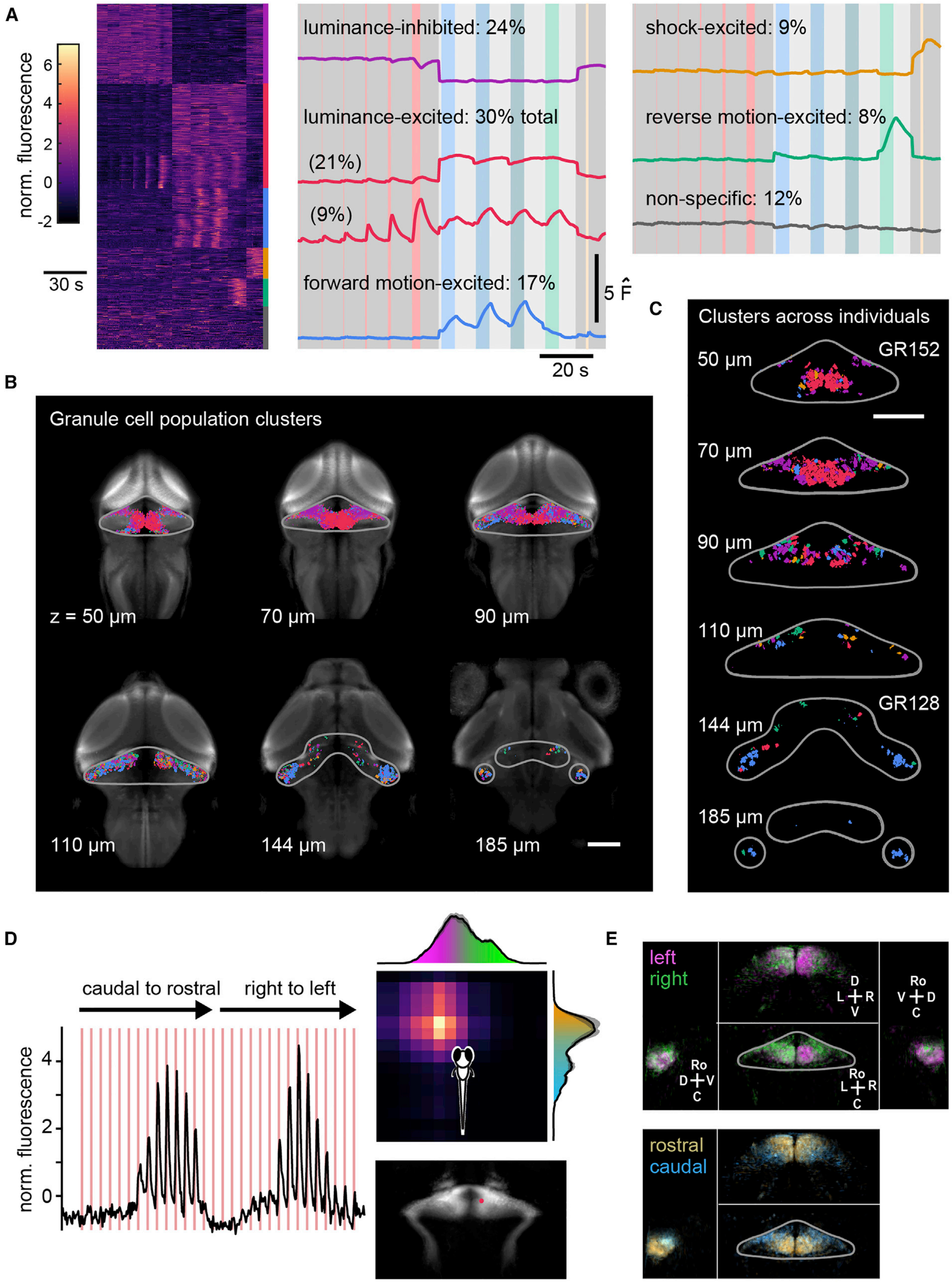

(legend on next page)

different response profiles across cells (Figures 2C and S2). Granule cells spanned several imaging planes, and their activity could thus be tracked across multiple trials (Figures 2C and 2D). As a first step toward investigating significant stimulus-locked activity, all simultaneously recorded signals from a plane were cross-correlated and clustered, revealing well-defined functional groups (Figure 2E). The correlation matrix shows that activity was highly correlated within a group and that most granule cells were active during our experimental paradigm.

Quantifying the activity across all anatomically segmented granule cells from many experiments revealed that over 50% of all granule cells had a maximum change in fluorescence over baseline above 150% (Figure 2F; n = 16 fish). This represents a quantification of all granule cells, irrespective of their activity during the protocol, and suggests that the majority of granule cells present in the cerebellum were active in response to at least one of the 11 stimuli presented. Dense activation of granule cells was also observed in response to a movie of natural underwater scenes that had the same average luminance as whole-field flashes (data not shown).

Granule cells express NMDA receptors whose activation by synaptic inputs could also contribute to calcium signals [37]. In order to identify whether we were actually monitoring granule cell spiking, we imaged the parallel fibers in every experiment (Figure 2G; Movie S3). Parallel fiber activity showed the same response dynamics and profiles as the somatic signals (Figure 2G). Additionally, 26/26 electrophysiological recordings from granule cells showed reliable responses to at least one of the stimuli presented, with spiking patterns that precisely reproduce the responses obtained from functional imaging when convolved with the GCaMP kernel (Figures S3A and S3B). These data give us confidence that the activity reported by the calcium indicator indeed reports granule cells firing.

The Granule Cell Layer Is Organized Anatomically by Functional Response Type and Displays a Visuotopic Map

Our population imaging results suggested that granule cells had highly stereotyped responses to certain stimuli and pointed toward an enrichment of these response profiles in different areas of the cerebellum. Although it is known that granule cell populations in the different lobes of the zebrafish cerebellum have different developmental pathways, genetic profiles, and parallel fiber projections [19, 20], it is unknown whether functional specializations are also organized topographically.

In order to look at the anatomical mapping of functional responses, we registered the results of our experiments across all 16 fish in three dimensions to a reference brain [28]. A mask was created from the reference anatomy to encompass the volume in which granule cell soma could reliably be found. We used an unbiased functional segmentation algorithm [28] with a high threshold to identify nearly 13,000 significantly active granule cells. The activity from all of these granule cells was used to estimate the intrinsic dimensionality of the representation, which resulted in a value around seven (see Supplemental Experimental Procedures).

We then performed k-means clustering on the average activity profiles of all neurons to identify seven main clusters from these responses (Figures 3A, S4A, and S4B; see Supplemental Experimental Procedures). These clusters corresponded to the following response types: luminance excited (this group included two clusters; see Figure S4), luminance inhibited, forward motion excited, reverse motion excited, shock excited, and non-specific. We also found several of these same response profiles by performing cell-attached electrophysiological recordings of granule cells with this stimulus set (Figures S3 and S5). Approximately half of all granule cells from our imaging experiments responded to luminance (30% and 23% of all cells were luminance excited and inhibited, respectively). All motion-excited cells were direction selective, with 17% of granule cells being excited by forward motion and half as many responding to reverse motion. No cells were found that showed inhibition in response to motion. Another 9% of cells were shock excited, and the remaining 12% of cells showed no stimulus-locked responses.

In order to look at the distribution of these functional groups across the cerebellum, we used our registration maps for all experiments to color code every voxel in the reference brain based on the most frequent response type of all cells spanning

Figure 3. Granule Cells across the Cerebellum Are Organized Topographically with Respect to Stimulus Response Profile and Visual Receptive Field

(**A**) Left: heatmap of z scored activity of all 12,283 granule cells (n = 16 fish) sorted into seven clusters by k means clustering. Despite GCaMP6S and GCaMP6F signals having different kinetics, granule cells with similar response profiles nonetheless cluster together. Right: the average activity trace from each cluster is shown at the right and labeled according to stimulus response type and what percentage of granule cells belong to that cluster. Note that two clusters appear to be "luminance-excited": these are grouped together in subsequent panels. See Figure S3 for example activity traces from individual cells (calcium imaging and electrophysiology) and anatomical organization of luminance-excited subclusters.

(B) Single planes at different depths from the surface of the brain showing the most likely response profile to be found in the granule cell soma layer when fish across all experiments (n = 24) are combined, together with pan-neuronal expression for anatomical reference. Colors are coded for response profile as in (A). The gray outline shows the approximate boundaries of the cerebellum for reference. The scale bar represents 100 μm.

(C) Same as for (B), showing example planes from individual fish from different transgenic lines.

(D) To investigate retinotopy, the visual field was divided into 15 horizontal and vertical bars that were flashed for 1 s (red shading). For every neuron (average for one sample neuron across planes shown in black), this allowed us to estimate the receptive field (color coded on the top right for the same neuron). The location of the sample neuron is shown on the bottom right. The histograms showing the probability distribution of the location of the centroid of all receptive fields are shown (left-right location in magenta-purple and rostro-caudal location in orange to cyan) (average across six fish with a total of 2,603 granule cells; the shaded region indicates the SE). The scale is the same as for (B).

(E) Granule cells have been color coded according to the centroid of their visual receptive field using the same color code as in (D). Top: lateralization of receptive fields. The outlined cerebellum is shown for reference over the bird's eye view. Additional sagittal and coronal views are indicated by the axes (C, caudal; D, dorsal; L, lateral; M, medial; Ro, rostral; V, ventral). Bottom: the same views as in the top panel, but showing rostro-caudal receptive fields. The scale is the same as for (D).

See also Figures S3 and S4.

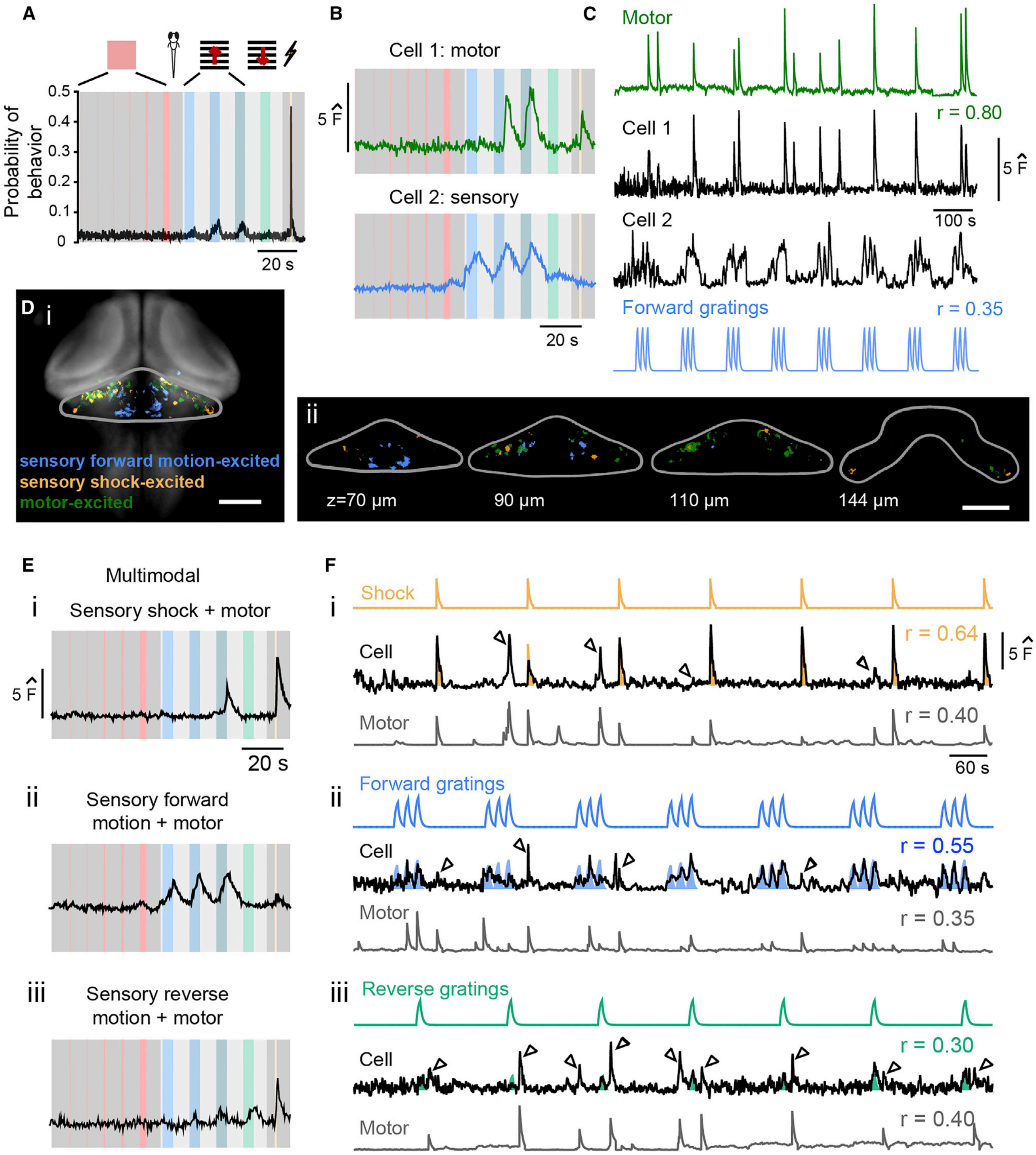

Figure 4. Granule Cells Can Encode Purely Sensory or Motor Information as well as Multimodal Sensorimotor Combinations

(A) Typical behavior evoked by our stimuli in head-embedded imaging experiments with the tail freed from the agarose. Only forward-moving gratings and the mild electric shock elicit behavior. n = 5.

(B) Green trace is the convolved regressor of motor activity, black traces are the simultaneously acquired z scored fluorescence traces for the two granule cells shown in (A), and blue trace is the convolved regressor for forward-moving stimuli. Correlation coefficients between the activity of each cell and its best regressor are shown.

(C) Two example activity profiles of simultaneously recorded granule cells from behaving fish excited by moving forward gratings that were distinguished as having motor-related (upper trace) or sensory-related (lower trace) activity.

(legend continued on next page)

that voxel. Our map reveals a clear link between anatomical location and response profiles of granule cells in support of a modular, lobe-specific specialization of the cerebellum (Figure 3B). Luminance-excited cells occupy a dense, bilateral area in the most dorsal and medial region of the CCe that is neighbored rostrally and laterally by similarly dense regions of luminance-inhibited cells. The vast majority of granule cells responding to directional motion or to electric shock in the dorsal cerebellum were located in the caudal-most band of cells that compose the LCa. Moving ventrally and laterally, the granule cell response profiles shift to become a mixture of mostly forward and reverse motion-excited responses (Figure 3B). The EG, located at the most lateral edges of the cerebellum, is enriched for motion- and shock-excited responses, as is the rostral Va region at this same depth (Figure 3B). The location of these anatomical clusters was reproducible in an individual cerebellum and highly conserved across fish, regardless of the transgenic driver line (Figures 3B and 3C).

Given that many granule cells were identified as luminance excited, we wondered whether this group could be further subdivided with respect to visual receptive field location. There is evidence for fractured somatotopy in the mammalian cerebellum [38], but due to the difficulty of probing visuotopic maps in an awake, non-decerebrate preparation, a comprehensive mapping of visual responses within the granule cell layer in an awake animal has not been performed until now. In order to determine whether visual responses were organized within a retinotopic map, we divided the visual field into 15 equal vertical (rostro-caudal) and horizontal (left-right) bars that were flashed for 1 s before returning to darkness (Figure 3D; see Supplemental Experimental Procedures). This allowed us to estimate the spatial receptive fields of active cells assuming a simple direct product structure.

We found that the majority of luminance-excited granule cells had receptive fields that covered between 5% and 25% of the visual field (data not shown). Receptive fields were equally distributed between the left and right of the visual field, but most of them corresponded to the rostral half (Figure 3E). To visualize whether any topographic map existed, we color coded each granule cell based on the position of center of mass of its receptive field (left to right colored in magenta to green and rostral to caudal in orange to cyan). The results show that a symmetrical topographic map indeed exists (Figure 3E). Whereas a fine-scale retinotopic map was not observed, we found that most granule cells in the left cerebellum have their receptive fields on the right-hand side of the visual field and vice versa. In addition, most granule cells in the rostro-ventral cerebellum (the Va) had their receptive fields in the caudal half of the visual field. This result shows that, in addition to sensory modality, granule cells in the cerebellum of larval zebrafish convey information about the spatial location of the sensory stimulus. These experiments reveal for the first time a visuotopic map in the granule cell layer of an awake, behaving animal.

Granule Cells Can Encode Purely Sensory or Motor Information as well as Multimodal Sensorimotor Combinations

In addition to processing information about sensory context, such as luminance, the cerebellum plays an important role in coordinating movement and motor learning [39]. We therefore expect to find granule cells that encode information about visual motion as well as the motion of the animal itself. In order to disambiguate sensory and motor-related responses (such as efference copies of signals to spinal locomotor networks) to stimuli that evoke behavior, we performed calcium imaging from granule cells in awake, head-embedded zebrafish (n = 5) while monitoring the movement of the tail, which was freed from the agarose.

Forward-moving gratings elicited periods of swimming known as bouts, whose latency, duration, and frequency can vary considerably from trial to trial as does the behavioral response to shock. The variable, non-saturating behavioral responses to the moving forward gratings and shock stimulus allow us to disambiguate sensory and motor representations across the granule cell population (Figure 4A). The motor output signal from the fish for each trial was convolved with the kinetics of the calcium indicator to produce a motor regressor that we used to identify motor-related granule cells (Figure 4B; see Supplemental Experimental Procedures). A regressor for other stimuli, such as forward visual motion, was created to identify sensory responses that would be consistent across trials.

Very high correlations could be found between the calcium signals of individual granule cells and the motor regressor across trials to the extent that all activity peaks in the calcium signal align with an episode of swimming (Figures 4B and 4C). A single granule cell can therefore encode the motor activity of the animal irrespective of the sensory stimulus that produces the behavioral response (moving gratings or shock). We hypothesize that these granule cells are receiving motor efference copies and thus coding for the motor activity of the animal, although these responses could also be mediated by reafferent sensory input, such as proprioception or lateral line signals. In contrast, other granule cells were identified whose activity correlated best with forward-moving gratings, regardless of the behavioral response of the fish to the gratings, suggesting that their responses were purely sensory (Figures 4B and 4C). Using this regression-based approach

---

(D) (i) Maximum projection of 212 granule cells that could be classified as sensory (forward motion or shock) or motor from behaving fish (n = 5). Pan-neuronal reference anatomy and an outline of the approximate boundary of the cerebellum are shown in gray. (ii) Single planes at different depths from the stack showing the dorsal-ventral distribution of response types. The scale bars represent 100 μm.

(E) Three example cells showing multimodal responses to (i) sensory shock and motor activity, (ii) sensory forward motion and motor activity, and (iii) sensory reverse motion and motor activity.

(F) (i) Activity from individual planes of the granule cells in (E) are concatenated and correlated with regressors for the most relevant sensory stimulus and the convolved simultaneous motor activity of the fish. Yellow trace is the convolved regressor for shock stimuli, black trace is the z scored fluorescence for the cell in (Ei) across seven planes, and gray trace is the convolved vigor regressor of behavior from these planes. The sensory regressor also appears in the middle trace as a shaded area that highlights the correlation of the granule cell activity with sensory stimuli. Open arrowheads highlight peaks that correlate with motor activity, but not sensory stimuli. Corresponding correlation coefficients of granule cell activity with the regressors are indicated. (ii and iii) The same as for (i) is shown, instead showing the activity of cells from (Eii) and (Eiii).

and a threshold for correlation coefficients to motor and sensory variables (see Supplemental Experimental Procedures), we identified granule cells from these behaving experiments whose responses to behaviorally relevant stimuli (forward gratings and shock) could be categorized either as sensory or motor related.

Mapping the locations of granule cells onto the reference anatomy revealed distinct areas occupied by these three groups (Figure 4D). Granule cells that had a sensory response to forward motion were located more dorsally than the other groups, in the LCa and medial CCe, whereas granule cells with sensory responses to shock or with motor responses were spread out in more ventral areas of the CCe as well as the EG and Va (Figure 4D). These results suggest that some of the ventrally located areas with forward-motion- or shock-excited responses mapped in Figure 3B may in fact correspond to motor responses.

Having identified several clear examples of granule cells that responded to just one of the sensory or motor variables in this experimental paradigm, we also wanted to investigate whether information from multiple sensory and/or motor streams could be encoded in individual granule cells. Although most granule cells appeared to respond to just one sensory or motor variable, our analyses revealed the presence of a small number of granule cells responding to both a sensory and motor-related stimulus (Figures 4C and 4D; see Supplemental Experimental Procedures). We hypothesized that these might be multimodal granule cells, capable of encoding (and integrating) multiple streams of sensorimotor information. We again used a regressor-based approach to determine what kinds of information putative multimodal granule cells could be encoding.

Correlations of granule cell activity signals across planes with regressors for sensory stimuli and motor activity revealed granule cells that coded for a single sensory stimulus (motion or shock) in addition to motor activity (Figures 4E and 4F). These granule cells could be identified by our methods because they appeared to combine information from these different streams in a relatively linear manner, resulting in high-correlation coefficients for both a sensory and motor regressor (Figure 4F). Furthermore, the contribution of different regressors to the overall signal could be attributed to individual peaks in the granule cell activity trace (Figure 4F). Across all behaving experiments (for which we could unambiguously identify motor-related signals), only three combinations of multimodal responses were seen in the populations, all for motor activity and an additional single sensory stimulus: shock; forward motion; or reverse motion (Figures 4E and 4F). Even in these multimodal granule cells, it appears that the presentation of a simple stimulus is sufficient to drive spiking (Figure 4F). Coincident stimuli from different modalities are therefore not necessary for these cells to reach threshold, as has also been demonstrated for sensory responses in granule cells in mice [40].

Surprisingly, no granule cells were found that coded for both luminance and motor activity despite the respectively large number of luminance-responsive granule cells that were identified (Figure 3A). Furthermore, across all behaving (n = 5 fish) and paralyzed population imaging experiments (n = 21 fish), we failed to find any granule cells that appeared to encode more than one type of sensory stimulus. Instead, all multimodal cells we identified encoded one sensory and one motor-related variable. Although for practical reasons only two sensory modalities and a limited parameter space was explored in these experiments, these results suggest that multimodality in larval zebrafish granule cells may be specialized for sensorimotor integration rather than the integration of multimodal sensory signals.

Changes in Granule Cell Sensory and Motor Representations Correlate with a Pharmacologically Induced Change in Behavioral Sensitivity

In order to investigate the behavioral relevance of the granule cell representations we observed, we developed a pharmacological protocol that elicited swimming responses to previously neutral changes in luminance. Both local unilateral (n = 8) and bilateral (n = 7) injections of 10 mM bicuculline, a GABAA receptor antagonist, led to an immediate increase in luminance-evoked swimming behavior (Figure 5A). This robust behavioral phenotype emerged rapidly following injection and then behavior returned to baseline following washout of the drug (Figure 5A). The same behavioral phenotype was observed and maintained in the continuing presence (20–30 μM bath application) of bicuculline (n = 29; data not shown).

Having established a paradigm to acutely change sensorimotor behavior, we next performed two-photon functional imaging of a single cerebellar plane in order to monitor the activity of granule cells over this time course. We observed the widespread activation of granule cells following bicuculline treatment that correlated highly with the increased behavioral responsiveness of fish to visual stimuli (Figure 5B). Many granule cells acquired responses that correlated with motor activity whereas others showed newly acquired responses to luminance (Figures 5B–5D). Electrophysiological recordings also revealed that single granule cells that were previously unresponsive to whole-field flashes started to fire strongly in response to these stimuli following bicuculline treatment (n = 3; data not shown). Although these data are only correlational in nature, they suggest that changes in behavior, here mediated by the acute pharmacological blockade of GABAergic signaling in the cerebellum, are accompanied by alteration changes in granule cell representations at both the single-cell and population level.

Cerebellar Granule Cells Show No Evidence for Temporal Patterning in the Coding of Different Stimulus Durations

Classical theories of cerebellar function predict that representations of a sensory stimulus should be both sparse across the population as well as in time. In this context, granule cells effectively act as leaky integrators whose time constants contribute to temporal patterned output of mossy fiber input [18]. We hypothesized that, by presenting simple visual stimuli (flashes) of different durations, we would elicit visual responses from granule cells with a distribution of temporal patterns. Our calcium-imaging experiments showed that responses were not sparse across the population but could not resolve to what extent an individual granule cell responds to a stimulus with a sparse, temporally patterned spiking output. We performed cell-attached and whole-cell recordings from granule cells in awake, paralyzed larvae to examine visually evoked spiking and synaptic inputs at high temporal resolution.

Contrary to the expectation that we would find diverse temporal patterning across both stimulus durations and different granule cells, we instead found that granule cells responded to

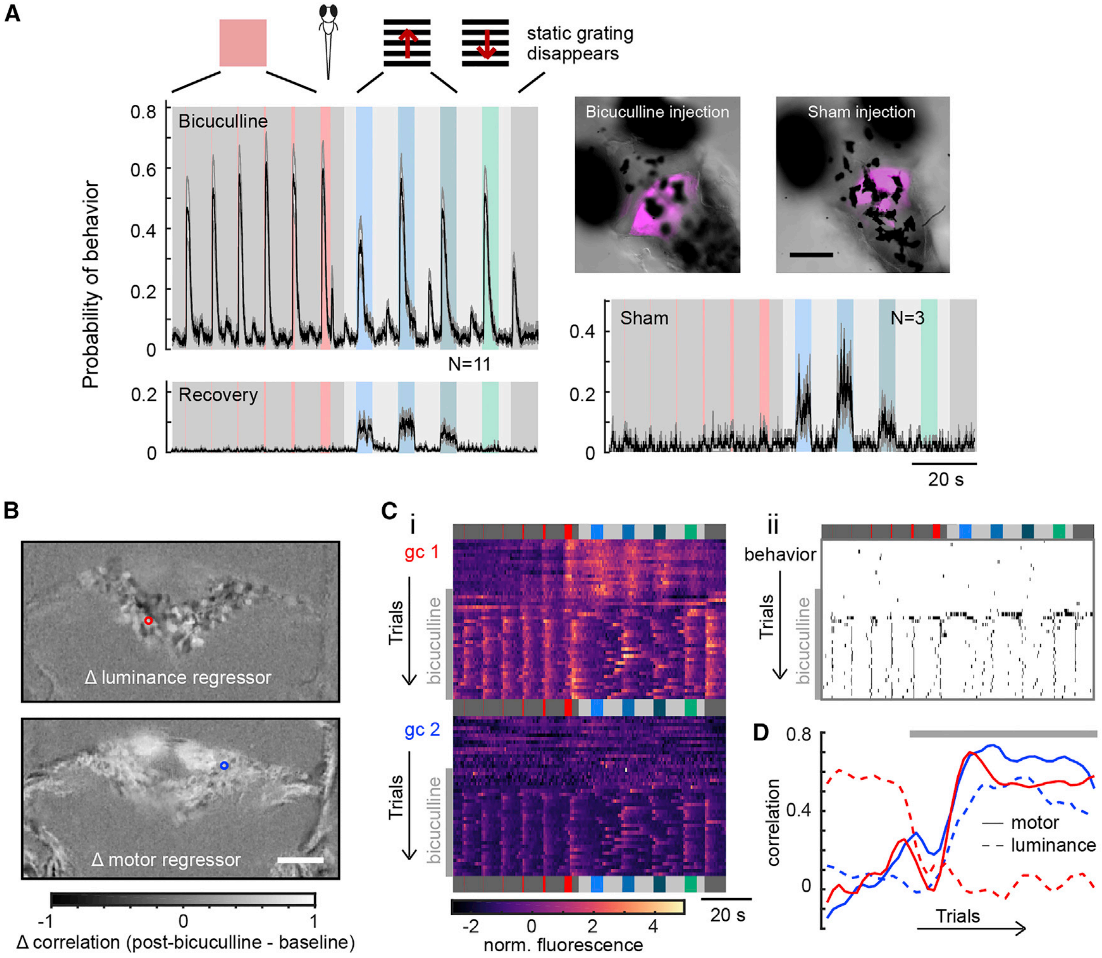

Figure 5. Changes in Granule Cell Representations Correlate with a Behavioral Change in Sensitivity to Sensory Stimuli

(A) Upper-left trace: probability of a behavioral response to visual stimuli in the ten trials immediately following injection of 10 mM bicuculline, a GABAA receptor antagonist, into the cerebellum (n = 11). The average behavior is shown with shaded SE. Note that no electrical stimulus was presented in this subset of experiments. Lower-left trace: behavioral responses in these same animals recover as bicuculline washes out. Lower-right trace: sham injections into the cerebellum failed to elicit any increase in luminance-evoked behavior. Upper right: example epifluorescence micrographs showing the extent of the bicuculline (with rhodamine) injections. The scale bar represents 100 μm. The shaded region in behavioral traces indicates the SE.

(B) Heatmaps from the same imaging plane through the granule cell layer in a 7-dpf GR152:gal4; UAS:GCaMP6s fish showing the change in pixelwise correlations to luminance (upper) and motor (lower) regressors following the addition of bicuculline. The scale bar represents 50 μm. Colored circles indicate example granule cells analyzed in subsequent panels.

(C) Heatmaps of activity from (i) two example granule cells that change their responses following the addition of bicuculline. The upper cell, gc 1, becomes less responsive to luminance and more responsive to motor activity, whereas the bottom cell, gc 2, becomes newly responsive to luminance and motor activity. Location of granule cells is shown in (B). (ii) Heatmap showing the behavioral responses over the experiment.

(D) The plotted change in regressor over trials for the two example granule cells, color coded for the two example cells as in (Ci). The gray bar indicates the presence of 30 μm bicuculline.

changes in luminance in a highly stereotyped manner with no evidence of temporal patterning. This was true for both luminance-excited (Figures 6A and 6B) and luminance-inhibited cells (Figures 6C and 6D). Both types of luminance-responsive granule cells also produced bursts of spikes during moving gratings that were fixed to the frequency of luminance transitions in either a forward or backward direction (Figures S5A–S5C), showing that their stereotyped responses to luminance were not altered by motion.

Looking across all recordings from luminance-excited cells, we see an average temporal profile of increased firing activity that begins following a short latency delay (<100 ms) and peaks several hundred milliseconds after stimulus onset (Figure 6B, left panel; n = 9). Firing rates remain elevated relative to baseline until stimulus offset, at which point they return to pre-stimulus levels within several hundred milliseconds (Figure 6B, right panel).

Luminance-inhibited granule cells, in contrast, showed a reduction in firing rate during flash stimuli from already low baseline rates to almost zero (Figures 6C and 6D, left panel; n = 6); however, this population may in fact be underestimated due to a floor effect: the difficulty in resolving small changes in firing rate from cells with an already low baseline activity. Our

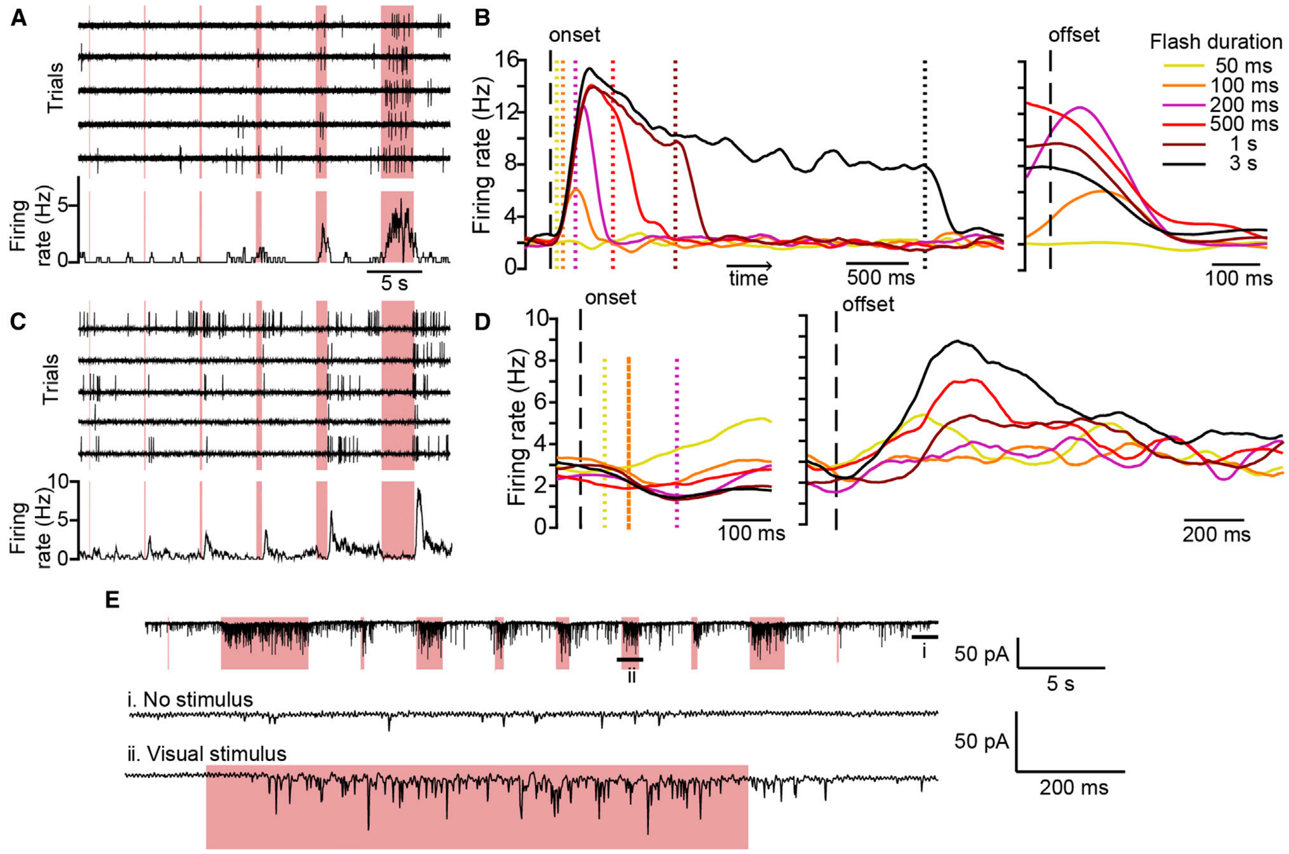

Figure 6. Granule Cells Do Not Exhibit Temporal Patterning

(A) Top: cell-attached electrophysiological recordings from a luminance-excited granule cell showing its response to whole-field flashes over five repeated trials. Bottom: average firing rate across all trials (n = 12 trials).

(B) Averaged population firing rate for the six durations of red flash stimuli from cell-attached recordings of luminance-excited granule cells (n = 9 cells) aligned to stimulus onset (left) and stimulus offset (right).

(C) Same as for (A) but showing responses from an example luminance-inhibited cell (n = 21 trials).

(D) Same as for (B) for the luminance-inhibited granule cells (n = 6 cells). See Figure S4 for additional electrophysiological recordings and analyses from luminance-, motion-, and shock-responsive cells.

(E) Whole-cell patch-clamp recording from a luminance-excited granule cell held at −65 mV. The upper trace shows an overview of responses to red flashes of varying durations. (i) Expanded view from the upper trace shows baseline activity. (ii) Expanded view from the upper trace shows the sustained increase in synaptic currents during a 1-s red flash.

See also Figures S5 and S6.

electrophysiological recordings revealed an interesting additional feature of luminance-inhibited granule cells, the presence of a post-stimulus rebound increase in firing (Figures 6C and 6D). The firing rate rebounded strongly in a period several hundred milliseconds following stimulus offset, to a maximum firing rate that scaled with longer periods of inhibition as determined by stimulus duration (Figure 6D).

Whereas the firing rates of luminance-excited and inhibited cells did not further increase or decrease, respectively, beyond 500 ms, rebound spiking in the latter group reached firing rates that increased linearly with stimulus duration (Figure S4D). Further whole-cell electrophysiological analyses of these cells is needed to determine whether the post-inhibitory rebound is due to intrinsic or synaptic properties, but this may be one way in which either the representation of a stimulus can be expanded in time following stimulus offset or the duration of the preceding flash may be decoded by measuring the magnitude of the rebound.

Additional cell-attached recordings were obtained from granule cells with other response profiles, including forward-motion-excited (n = 5) and shock-excited (n = 6) cells (Figure S5). The spiking of cells to their preferred stimulus within a response type was highly stereotyped with respect to temporal patterning, tuning preference, latency to the first spike, and change in gain of firing during their preferred stimulus (Figure S5). The temporal profile of these responses were furthermore consistent across repeated trials for a given granule cell (Figure S6).

In order to examine the temporal patterning of inputs to granule cells in more detail, we obtained a whole-cell recording from a luminance-excited granule cell while presenting whole-field flashes of ten different durations, ranging from 50 ms to 5 s (Figure 6E). The frequency of excitatory synaptic input to this cell is low at baseline but increases strongly in response to whole-field flashes. The temporal patterning of the synaptic input during stimulus presentation closely matches the firing patterns seen in the cell-attached recordings as well as recordings from other granule cells [10, 17]. These data support previous observations that the relationship between granule cells depolarization and spiking output is fairly linear during low-intensity sensory activation [14, 15]. In summary, our electrophysiological data show that luminance-responsive granule cells can encode the presence of a visual stimulus, such as a whole-field flash, by increasing or decreasing their firing rate over this same duration but do not produce further temporal patterning.

DISCUSSION

Granule Cell Population Recordings in the Behaving Animal

Decades of cerebellar research led to an intricate understanding of cerebellar anatomy and considerable knowledge about the physiological properties, including synaptic plasticity, of the principal cell types. In parallel with these studies, elegant theories of how cerebellar circuits carry out motor control and learning have been proposed [1–3]. In particular, a central tenet of cerebellar theory proposes that the role of the granule cell layer is to produce a sparse, high-dimensional, temporally patterned recoding of incoming mossy fiber signals. Our large-scale functional imaging of the cerebellar granule cell population in the awake, behaving zebrafish instead reveals a dense, low-dimensional representation of sensory and motor information that together with electrophysiological data shows no evidence of temporal patterning. Instead, many granule cells are strongly driven to fire in a stereotyped manner by a preferred sensory or motor stimulus.

Granule Cell Representations Are Sparse and Low Dimensional

The notion that granule cell representations should be sparse has pervaded theories of cerebellar function. At a population level, a sparse-dispersed code is one in which many neurons are available yet only a small subset is active in response to a given stimulus and different stimuli activate different subsets [41]. However, establishing population sparseness requires the monitoring of activity throughout the whole population of neurons. Our experimental stimuli explored a limited parameter space within only two sensory modalities in addition to motor-related inputs, yet our imaging results show that a large percentage of the overall population of granule cells responds to a given stimulus. However, in agreement with the idea that representations are dispersed across the population, we do find that the overwhelming majority of granule cells respond to a single stimulus in our experiments and thus belong clearly to one functional "subset" of the population.

The large number of luminance-responsive granule cells is unexpected given the expectation of sparse coding in the cerebellar input layer (but see [42]) and the lack of a behavioral response in larval zebrafish to our presentation of whole-field flashes. Nonetheless, from larval stages, zebrafish do show a robust preference for light areas over dark and produce a startle response following large, abrupt changes in light intensity [36]. This suggests that relatively simple visual information, such as luminance levels, have a high ethological relevance for the larval zebrafish. In accordance with this, a red flash has been successfully used as a conditioned stimulus to drive behavior in associative learning in zebrafish larvae [30]. Although the sparseness of representations in the zebrafish cerebellum may change during further development, our findings provide evidence for dense representations of sensory and motor information at a stage in which the zebrafish cerebellum is needed for sensorimotor adaptation and associative learning.

A different notion of sparseness applies to an individual neuron's activity, that of lifetime sparseness [41]. For a neuron to be sparse in this sense, it should be strongly activated in the presence of its preferred stimulus but otherwise fire only rarely. It has been shown that granule cells have a very low basal firing rate but can fire readily with single presynaptic mossy fiber activation, allowing granule cells to relay incoming sensory or motor information to downstream Purkinje cells with high fidelity [40]. Our experiments reveal granule cells with a range of low to moderate baseline firing rates that switched to firing at relatively high frequencies in response to their preferred stimulus, suggesting that these response profiles indeed showed lifetime sparseness.

Granule Cells Do Not Exhibit Temporal Patterning

The extremely high stereotypy of responses across granule cells as measured by both electrophysiology and calcium imaging suggests that these cells may not exhibit diverse temporal patterning in response to simple stimuli, in contrast to observations in some other systems [43]. Instead, granule cell spiking under the conditions of low to moderate sensory stimulation in our study may faithfully follow the timing of mossy fiber excitation as has been shown in the responses of mammalian granule cells to somatosensory stimulation [14, 15]. More work is needed to characterize the physiology of mossy fiber inputs to granule cells in order to understand how incoming information is transformed by or represented in granule cells.

Certainly, if all luminance-responsive granule cells encode luminance parameters in the same stereotyped way, it is not clear how sensorimotor calibration/adaptation would proceed. Nonetheless, because larval zebrafish are capable of visually guided motor adaptation [29, 44] and cerebellar-dependent associative learning of a visual stimulus [30], this suggests that motor learning can nonetheless occur within this framework. Granule cells in the zebrafish cerebellum may produce temporally patterned responses in other experimental paradigms, at later developmental stages or after a given stimulus acquires behavioral relevance. Having characterized the responses of granule cells in the naive animal to relatively simple, low-dimensional stimuli, we now have a basis from which to explore possible higher-dimensional representations that could be engaged in motor adaptation and learning in the awake, behaving zebrafish.

A Small Number of Granule Cells Show Multimodal Responses that May Preferentially Integrate Sensory and Motor Information

In our study, most granule cells have activity across trials that correlates very well with a single sensory or motor variable in our experimental paradigm but rarely multiple modalities of those tested. Indeed, the anatomy of these granule cells, which have on average of just two or three claws (rather than the typical four found across mammalian species), suggests that the opportunities for multimodality in these cells' inputs is more limited. Although our electrophysiological recordings could not extensively sample across the entire cerebellum, our population imaging experiments found only a small number of multimodal granule cells despite the wide coverage. We could not probe all sensory modalities in this study; however, it is revealing that, of the large number of granule cells that we observed that responded to changes in luminance, not a single one of these cells also had responses to shock or to motor activity, despite these responses also being present in large numbers of granule cells. It has been previously shown that multiple inputs to granule cells can carry information from the same sensory modality, thereby increasing the signal to noise ratio for a particular stimulus [14, 15]. This apparent trade-off between coincidence detection and robust signal processing may explain why functional studies have found the percentage of multimodal granule cells to vary greatly depending on the specific cerebellar region and modalities being tested [11, 15, 45].

We found no granule cells that were responsive to more than one type of sensory stimulus presented, yet we nonetheless identified some granule cells that encode information about both sensory and motor information by using sensory stimuli that were carefully titrated to make it possible to disambiguate these variables in the responses. We believe that the motor-related activity observed here resembles a motor efference copy that is sent to the granule cell layer [46], although we cannot rule out a contribution of lateral line or mechanosensory inputs. We are only just starting to understand which aspects of motor output are encoded in the activity of cerebellar neurons, including granule cells [17]; however, our findings raise interesting considerations about how granule cells may carry out sensorimotor coordinate transformations by simultaneously coding for sensory and motor variables [47]. Our pharmacological experiments furthermore revealed large changes in sensorimotor representations in granule cells during a pharmacologically induced behavioral sensitization, representing the first step toward characterizing how sensorimotor variables specific for both innate and newly acquired behaviors are encoded in the cerebellum. These findings provide evidence for sensory and motor integration in single granule cells but in general suggest that the zebrafish cerebellum may be better suited in this context to reliably transmit sensory or motor-related signals than perform coincidence detection. Future work exploring responses to a broader set of sensory stimuli in the larvae or using anatomical methods to map mossy fiber inputs to single cells will allow us to better characterize the degree to which multimodality is a common property of granule cells in the zebrafish cerebellum.

Maps and Topography

The mapping of granule cell proprioceptive and tactile receptive fields using classical electrophysiology suggested the presence of a "fractured" somatotopic map present in the cerebellar input layer [48], although it is unclear whether these maps are actually present under physiological conditions [49]. Due to the difficulty of recording sensory responses from the cerebellum in the awake animal, there is little knowledge of the fine-scale mapping of other sensory modalities, such as vision or audition across the granule cell layer. Here, we reveal a map of activation in the granule cell layer, where responses to different modalities are clustered within subregions of the input layer. Matsui et al. [27] have previously mapped Purkinje cell activity during the optomotor (OMR) and optokinetic responses (OKR) in the larval zebrafish cerebellum, revealing loci of activity in distinctive rostromedial and caudal areas of the cerebellum, respectively. In keeping with these findings, our results show that the parallel fibers of granule cells responding to forward-moving stimuli (that evoke OMR) pass through the medial cerebellum. Furthermore, our functional imaging revealed many active putative presynaptic parallel fiber terminals in this area that could contact Purkinje cell dendrites. These converging results support a modular organization of the larval zebrafish cerebellum where distinct regions may be involved in controlling different sensorimotor behaviors.

We also show that a clear lateralization of information is present within the visually responsive subregion, suggesting that incoming mossy fiber afferents are ordered with respect to the visual world. Nevertheless, as all retinal ganglion cell axons in zebrafish cross the midline and the granule cell visual receptive fields are not purely contralateral, this indicates that the cerebellum receives visual information that has already undergone a certain level of spatial processing. This work provides a functional map of visual-, shock-, and motor-related input to the granule cell layer and underscores a need to understand the mapping of diverse presynaptic inputs onto individual and potentially multimodal granule cells.

Outlook

In summary, by leveraging the possibilities offered by larval zebrafish as a vertebrate model organism, in this study, we were able to monitor the activity of most cerebellar granule cells in an animal while it performed a sensorimotor behavior. By characterizing the responses at a population level, we were able to observe that these neurons are highly organized according to sensory stimulus, visual receptive field, and behavioral relevance of the stimulus. Our results reveal representations that are dense at the population level and at the individual level show little to no temporal patterning at a stage when the larval zebrafish is capable of performing cerebellar-dependent sensorimotor adaptation and learning. As the zebrafish cerebellum matures, we may expect structural and functional changes in these circuits with concomitant changes in sparseness, multimodality, and temporal patterning [50]. In particular, the characteristics of granule cell coding may change to support the growing behavioral complexity of the animal. Although the study raises many questions, we believe that it provides valuable insights that will help us understand the sensorimotor transformations that occur at the granule cell layer and in the vertebrate cerebellum as a whole.

EXPERIMENTAL PROCEDURES

A mix of Tuepfel long-fin (TL) wild-type strain as well as the following transgenic lines were used for experiments: Tg(gSA2AzGFF152B), Tg(gSAIzGFFM765B), Tg(gSAG6A), Tg(gSAIGFF23C), Tg(SAGFF(LF)128A), Tg(hspGFF57A), Tg(SAGFF(LF)157B), and Tg(hspGFFDMC90A), acquired from M. Hibi and K. Kawakami [32]. All experiments were performed using larvae at 6 and 7 dpf in accordance with approved protocols set by the Max Planck Society and the Regierung von Oberbayern. Anatomical labeling, behavior, functional imaging, electrophysiology, and data analysis are described in Supplemental Experimental Procedures.

SUPPLEMENTAL INFORMATION

Supplemental Information includes Supplemental Experimental Procedures, six figures, and three movies and can be found with this article online at http://dx.doi.org/10.1016/j.cub.2017.03.029.

AUTHOR CONTRIBUTIONS

L.D.K. and R.P. designed the study and experiments with help from E.I.D. L.D.K. and E.I.D. performed the imaging experiments. L.D.K. performed the electrophysiology experiments. R.P. wrote the data acquisition and analysis software, with help from L.D.K. and V.Š. L.D.K. and R.P. performed data analysis, with help from E.I.D. and V.Š. D.A.M. performed single-cell labeling of granule cells and tracing of dendritic and axonal projections. L.D.K. and R.P. wrote the manuscript with help from all authors.

ACKNOWLEDGMENTS

All experiments were approved by the Regierung von Oberbayern via the TVA 55-2-1-54-2532-101-12 and 55-2-1-54-2532-82-2016. We thank Axel Borst, Winfried Denk, Nadine Gogolla, Andreas Kist, Tugce Yildizoglu, and Patricia Cooney for useful discussions. We thank Eva Laurell for generous assistance with anatomical experiments in 21 dpf fish. We thank Isaac Bianco for sending us the pCS2-GAP43-GFP/mCherry electroporation constructs, Koichi Kawakami and Masahiko Hibi for sharing transgenic fish lines, and Emre Aksay for discussing his unpublished data with us. We thank Alexander Arenz, James Fitzgerald, Martin Haesemeyer, and Tobias Bonhoeffer for critical comments on early versions of the manuscript. L.D.K. was funded by the Humboldt Foundation, Carl von Siemens Foundation, and Max Planck Gesellschaft (MPG). E.I.D. and V.Š. were funded by the GSN and MPG. D.A.M. was funded by the IMPRS and MPG. R.P. was funded by the MPG.

Received: November 11, 2016
Revised: February 24, 2017
Accepted: March 14, 2017
Published: April 20, 2017

REFERENCES

1. Ito, M. (2006). Cerebellar circuitry as a neuronal machine. Prog. Neurobiol. *78*, 272–303.
2. Marr, D. (1969). A theory of cerebellar cortex. J. Physiol. *202*, 437–470.
3. Albus, J.S. (1971). A theory of cerebellar function. Math. Biosci. *10*, 25–61.
4. Eccles, J.C., Ito, M., and Szentágothai, J. (1967). The Cerebellum as a Neuronal Machine (Springer).
5. Galliano, E., Gao, Z., Schonewille, M., Todorov, B., Simons, E., Pop, A.S., D'Angelo, E., van den Maagdenberg, A.M.J.M., Hoebeek, F.E., and De Zeeuw, C.I. (2013). Silencing the majority of cerebellar granule cells uncovers their essential role in motor learning and consolidation. Cell Rep. *3*, 1239–1251.
6. Rosenblatt, F. (1958). The perceptron: a probabilistic model for information storage and organization in the brain. Psychol. Rev. *65*, 386–408.
7. Ohyama, T., Nores, W.L., Murphy, M., and Mauk, M.D. (2003). What the cerebellum computes. Trends Neurosci. *26*, 222–227.
8. Johansson, F., Jirenhed, D.-A., Rasmussen, A., Zucca, R., and Hesslow, G. (2014). Memory trace and timing mechanism localized to cerebellar Purkinje cells. Proc. Natl. Acad. Sci. USA *111*, 14930–14934.
9. Chadderton, P., Margrie, T.W., and Häusser, M. (2004). Integration of quanta in cerebellar granule cells during sensory processing. Nature *428*, 856–860.
10. Arenz, A., Silver, R.A., Schaefer, A.T., and Margrie, T.W. (2008). The contribution of single synapses to sensory representation in vivo. Science *321*, 977–980.
11. Ishikawa, T., Shimuta, M., and Häusser, M. (2015). Multimodal sensory integration in single cerebellar granule cells in vivo. eLife *4*, e12916.
12. Chabrol, F.P., Arenz, A., Wiechert, M.T., Margrie, T.W., and DiGregorio, D.A. (2015). Synaptic diversity enables temporal coding of coincident multisensory inputs in single neurons. Nat. Neurosci. *18*, 718–727.
13. Huang, C.C., Sugino, K., Shima, Y., Guo, C., Bai, S., Mensh, B.D., Nelson, S.B., and Hantman, A.W. (2013). Convergence of pontine and proprioceptive streams onto multimodal cerebellar granule cells. eLife *2*, e00400.
14. Bengtsson, F., and Jörntell, H. (2009). Sensory transmission in cerebellar granule cells relies on similarly coded mossy fiber inputs. Proc. Natl. Acad. Sci. USA *106*, 2389–2394.
15. Jörntell, H., and Ekerot, C.-F. (2006). Properties of somatosensory synaptic integration in cerebellar granule cells in vivo. J. Neurosci. *26*, 11786–11797.
16. Ozden, I., Dombeck, D.A., Hoogland, T.M., Tank, D.W., and Wang, S.S.-H. (2012). Widespread state-dependent shifts in cerebellar activity in locomoting mice. PLoS ONE *7*, e42650.
17. Powell, K., Mathy, A., Duguid, I., and Häusser, M. (2015). Synaptic representation of locomotion in single cerebellar granule cells. eLife *4*, 1–18.
18. Dean, P., Porrill, J., Ekerot, C.-F., and Jörntell, H. (2010). The cerebellar microcircuit as an adaptive filter: experimental and computational evidence. Nat. Rev. Neurosci. *11*, 30–43.
19. Volkmann, K., Rieger, S., Babaryka, A., and Köster, R.W. (2008). The zebrafish cerebellar rhombic lip is spatially patterned in producing granule cell populations of different functional compartments. Dev. Biol. *313*, 167–180.
20. Bae, Y.K., Kani, S., Shimizu, T., Tanabe, K., Nojima, H., Kimura, Y., Higashijima, S., and Hibi, M. (2009). Anatomy of zebrafish cerebellum and screen for mutations affecting its development. Dev. Biol. *330*, 406–426.
21. Hamling, K.R., Tobias, Z.J.C., and Weissman, T.A. (2015). Mapping the development of cerebellar Purkinje cells in zebrafish. Dev. Neurobiol. *75*, 1174–1188.
22. Hsieh, J.Y., Ulrich, B., Issa, F.A., Wan, J., and Papazian, D.M. (2014). Rapid development of Purkinje cell excitability, functional cerebellar circuit, and afferent sensory input to cerebellum in zebrafish. Front. Neural Circuits *8*, 147.
23. Sengupta, M., and Thirumalai, V. (2015). AMPA receptor mediated synaptic excitation drives state-dependent bursting in Purkinje neurons of zebrafish larvae. eLife *4*, 1–21.
24. Borla, M.A., Palecek, B., Budick, S., and O'Malley, D.M. (2002). Prey capture by larval zebrafish: evidence for fine axial motor control. Brain Behav. Evol. *60*, 207–229.
25. McKay, B.E., and Turner, R.W. (2005). Physiological and morphological development of the rat cerebellar Purkinje cell. J. Physiol. *567*, 829–850.
26. Scalise, K., Shimizu, T., Hibi, M., and Sawtell, N.B. (2016). Responses of cerebellar Purkinje cells during fictive optomotor behavior in larval zebrafish. J. Neurophysiol. *116*, 2067–2080.
27. Matsui, H., Namikawa, K., Babaryka, A., and Köster, R.W. (2014). Functional regionalization of the teleost cerebellum analyzed in vivo. Proc. Natl. Acad. Sci. USA *111*, 11846–11851.
28. Portugues, R., Feierstein, C.E., Engert, F., and Orger, M.B. (2014). Whole-brain activity maps reveal stereotyped, distributed networks for visuomotor behavior. Neuron *81*, 1328–1343.
29. Ahrens, M.B., Li, J.M., Orger, M.B., Robson, D.N., Schier, A.F., Engert, F., and Portugues, R. (2012). Brain-wide neuronal dynamics during motor adaptation in zebrafish. Nature *485*, 471–477.
30. Aizenberg, M., and Schuman, E.M. (2011). Cerebellar-dependent learning in larval zebrafish. J. Neurosci. *31*, 8708–8712.

31. Altman, J. (1982). Morphological development of the rat cerebellum and some of its mechanisms. Exp. Brain Res. *6*, 8–49.
32. Takeuchi, M., Matsuda, K., Yamaguchi, S., Asakawa, K., Miyasaka, N., Lal, P., Yoshihara, Y., Koga, A., Kawakami, K., Shimizu, T., and Hibi, M. (2015). Establishment of Gal4 transgenic zebrafish lines for analysis of development of cerebellar neural circuitry. Dev. Biol. *397*, 1–17.
33. Palay, S.L., and Chan-Palay, V. (2012). Cerebellar Cortex: Cytology and Organization (Springer Science & Business Media).
34. Billings, G., Piasini, E., Lőrincz, A., Nusser, Z., and Silver, R.A. (2014). Network structure within the cerebellar input layer enables lossless sparse encoding. Neuron *83*, 960–974.
35. Burgess, H.A., and Granato, M. (2007). Modulation of locomotor activity in larval zebrafish during light adaptation. J. Exp. Biol. *210*, 2526–2539.
36. Easter, S.S., Jr., and Nicola, G.N. (1996). The development of vision in the zebrafish (Danio rerio). Dev. Biol. *180*, 646–663.
37. D'Angelo, E., De Filippi, G., Rossi, P., and Taglietti, V. (1995). Synaptic excitation of individual rat cerebellar granule cells in situ: evidence for the role of NMDA receptors. J. Physiol. *484*, 397–413.
38. Apps, R., and Hawkes, R. (2009). Cerebellar cortical organization: a one-map hypothesis. Nat. Rev. Neurosci. *10*, 670–681.
39. Mauk, M.D., Medina, J.F., Nores, W.L., and Ohyama, T. (2000). Cerebellar function: coordination, learning or timing? Curr. Biol. *10*, R522–R525.
40. Rancz, E.A., Ishikawa, T., Duguid, I., Chadderton, P., Mahon, S., and Häusser, M. (2007). High-fidelity transmission of sensory information by single cerebellar mossy fibre boutons. Nature *450*, 1245–1248.
41. Willmore, B., and Tolhurst, D.J. (2001). Characterizing the sparseness of neural codes. Network *12*, 255–270.
42. Spanne, A., and Jörntell, H. (2015). Questioning the role of sparse coding in the brain. Trends Neurosci. *38*, 417–427.
43. Kennedy, A., Wayne, G., Kaifosh, P., Alviña, K., Abbott, L.F., and Sawtell, N.B. (2014). A temporal basis for predicting the sensory consequences of motor commands in an electric fish. Nat. Neurosci. *17*, 416–422.
44. Portugues, R., and Engert, F. (2011). Adaptive locomotor behavior in larval zebrafish. Front. Syst. Neurosci. *5*, 72.
45. Sawtell, N.B. (2010). Multimodal integration in granule cells as a basis for associative plasticity and sensory prediction in a cerebellum-like circuit. Neuron *66*, 573–584.
46. Gao, Z., Proietti-Onori, M., Lin, Z., Ten Brinke, M.M., Boele, H.J., Potters, J.W., Ruigrok, T.J.H., Hoebeek, F.E., and De Zeeuw, C.I. (2016). Excitatory cerebellar nucleocortical circuit provides internal amplification during associative conditioning. Neuron *89*, 645–657.
47. Pouget, A., Deneve, S., and Duhamel, J.-R. (2002). A computational perspective on the neural basis of multisensory spatial representations. Nat. Rev. Neurosci. *3*, 741–747.
48. Shambes, G.M., Gibson, J.M., and Welker, W. (1978). Fractured somatotopy in granule cell tactile areas of rat cerebellar hemispheres revealed by micromapping. Brain Behav. Evol. *15*, 94–140.
49. Manni, E., and Petrosini, L. (2004). A century of cerebellar somatotopy: a debated representation. Nat. Rev. Neurosci. *5*, 241–249.
50. Gao, Z., van Beugen, B.J., and De Zeeuw, C.I. (2012). Distributed synergistic plasticity and cerebellar learning. Nat. Rev. Neurosci. *13*, 619–635.

Current Biology, Volume *27*

Supplemental Information

Sensorimotor Representations in Cerebellar Granule Cells in Larval Zebrafish Are Dense, Spatially Organized, and Non-temporally Patterned

Laura D. Knogler, Daniil A. Markov, Elena I. Dragomir, Vilim Štih, and Ruben Portugues

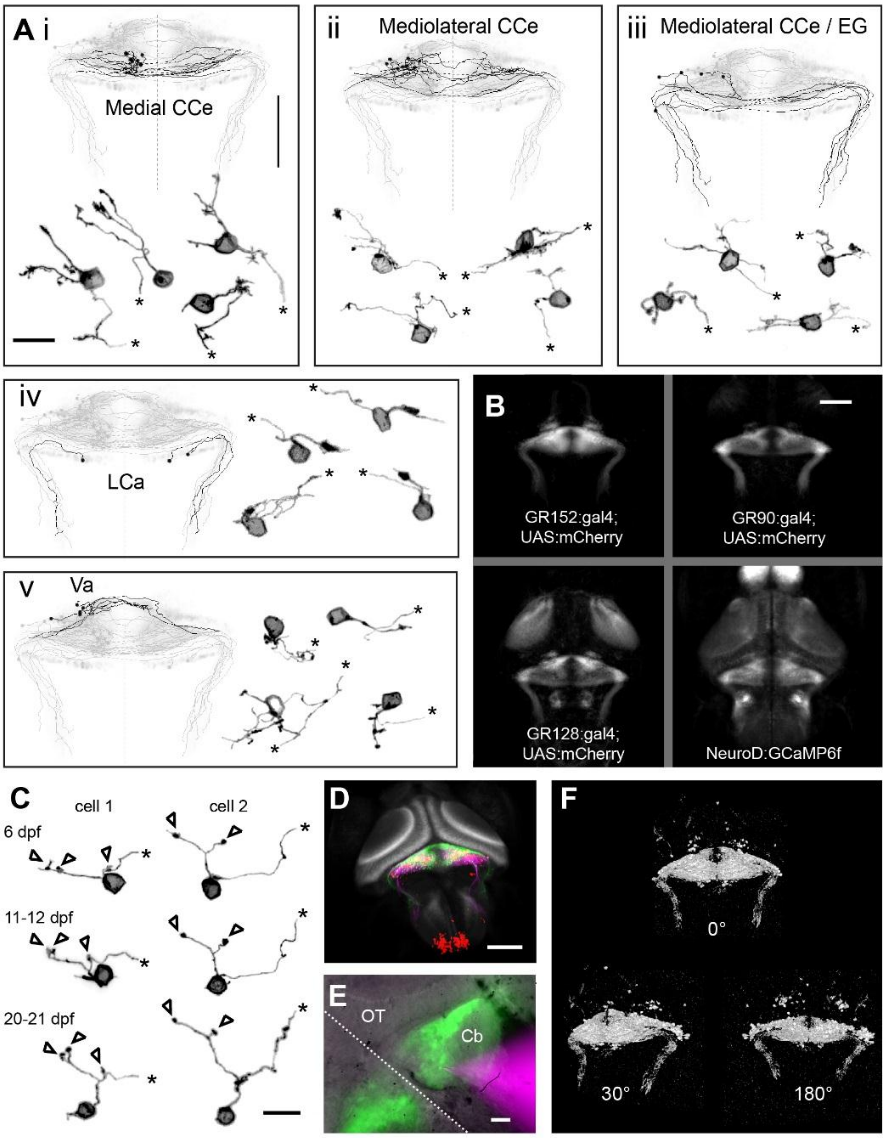

Figure S1. Detailed morphology of individual granule cells and transgenic populations. Related to Figure 1.
Ai-v) Example additional dendritic morphologies of twenty granule cells are grouped by somata location and axonal projection (refer to Figure 1 for information on abbreviated anatomical regions). Truncated parallel fibers in the detailed morphology are indicated by asterisks. Scale bar = 10 microns. The traced parallel fiber projections (shown in black) for these cells and others with somata in the same region are morphed to a common reference anatomy (shown in grey). Scale bar = 100 microns for the parallel fiber overviews. **B)** Z-projections of confocal stacks from transgenic lines labeling the granule cells used in our experiments. Morphologies were obtained from (clockwise, starting at upper left) N= 6, 5, 3, and 2 fish. Scale bar = 100 microns. **C)** Dendritic morphology of two granule cells in the CCe at three developmental time points showing the stability of dendritic claw number and overall morphology. Scale bar = 10 microns. **D)** Tilted view showing pan-neuronal GCaMP6f in the zebrafish brain in grey (the moon-shaped optic tecta are very salient). The cerebellum has a stereotypical tri-layered configuration where the granule cell layer (green) sends parallel fibers to the molecular layer, where they contact the dendrites of

the Purkinje cells (magenta). Inferior olivary neurons (red) also provide inputs to the Purkinje cells. Scale bar = 100 microns. **E)** Composite whole-field image from a cell-attached electrophysiological recording of a granule cell. A large granule cell population is labelled by GR90:gal4;UAS:GFP (in green), the pipette (with intracellular solution containing sulforhodamine dye) is labelled in magenta, and the bright-field anatomy is shown in grey. Scale bar = 20 microns. **F)** Whole-brain imaging of fish expressing GCaMP6s in granule cells provided datasets such as the one shown here that can be easily segmented functionally by using local fluorescence correlations. All the significantly active voxels for one experiment are shown here at three different roll angles: 0 degrees (from above) showing parallel fibers, 30 degrees and 180 degrees (from below) showing granule cell somata (see also Movie S1). Scale same as for (B).

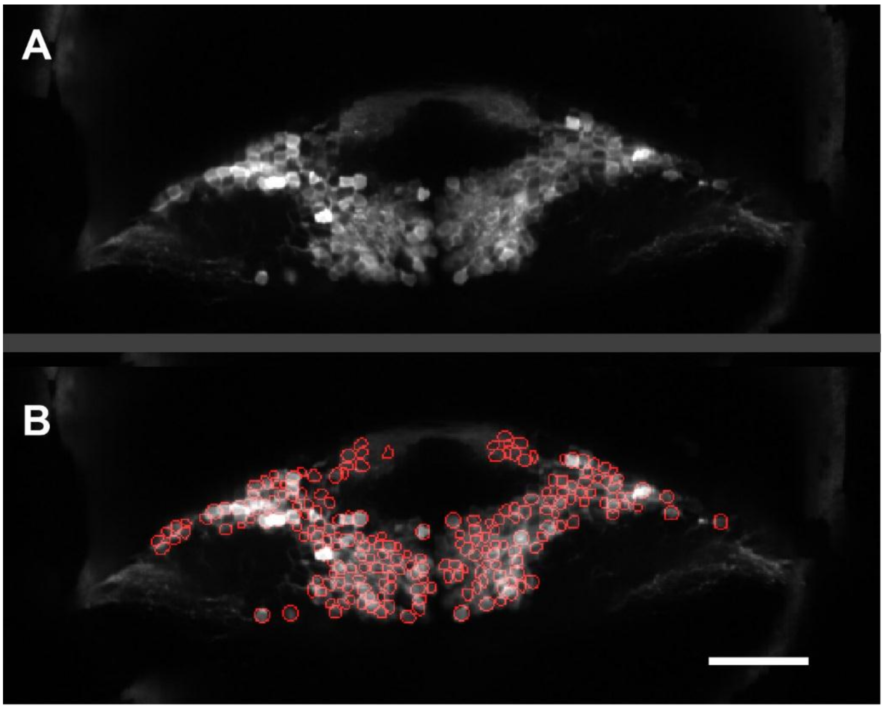

Figure S2. Automated segmentation of granule cell somata from whole-brain imaging data. Related to Figure 2.

A) Anatomical image of one imaging plane through the granule cell layer. **B)** Same plane with automated anatomical segmentation of granule cell somata indicated by red circles. In this plane, 252 cells were segmented. Scale bar = 50 microns.

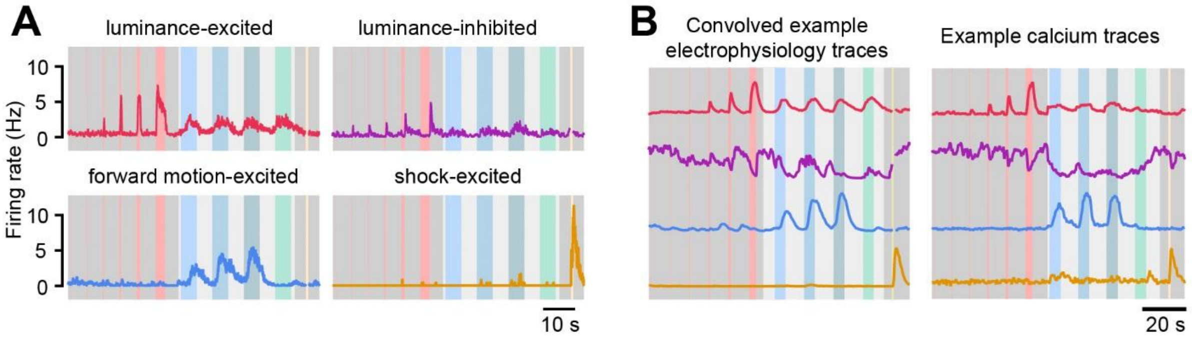

Figure S3. Electrophysiological recordings of spiking in granule cells show activity patterns corresponding to those obtained in functional imaging. Related to Figures 2 and 3.
A) Average granule cell firing rates in response to the stimuli presented (see Figure 2A) from four cell-attached electrophysiological recordings. These plots are color-coded to reflect activity that corresponds to different response types. **B)** Left, the recordings in (A) convolved with a kernel that mimics the GCaMP6s kinetics. Right, example granule cell activity traces from functional imaging show very similar responses as convolved granule cell spiking.

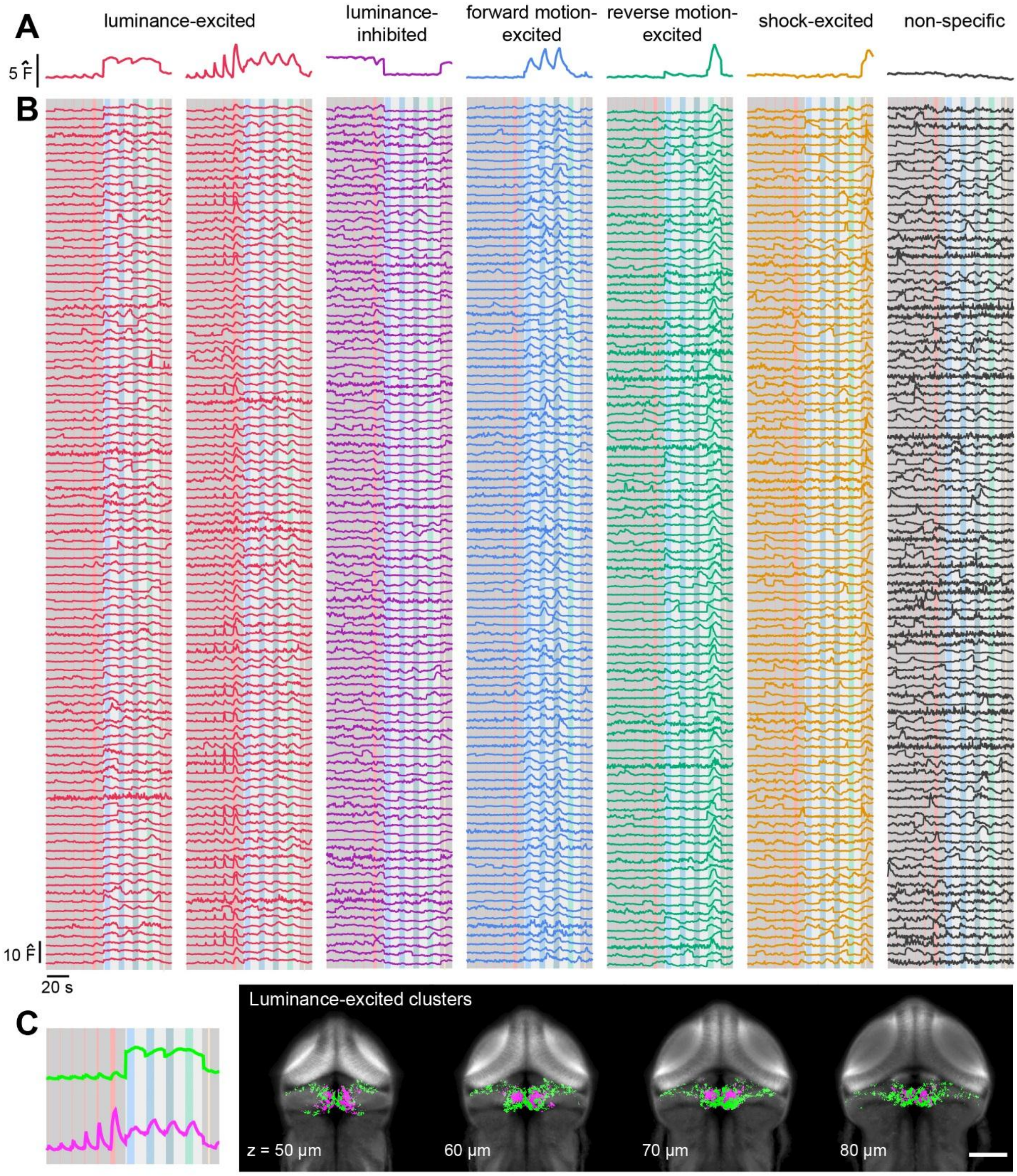

Figure S4. Detailed examination of response profiles within a cluster. Related to Figure 3.
A) The average response profile is shown for the seven granule cell clusters labelled as for Figure 3A. **B)** Each column shows the z-scored activity traces from one hundred randomly selected cells belonging to the cluster shown in (A). **C)** Left, based on their shared functional increase in activity when luminance increases, we group the two clusters of luminance-excited cells together in this study. Right, anatomical clustering of these two profiles separately (equivalent to the combined red cluster in Figure 3B) shows differences in location, with the smaller, magenta cluster more medially-located.

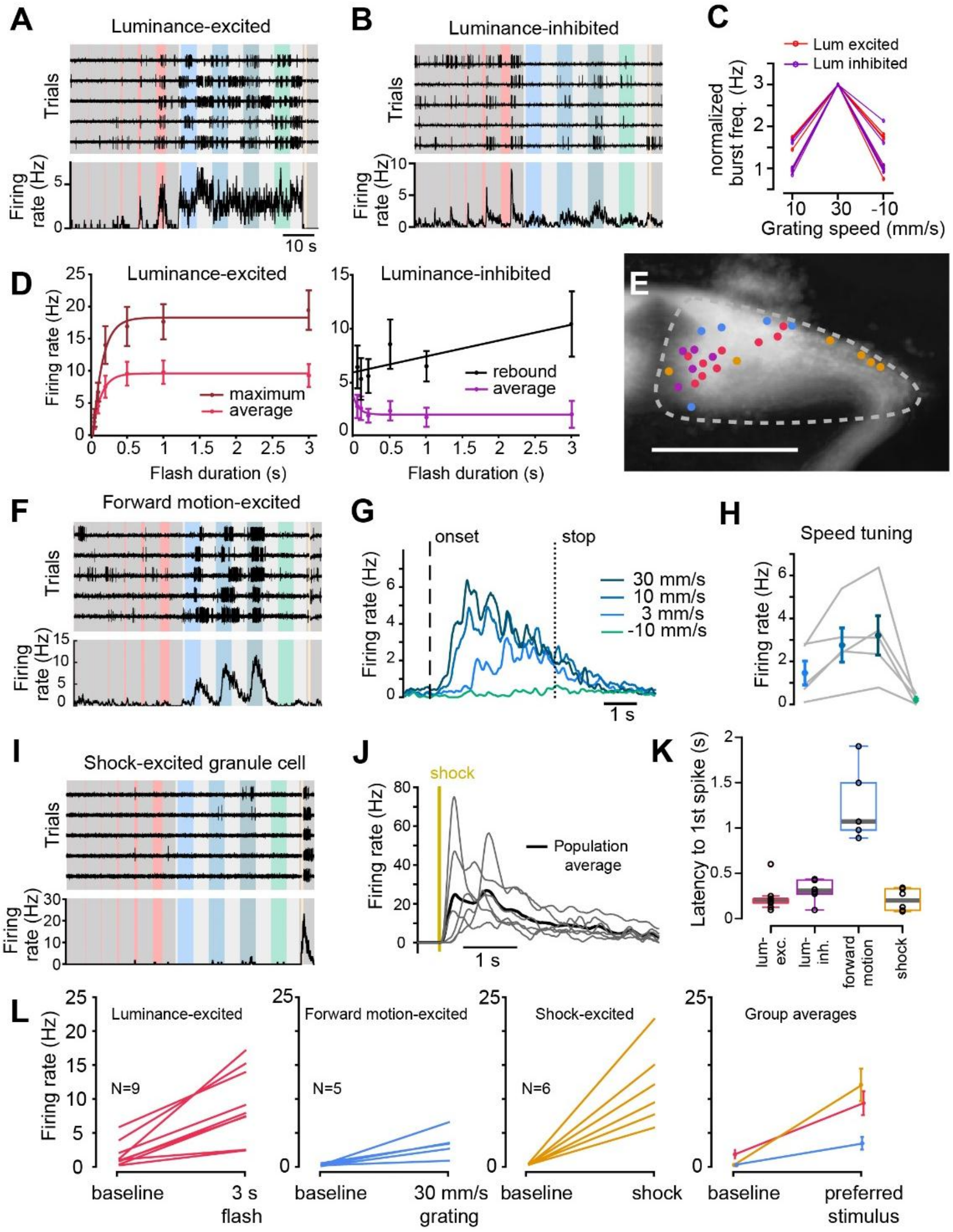

Figure S5. Granule cells show stereotyped temporal responses within a stimulus modality. Related to Figure 3 and Figure 6.

A) Upper panel, cell-attached electrophysiological recordings from a luminance-excited granule cell showing its response to stimuli over five repeated trials. A 500 ms period following the shock stimulus is blanked to remove the stimulus artifact. Lower panel, average firing rate of this granule cell across all trials. **B)** Same as for (A), instead showing an example luminance-inhibited cell. **C)** The relationship between burst frequency and grating speed in all luminance-responsive cells shows that these bursts depend on the frequency of the moving bars and not their direction of motion (n=9 luminance-excited; n=6 luminance-inhibited). **D)** Left, cells with luminance-excited responses saturate both their average and maximum firing rate with increasing stimulus duration beyond 200-500 ms. Right, cells with luminance-inhibited responses show a saturating decrease in average firing rate with increasing stimulus duration beyond 200ms however rebound excitation following inhibition increases linearly with longer durations. Data are represented as mean ± SEM and are fit with least-squares nonlinear curves or a straight line as appropriate. **E)** granule cell locations from all electrophysiological recordings mapped onto the reference anatomy and color-coded according to response profile (see Figure 3 for details). Scale bar is 100 microns. **F)** Same as for (A), instead showing an example forward motion-excited cell. **G)** Averaged population firing rate and **H)** Speed tuning curves for all electrophysiological recordings from motion-selective cells (n=5). Mean ± SEM across all fish is displayed in color. **i)** Same as for (A), instead showing an example shock-excited cell. **J)** Average firing rate in response to the shock stimulus from all cell-attached recordings of shock-excited granule cells (n=6). The population average is shown in black and appears to have multiple peaks due to the variability in the timing of an individual cell's response, which may reflect experimental variability in the placement of the electrodes relative to the cell being recorded. **K)** The first spike following preferred stimulus onset occurs with an average latency of several hundred milliseconds for luminance- and shock-responses, but with a much longer latency for cells that respond to forward motion. Grey center lines show the means; box limits indicate the 25th and 75th percentiles; whiskers extend 1.5 times the interquartile range from the 25th and 75th percentiles; data points are plotted as open circles. n = 9, 6, 5, 6 sample points. **L)** The mean baseline firing rate and firing rate of each cell within its category of preferred stimulus is plotted from cell-attached electrophysiological recordings (preferred stimulus indicated in each subplot). Mean ± SEM across groups are plotted in the panel at the right.

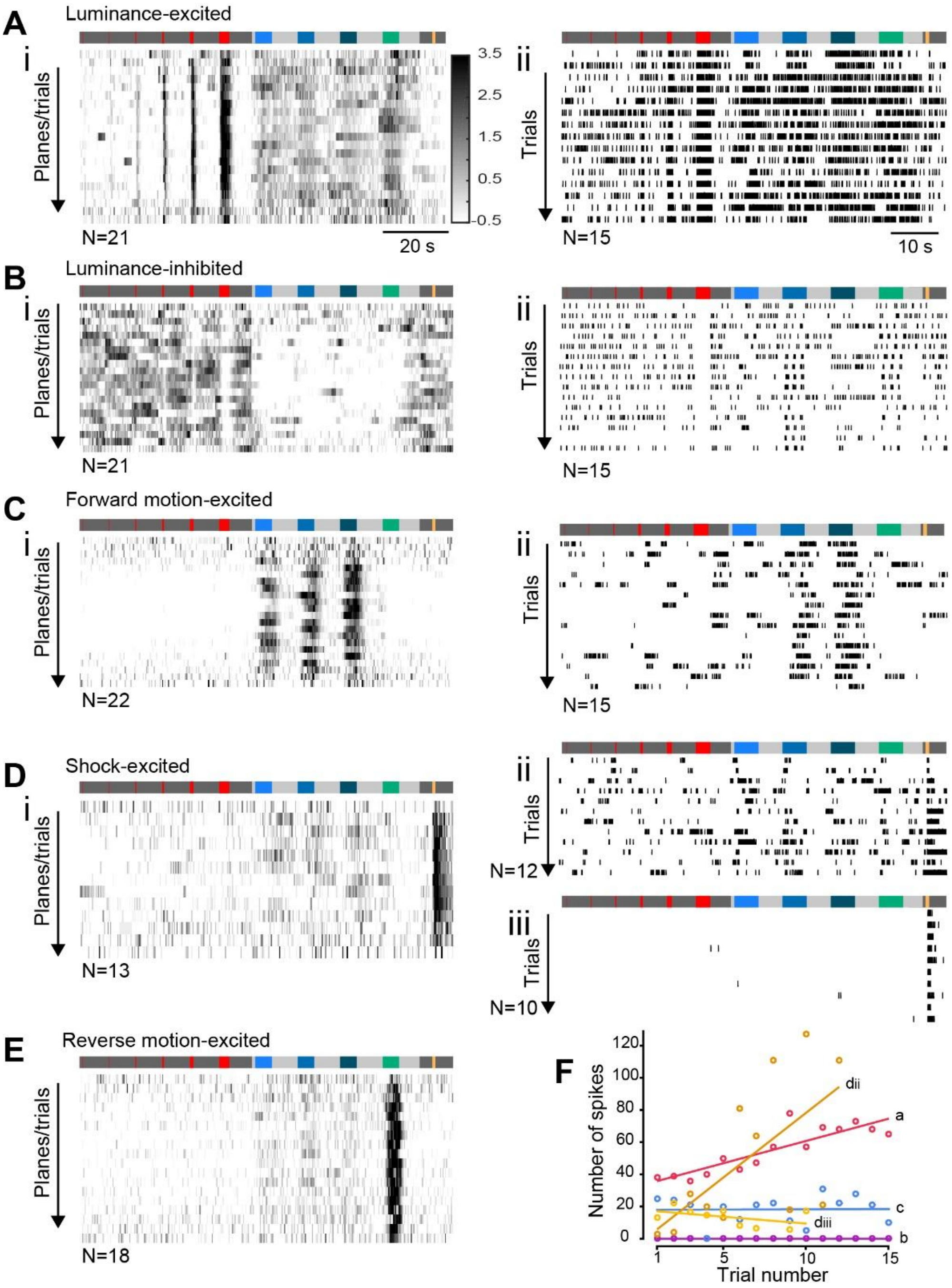

Figure S6. Granule cell responses generally show low variability across trials. Related to Figure 6. Ai) Heatmap of normalized activity for an example granule cell of the indicated response profile imaged over several planes. The number of planes (equivalent to the number of trials) is indicated. **Aii)** Spike raster plot for an example granule cell with a similar response profile recorded from for several trials (indicated). **B-E)** Same as for (A), with the exception that two recordings are shown for D (shock-excited cells) and none for E (no electrophysiological recordings from reverse motion-excited cells were obtained). **F)** The number of spikes evoked by the preferred stimulus is plotted for the four electrophysiological recordings in A-D (open circles). The linear fits for the trend in spike number across trials for all cells are plotted as a solid line. Data is color-coded according to the preferred stimulus for each cell.

Supplemental Experimental Procedures

Zebrafish maintenance

Zebrafish (*Danio rerio*) were maintained at 28˚C on a 14hr light/10hr dark cycle using standard protocols. All animal procedures were performed in accordance with approved protocols. A mix of Tuepfel long-fin (TL) wild type strain as well as the following transgenic lines were used: Tg(gSA2AzGFF152B), Tg(gSAIzGFFM765B), Tg(gSAG6A), Tg(gSAIGFF23C), Tg(SAGFF(LF)128A), Tg(hspGFF57A), Tg(SAGFF(LF)157B), and Tg(hspGFFDMC90A), acquired from M. Hibi and K. Kawakami [S1]. All experiments (with the exception of those for single-cell labelling, see below) were performed using larvae at 6 and 7 dpf.

Single-cell labeling

Labeling of individual granule cells was achieved by using either DNA microinjection, single-cell electroporation, or by crossing a gal4 driver with a sparse UAS reporter line. For DNA microinjection a plasmid containing 14 repeats of upstream activating sequence driving membrane-tagged tagRFP (a.k.a. Fyn-tagRFP) at a concentration of 40 ng/µl and 35 ng/µl tol2 mRNA was injected into transgenic Tg(gSAIGFF23C); UAS:GFP zebrafish [S1] at the one-cell stage with a fine glass electrode and a picospritzer (Parker Hannifin, Fairfield, NJ). For single-cell electroporation, 5-6 dpf Tg(gSA2AzGFF152B); UAS:mCherry larvae were embedded in 1.5% low melting point agarose, anesthetized with tricaine, and granule were electroporated using a confocal microscope (LSM 780, Carl Zeiss, Germany) as described previously [S2]. Briefly, a fine borosilicate glass electrode with filament (final tip diameter ~ 1 µm) was filled with plasmid DNA pCS2-GAP43-GFP construct (provided by Isaac Bianco) at concentration of ~1 µg/µl in distilled water and manipulated through the tissue to a target fluorescent granule cells with a micromanipulator (Sutter Instruments, Novato, CA). 1 - 3 square trains of electric pulses with frequency of 200 Hz, duration of 1s and magnitude of 20-30 V were applied to inject DNA constructs into a single cell using an Axoporator 800A (Molecular Devices, Silicon Valley, CA). Finally, single-cell labelling was also achieved by crossing fish from a Tg(gSA2AzGFF152B); UAS:GFP line with a sparsely-expressing UAS:ChR2-mCherry line.

Results of single cell labeling were imaged in anaesthetized larvae at 6-7 dpf and 11-12 dpf with a confocal microscope (LSM 700 or LSM 780, Carl Zeiss, Germany). Additional imaging of dendritic morphology from 20-22 dpf fish was also carried out in fixed tissue as previously described [S3]. Briefly, 80 µm vibratome sections were cut from fixed 20-22 dpf fish embedded in blocks of gelatin/albumin and stained with a chick anti-GFP primary antibody (GTX13970 GeneTex) followed by Alexa Fluor-488 secondary antibodies (Invitrogen). Low-magnification stacks were acquired to visualize the span of parallel fibers, and higher magnification was used to visualize dendritic morphology of labeled granule cells. Single granule cells were traced and skeletonized, and the background noise was removed with Simple Neurite Tracer plugin for FIJI [S4]. Tracings from different larvae were morphed to each other using Computational Morphometry Toolkit (see “Anatomical registration” section in Online Methods). Dendritic claws were manually quantified by three independent counters. See

Stimuli

For the main experiments in the paper, three types of stimuli were presented. The first type consisted of a whole-field flash of red light (luminance, in lux: flashes, 15; dark background, 2; whole-field gratings, 7). Six different durations were presented (in ms: 50, 100, 200, 500, 1000, 3000). The second type of stimulus consisted of square wave gratings of period 1 cm. Three speeds were presented drifting in the caudal to rostral direction (3, 10 and 30 mm/s) and one speed in the rostral to caudal direction (-10 mm/s). The third stimulus type consisted of a 25 ms, 2 mA electric shock that was delivered from an AM Systems via two platinum coated wires immersed in the bath on either side of the fish. The three different stimulus blocks (flashes, gratings, shock) were presented in a randomized order in each plane, and the order of different durations and speeds within a block was also randomized. Stimuli in all programs were controlled by Labview (National Instruments).

For additional experiments investigating visuotopy (Figure 3D,E), we divided the visual field into fifteen equal vertical (rostro-caudal) and horizontal (left-right) red bars which were flashed on, one at a time, for one second before returning to darkness. The contribution to the receptive field from pixel (i,j) in the visual scene, where i denotes the row and j the column was then estimated to be R(i,:)R(:,j), where R(i,:)

denotes the normalized fluorescence response when flashing the i-th horizontal bar and R(:,j) denotes the response measured when flashing the j-th vertical bar. The centroid of the receptive field was then calculated as the center of mass (the average of position weighted by the response magnitude across pixels). To estimate the size of the receptive field, pixels were considered as active if their contribution to the receptive field was above 50% of the maximum contribution.

Pharmacology

Zebrafish larvae were embedded in agarose in a 35mm petri dish containing extracellular (Evans) solution. The skin overlying the cerebellum was carefully removed with a glass electrode. Bicuculline (Sigma) diluted in E3 solution was either bath applied (20-30 µM) or injected at a higher concentration (10 mM) directly into one or both halves of the cerebellum using a glass electrode and low pressure. Low molecular weight rhodamine dye was included in the electrode to visualize the extent of the injection. Sham injections (E3 solution only) were performed in the same way.

Electrophysiology

Standard cell-attached and whole-cell recordings [S5] were performed in 6-7 dpf larvae. Briefly, pigmented wild-type or transgenic zebrafish larvae with GFP-positive granule cells were paralyzed in bath-applied buffered 1 mg/ml alpha-bungarotoxin (Cayman Scientific, Concord, CA) and embedded in 1.5% low melting point agarose in a 35mm petri dish. External solution was composed of Evans solution (134 mM NaCl, 2.9 mM KCl, 2.1 mM $CaCl_2$, 1.2 mM $MgCl_2$, 10 mM glucose, 10 mM HEPES, pH 7.8 with NaOH). Patch-clamp electrodes for neuron recordings (6-18 MΩ for whole-cell recordings, 10-25 MΩ for cell-attached recordings) were pulled from thick-walled borosilicate glass with filament and were filled with the following intracellular solution (in mM): 105 D-gluconic acid, 16 KCl, 2 $MgCl_2$, 10 HEPES, and 10 EGTA, adjusted to pH 7.2, 290 mOsm [S5]. Sulforhodamine B (0.1%) was also included in the intracellular solution to visualize the electrode and to label cells during whole-cell recordings. The skin overlying the cerebellum was carefully removed with a glass electrode prior to recording.

Standard cell-attached and whole-cell recordings were obtained using an Axopatch Multiclamp 700B amplifier, a Digidata series 1550 Digitizer, and pClamp 9 software (Axon Instruments, Molecular Devices). Data were acquired at 8-20 kHz and low-pass filtered at 2-10 kHz using Clampex 10.2. Cells in cell-attached configuration were recorded in current clamp mode. Cells in patch-clamp configuration were held in voltage clamp near their resting potential at -65 mV. Visual stimuli (see above) were projected at 60 frames per second across the bottom of the petri dish containing the zebrafish larva using an Asus P2E microprojector and a red long-pass filter (Kodak Wratten No.25). Blank traces were also interspersed with stimuli to obtain baseline responses.

Electrophysiological analyses were performed offline with Clampfit 10.2 software (Molecular Devices) and Matlab (Mathworks, Natick MA). Cell-attached traces were high-pass filtered at 10 Hz and reshuffled into time blocks preceding and following each stimulus within a trial. Spikes were counted by setting a threshold for the trace for each cell. For shock-excited cells, semi-automated template matching of spike waveforms was used to pick out spikes from the shock artifact. For other cells, a 200-300 ms period following the shock was blanked where the artifact would have crossed the spike threshold but no spikes were present. Spike times were convolved into average firing rates using a moving 10 ms bin. The windows over which to measure stimulus-evoked changes in firing rate differed between response profiles. For luminance- and motion-excited cells we took a window from stimulus onset to 200 ms following stimulus onset, so that we caught the peak in firing for both short- and long-latency flash durations. For luminance-inhibited cells, we used a window only during the stimulus itself, and a separate window from stimulus offset to 200 ms following offset to calculate firing rates for the rebound excitation. Shock-excited cells had a window of stimulus onset to four seconds following offset. Baseline firing rate was calculated using a window from two to four seconds following flash offset and corresponded to periods where no visual stimuli were present (black background). The latency to the first spike following stimulus onset was calculated up to a maximum latency of one second for luminance-responsive cells to whole-field flashes and up to five seconds for moving gratings.

Functional imaging

6-7 dpf nacre (mitfa-/-) transgenic zebrafish larvae with GCaMP6s or 6f expressed in granule cells were embedded in 1.5-2% agarose prior to imaging. In some experiments, fish were paralyzed with alpha-bungarotoxin. For experiments in which behavior was tracked, fish were not paralyzed and the agarose around the tail, caudal to the pectoral fins was cut away with a fine scalpel to allow for movement. The dish was placed onto a light-diffusing screen and imaged on a custom-built two-photon microscope. A Ti-Sapphire laser (Spectra Physics Mai Tai) tuned to 900 nm (920 nm in behaving experiments) was used for excitation. Larval brains were systematically imaged while presenting visual and mild shock stimuli. Visual stimuli (see above) were projected at 60 frames per second using an Asus P2E microprojector and a red long-pass filter (Kodak Wratten No.25) to allow for simultaneous imaging and visual stimulation.

Full frames were acquired every 368.44 ms in four, 0.83-µm-spaced interlaced scans, which results in x and y pixel dimensions of 0.83 µm. Imaging stacks were acquired in the dorsal to ventral direction. After all stimuli were shown in one plane, the focal plane was shifted ventrally by 1 µm and the process was repeated. Exceptionally, stimuli were presented in a non-randomized order to one fish in order to make Movies S2 and S3. Non-paralyzed fish were illuminated from above using infrared light-emitting diodes (850 nm wavelength) and the fish was imaged from below at up to 200 frames per second using an infrared-sensitive charge-coupled device camera (Pike F032B, Allied Vision Technologies). Tail image data were streamed to hard disk using software written using National Instruments LabView.

Image analysis

Image analysis was performed with MATLAB (MathWorks). Any experiments during which the fish drifted significantly in z were stopped and the data discarded. To correct for drift or small movements of the fish, each image frame was aligned, using translation only, to the average image of that z-plane, and consecutive z-planes were aligned to each other with subpixel precision. Occasionally, vigorous swimming movements caused a large motion in a single frame. Such isolated frames that could not be aligned with a correction of less than two pixels were removed from analysis. ROI segmentation for functional analyses was performed using automated algorithms, based on local correlations between pixels (see [S6] for details). Tail image data giving positive and negative displacements of the tail from baseline were processed to yield a vigor measurement that is greater than zero when the fish is moving [S7]. When stimuli were presented in a randomized order, the stimulus sequence was saved and image frames (both calcium imaging and tail tracking) were reshuffled following alignment. In order to quantify the number of total granule cells, we performed image segmentation on the summed GCaMP6 fluorescence across the place following the approach followed in analyzing tectal responses in Akerboom et al. [S8] and discussed in Rose et al. [S9] but extended to three dimensions.

Anatomical registration

Image registration for two-photon imaging and anatomical tracings was performed using the free Computational Morphometry Toolkit (CMTK; http://www.nitrc.org/projects/cmtk/) [S10]. For each fish, an anatomical stack was computed by summing the GCaMP6 (two-photon imaging) or GFP (anatomical tracing) fluorescence. One of the these stacks was chosen as the reference brain, and nonaffine volume transformations were computed to align each fish's anatomical stack to this reference stack using the affine and warp functions. These transformations were then used to transform individual ROIs from each fish into the frame of reference of the reference brain, allowing us to compare the anatomical location of ROIs from different fish. The precision of this registration is less than 5 microns from the transformed brains to the reference brain [S6].

Data analysis

Cluster analysis of the traces was performed both for individual fish and across all granule cell profiles for a given brain region using the k-means method. The optimal number of clusters was selected by inspection of silhouette plots for different numbers of clusters. Different numbers of clusters were tested, and the number of 7 clusters was selected manually because it gave the clearest separation of functional classes. Clustering with larger numbers produced inconsistent fracturing of anatomical structures or segregation of clusters across fish (e.g. GCaMP6f versus 6s signals), suggesting that true functional classes were being artificially divided. Electrophysiological recordings were manually assigned to these same clusters based on their average firing rate across stimuli. To make color-coded images from functional imaging data (**Figure 3B,C, Figure S3D, Figure 4D**), each pixel was assigned a hue based on the cluster assignment of the most prevalent granule cell profile located at that pixel. In the event of a tie (<0.05% of cases), the winner was chosen randomly. Different anatomical regions were defined manually in the reference brain. Three-dimensional renderings (**Figure 1C and Figure S1**) were performed using the ImageJ 3D Viewer plugin.

Regressors and correlation analysis

Regressors for correlation analysis as described in Miri et al. [S11] were constructed from a set of 11 sensory stimulus-related variables and one behavioral variable (tail motion). These were convolved with a kernel with an exponential decay based on the measured half-decay time for GCaMP6s (0.1796 s) [S12] to produce a set of predicted fluorescence traces and were compared with the measured fluorescence traces by correlation. Correlation analysis was performed for automatically segmented granule cells to identify the variable that best described the signal of individual granule cells. To assign voxels to a particular functional group, we required a threshold of at least 0.3 for the best absolute correlation coefficient. Based on comparisons with shuffled sets of regressors, this level of correlation rarely arises by chance and is therefore a conservative choice for detecting voxels with behavioral correlation. Granule cells that had high regressor correlation coefficients across different sensory and/or motor variables were selected as putative multimodal cells for further investigation. The activity of these cells was assessed manually to look for calcium signals that were consistently correlated with all occurrences of that particular sensory and/or motor variable.

Supplemental References

S1. Takeuchi, M., Matsuda, K., Yamaguchi, S., Asakawa, K., Miyasaka, N., Lal, P., Yoshihara, Y., Koga, A., Kawakami, K., Shimizu, T., *et al.* (2015). Establishment of Gal4 transgenic zebrafish lines for analysis of development of cerebellar neural circuitry. Dev. Biol. *397*, 1–17.
S2. Tawk, M., Bianco, I.H., and Clarke, J.D.W. (2009). Focal Electroporation in Zebrafish Embryos and Larvae. Zebrafish *546*, 145–151.
S3. Robles, E., Filosa, A., and Baier, H. (2013). Precise Lamination of Retinal Axons Generates Multiple Parallel Input Pathways in the Tectum. J. Neurosci. *33*, 5027–5039.
S4. Longair, M.H., Baker, D.A., and Armstrong, J.D. (2011). Simple neurite tracer: Open source software for reconstruction, visualization and analysis of neuronal processes. Bioinformatics *27*, 2453–2454.
S5. Drapeau, P., Ali, D.W., Buss, R.R., and Saint-amant, L. (1999). In vivo recording from identifiable neurons of the locomotor network in the developing zebrafish. J. Neurosci. Methods *88*, 1–13.
S6. Portugues, R., Feierstein, C.E., Engert, F., and Orger, M.B. (2014). Whole-brain activity maps reveal stereotyped, distributed networks for visuomotor behavior. Neuron *81*, 1328–1343.
S7. Portugues, R., and Engert, F. (2011). Adaptive locomotor behavior in larval zebrafish. Front. Syst. Neurosci. *5*, 72.
S8. Akerboom, J., Chen, T.-W., Wardill, T.J., Tian, L., Marvin, J.S., Mutlu, S., Carreras Caldéron, N., Esposti, F., Borghuis, B.G., Sun, X.R., *et al.* (2012). Optimization of a GCaMP Calcium Indicator for Neural Activity Imaging. J. Neurosci. *32*, 13819–13840.
S9. Rose, T., Goltstein, P.M., Portugues, R., and Griesbeck, O. (2014). Putting a finishing touch on GECIs. Front. Mol. Neurosci. *7*, 1–15.
S10. Rohlfing, T., and Maurer, C.R. (2003). Nonrigid image registration in shared-memory multiprocessor environments with application to brains, breasts, and bees. IEEE Trans. Inf. Technol. Biomed. *7*, 16–25.
S11. Miri, A., Daie, K., Burdine, R.D., Aksay, E., and Tank, D.W. (2011). Regression-Based Identification of Behavior-Encoding Neurons During Large-Scale Optical Imaging of Neural Activity at Cellular Resolution. J. Neurophysiol. *105*, 964–980.
S12. Chen, T.-W., Wardill, T.J., Sun, Y., Pulver, S.R., Renninger, S.L., Baohan, A., Schreiter, E.R., Kerr, R.A., Orger, M.B., Jayaraman, V., *et al.* (2013). Ultrasensitive fluorescent proteins for imaging neuronal activity. Nature *499*, 295–300.

Manuscript 2: Evidence accumulation during a sensorimotor decision task revealed by whole-brain imaging

Elena I. Dragomir, **Vilim Štih**, Ruben Portugues

Published in: Nature Neuroscience - Volume 23, Issue 1, 2. December 2019 nature neuroscience

ARTICLES

https://doi.org/10.1038/s41593-019-0535-8

Evidence accumulation during a sensorimotor decision task revealed by whole-brain imaging

Elena I. Dragomir[1,2], Vilim Štih[1,2] and Ruben Portugues[1]*

Although animals can accumulate sensory evidence over considerable time scales to appropriately select behavior, little is known about how the vertebrate brain as a whole accomplishes this. In this study, we developed a new sensorimotor decision-making assay in larval zebrafish based on whole-field visual motion. Fish responded by swimming in the direction of perceived motion, such that the latency to initiate swimming and the fraction of correct turns were modulated by motion strength. Using whole-brain functional imaging, we identified neural activity relevant to different stages of the decision-making process, including the momentary evaluation and accumulation of sensory evidence. This activity is distributed in functional clusters across different brain regions and is characterized by a wide range of time constants. In addition, we found that the caudal interpeduncular nucleus (IPN), a circular structure located ventrally on the midline of the brain, reliably encodes the left and right turning rates.

In contrast to reflexive behaviors, in which motor responses are immediately elicited after sensory stimuli, the process of making a decision takes a course over time scales that are orders of magnitude longer than action potentials. Because momentary sensory cues are often noisy and uncertain, to properly infer the state of the world, animals need to integrate sensory evidence over time. Once this accumulated evidence reaches a threshold, animals use this valuation to decide on the appropriate behavioral response. This 'evidence accumulation' model[1,2] accurately describes decision paradigms involving multiple sensory modalities across various organisms, including non-human primates[3–6], rodents[7–9], humans[10–12] and fruit flies[13]. Many neurophysiological experiments have revealed activity related to this process in several brain regions[3–9],[14–17]. However, the flow of information throughout these regions and their explicit involvement in the various steps of the decision-making process are controversial and not fully understood[18–21].

Here we present a new assay in larval zebrafish adapted from the well-established random dot motion (RDM) paradigm first used in primates[14]. In our case, the behavior was not trained; we relied on the innate optomotor response, which induces fish to align themselves and swim in the direction of perceived visual motion[22,23]. Because our assay did not involve operant conditioning, we were able to use it to isolate the neuronal correlates of untrained decision-making, in which zebrafish larvae use noisy sensory cues to estimate the state of their visual environment and update this estimate with the continuous inflow of sensory evidence.

We found that turn latency, turn rate and accuracy were modulated as the stimulus strength was varied, and that both sensory and motor history affected the selection of the current behavioral choice. We performed whole-brain functional imaging experiments and used the framework of integration of sensory evidence to identify all neural activity relevant to the different stages of the decision-making process that results in the binary choice of either left or right turning. These neural correlates were localized in several anatomical clusters distributed across the brain and were lateralized on the basis of stimulus direction. Neurons encoding momentary sensory evidence were concentrated in the midbrain region, adjacent to and including the pretectum, and medial parts of the reticular formation in the anterior hindbrain, whereas neurons that integrated sensory evidence included lateral parts of the reticular formation, the dorsal raphe nucleus (DRN) and the IPN in the ventral hindbrain, the dorsal part of the pretectum, the dorsal thalamus and the torus longitudinalis in the midbrain and the habenula in the forebrain. The neural responses representing accumulated sensory evidence exhibited a continuous distribution of time constants, with different units integrating evidence over varying time windows, which encompassed up to tens of seconds, reminiscent of units representing sensory history found in other decision-making studies[7,8].

On the basis of the behavior and the results from the imaging analysis, we propose a model in which the sensory evidence variable, which results from bidirectional integration, sets the behavioral turning rate of the fish. This enables us to link the observed neuronal activity with the resulting behavior. An unbiased whole-brain analysis revealed that most units that encode this behavioral turning rate are located in the IPN, which is a circular structure in the ventral midbrain–hindbrain boundary. This structure is an important integrative center of the limbic system[24] and has been previously shown to correlate with locomotor- and navigation-related variables in rodents[25,26]. We showed that activity in the IPN is lateralized and tracks the left and right turning rates reliably, and we discuss the possibility that evidence may be accumulated not in terms of sensory evidence but in terms of likely behavioral output.

Results

Larvae modulate their turning with increasing visual motion strength. To investigate whether larval zebrafish modulate their behavior when exposed to visual motion of varying strength, we presented freely swimming larval zebrafish with a coherent dot motion stimulus projected from below. Briefly, the coherence of the stimulus was controlled so that a fraction of dots, ranging from 0 to 1, moved to either the left or the right of the fish, with the remaining fraction moving randomly (Fig. 1a and Methods). The fish were tracked in real time, and a closed-loop assay[27] was implemented such that the direction of the stimulus relative to the fish's orientation

---

[1]Sensorimotor Control Research Group, Max Planck Institute of Neurobiology, Martinsried, Germany. [2]Graduate School of Systemic Neurosciences, Munich, Germany. *e-mail: rportugues@neuro.mpg.de

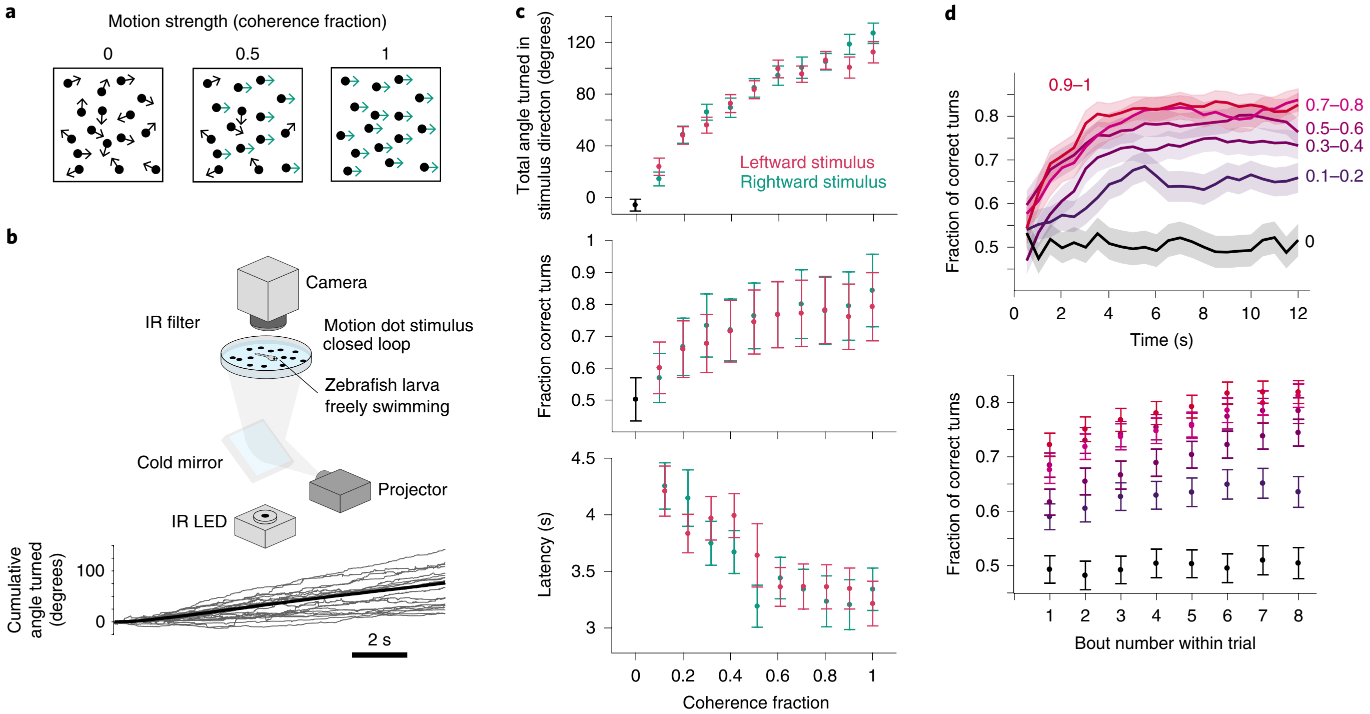

Fig. 1 | Turning behavior of larval zebrafish is dependent on motion stimulus coherence and displays accumulation of evidence. a, Schematic of visual motion stimulus, displaying three different examples of motion strengths: 0, 0.5 and 1 coherence. **b**, Top: schematic of the behavioral closed-loop setup used for freely swimming experiments. Bottom: example traces (in gray) of cumulative angle turned in a 12-s trial for an individual fish during trials with coherence of 0.6 to the left. The average is shown in black. **c**, Top: the total angle turned as a function of coherence averaged across fish. Middle: fraction of correct turns (in the direction of presented coherence). Bottom: latency (time from stimulus onset) to first correct turn as a fraction of stimulus coherence. **d**, Fraction of correct turns as a function of time (top) and trial bout number (bottom), for different coherence categories, averaged across all fish ($n = 55$ fish; 11,733 trials and 95,981 bouts). All error bars and shaded intervals denote s.e.m.

remained constant in time throughout a 12-s trial despite the fish turning (Fig. 1b and Supplementary Video 1).

Larval zebrafish swim in discrete motor events called bouts, which typically last several hundred milliseconds and are elicited at an average rate of 1 Hz. Over a 12-s trial, the total angle turned by larvae depended on the stimulus coherence and was larger in magnitude with increasing coherence (Fig. 1c, top). We divided all swimming bouts into left turns, right turns and forward swims (Extended Data Fig. 1). Defining a correct turn to be one in the direction of the effective stimulus direction, the fraction of correct turns increased from 0.5 for no coherence to 0.8 for a fully coherent stimulus (Fig. 1c, middle). In addition, the latency to the first correct turn from stimulus onset became shorter as the coherency increased, from over 4 s at low coherences to just over 3 s for high coherences (Fig. 1c, bottom). These psychometric curves are reminiscent of those obtained in primate experiments where animals were presented with a similar stimulus in either forced-choice or response-time tasks[28], and they indicate that larval zebrafish react to RDM stimuli of increasing coherence as motion percepts of increasing strength. Improved turning accuracy was also apparent as the time and bout number progressed within the trial (Fig. 1d), and these results were corroborated in a set of experiments where we provided pulses of coherent motion for 7 durations ranging from 1 to 10 s (Extended Data Fig. 2). These results indicate that the turning rate depends on the time that the coherence-based stimulus has been shown. This behavior is consistent with a temporal accumulation of evidence but not with a fixed time delay between sensory stimulus and motor output. Even if the stimulus set a stochastic mechanism to generate bouts, one would observe a discrete jump in the behavioral turning rate occurring when the rate parameter change was implemented and not a gradual change in turning rates. Second, the results show that the evidence accumulated was not reset when performing a bout and lead us to examine the dependence on sensory and motor history more closely.

Behavior depends on both sensory and motor history. Having observed that larval zebrafish turn more when presented with RDM of increasing coherence, we investigated whether this turning behavior depended only on the current stimulus or whether it displayed any dependence on either the previous stimulus shown or the previous motor output produced. We therefore repeated the experiment with a reduced set of coherences (0.3, 0.6 and 1), with trials such that every coherence transition was probed an equal number of times. Dividing all trials for a given coherence according to the previous coherence showed that the turning behavior depended not only on the current coherence but also on the direction (and not the magnitude) of the previous coherence (Fig. 2a,b and Extended Data Fig. 3a,b). This effect is particularly noticeable after trial transitions of opposite direction coherences, where fish exhibit an inertia-like behavior and only start turning in the correct direction after about 2 s. To investigate whether this history dependence comprised both a sensory and a motor effect, we further divided trials in which the current coherence was the same into four categories, depending on whether the coherence and the last bout in the previous trial was in the same or opposite direction. Trajectories elicited by the same stimulus transition differed significantly from each other during the current trial, depending on whether the previous motor output had been in one direction or the other. The same inertia-like behavior was also present if only the turn preceding the stimulus transition was in the opposite

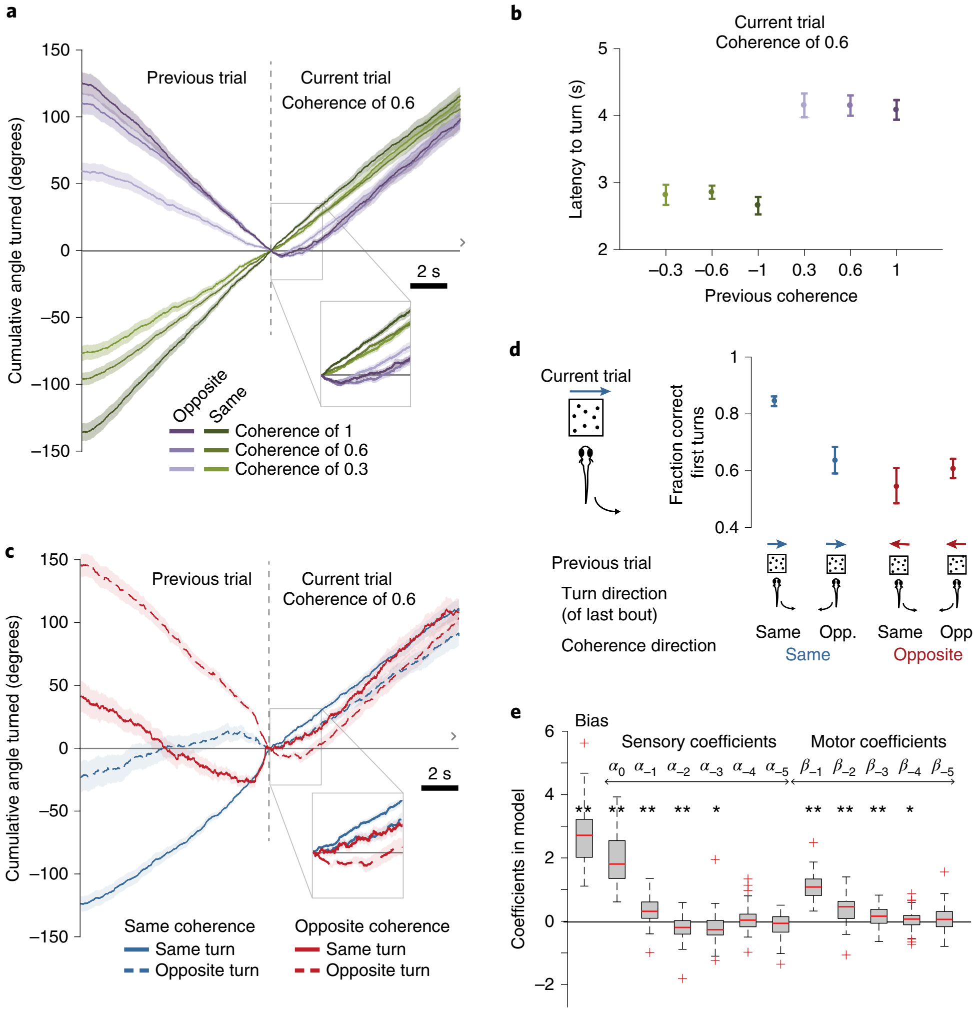

Fig. 2 | Turning behavior is dependent on both sensory and motor history. a, Turning behavior during trials of coherence of 0.6 as a function of the coherence presented during the preceding trial. Trajectories are split by both magnitude and direction of the preceding trial. **b**, Latency to first correct turn in trials of coherence of 0.6 as a function of the coherence of the preceding trial. Negative coherences indicate previous coherence in the opposite direction, and positive coherences indicate previous coherences in the same direction as the current trial coherence. **c**, Turning behavior during trials of coherence of 0.6 as a function of both the direction of the coherence presented during the preceding trial and the direction of the last turn in the preceding trial. Only preceding trials with coherence of magnitude 0.6 were included. **d**, Fraction of correct first turns during trials of coherence of 0.6 as a function of both the direction of the coherence of the preceding trial and the direction of the last turn in the preceding trial. Only preceding trials with coherence of magnitude 0.6 were included. The analogs of panels **a**–**d** for coherences 0.3 and 1 are shown in Extended Data Fig. 2. Opp., opposite. **e**, Values of coefficients for multivariate logistic regression model averaged across fish (see Methods for details). α_n corresponds to the coherence presented during the nth previous bout, and βn corresponds to the behavior of that bout. Red lines denote medians, boxes encompass 25th and 75th percentiles, and crosses denote outliers. Asterisks denote that the coefficient is significantly different from 0 (Wilcoxon signed-rank test, $P < 0.05$ and $P < 0.001$). (**a**–**d**: $n = 50$ fish, 18,964 trials and 166,059 bouts; **e**: $n = 37$ fish; 5,688 trials and 126,754 bouts). All error bars and shaded intervals denote s.e.m. except in **e**.

direction, even if the stimulus direction remained the same (see, for example, the red solid and dotted lines in Fig. 2c and Extended Data Fig. 3c). In addition, the fraction of correct first turns showed a similar dependency on previous motor output (Fig. 2d and Extended Data Fig. 3d). To describe and quantify the sensory and motor influences, we constructed a multivariate logistic regression model that defines the likelihood of observing a left turn versus a right turn based on both the coherence shown during previous bouts and the direction turned (see Methods for details). The significant sensory coefficients extended from the current to the previous three bouts, whereas the significant motor coefficients included the previous four bouts (Fig. 2e). Overall, our analysis showed that both sensory and motor history influence the current behavioral choice, corroborating results found in other decision-making studies, where it was specifically shown that such biases can both improve and worsen the behavior, depending on whether the stimuli are in agreement or conflicting[8,29,30].

Whole-brain imaging uncovers neuronal correlates. After quantifying this behavior, we postulated that there should be neurons in the brain capable of integrating evidence for time scales on the order of seconds that would underlie the long latencies observed in Figs. 1d and 2a,b. To locate the neural correlates related to this decision-making process, we adapted our assay to a preparation in which the larval zebrafish had its head restrained yet was able to move its tail[31] while it was being shown a reduced set of coherence stimuli (Methods). This allowed us to monitor both neuronal activity and behavioral output on a trial-by-trial basis. Although the behavior observed was not as reliable as in the assay with freely swimming fish, it still showed a clear lateralization dependent on the stimulus

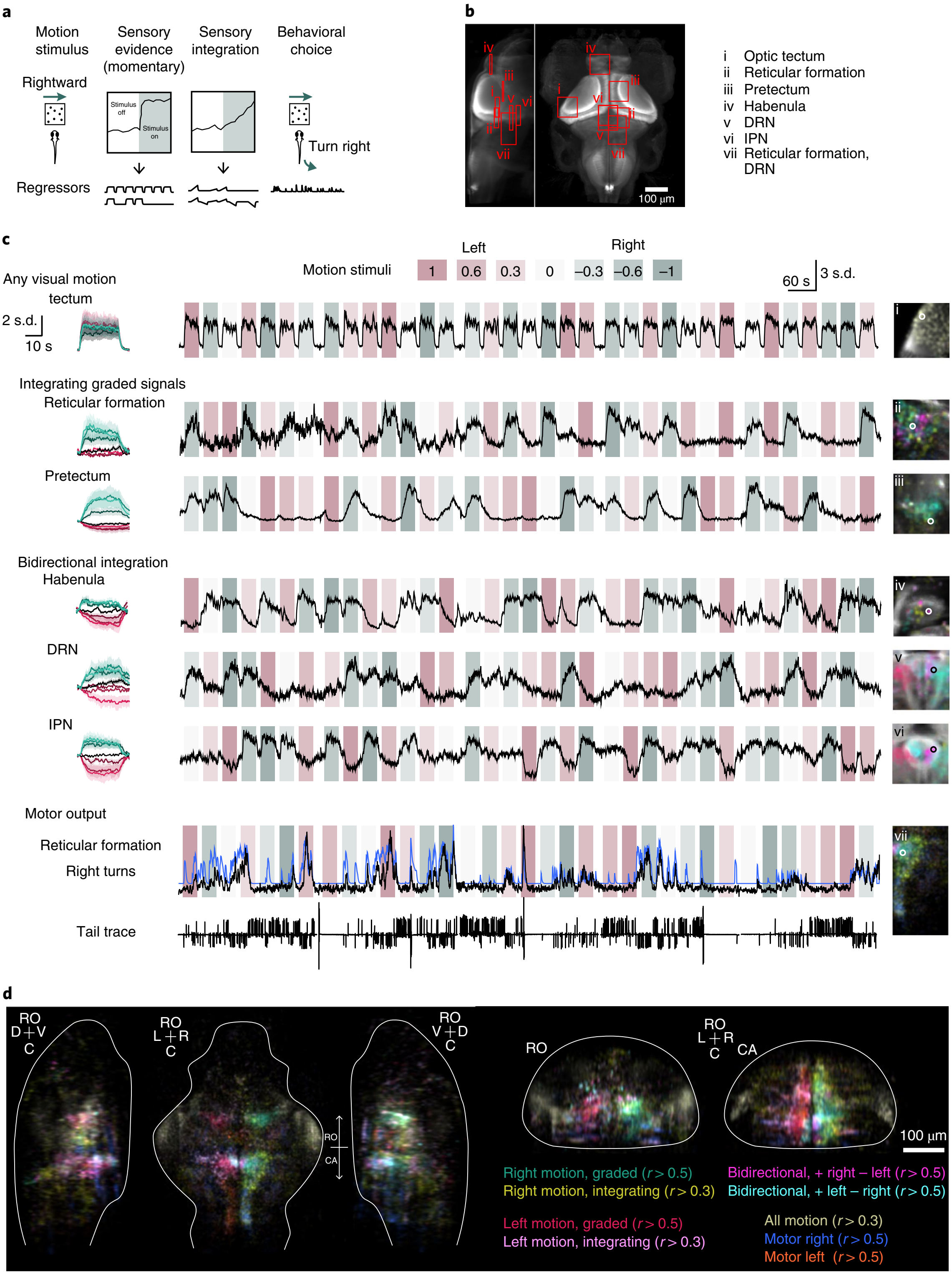

Fig. 3 | Neural correlates of the decision-making process are anatomically clustered and segregated based on stimulus and motor parameters. **a**, Schematic of the decision-making steps and some regressor examples (the full regressor list is in Extended Data Fig. 4). **b**, Reference brain with location of each anatomic inset and its representative trace displayed in **c**. **c**, ROI types in six different brain regions with representative raw traces (in black) spanning at least six planes. For the motor ROIs, the corresponding regressor (right and left turns in blue and orange, respectively) and tail trace (arbitrary units with positive upward deflections denoting leftward turns) are also displayed. **d**, Whole-brain ROI maps color-coded according to various sensory and motor-related regressors (each regressor and corresponding thresholds for ROIs shown here are displayed at the bottom right). From left to right: ROI projection views from lateral left, dorsoventral and lateral right. RO and CA show medial views corresponding to rostral and caudal parts of the zebrafish brain, respectively. Shaded intervals throughout denote s.e.m.

shown (Extended Data Fig. 4), and the psychometric curves for both the fraction of correct turns and the latency to the first correct turn (Extended Data Fig. 4e) mimicked the ones observed in the setup with freely swimming fish (Fig. 1d). The brains of 22 animals were imaged comprehensively under a scanning two-photon microscope (Extended Data Fig. 5). The raw data were processed to remove motion artifacts and identify and segment active neurons on the basis of local correlations in an unbiased way (Methods). All units were registered to a reference brain, and their regions of interest (ROIs) were included in all further analysis (for a total of 2,170,552 ROIs in 22 fish). Regressors were built to identify whether any of the neurons had signals that could be associated with the decision-making process, which is usually regarded as a three-step process consisting of (i) the transformation of the sensory stimulus into a momentary sensory drive; (ii) the integration of this sensory drive in time as accumulation of evidence; and (iii) a threshold-crossing stage resulting in the behavioral choice (Fig. 3a and Extended Data Fig. 6a). In particular, we looked for signals that correlated with the presence of visual motion, the coherence (motion strength) of the stimulus and the integration of this sensory evidence in time, either unilaterally or bilaterally.

Neural activity representing the presence of visual motion (irrespective of direction or stimulus magnitude) was found in the optic tectum, whereas signals that were graded according to the coherence magnitude were found in multiple areas, including the dorsal left habenula, pretectum, reticular formation (in the anterior hindbrain), DRN and IPN (Fig. 3b-d, Extended Data Fig. 6b and Supplementary Video 2). Except for the habenula and optic tectum, leftward and rightward visual motion was lateralized and located on the left and right side of the brain, respectively. In the pretectum, for example, we observed directional visual motion signals modulated by coherence magnitude, in agreement with previous studies that showed similar activation in response to whole-field visual motion[31–33]. Motor-related ROIs corresponding to acute directional turns were also lateralized and found in the reticular formation (Fig. 3c, image vii), the lateral parts of the DRN, the tegmentum and the caudal part of the hindbrain (Fig. 3d and Supplementary Video 2). In the medial anterior region of the hindbrain, we also found graded sensory responses in regions previously identified with turning motor activity[34–36]. In addition to typically fast-rising responses that were graded by coherence, present mostly in the pretectum and reticular formation, some ROIs showed integrating-like activity patterns, with slower rises, that were also dependent on the coherence magnitude. These tended to be clustered more medially and dorsal in the pretectum, dorsal thalamus and torus longitudinalis in the midbrain and the habenula in the forebrain and more laterally in the reticular formation, DRN and IPN in the hindbrain (Fig. 3c,d and Supplementary Video 2). Interestingly, the habenula, DRN and IPN, which are anatomically connected (see ref. [37] for a review), also showed a different category of stimulus-related responses, integrating activity in a bidirectional manner: excitation for the preferred direction and inhibition for the opposite direction (Fig. 3c, images iv–vi). As shown explicitly in Fig. 3c, the integrating signals described did not arise from averaging step responses across multiple trials but were already present at the level of individual trials.

Mapping a decision-making model to the neuronal data. Theoretical frameworks proposed to understand this decision-making process involved two integrators, one for each of the possible behavioral choices, which accumulate corresponding evidence in support of that particular choice[38]. These integrators may solely accumulate ipsilateral momentary sensory evidence or, in addition, may be inhibited by either contralateral momentary sensory evidence (the feed-forward inhibition model[39]) or the opposing integrator (leaky competing accumulator model[40]) (reviewed in (refs. [41,42])). A reliable distinction between these two architectures is not possible within the experimental paradigm we used (see attached notebook in the code repository), so we defined a general model architecture based on feed-forward inhibition to describe individual ROI responses. The model describes the activity of an ROI as the sum of leftward and rightward sensory streams. In each stream, the visual processing that leads from partially coherently moving dots to momentary sensory evidence is modeled as a power nonlinearity. This is subsequently integrated by units with time constants that are independent for the left and right streams and summed with weights that can be either positive or negative (Fig. 4a and Methods). This model can describe units that respond equally to all motion directions, units that respond to uni-directional motion in either a graded or an ungraded way and units that integrate either uni-directional or bi-directional motion positively and/or negatively (Fig. 4b). We fitted this model to the activity of every individual ROI and used the goodness-of-fit test to identify all brain regions that were involved in the decision-making process (Fig. 4c). Notably, this analysis was able to pinpoint relevant neuronal activity to a few anatomic locations, which we describe below.

From the five parameters (the power of the nonlinearity, as well as the weight and time constant for each side), we examine two derived parameters, namely the relationship between response to the two motion directions, expressed as an angle in the weight plane (Fig. 4d) and the dominant time constant (defined as the sum of the two integrator time constants weighted by the input weights). We observed a continuum of time constants that extended all the way into the tens of seconds. Interestingly, the widest range of time constants, including the longest ones, belonged to ROIs that were strongly excited by motion in one direction and slightly inhibited by motion in the opposite direction (Fig. 4d; between $\pi/2$ and $3\pi/4$).

Because each ROI was fitted independently, we were able to investigate the anatomical distribution of the fitting parameters throughout the brain of the larval zebrafish. As shown in Fig. 4c,e, most units of relevance were found in the pretectum, thalamus, the hindbrain region around the reticular formation and the ventral hindbrain corresponding to the DRN and the IPN, in agreement with the regression-based analysis shown in Fig. 3. Responses dominated by contralateral inhibition were located almost exclusively in the DRN, IPN and habenula (pink ROIs in Fig. 4d–f,h). As shown in Fig. 4f (rostral), responses in the pretectal region exhibited a continuous gradation from lateral/ventral responses corresponding to some bi-directional but mostly uni-directional excitation, to medial and dorsal responses that included modest contralateral inhibition. In agreement with Fig. 3, units that were more excited by rightward or leftward motion were almost uniquely found on the right and left side of the brain, respectively (Fig. 4g). ROIs with long time constants (>5 s) were located in several brain regions (Fig. 4h), including the dorsal and lateral hindbrain around the reticular formation and more ventrally in the DRN and IPN (Fig. 4h, caudal), the dorsal pretectum (corresponding to those units that included slight contralateral inhibition) (Fig. 4h, rostral), torus longitudinalis and habenula. We note that this is a comprehensive map: no other units throughout the brain exhibited activity related to visual motion in this experimental paradigm. These ROIs must therefore underlie the coherence-dependent behavior we observed and described in Figs. 1 and 2.

Generation of motor output. The ROIs we have described so far relate to sensory evidence and its integration. As shown in Fig. 1c and expanded on in Fig. 2, the evidence integrator is not reset upon performing a turn. The question still remains as to how the integrated evidence actually influences turning. It has been shown before[43] that the initiation of forward swims when presented with optomotor stimuli of varying speeds can be to a certain extent modeled as a Poisson process, whose rate is a function of the stimulus speed. We tested whether a similar mechanism could underlie the

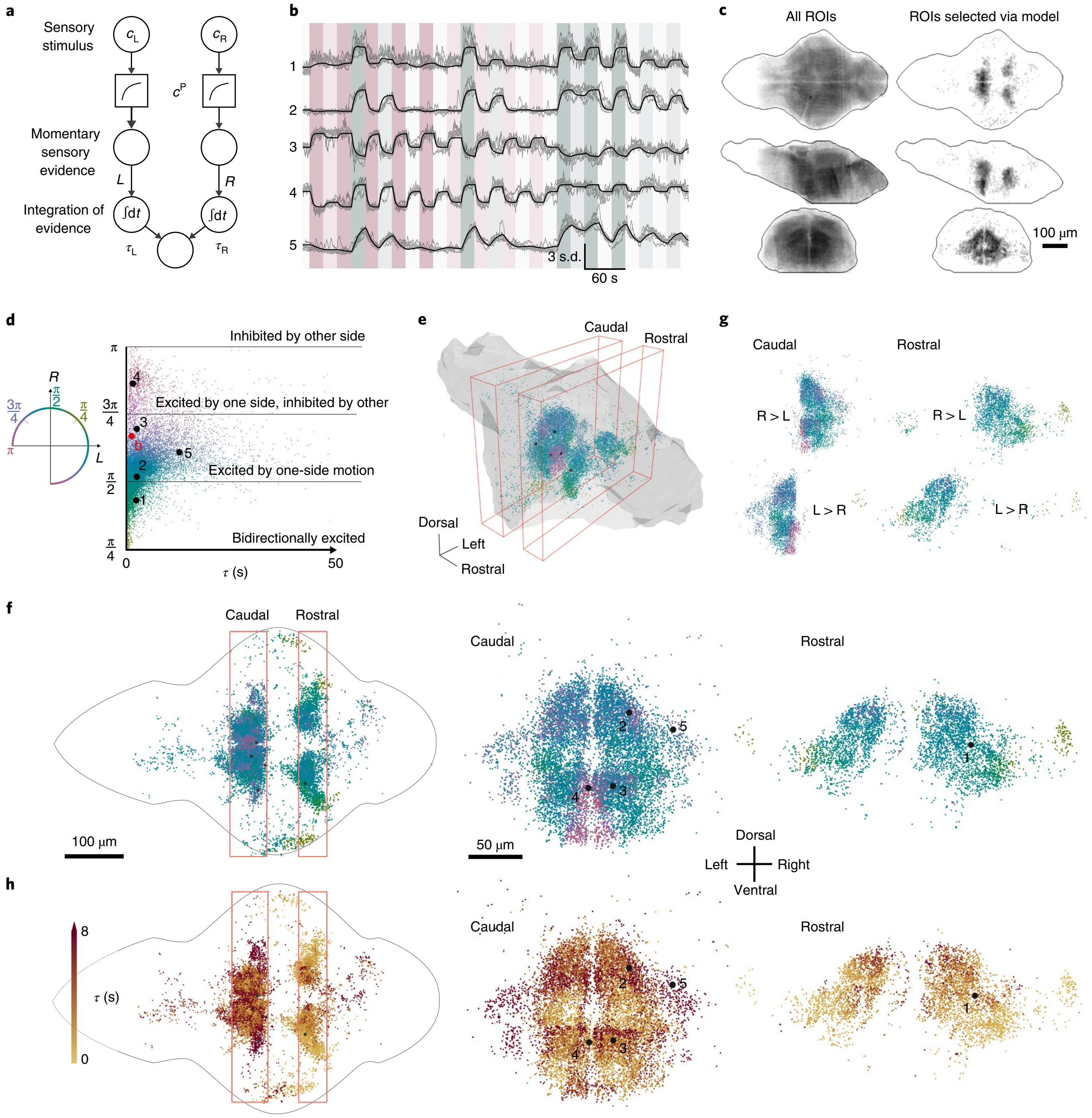

Fig. 4 | Fitting a general integrator model to the neural data uncovered integrator time constants and their anatomic distribution. a, General model that incorporates previously suggested models within its parameter space. **b**, Sample traces showing fits (in black) to neural activity (individual trials in gray) from different parts of the model parameter space; the explained variance for each trace is (in order) 0.612, 0.813, 0.734, 0.790 and 0.827. Extended Data Fig. 7a shows the error variance for all ROIs. **c**, Of the 1,142,100 units, over 70% of the variance in the activity of 8,953 units is described by the model. **d**, Characterization of the resulting model fits. The *x* axis is a sum of the time constants weighted by the absolute values of the left and right weights; the *y* axis is the amount of inhibition versus excitation for the dominant side (see Methods for details). The neurons shown in **b** are labeled 1 through 5, and the red b shows the parameters obtained from the swim-generation model fit (Fig. 5 and Extended Data Fig. 7b). **e**, Three-dimensional anatomic map of model parameters: the colors are from **d**, showing regions where ipsilateral excitation or contralateral inhibition dominate. Two transversal slices of the brain volume containing most of the relevant ROIs are displayed below: the caudal slice (anterior hindbrain) and the rostral slice (midbrain). **f**, Anatomical map of model parameters, with the same transversal slices displayed in **e**. **g**, Transversal slices already shown in **f** (caudal) and **f** (rostral), but here ROIs are split into those for which the input when presented with a leftward stimulus produces more excitation than a rightward stimulus (L > R) and vice versa to depict the pronounced lateralization. **h**, Anatomical map of model time constants, with same transversal slices displayed in **e**.

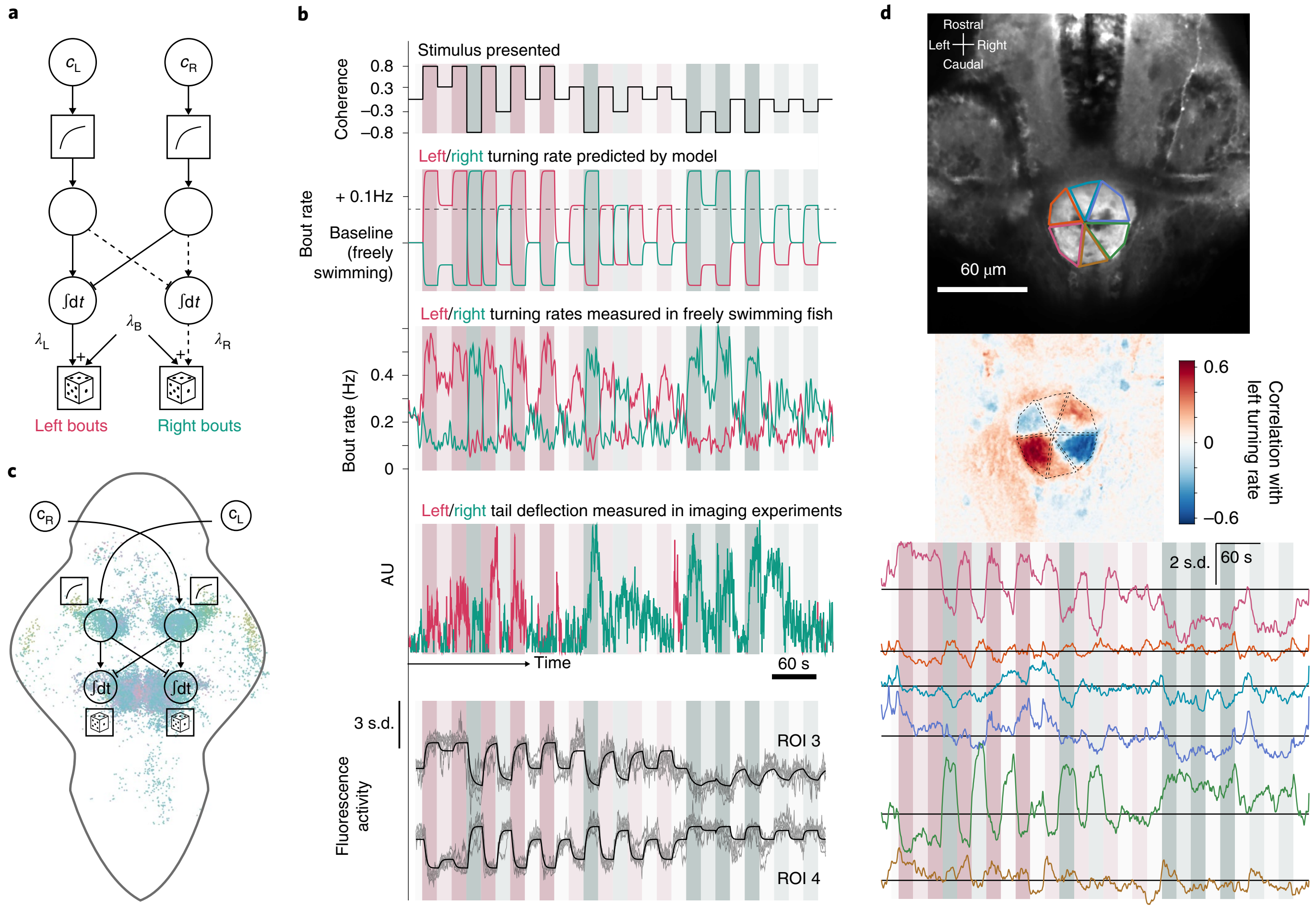

Fig. 5 | The interpeduncular nucleus encodes the rate of left and right turns. a, Version of the model that relates the evidence integration process to bout generation. **b**, Top: direction and coherence of the stimulus sequence. Second panel: the turning rates predicted by the model fitted on data from Figs. 1 and 2a; the gray line denotes a new zero, below which all turns would be truncated in the head-restrained case, as described in the text. Third and fourth panels: turning behavior in freely swimming fish (third panel) and embedded fish (fourth panel). Bottom: fluorescence traces (different trials in gray and fit in black) reproduced from Fig. 4, with similar parameters as in the behavioral model. **c**, Mapping of brain areas to parts of the evidence integration process. The colors are from Fig. 4d, showing regions where ipsilateral excitation or contralateral inhibition dominate. **d**, Activity in the IPN correlates with the integrated evidence. The anatomy showing the location of the IPN (top), with six regions selected from the pixel-wise correlation (middle) with modeled left-turning rate (the magenta trace in the second panel of **b**). Bottom: example traces from the six segments selected in the above panels.

generation of behavior in the present behavioral paradigm: the left and right turns were modeled as two independent Poisson processes whose rates are linearly modulated by the left and right integrator values, respectively. As shown in Fig. 5a, we combined two integrator units already described in Fig. 4a (but now setting τ_L and τ_R to be equal) to encode the left and right turning rates, respectively (λ_L and λ_R), superimposed on a tonic baseline turning rate λ_B. The model was fit to reproduce the behavior observed during one of the two behavioral paradigms tested, and the synthetic trajectories generated show both qualitative and quantitative similarities to those found experimentally (Methods and Extended Data Fig. 7b). This same model was then applied to predict the turning rate expected during the stimulus sequence (Fig. 5b, first panel) presented in the imaging setup, during which the larvae were head restrained (Fig. 5b, second panel, and Methods). The freely swimming behavior expected when this stimulus is presented showed a very close agreement with the model (compare the second and third panels in Fig. 5b) with very similar deviations from baseline occurring as a function of the coherence presented. For the head-restrained behavior (Fig. 5b, fourth panel), salient behavioral features were also similar, such as the predominant turning direction during each stimulus and relative turning frequencies. Nevertheless, the swimming in head-restrained zebrafish larvae is known to occur at a much decreased rate, which in our model could correspond to a decrease in λ_B and/or a reduced input to the turning integrators. This would result in an overall homogeneous decrease of turning rates (see gray line in Fig. 5b, second panel). Note that, in addition, the proposed mechanism can also explain why, even for very high coherences, fish will sometimes perform an incorrect turn. This is due to the stochasticity of the model and the fact that the baseline turning rate, determined by λB, is non-zero for both freely swimming and head-restrained behavior.

As shown in Fig. 5b (second panel), these units representing the turning rate display positive and negative deviations from a baseline activity depending on whether the sensory evidence coincides or not with the turning behavior they encode. In the parametrization from Fig. 4d, they must therefore lie around the value 3π/4 and should appear pink in Fig. 4d–g, such as ROIs 3 and 4 from Fig. 4b, which are reproduced at the bottom of Fig. 5b. Most of these ROIs are found in the hindbrain (Fig. 4f, caudal section). In addition, as already shown in Fig. 4g, all ROIs that are predominantly excited by leftward coherence are almost uniquely located on the left side of the brain and similarly for the rightward coherence. This allows us to establish a functional circuit model (Fig. 5c) where rate-encoding units in the anterior hindbrain receive ipsilateral excitatory and contralateral inhibitory inputs that must originate in the pretectum, the only visual sensory region that is active in a coherence-graded fashion. We note that the circuit model in Fig. 5c is not an anatomical model but a functional one, and that inhibitory inputs to the turning-rate–encoding neurons could anatomically arise from neurons in the contralateral hindbrain.

Using our whole-brain imaging dataset as a functional screen, we revisited the regions in the medial ventral anterior hindbrain, which, as pointed out above, were colored pink in Fig. 4 and could correspond to turning-rate–encoding units. We found that the IPN, a structure located on the midline of the larval zebrafish brain, contained most of these units. We correlated the activity in this region with the left-turn rate and found that activity in the caudal IPN was markedly lateralized, with activity on each side being highly correlated for ipsiversive turns and anticorrelated for contraversive ones, whereas this pattern was switched in the more rostral IPN (Fig. 5d). This is confirmed by partitioning this region into six segments: deviations from baseline in the activity in the pink segment closely tracked the deviations from baseline in the left-turning rate (cf with Fig. 5b) and similarly for the green segment and right turns (see also Supplementary Video 3).

It is unclear how these turning rates are transformed into motor output. To start addressing this question, we computed the motor-triggered neuronal activity (MTNA) averages for all the ROIs identified in our behavioral analysis from the imaging experiments, for the three behaviors we observed, namely left and right turns and forward swims (for simplicity, only left turns were considered in Extended Data Fig. 8, except in **e**). We defined a set of activity profiles of interest, which we referred to as motor triggers. For example, the triggers in Extended Data Fig. 8a corresponded to neuronal activity that increased or decreased in a step-up fashion upon motor output; the trigger in Extended Data Fig. 8d corresponded to neuronal activity that started ramping down several tens of seconds before a motor event, after which it was instantaneously reset; and the trigger in Extended Data Fig. 8e corresponded to neuronal activity concurrent with a motor event such as would be expected from a motor neuron. We correlated the activity of each individual MTNA with these motor triggers and kept ROIs that had a high correlation coefficient (>0.7). Note that we did not find a significant number of ROIs with MTNAs that were highly anticorrelated with the trigger in Extended Data Fig. 8d—that is, integrated activity that was reset upon motor output. Analyzing ROIs with prominent leftward-turning MTNAs (Extended Data Fig. 8a–d) revealed functional classes corresponding to different activity patterns, which were anatomically lateralized: for each pair, the ROIs with the green trigger were mainly located on the right side of the brain, whereas those with the magenta trigger, which perfectly anticorrelated with the green trigger, were located on the left side of the brain. Note that the motor triggers we displayed corresponded to leftward turns, and a mirror symmetric configuration was observed for rightward turns (data not shown). The pronounced lateralization of functional types suggests that an intricate interplay of cross-midline excitation and inhibition is behind the translation of the behavioral turning rates observed in the IPN into locomotor output. Interestingly, ROIs with significant MTNAs were enriched in the telencephalon, which contains, among other structures, the homologs of the basal ganglia. In addition, most of these ROIs were located in the regions already identified as being of interest in Fig. 4, namely the reticular formation and the DRN, suggesting that these regions are involved not only in the integration of sensory evidence but also in the generation of motor output. Further research is needed to uncover the exact circuit mechanism that underlies this generation of behavior.

Discussion

In this study, we showed that visual motion of varying strength modulates turning behavior in larval zebrafish, with improved accuracy and decreased latency corresponding to higher coherences of the stimulus presented.

We also showed that larval zebrafish perceive RDM stimuli as visual motion of varying strength and that they react to them by turning in such a way that, when the coherence is higher, they perform more correct turns and take a shorter time to perform a correct turn. The time scales involved in this behavior ranged from several seconds in the freely swimming case to ~ 10 s when head restrained. When performing a whole-brain imaging screen for neuronal activity that could underlie the behavior observed, we found neurons with these time constants in the pretectum and anterior hindbrain and further identified the IPN as the only region in the brain to encode the left and right behavioral turning rates.

Although this assay bears some similarities to those performed in primates, some important differences need to be highlighted. In most perceptual decision-making assays in primates and rodents, the accumulation of evidence is automatically reset upon performing a behavioral choice, yet this is not what we observed here. We think that this can be understood by considering that, in those tasks, the behavior arises from training aimed at obtaining a reward. After obtaining this reward, the accumulated evidence has no subsequent importance. In our assay, on the basis of the reflexive optomotor response, fish swam in the direction of perceived motion and were able to align with this motion despite swimming in discrete bouts[44]. In our assay, larvae were trying to continuously estimate the state of their visual surroundings to behave accordingly, and evidence accumulated before a bout will still be relevant in estimating the state after the bout. In essence, the external state or evidence variable was encoded in the behavioral space as the most appropriate turning rate that should result given current evidence and beliefs. The time constants of the integrators involved in the behavior therefore reflect the temporal statistics of behaviorally relevant visual stimuli that larvae are exposed to. Our analysis shows that time constants much longer than those required to describe the behavior are also present in the zebrafish brain. We think that these may be involved in circuits required to modulate behavior in time scales ranging into the tens of seconds and may be called into play when considering reward, conditioning and other circumstances in which behavioral choice needs to be biased, such as the posterior–parietal cortex neurons recently identified in rats[7,8].

A second possibility is that these longer time constants are part of a continuum within a network, which has an effective time constant that matches that of the behavior. This, together with the various ranges of excitation and inhibition observed, is reminiscent of what has been previously described in the oculomotor network in the prepositus–vestibular complex neurons (reviewed in (ref. [45])), which can encode a variety of velocity and position combinations with heterogeneous individual time constants. Although these oculomotor integrators of neuronal activity have been well studied in fish[46–49], the neuronal activity we observed here reflects the temporal integration of external sensory evidence that directly drives behavior and may precede it by many seconds, as opposed to an internally generated efferent signal. We hope that future work will be able to reveal whether individual cell biophysical properties or emergent network features underlie the ability of these neurons to integrate in time. It is worth noting, though, that fish perform the optokinetic reflex to minimize retinal slip, and it is likely that the RDM stimuli we showed may also elicit some eye movements in addition to the locomotor activity we quantified.

In our study, we observed two main regions where sustained and integrated activity was present: the pretectal–thalamic region and the rostral hindbrain region. The pretectum, the analog of the mammalian nucleus of the optic tract, is likely to be involved in the visual aspect of this task[32,33], whereas the hindbrain is likely to be directly responsible for turning and swim generation[35,36]. Interestingly, our study showed that neurons in the dorsal region of the pretectum were able to integrate visual sensory drive in time, a feature that has not been previously described. This modular architecture, schematized in our circuit model in Fig. 5c (see also (ref. [33])), could easily accommodate the addition of more turn-inducing stimuli from multiple modalities, and we hypothesize that the sensory drive, from regions analogous to the pretectum, will converge onto the same hindbrain turn generator.

Finally, our whole-brain functional screen, together with our modeling approach, uncovered the IPN as a site whose activity strongly correlated with the turning rate of the fish. This nucleus is interconnected with the left dorsal habenula and the DRN, structures that also contained units with long time constants and are known to be involved in reward-based modulation of behavior[37]. Notably, the IPN has also been implicated in a variety of deficits observed in navigation-based assays in rodents[25,26]. It is reassuring that this area, among others, is also acutely related to motor output, as shown by our motor–trigger analysis. We hope that this study will help inspire future research able to further unravel the integration between sensory stimuli and internal states and how they come together to form behavioral representations and actions.

Online content

Any methods, additional references, Nature Research reporting summaries, source data, extended data, supplementary information, acknowledgements, peer review information; details of author contributions and competing interests; and statements of data and code availability are available at https://doi.org/10.1038/s41593-019-0535-8.

Received: 15 May 2019; Accepted: 7 October 2019;

References

1. Ratcliff, R. A theory of memory retrieval. *Psychol. Rev.* **85**, 59–108 (1978).
2. Stone, M. Models for choice-reaction time. *Psychometrika* **25**, 251–260 (1960).
3. Newsome, W. T., Britten, K. H. & Movshon, J. A. Neuronal correlates of a perceptual decision. *Nature* **341**, 52–54 (1989).
4. Shadlen, M. N. & Newsome, W. T. Motion perception: seeing and deciding. *Proc. Natl Acad. Sci. USA* **93**, 628–633 (1996).
5. Hanes, D. P. & Schall, J. D. Neural control of voluntary movement initiation. *Science* **274**, 427–430 (1996).
6. Gold, J. I. & Shadlen, M. N. The neural basis of decision making. *Annu. Rev. Neurosci.* **30**, 535–574 (2007).
7. Scott, B. B. et al. Fronto–parietal cortical circuits encode accumulated evidence with a diversity of timescales. *Neuron* **95**, 385–398 (2017).
8. Akrami, A., Kopec, C. D., Diamond, M. E. & Brody, C. D. Posterior parietal cortex represents sensory history and mediates its effects on behaviour. *Nature* **554**, 368–372 (2018).
9. Licata, A. M. et al. Posterior parietal cortex guides visual decisions in rats. *J. Neurosci.* **37**, 4954–4966 (2017).
10. Brunton, B. W., Botvinick, M. M. & Brody, C. D. Rats and humans can optimally accumulate evidence for decision-making. *Science* **340**, 95–98 (2013).
11. O'Connell, R. G., Dockree, P. M. & Kelly, S. P. A supramodal accumulation-to-bound signal that determines perceptual decisions in humans. *Nat. Neurosci.* **15**, 1729–1735 (2012).
12. Wyart, V., de Gardelle, V., Scholl, J. & Summerfield, C. Rhythmic fluctuations in evidence accumulation during decision making in the human brain. *Neuron* **76**, 847–858 (2012).
13. DasGupta, S., Ferreira, C. H. & Miesenböck, G. FoxP influences the speed and accuracy of a perceptual decision in *Drosophila*. *Science* **344**, 901–904 (2014).
14. Newsome, W. T. & Paré, E. B. A selective impairment of motion perception following lesions of the middle temporal visual area (MT). *J. Neurosci.* **8**, 2201–2211 (1988).
15. Horwitz, G. D. & Newsome, W. T. Separate signals for target selection and movement specification in the superior colliculus. *Science* **284**, 1158–1161 (1999).
16. Kim, J. N. & Shadlen, M. N. Neural correlates of a decision in the dorsolateral prefrontal cortex of the macaque. *Nat. Neurosci.* **2**, 176–185 (1999).
17. Ding, L. & Gold, J. I. Separate, causal roles of the caudate in saccadic choice and execution in a perceptual decision task. *Neuron* **75**, 865–874 (2012).
18. Hanks, T. D. et al. Distinct relationships of parietal and prefrontal cortices to evidence accumulation. *Nature* **520**, 220–223 (2015).
19. Hanks, T. D., Ditterich, J. & Shadlen, M. N. Microstimulation of macaque area LIP affects decision-making in a motion discrimination task. *Nat. Neurosci.* **9**, 682–689 (2006).
20. Katz, L., Yates, J., Pillow, J. W. & Huk, A. Dissociated functional significance of choice-related activity across the primate dorsal stream. *Nature* **535**, 285–288 (2016).
21. Brody, C. D. & Hanks, T. D. Neural underpinnings of the evidence accumulator. *Curr. Opin. Neurobiol.* **37**, 149–157 (2016).
22. Neuhauss, S. C. et al. Genetic disorders of vision revealed by a behavioral screen of 400 essential loci in zebrafish. *J. Neurosci.* **19**, 8603–8615 (1999).
23. Orger, M. B., Smear, M. C., Anstis, S. M. & Baier, H. Perception of Fourier and non-Fourier motion by larval zebrafish. *Nat. Neurosci.* **3**, 1128–1133 (2000).
24. Morley, B. J. The interpeduncular nucleus. *Int. Rev. Neurobiol.* **28**, 157–182 (1986).
25. Sharp, P. E., Turner-Williams, S. & Tuttle, S. Movement-related correlates of single cell activity in the interpeduncular nucleus and habenula of the rat during a pellet-chasing task. *Behav. Brain Res.* **166**, 55–70 (2006).
26. Clark, B. J. & Taube, J. S. Deficits in landmark navigation and path integration after lesions of the interpeduncular nucleus. *Behav. Neurosci.* **123**, 490–503 (2009).
27. Orger, M. B., Kampff, A. R., Severi, K. E., Bollmann, J. H. & Engert, F. Control of visually guided behavior by distinct populations of spinal projection neurons. *Nat. Neurosci.* **11**, 327–333 (2008).
28. Roitman, J. D. & Shadlen, M. N. Response of neurons in the lateral intraparietal area during a combined visual discrimination reaction time task. *J. Neurosci.* **22**, 9475–9489 (2002).
29. Hwang, E. J., Dahlen, J. E., Mukundan, M. & Komiyama, T. History-based action selection bias in posterior parietal cortex. *Nat. Commun.* **8**, 1242 (2017).
30. Gold, J. I., Law, C.-T., Connolly, P. & Bennur, S. The relative influences of priors and sensory evidence on an oculomotor decision variable during perceptual learning. *J. Neurophysiol.* **100**, 2653–2668 (2008).
31. Portugues, R., Feierstein, C. E., Engert, F. & Orger, M. B. Whole-brain activity maps reveal stereotyped, distributed networks for visuomotor behavior. *Neuron* **81**, 1328–1343 (2014).
32. Kubo, F. et al. Functional architecture of an optic flow-responsive area that drives horizontal eye movements in zebrafish. *Neuron* **81**, 1344–1359 (2014).
33. Naumann, E. A. et al. From whole-brain data to functional circuit models: the zebrafish optomotor response. *Cell* **167**, 947–960 (2016).
34. Huang, K.-H. H., Ahrens, M. B., Dunn, T. W. & Engert, F. Spinal projection neurons control turning behaviors in zebrafish. *Curr. Biol.* **23**, 1566–1573 (2013).
35. Dunn, T. W. et al. Neural circuits underlying visually evoked escapes in larval zebrafish. *Neuron* **89**, 613–628 (2016).
36. Wolf, S. et al. Sensorimotor computation underlying phototaxis in zebrafish. *Nat. Commun.* **8**, 651 (2017).
37. Bianco, I. H. & Wilson, S. W. The habenular nuclei: a conserved asymmetric relay station in the vertebrate brain. *Philos. Trans. R. Soc. B. Biol. Sci.* **364**, 1005–1020 (2009).
38. Bogacz, R. Optimal decision-making theories: linking neurobiology with behaviour.*Trends Cogn. Sci.* **11**, 118–125 (2007).
39. Shadlen, M. N. & Newsome, W. T. Neural basis of a perceptual decision in the parietal cortex (area LIP) of the rhesus monkey. *J. Neurophysiol.* **86**, 1916–1936 (2001).
40. Usher, M. & McClelland, J. L. The time course of perceptual choice: the leaky, competing accumulator model. *Psychol. Rev.* **108**, 550–592 (2001).
41. Mazurek, M. E., Roitman, J. D., Ditterich, J. & Shadlen, M. N. A role for neural integrators in perceptual decision making. *Cerebral Cortex* **13**, 1257–1269 (2003).
42. Teodorescu, A. R. & Usher, M. Disentangling decision models: from independence to competition. *Psychol. Rev.* **120**, 1–38 (2013).
43. Portugues, R., Haesemeyer, M., Blum, M. L. & Engert, F. Whole-field visual motion drives swimming in larval zebrafish via a stochastic process. *J. Exp. Biol.* **218**, 1433–1443 (2015).
44. Severi, K. E. et al. Neural control and modulation of swimming speed in the larval zebrafish. *Neuron* **83**, 692–707 (2014).
45. Robinson, D. A. Integrating with neurons. *Annu. Rev. Neurosci.* **12**, 33–45 (1989).
46. Aksay, E., Baker, R., Seung, H. S. & Tank, D. W. Anatomy and discharge properties of pre-motor neurons in the goldfish medulla that have eye-position signals during fixations. *J. Neurophysiol.* **84**, 1035–1049 (2000).
47. Miri, A. et al. Spatial gradients and multidimensional dynamics in a neural integrator circuit. *Nat. Neurosci.* **14**, 1150–1161 (2011).
48. Daie, K., Goldman, M. S. & Aksay, E. R. F. Spatial patterns of persistent neural activity vary with the behavioral context of short-term memory. *Neuron* **85**, 847–860 (2015).
49. Joshua, M. & Lisberger, S. G. A tale of two species: neural integration in zebrafish and monkeys. *Neuroscience* **296**, 80–91 (2015).

Methods

For information relating to how sample sizes were determined and replication, randomization and blinding of experiments, please refer to the Life Sciences Reporting Summary that accompanies this article.

Zebrafish lines. All experiments were performed with 6–7 days post-fertilization (dpf) zebrafish larvae (Danio rerio) of yet undetermined sex. The Tuepfel long-fin (TL) wild-type strain was used for freely swimming behavioral experiments. The nacre (*mitfa*−/−) transgenic zebrafish lines *Tg(elavl3:GCaMP6s+/+)*[50] and *Tg(elavl3:GCaMP6f+/+)*[36] were used for functional imaging experiments. All animal experimental procedures were approved by the Max Planck Society and the local government (Regierung von Oberbayern).

Freely swimming behavioral experiments. Fish were placed in an 8.8-cm Petri dish, on top of a diffusive screen mounted on a clear acrylic support, and illuminated from below using an array of IR LEDs. Freely swimming larvae were monitored using a high-speed camera (Mikrotron) running at 200 fps, equipped with a lens (Edmund Optics) and an IR band pass filter. The visual stimuli were displayed from below using an Asus P2E microprojector and a cold mirror (Edmund Optics). Custom-written software in LabView was used for tracking of the fish swim dynamics and for generating the closed-loop RDM stimulus. The stimulus consisted of randomly moving dots, a fraction of which moved coherently to the left or to the right of the fish. The stimulus was constructed such that dots could not move in the same direction after three consecutive frames, thus avoiding that fish would follow individual dots. Specifically, every dot was assigned a random lifetime shorter than 250 ms. At every frame, dots whose lifetime had expired were removed, and new ones with random lifetimes were generated. Several dots were randomly selected to move in a common direction, determined by the coherence. These dots were shifted by the time difference multiplied by the velocity in the true direction of the stimulus, whereas the others were shifted with the same velocity in a random direction. Dots that exited the field of view were redrawn on the opposite end with toroidal boundary conditions. For details, see https://github.com/portugueslab/stytra/blob/master/stytra/stimulation/stimuli/kinematograms.py class RandomDotKinematogram. Fish orientation was constantly monitored, and, after each turn, the direction of the coherent dot motion was immediately updated, such that its direction remained to the left or right of the fish. The coherence, which ranged from +1 (left) to −1 (right), in increments of 0.1, was maintained constant for a 12-s trial before being immediately changed to a new value in a next trial. A set of stimuli consisted of 22 trials, containing coherences of all magnitudes in both directions, and presented in a randomized order. Fish that did not complete at least five sets of stimuli were excluded from the analysis. In the fixed–transition experiments, trials contained only coherences of magnitude 0, 0.3 and 0.6, immediately following one another. A set of stimuli contained all possible combinations of transition involving coherence magnitude and coherence direction. Here, too, fish that did not complete at least five sets of stimuli were excluded from the analysis. Fish swim dynamics and behavioral analysis was performed with custom-written software in MATLAB.

Whole-brain imaging experiments. Larvae were placed in 3.5-cm Petri dishes and embedded in 1.5–2% agarose before imaging. The agarose around the tail, caudal to the pectoral fins, was cut away with a fine scalpel to allow for tail movement. The dish was placed onto an acrylic support with a light-diffusing screen and imaged on a custom-built two-photon microscope. A TiSapphire laser (Spectra Physics Mai Tai) tuned to 905 nm was used for excitation. Larval brains were systematically imaged while being presented the RDM visual stimuli. Visual stimuli (see above) were generated using a custom-written Python script and were projected at 60 frames per second using an Asus P2E microprojector and a red long-pass filter (Kodak Wratten No. 25) to allow for simultaneous imaging and visual stimulation. Full frames were acquired every 334.51 ms in four 0.83-μm-spaced interlaced scans, which resulted in *x*- and *y*-pixel dimension between 0.51 and 1 μm (varying resolutions here depended on field of view covered). Imaging stacks were mostly acquired in the dorsal-to-ventral direction and, for some fish (covering deep hindbrain areas), in the ventral-to-dorsal direction. Two types of experimental paradigms were used: one in which the stimulus sequence was randomized and coherences were separated by pauses of no motion, and another in which coherences directly followed one another, with no pauses, in a nonrandomized fashion. In the randomized paradigm, the set of stimuli used in imaging experiments consisted of coherences 0, 0.3, 0.6 and 1, in both directions, with a duration of 30 s, and separated by 10 s of pause (dots remained on the screen but were static). In the direct transition paradigm, coherences 0.8, 0.3 and 0 were probed, with no break in between, and sampling every possible transition between direction and coherence magnitude. After all stimuli were shown in one plane, the focal plane was shifted ventrally or dorsally by 2 μm (for some fish, 1 μm), and the process was repeated, with either the randomized sequence or direct transition of stimuli in each plane. Fish were illuminated from above using IR light-emitting diodes (850 nm wavelength), and the fish were imaged from below at up to 200 frames per second using an IR-sensitive charge-coupled device camera (Pike F032B, Allied Vision Technologies). Tail movement was monitored using custom-written software in Python. Fish that did not behave at least three times per plane were excluded from the analysis.

Head-restrained behavioral analysis. For the behavioral analysis presented in Extended Data Fig. 4, larvae were embedded in agarose, and the stimuli were presented while the behavior was tracked using Stytra[51]. For each bout, a laterality index was computed by adding the cumulative tail angle recorded for the first 60 ms of the bout, as this was the time frame over which forward swims and turns differed most prominently[34]. For every fish, the histogram of laterality indices across all bouts in all conditions was plotted and fit with the sum of three Gaussian distributions, as shown in Extended Data Fig. 4c. This ensured that differences in the embedding and preparation were accounted for in a fish-by-fish basis. The two minima between the three peaks were chosen as the thresholds to distinguish between the three types of swim bout: forward and left and right turns. No fish were excluded from the analysis.

Image analysis. Image analysis was performed as previously described[30].

Anatomical registration. Image registration for two-photon imaging was performed using the free Computational Morphometry Toolkit[52](http://www.nitrc.org/projects/cmtk/), as previously described[31].

Regressors and correlation analysis. Regressors for correlation analysis[31] were constructed from a set of sensory stimulus and motor-related variables. These were convolved with a kernel with an exponential decay based on the measured half-decay time for GCaMP6s (1.796 s) and GCaMP6f (0.4 s)[53] to produce a set of predicted fluorescence traces and were compared with the measured fluorescence traces by correlation. Correlation analysis was performed for automatically segmented ROIs to identify the variable that best described the signal of individual neurons. To assign voxels to a particular functional group, we required a threshold of at least 0.5 for the best absolute correlation coefficient.

Computation of motor triggers. In Extended Data Fig. 7, we present the fluorescence of ROIs triggered on motor events (the motor-triggered fluorescence average), which we refer to as motor triggers. This can be computed because behavior was monitored during imaging. We defined a set of interesting features of neuronal activity that could be associated with motor activity. This set comprised the triggers shown in Extended Data Fig. 7, including the additive inverse of the trigger in 7d. The motor event can be a leftward turn, a rightward turn or a forward swim. All ROIs with a correlation value with the motor trigger greater than 0.7 were included.

Model fitting. To explain the stimulus-related responses, we constructed a model based on the feed-forward inhibition integrator[28]. Since we frequently observed responses with different time constants for ipsi and contralateral excitation, we allowed independent integration of motion to both sides and took a weighted sum. The model is depicted in Fig. 4a and is described by the following equations:

$$\tau_L \frac{dI_L}{dt} = Ls_L^P - I_L$$

$$\tau_R \frac{dI_R}{dt} = Rs_R^P - I_R$$

$$a = I_L + I_R$$

where I_L and I_R are the levels of integrators, t_L and t_R are their respective time constants, *L* and *R* are the input stimulus weights, s_L and s_R are the current coherences to the left and right side, P is the power of the nonlinearity and a is the level of activity of the modeled unit.

Within the parameter space of this model are responses that are driven purely by momentary evidence, and no integration takes place (both τ_L and τ_R are around 0), responses which can be explained as a single integrator (τ_L and τ_R are equal) and responses to a single motion direction (either R or L weights are 0). The model allows for a nonlinear response to motion coherence; however, by regularized fitting, we found almost no units where this nonlinearity was present. We fitted this model to all ROIs spanning more than one plane and retained those whose unexplained variance was smaller than 0.4 of the variance of the trace. The model was implemented as a function in the Julia language, with exact integration (as the system is linear after the input nonlinearity) and application of an exponential kernel with the GCaMP6s time constant. The model fit was optimized using the gradient-based BFGS method, as implemented in the Optim.jl Julia package[54]. Three-fold cross validation was used to determine the regularization parameter λ, which weighted a sum of the absolute values of the model features (weights, time constants, difference of time constants and the logarithm of the power of the nonlinearity). The code implementing the model and the fitting is in the supplied repository: https://github.com/portugueslab/Dragomir-et-al-2019-modelfit.

Poisson model for generation of turns. We can extend the proposed architecture to explain the turning behavior: the output of two symmetrically build modules (as in Fig. 4a) modulated linearly the deviation from the baseline rate of a Poisson process that initiates turns. We can determine all the parameters for this model from behavioral experiments. First, we used the data of turn rates for each coherence (Fig. 1d) to determine the steady-state parameters and the baseline rate of turns. This fixed the nonlinearity power P and the relative weights of inputs to the integrators in the contralateral or ipsilateral side. Then, from the transition experiments in Fig. 2a, we determined the three remaining free parameters: the angle of a turn and the time constants τ_I and τ_C. Equally good fits can be obtained for different choices of τ_I and τ_C, so we opted for the point in parameter space where the time constants are equal. This resulted in an even simpler model of turn generation, where instead of two Fig. 4 a modules, there was only one, with additional inhibitory connection to the contralateral integrator, where both of the integrators had the same time constant and directly modified the Poisson rate for the respective side. The values obtained for the model were a time constant, $\tau = 0.96$ s, and a turning angle per bout of 58.27 degrees (although this value was relatively large compared to an usual turning angle; in this way, forward turns that were slightly biased to one direction or another were also accounted for, while keeping the behavioral rate consistent with other experiments). For details, see the notebook in the repository attached to this article: https://github.com/portugueslab/Dragomir-et-al-2019-modelfit.

Generation of synthetic freely swimming behavior. In the experiments for freely swimming fish, all stimulus coherences from −1 to +1 in 0.1 steps were tested with random transitions. To generate the traces shown in Fig. 5b, we identified the transitions that appeared in the stimulus sequence shown in Fig. 5b and selected 10 s of the pretransition behavior and 10 s of the post-transition behavior. This allowed us to construct an estimate of the expected behavior to this stimulus sequence for every fish tested.

Logistic multivariate regression model. To identify the dependence of the turning behavior on the current stimulus, the stimuli being presented during previous bouts and the motor output of the previous bouts, we set up a logistic multivariate regression model. This expressed the likelihood odds ratio as a sum:

$$\log\left(\frac{P_L}{P_R}\right) = K + \sum_{i=0}^{k} \alpha_i C_i + \sum_{i=1}^{k} \beta_i B_i$$

where C_i labels the stimulus being presented, B_i is the motor output of the previous i-th bout, K represents the bias and up to the k-th previous bout is considered. Rightward bouts were set to belong to category 2, leftward bouts were set to belong to category 1, rightward coherences were set as negative and leftward coherences were set as positive. We collected and used a dataset comprising 126,754 total bouts across 5,688 trials (lasting 30 s each) across 37 fish and fitted the model using the mrnfit routine in MATLAB for each fish and then averaged across fish. The results are shown in Fig. 2e. The only significant values found were $K = 2.76$, $\alpha_0 = 1.96$, $\alpha_{-1} = 0.36$, $\alpha_{-2} = -0.22$, $\alpha_{-3} = -0.17$, $\beta_{-1} = -0.97$, $\beta_{-2} = -0.34$, $\beta_{-3} = -0.20$ and $\beta_{-4} = -0.09$ (these are medians; means are: 2.66, 2.01, 0.40, −0.22, −0.18, −0.97, −0.42, −0.22 and −0.10).

To understand this equation, consider the following example. Keeping all other variables constant, what happens when we increase the coherence of the stimulus being currently presented from 0 (uncorrelated) to 1 (full motion to the left)? What changes is the value C0, from 0 to 1, so the ratio of the probabilities of having a leftward bout to a rightward bout—that is, the likelihood—changes by $\exp(1.96) = 7.1$. Similarly, if the previous bout was rightward, ignoring everything else, the probability that this bout will be leftward will be $\exp(-1.94)/\exp(-0.97) = 0.38$ times the probability that it will be to the right. In Fig. 2e, the motor coefficients were multiplied by −1 to coincide with the direction of the sensory coefficients.

Statistics. A two-tailed Wilcoxon signed-rank test was performed in Fig. 2e. Stimuli were randomized throughout except in the experiments shown in Figs. 4 and 5. Because different experimental groups did not exist, data collection and analysis were not performed with blinding to the conditions of the experiments. Data were not assumed to be normally distributed.

Reporting Summary. Further information on research design is available in the Nature Research Reporting Summary linked to this article.

Data availability

Processed imaging data are available on Zenodo (https://doi.org/10.5281/zenodo.3453488). Original imaging data and behavioral data are available upon reasonable request from the corresponding author.

Code availability

Code for Figs. 4 and 5 is available on GitHub (https://github.com/portugueslab/Dragomir-et-al-2019-modelfit). Parts of the analysis can be explored online via Binder. Stimulus code is available as part of Stytra v0.8.22 (http://portugueslab.com/stytra and https://doi.org/10.5281/zenodo.3451302), and explicit experimental protocols are available on GitHub (https://github.com/portugueslab/Dragomir-et-al-2019-protocols). MATLAB code is available upon reasonable request from the corresponding author.

References

50. Kim, D. H. et al. Pan-neuronal calcium imaging with cellular resolution in freely swimming zebrafish. *Nat. Methods* **14**, 1107–1114 (2017).
51. Štih, V., Petrucco, L., Kist, A. M. & Portugues, R. Stytra: an open-source, integrated system for stimulation, tracking and closed-loop behavioral experiments. *PLoS Comput. Biol.* **15**, e1006699 (2019).
52. Rohlfing, T. & Maurer, C. R. Nonrigid image registration in shared-memory multiprocessor environments with application to brains, breasts, and bees. *IEEE Trans. Inf. Technol. Biomed.* **7**, 16–25 (2003).
53. Chen, T.-W. et al. Ultrasensitive fluorescent proteins for imaging neuronal activity. *Nature* **499**, 295–300 (2013).
54. Mogensen, P. K. & Riseth, A. N. Optim: a mathematical optimization package for Julia. *J. Open Source Softw.* **3**, 615 (2018).

Acknowledgements

We thank M. Wulliman for advice on anatomic references. We thank A. Kist and D. Markov for technical help. We thank A. Borst and N. Gogolla for conversations and useful comments throughout the project and J. Fitzgerald for comments on the manuscript. We thank D.G.C. Hildebrand, I.H. Bianco and F. Engert (Harvard University) for sharing the Tg(*elavl3:GCaMP6f*) transgenic fish before publication. E.I.D. was partly funded by the Graduate School of Systemic Neurosciences, and all authors were funded by the Max Planck Gesellschaft. This research was also partially funded by Human Frontier Science Program grant RGP0027/2016 and a Life? grant from the Volkwagen Stiftung.

Author contributions

E.I.D. and R.P. conceived the project and designed the experiments. E.I.D. performed all experiments. E.I.D. and R.P. analyzed experimental data. V.Š. and R.P. designed and implemented the model. E.I.D. and R.P. wrote the manuscript with help from V.Š.

Competing interests

The authors declare no competing interests.

Additional information

Extended data is available for this paper at https://doi.org/10.1038/s41593-019-0535-8.

Supplementary information is available for this paper at https://doi.org/10.1038/s41593-019-0535-8.

Correspondence and requests for materials should be addressed to R.P.

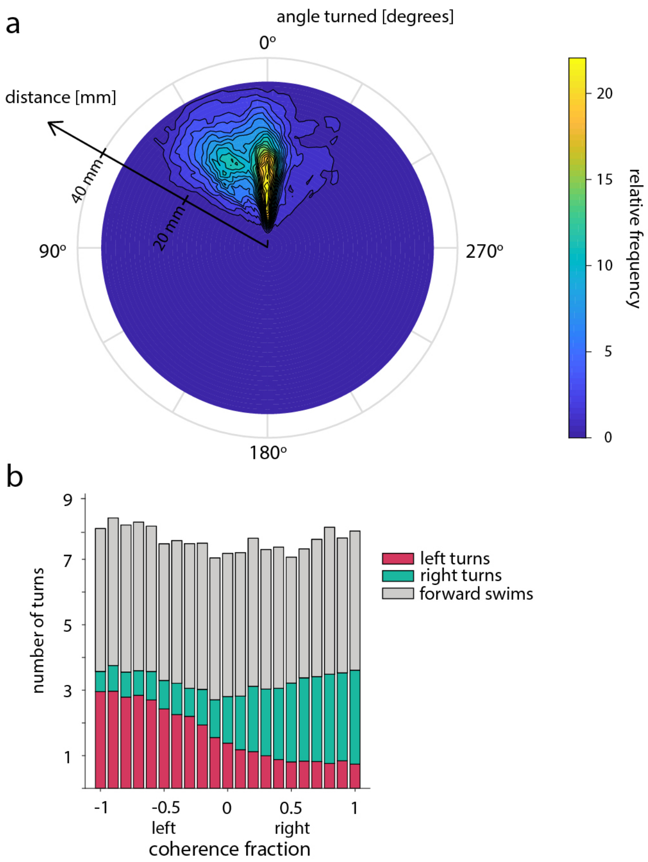

Extended Data Fig. 1 | Categorization of a turn. a, Two-dimensional contour plot showing the distance moved and angle turned averaged across all 51 fish when presented with coherence >0.5. Most swim bout events are clustered around 0 degrees, and represent forward swims, while lateralized turns begin around after 15 degrees. **b**, Number of left, right and forward swims as a function of stimulus coherence.

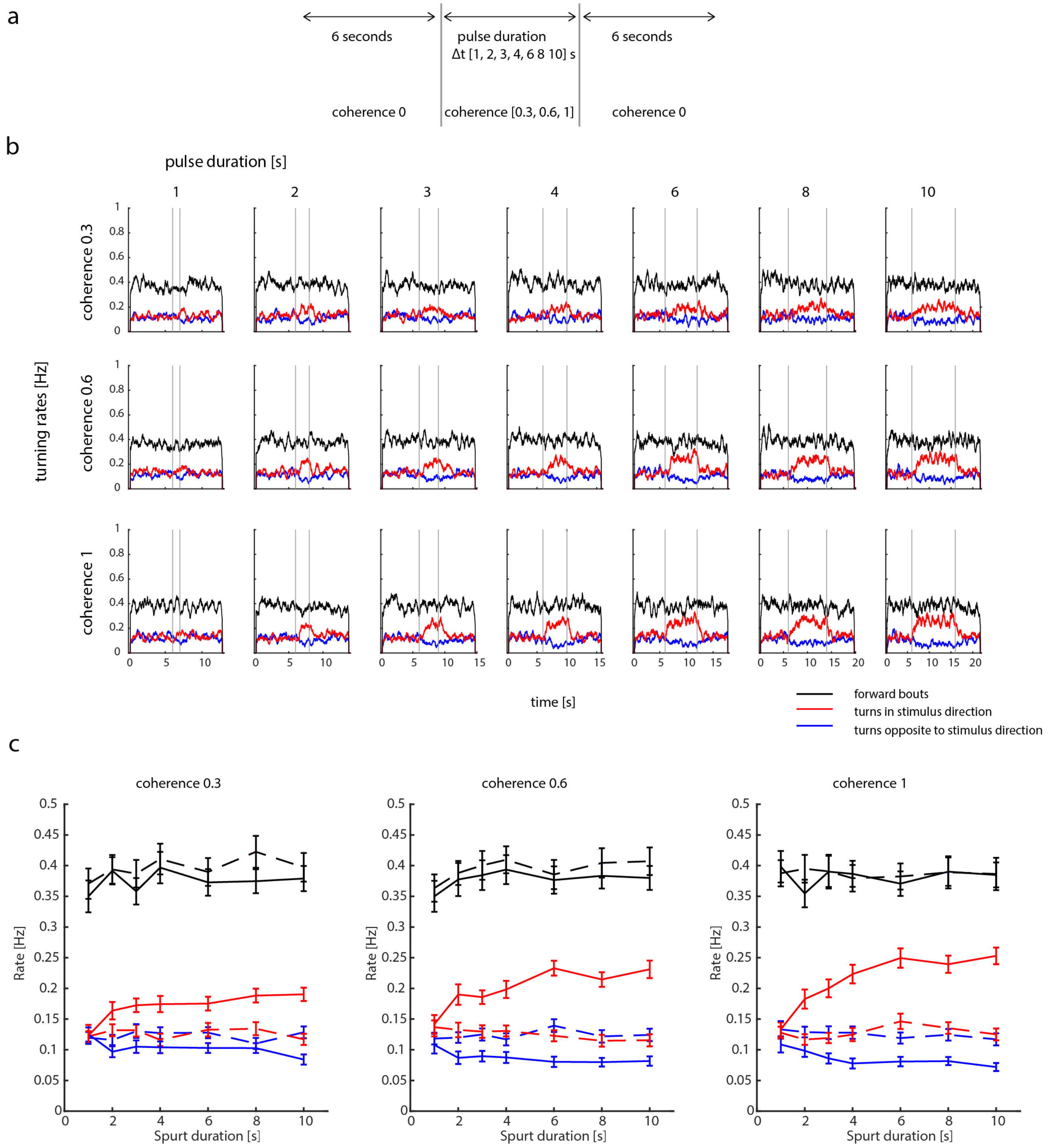

Extended Data Fig. 2 | Turning response to stimulus pulses. a, Schematic of experimental paradigm involving stimulus pulses. 6 seconds of coherence 0 were followed by a pulse coherence 0.3, 0.6 or 1. The stimulus pulse lasted 1, 2, 3, 4, 6, 8 or 10 seconds. After the pulse is over 6 seconds of coherence 0 were presented again. **b**, Forward swimming and turning rates for the three different coherences and the seven different pulse durations presented. The vertical grey lines denote pulse start and end. Instantaneous rates were computed by averaging over a 200 ms window. **c**, Average behavioral rates for forward swimming (black), turning in the direction of the stimulus (red), and against the stimulus (blue) averaged over the whole pulse as a function of the total pulse duration. In dotted lines the average baseline rates are shown computed over the 5 second window from second 1 to second 6 right before pulse onset (see panel **a**).

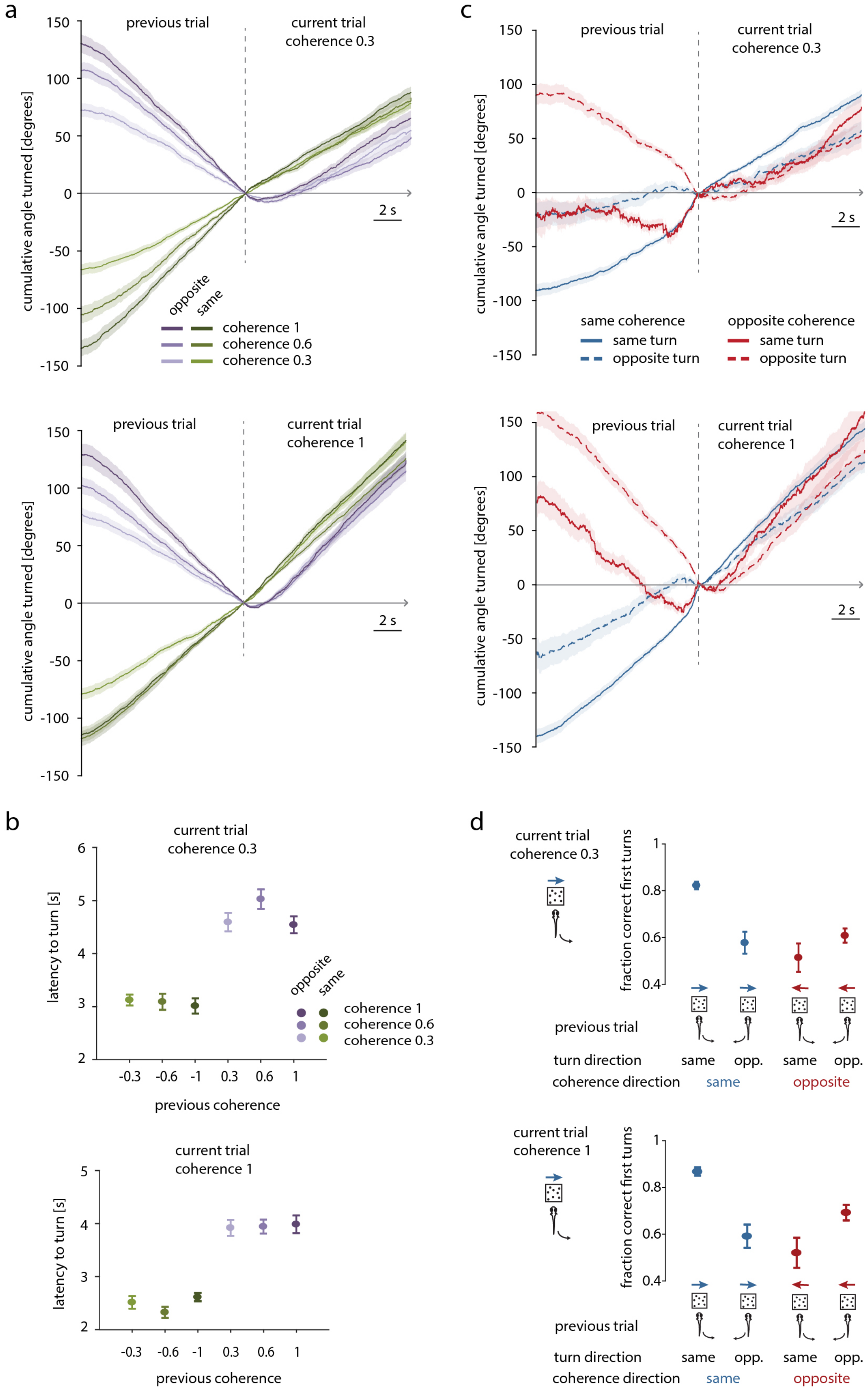

Extended Data Fig. 3 | see figure caption on next page.

Extended Data Fig. 3 | Sensory and motor history for coherences 0.3 and 1. a, Turning behavior during trials of coherence 0.3 (top) and 1 (bottom) as a function of the coherence presented during the preceding trial. Trajectories are split by both magnitude and direction of the preceding trial. **b**, Latency to first correct turn in trials of coherence 0.3 (top) and 1 (bottom) as a function of the coherence of the preceding trial. **c**, Turning behavior during trials of coherence 0.3 (top) and 1 (bottom) as a function of both the direction of the coherence presented during the preceding trial and the direction of the last turn in the preceding trial. Only preceding trials with coherence of magnitude 0.6 were included. **d**, Fraction of correct first turns during trials of coherence 0.3 (top) and 1 (bottom) as a function of both the direction of the coherence of the preceding trial and the direction of the last turn in the preceding trial. Only preceding trials with coherence of magnitude 0.3 (top) and 1 (bottom) were included.

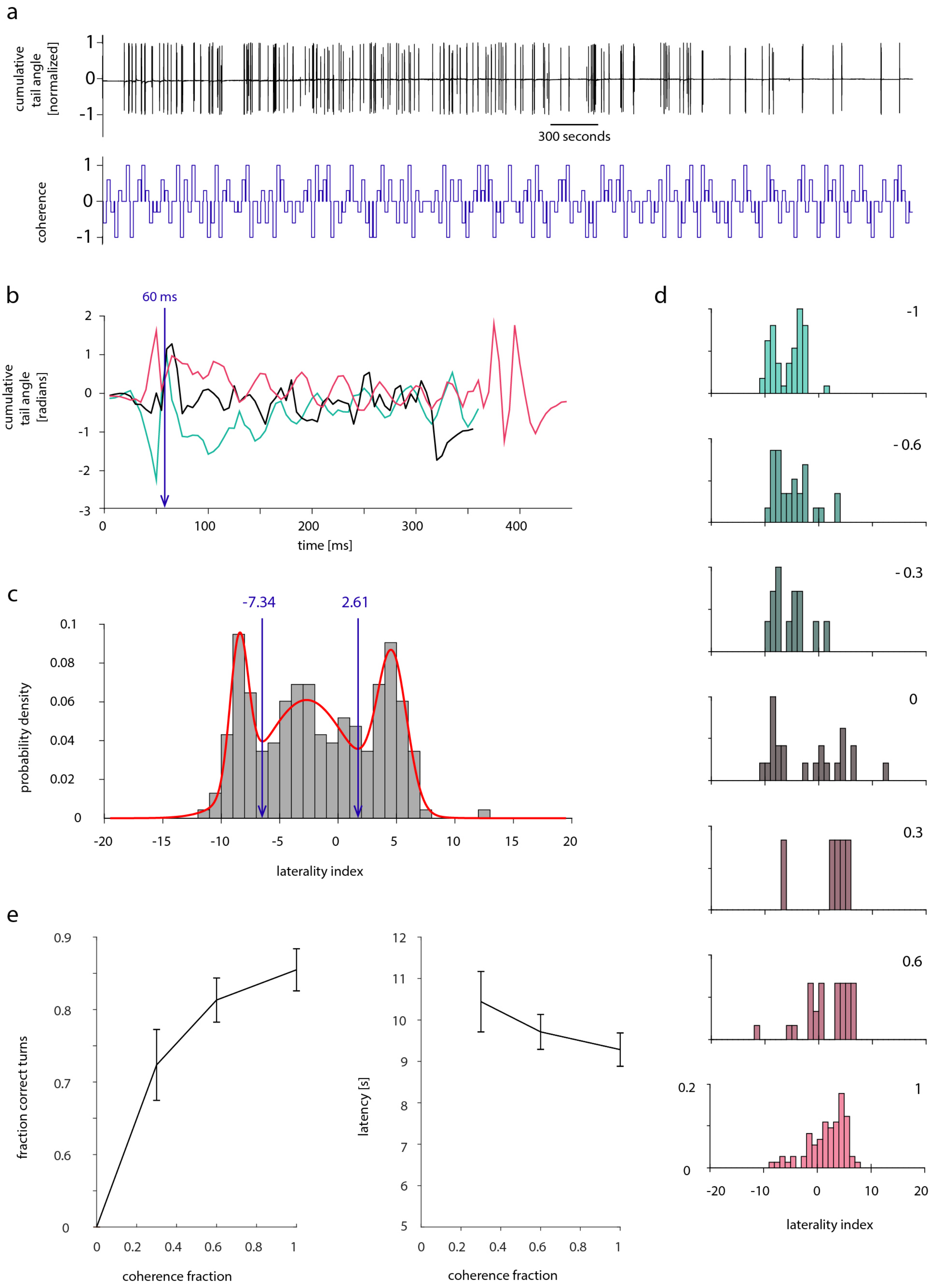

Extended Data Fig. 4 | see figure caption on next page.

Extended Data Fig. 4 | Turning behavior of head restrained larvae. a, Example tail trace during a full head restrained experiment with the coherence stimuli sequence (positive and negative numbers represent coherences to the left and right direction, respectively). **b**, Average tail traces of all bouts elicited during presentation of stimuli with coherence +1 (red), 0 (black) and −1 (green) for the fish shown in a above. Leftward turns, forward swims and rightward turns, which are the predominant behaviors during these stimuli presentations, can be clearly distinguished by computing the sum of the cumulative tail angle during the first 60 ms of the bout, which we refer to as the laterality index. **c**, Histogram of all laterality indices for the fish in a, showing a distribution with three peaks corresponding to left- and right-ward turns and forward swims. Thresholds can be imposed to distinguish between these behaviors, in this case −7.34 separates rightward and forward swims and 2.61 separates forward swims and left-ward turns. **d**, Individual histograms for all bouts elicited during stimulus presentations of the different coherences for the sample fish in a. e, Left: Average fraction of correct turns (in the direction of presented coherence). Right: Average latency (time from stimulus onset) to first correct turn as a fraction of stimulus coherence. Averages over N = 18 fish; error bars denote SEM.

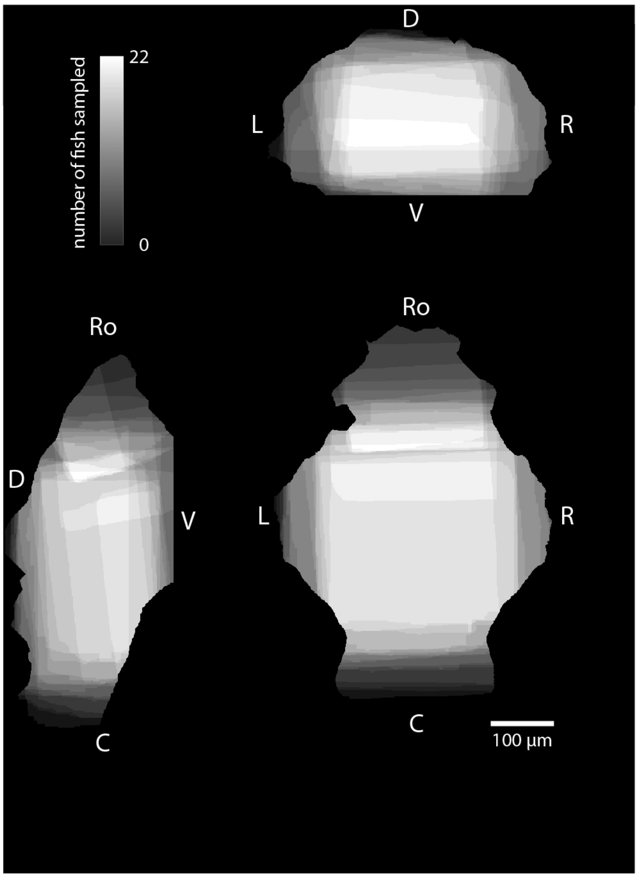

Extended Data Fig. 5 | Brain regions sampled during imaging experiments. Sum of projection footprints along the three axes for all brains that were imaged and could be registered to the reference brain.

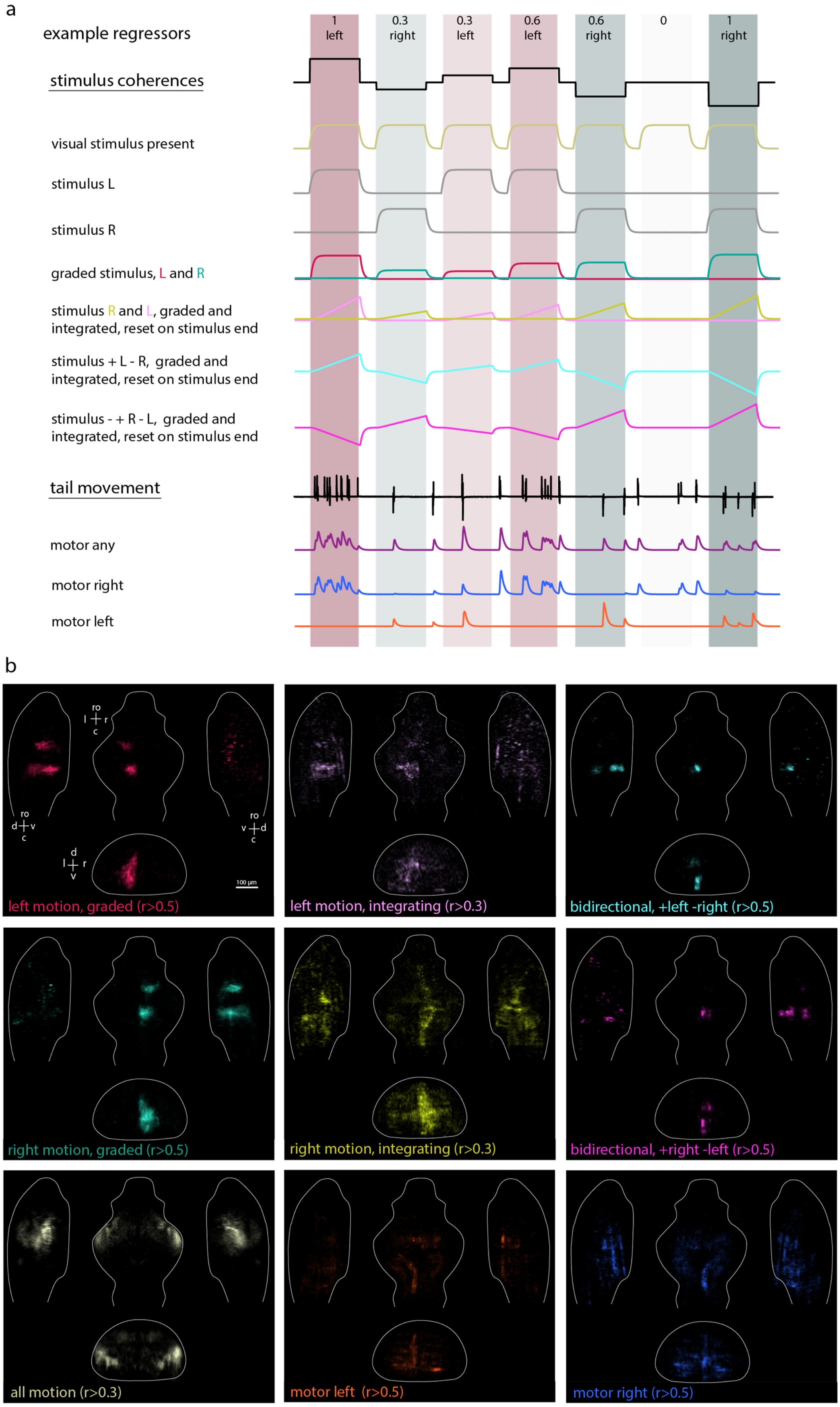

Extended Data Fig. 6 | see figure caption on next page.

Extended Data Fig. 6 | Full list of regressors used in imaging experiments. a, The regressors are constructed from the stimulus coherence shown and the tail movement recorded (both underlined) **b**, ROI maps color coded according to individual sensory and motor related regressors displayed in Fig. 3 (each regressor and corresponding thresholds for ROI shown here are displayed at the bottom). Each map has views from lateral left (left), dorsoventral (top central), lateral right (right) and rostro-caudal (bottom) ROI projections.

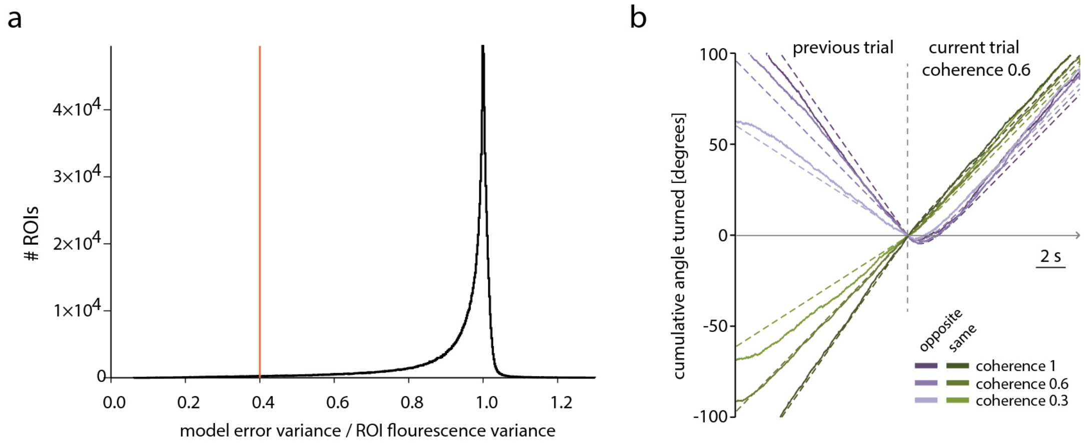

Extended Data Fig. 7 | Additional model fitting of neuronal data and behavioral prediction. a, Variance of ROIs explained by the model. The orange line is the cut of threshold for ROIs displayed in Fig. 4, chosen empirically to discard spurious fits due to artifacts. **b**, Simulated behavioral response of the integrator model (dashed line) to transitions in coherence and direction superimposed on data shown in Fig. 2a. The relative weights of excitation and inhibition and the nonlinearity P where extracted from data presented in Fig. 1c, whereas the time constant was extracted from behavioral data presented in Fig. 2a.

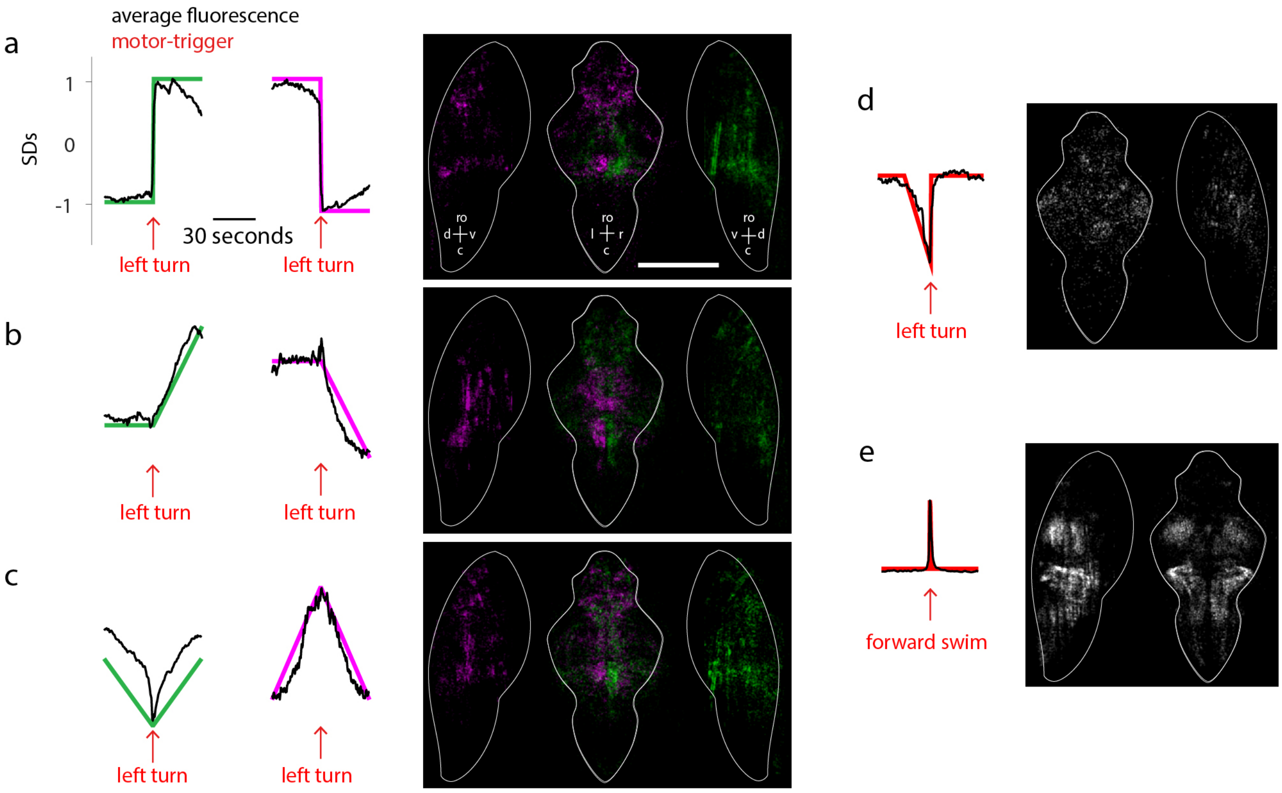

Extended Data Fig. 8 | Motor-triggered neuronal activity. a, Left: motor triggers corresponding to stepwise increases (green) and decreases (magenta) concurrent with leftward turns. The average activity of all ROIs with correlation >0.7 with the corresponding motor trigger is superimposed in black. Right: anatomical location of the motor triggers throughout the brain. Ro – rostral, c – caudal, l – left, r – right and scale bar = 300 microns. **b, c**, Similar to a but for neuronal activity which ramps up or down after a left turn **(b)** or neuronal activity which has a maximum or minimum coincident with the left turn **(c)**. **d**, Motor trigger corresponding to neuronal activity that decreases steadily and is reset upon a left turn. The number of ROIs with activity that increased steadily and was reset upon a left turn was negligible. **e**, All ROIs with activity coincident with a forward swim.

Manuscript 3: The interpeduncular nucleus exhibits structured optic flow-dependent activity

Vilim Štih, Luigi Petrucco, Hagar Lavian, Elena Dragomir, Emanuele Paoli, You Wu, Fabian Svara, Ruben Portugues

Unpublished manuscript

The interpeduncular nucleus exhibits structured optic flow-dependent activity

Vilim Štih[1,2], Luigi Petrucco[1,2,3], Hagar Lavian[1,3], Elena Dragomir[1], Emanuele Paoli[1,3], You Wu[1,3], Fabian Svara[4], Ruben Portugues[1,2,5]

[1]Max Planck Institute of Neurobiology, Martinsried, Germany

[2]Graduate School of Systemic Neurosciences (GSN-LMU), Munich, Germany

[3]Institute of Neuroscience, Technical University of Munich, Germany

[4]Caesar, Bonn, Germany

[5]Munich Cluster for Systems Neurology (SyNergy), Munich, Germany

Optic flow is one of the most salient visual stimuli for animals and in particular the larval zebrafish. To perform the optomotor response, which counteracts visual displacement, they have to estimate the direction in which the world is moving. With whole-brain imaging, we examine the locations where the directional optomotor signals are well represented. In addition to the sensory areas, a midbrain structure - the interpeduncular nucleus (IPN) contains parts tuned to all directions of motion, arranged in a striking anatomical pattern. To find the sources of this patterning, we performed imaging in several transgenic lines expressing a calcium sensor in different anatomical lines that highlight the input axons from the habenulae, the GABAergic neurons from inside the structure, and most cell bodies. We found that the pattern of tuning cannot be explained by the structure of the incoming axons, rather the activity is shaped by the cells belonging to the nucleus. Using electron microscopy (EM), we found cells of the IPN display a variety of branching patterns, consistent with the tuning regions. Prominently, a group of cells in the ventral part form 4 columns with axonal (lateral) and dendritic (medial) arborizations with tuned responses, where the dendritic tree shares the tuning direction of the input axons while the axonal part is tuned to the opposite direction, suggesting a role for axo-axonic inhibition. The presence of such synapses has been determined also in the EM data. By monitoring behavior during the imaging experiments, we confirm that this stimulus evokes biased tail motion consistent with previous freely-swimming studies, however the causal role of the structure remains to be determined.

Introduction

Whole-field motion is a stimulus that is of almost universal relevance among sighted animals. It plays a role in a whole spectrum of behaviors, from stabilizing reflexes to navigation. In the larval zebrafish the most prominent response to this stimulus is the optomotor response: the animal aligning itself with the direction of perceived motion and swimming along it[1]. The local motion signals, computed in the retina, are spatially and binocularly integrated in different brain regions, such as the pretectum[2,3]. However, most investigations of this pathway have dealt with the behavior on the acute time scale, while there is growing number of studies indicating that fish are influenced by stimuli over longer timescales[4,5].

A whole-brain screen in a previous study[6], with only left- and rightward stimuli, indicated a special property of responses in the interpeduncular nucleus: the functional regions of interest found there had bidirectional modulation of activity, corresponding to the modulation of

[1] Orger et al., “Control of Visually Guided Behavior by Distinct Populations of Spinal Projection Neurons”.

[2] Naumann et al., “From Whole-Brain Data to Functional Circuit Models”.

[3] Yildizoglu et al., “A Neural Representation of Naturalistic Motion-Guided Behavior in the Zebrafish Brain”.

[4] Wolf et al., “Sensorimotor Computation Underlying Phototaxis in Zebrafish”.

[5] Dunn et al., “Brain-Wide Mapping of Neural Activity Controlling Zebrafish Exploratory Locomotion”.

[6] Dragomir, Štih, and Portugues, “Evidence Accumulation during a Sensorimotor Decision Task Revealed by Whole-Brain Imaging”.

freely-swimming turn rates. In order to investigate which other regions have a good representation of whole-field motion, but are also potentially involved in modulating these longer-timescale states, we performed a whole-brain screen with lightsheet imaging. We confirmed that the interpeduncular nucleus (IPN), a midbrain structure, has areas with tuned responses to all directions of motion. Such a complete set of motion direction correspondences is present in only few brain regions.

Other lines of evidence recently highlighted the importance of this structure in spatial behavior[7], demonstrating that severing the habenula-to-IPN pathway impairs directional rule learning. We decided to investigate the response properties to directional motion in the IPN in greater detail, to distinguish which parts are directionally tuned, how the tuning is distributed through different parts of the structure, and how it comes about given what is known about the nucleus structure and its inputs. To achieve this, we imaged the IPN in different transgenic zebrafish larvae in a comparative fashion, while presenting directional motion stimuli to the animal. Different parts of the neuropil displayed a precise and consistent patterning of tuned regions, organized in large patches throughout the whole three-dimensional structure. To find out the possible source of this patterning, we reconstructed the IPN cells from electron microscopy data and discovered striking correspondences of the arborizations patterns of cells inside the nucleus to the functionally-identified regions. The activity in the somata also displayed the full range of tuning directions. This evidence together demonstrates the intricate functional geometry of the IPN, the purpose of which remains to be discovered.

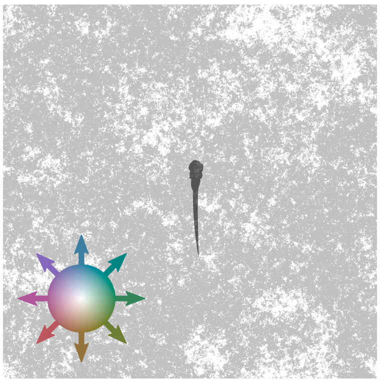

Figure 1: The stimulus and the 8 directions of movement superimposed showing the color encoding used thought the paper (the stimulus displayed to the fish is always monochromatic, at maximum contrast). For reference, the color encoding is displayed on the footer of every page

Results

The IPN is the only midbrain region that contains a complete map of optic flow directions

Whole-field motion causes the optomotor response: the fish tries to align itself to and follow the direction of motion. To probe the responses of different motion directions we used a seamlessly-tiling pink noise texture moved in 8 directions (Figure 1) at 10mm/s.

The behavior (summarized in Figure 2) shows clear stimulus-dependent bias in tail deflection on bout start. The tail deflection in freely swimming fish is highly correlated with turning angle, and the embedded behavior closely follows the results of the first study on turning in larval zebrafish[8].

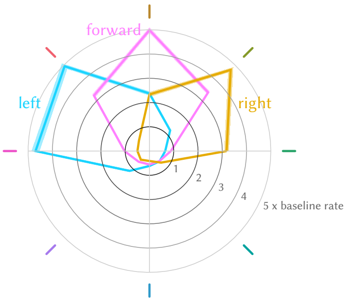

Figure 2: Rates of different types of swim events (forward swims and left and right turns) depending on the direction of motion. n=24 fish, the width of the bar is SEM, and the baseline rate refers to the baseline rate of all swim events (turns and forward swims).

To probe which areas of the brain contain signals related to whole-field motion, we performed whole-brain imaging in a pan-neuronal line (elavl3:GCaMP6s) while displaying the previously-described stimuli drifting for 10 s in each of the 8 directions, in a randomly permuted sequence. To quantify where in the brain the information about the stimulus directions is well represented, we performed a decoding analysis. Using the calcium signals in local patches, we decoded the stimulus direction from the activity during the last 7 seconds of each stimulus presentation (in order to ignore transient responses and find where the stimulus-relevant activity is persistent). The training of the decoders was done on a low-

[7] Cherng et al., "The Dorsal Lateral Habenula-Interpeduncular Nucleus Pathway Is Essential for Left-Right-Dependent Decision Making in Zebrafish".

[8] Orger et al., "Control of Visually Guided Behavior by Distinct Populations of Spinal Projection Neurons".

rank decomposition of activity in overlapping spherical patches of 40µm radius using the LGBM algorithm[9]. The patch centers were sampled in a isotropic grid in the reference brain[10] coordinates, mapped to individual imaging experiments.

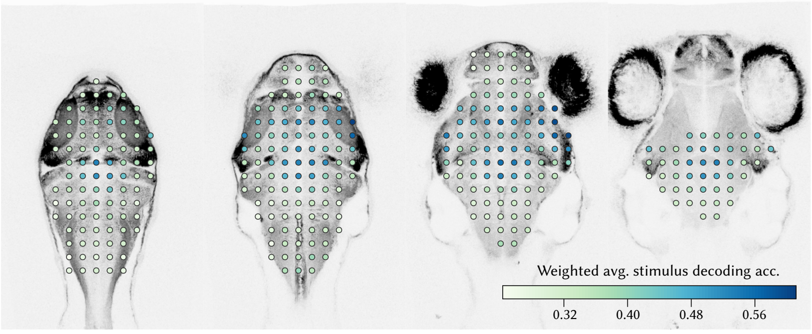

Figure 3: Decoding the accuracy of stimulus assignment by using activity in patches centered at the colored dots. The accuracy was averaged in all locations across at least 2 (out of 4) imaged fish. The patch radius is equal to the distance between the dots (40µm).

On Figure 3 we can see that besides the regions directly downstream of the eyes (the optic tectum and the arborization fields) and the cerebellar parts, the only region with higher accuracy of decoding is around the IPN (in the middle of the 4th panel) and the nuclei raphe.

The directionality of the tuning is distributed across the whole brain in patterns consistent across animals, with several prominent regions. The leftward and rightward motion is clearly separated across the hemispheres, as reported in many previous studies[11,12].

Beyond that, we see activity tuned to forward and backward motion in multiple regions, including the tectum, the habenulae, and prominently, in a pattern of small patches, in the IPN.

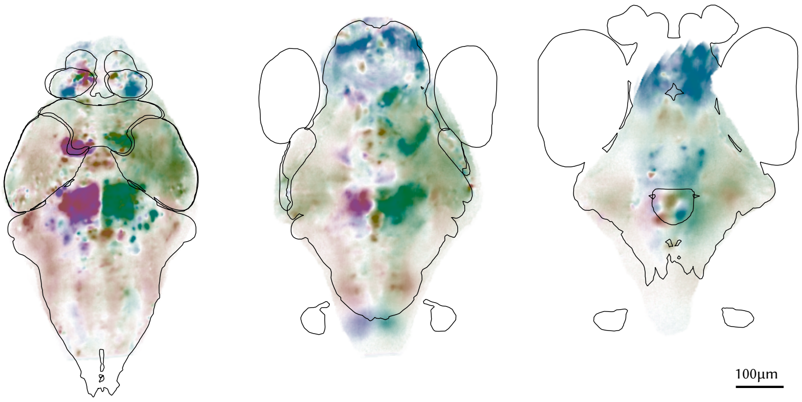

Figure 4: Directional tuning of voxel activity in one whole-brain imaging experiment, mapped to the reference space. The fish is facing forward, and the motion directions are shown in the upper-left corner. The habenulae, tectum, pretectum and IPN are outlined. Due to lower signal quality in ventral planes (right) the registration to reference is imperfect, resulting in the IPN not being perfectly aligned.

This pattern is consistent across fish, and forms a pinwheel-like structure with tuning in all directions (as see in Figure 5), which matches with the enhanced decoding performance using activity of this region.

The whole-brain experiments however cannot reveal the exact structure of the tuning patterns in the IPN, because of the pan-neuronal expression and significant resolution constraints of the lightsheet imaging paradigm. To investigate the tuning patterns in detail, we imaged activity in several different lines with the calcium indicators expressing in

[9] Ke et al., "LightGBM".

[10] Kunst et al., "A Cellular-Resolution Atlas of the Larval Zebrafish Brain".

[11] Dragomir, Štih, and Portugues, "Evidence Accumulation during a Sensorimotor Decision Task Revealed by Whole-Brain Imaging".

[12] Naumann et al., "From Whole-Brain Data to Functional Circuit Models".

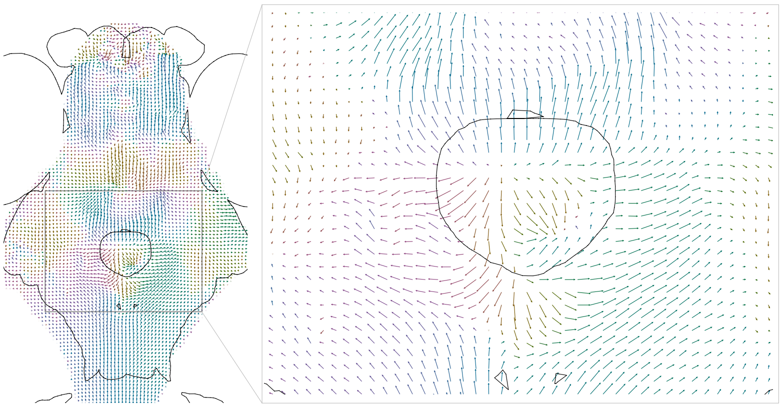

Figure 5: Directional tuning in a plane containing the IPN across 4 imaged fish. The right panel is an inset of the left panel

cell bodies and processes in this region, and used electron microscopy to investigate the possible neuroanatomical structures mediating these responses.

Structure of the interpeduncular nucleus

The interpeduncular nucleus is a midbrain structure, located close to the ventral boundary of the brain and bordered on the dorsal side by the reticular formation[13]. It consists of a region of dense neuropil enclosing a group of cell somas (Figure 7). The cells in the center of the nucleus divide it in a ventral IPN (vIPN) and dorsal IPN (dIPN).

One of the main sources of inputs to the IPN are the habenulae. Habenular axons are densely labelled in the entire IPN neuropil, as it can be seen in Figure 8. They leave the habenulae rostro-ventrally and extend in the fasciculus retroflexus bundles (FR). From the FR, they partially decussate and wrap around the IPN in a lateralized, asymmetric, and layered fashion: the right habenula innervates mostly the vIPN, the left habenula mostly the dIPN and the intermediate IPN[14]. Habenular axons have been reported to be glutamatergic and cholinergic in zebrafish larvae[15].

The space not covered by habenular axons in the IPN is entirely taken by the central somas (Figure 8, center). They form a large plane in the middle of the structure at the dIPN-vIPN boundary, and they are concentrated in a central triangular region in the vIPN. A large fraction of the IPN cells are inhibitory, as they are labelled in a gad1b:GFP line expressing GFP in GABAergic neurons (Figure 8, left and Supplementary Figure S1). Interestingly, while gad1b seems to express strongly in neurons in the central group of somas, most of the somas in the vIPN are not gad1b positive.

The rostral side of the dIPN is also bordered by a wall of densely packed somas that seems to be mostly GABAergic. A fraction of them are likely to be a part of the IPN microcircuit (see the next section). The gad1b:GFP line labelling is denser in 4 symmetrical patches that tile the rostral part of the vIPN, which we call gad1b columns (as visible in the bottom right panel of Figure 8).

[13] Morley, "The Interpeduncular Nucleus".

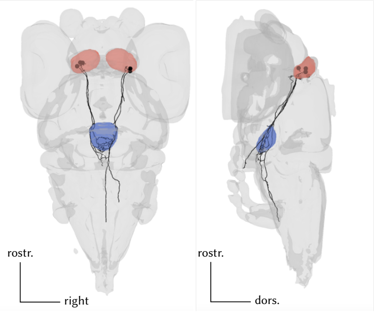

Figure 6: Location of the IPN within the larval zebrafish brain. The IPN is higlighted in blue, the habenulae in red. A few traced neurons from the Kunst et al. atlas that originate in the habenuale and terminate in the IPN are highlighted in black.

[14] Aizawa et al., "Laterotopic Representation of Left-Right Information onto the Dorso-Ventral Axis of a Zebrafish Midbrain Target Nucleus".

[15] Hong et al., "Cholinergic Left-Right Asymmetry in the Habenulo-Interpeduncular Pathway".

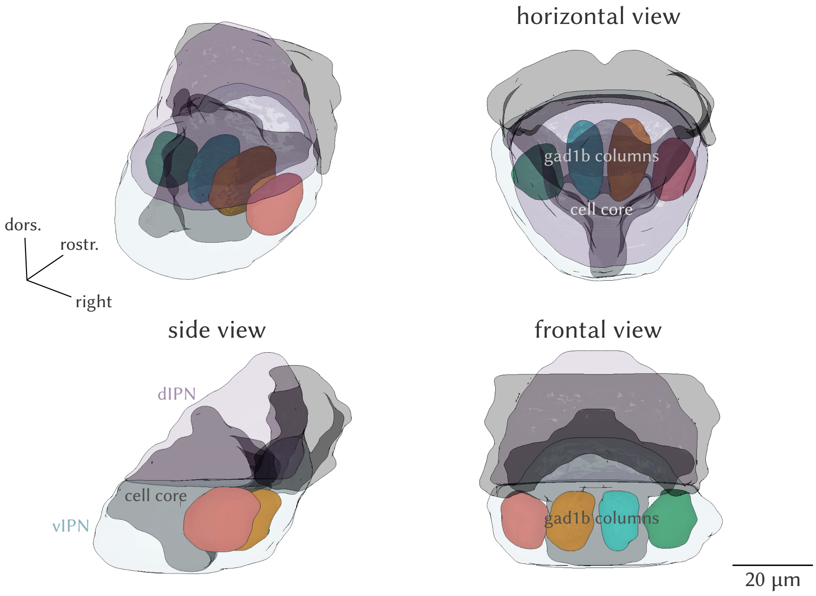

Figure 7: Anatomy of the interpeduncular nucleus. A dense neuropil region (light purple and light blue for the dorsal and ventral part) surrounds a core of cell somata (cell core, in gray) and is delimited in its dorso-rostral part by another region dense with cell somata. The ventral IPN is tiled by four regions of neuropil that are densely labelled in a gad1b:Gal4-UAS:GFP line (gad1b columns, colored).

Electron microscopy reveals precise arborization patterning

The morphology of neurons inside the zebrafish IPN has not been extensively characterized. A single work reported morphologies from single IPN neurons labelled via single-cell electroporation of IPN neurons, describing a wide range of variations in their arborization, but it could not really resolve the axonal or dendritic nature of the observed processes, and obtained data only from a limited number of neurons[16]. To gain a more complete understanding of the morphology and connectivity of the IPN, we turned to electron microscopy (EM). We commissioned tracing of neurons whose somata were located in the central part of the IPN, using a serial block-face electron microscopy (SBEM) dataset.

In the stack, the IPN encloses about 170 neurons. We analyzed the morphology of 74 neurons chosen to sample homogeneously all regions of the IPN (see Methods). The first striking feature of the IPN cells population is that their dendritic arborization tiles the IPN neuropil almost completely, especially the vIPN. Moreover, no dendrites extended outside the boundaries of this region (which in our IPN reference are defined using the localization axonal projections from the habenulae). Almost all (71/74) neurons had an axon extending dorsally. A significant fraction of these axons (32/74) then loop ventro-laterally, turning back toward and eventually crossing the midline.

To dissect more carefully the diversity of cell types in the IPN, we cluster them based on a similarity score calculated with the NBLAST algorithm[17]. With this approach, we identifies ten clusters. Cells belonging to different clusters tile with their dendritic tree different regions of the IPN neuropil. In some cases, the dendritic arbour was very precisely confined to a specific region of the IPN for all the cells of a cluster (e.g. clusters 1, 4, 9). Interestingly, these regions overlapped significantly with the columns described above from the GABAergic cells imaging. As observed above,

[16] Bianco et al., "Brain Asymmetry Is Encoded at the Level of Axon Terminal Morphology".

[17] Costa et al., "NBLAST".

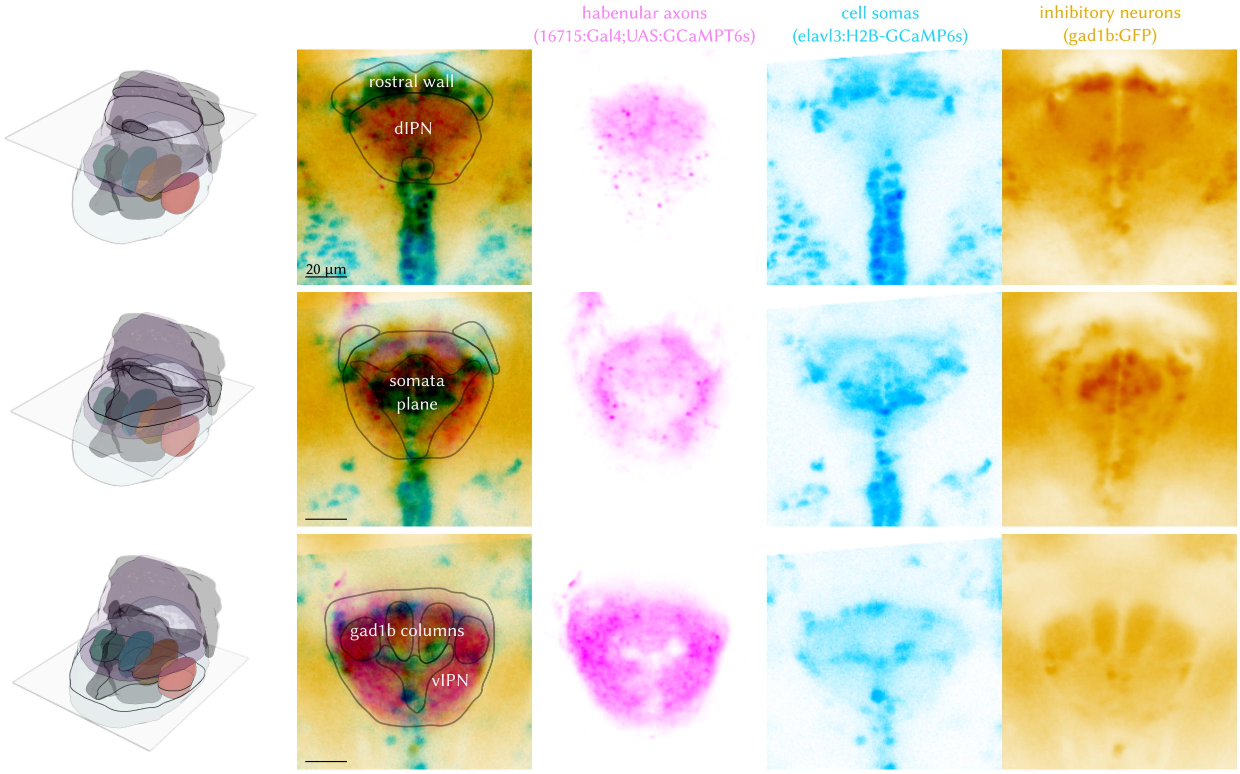

Figure 8: Confocal images of different transgenic lines showing the anatomical organization of cell somas and neuropil in the IPN.

only cells of cluster 7 seemed to extend dendrites in the dorsal IPN; 5/5 cells of this cluster were found on the left side of the IPN, suggesting that there could be some lateralization in the structure of this part of the habenulo-interpeduncular pathway. For some clusters, the axon remained outside the IPN after looping, targeting dorsal regions (cluster 1, 2, 3, 7, 8) or rostral ones (cluster 6). Other clusters had an axon that clearly re-enters in the IPN (cluster 4, 5, 9), suggesting the presence of recurrent connections within the structure.

The IPN neuropil activity is segmented and tuned

We used 4 different transgenic lines to compare the activity of different structures and cell types: The pan-neuronal elavl3:GCaMP6f, elavl3:GCaMP6s and nuclearly-localized elavl3:H2B-GCaMP6s lines, the 16715 enhancer trap line that marks the habenulae and their axons, as well as the GABAergic-selective gad1b:Gal4 line.

Two-photon imaging of the pan-neuronal line activity, we could confirm the presence of robust representations of visual field motion direction, as observed in the whole-brain screening. While in the dIPN we observed a smooth transition from a leftward motion-selective part (left dIPN) and a rightward motion-selective part (right dIPN), the responses in the vIPN formed an interesting pattern of motion direction tuning, with approximately 6-8 patches of different tuning (Figure 10). These tuned patches were roughly consistent in location across fish, with a mild variability in the exact direction (Supplementary Figure S2).

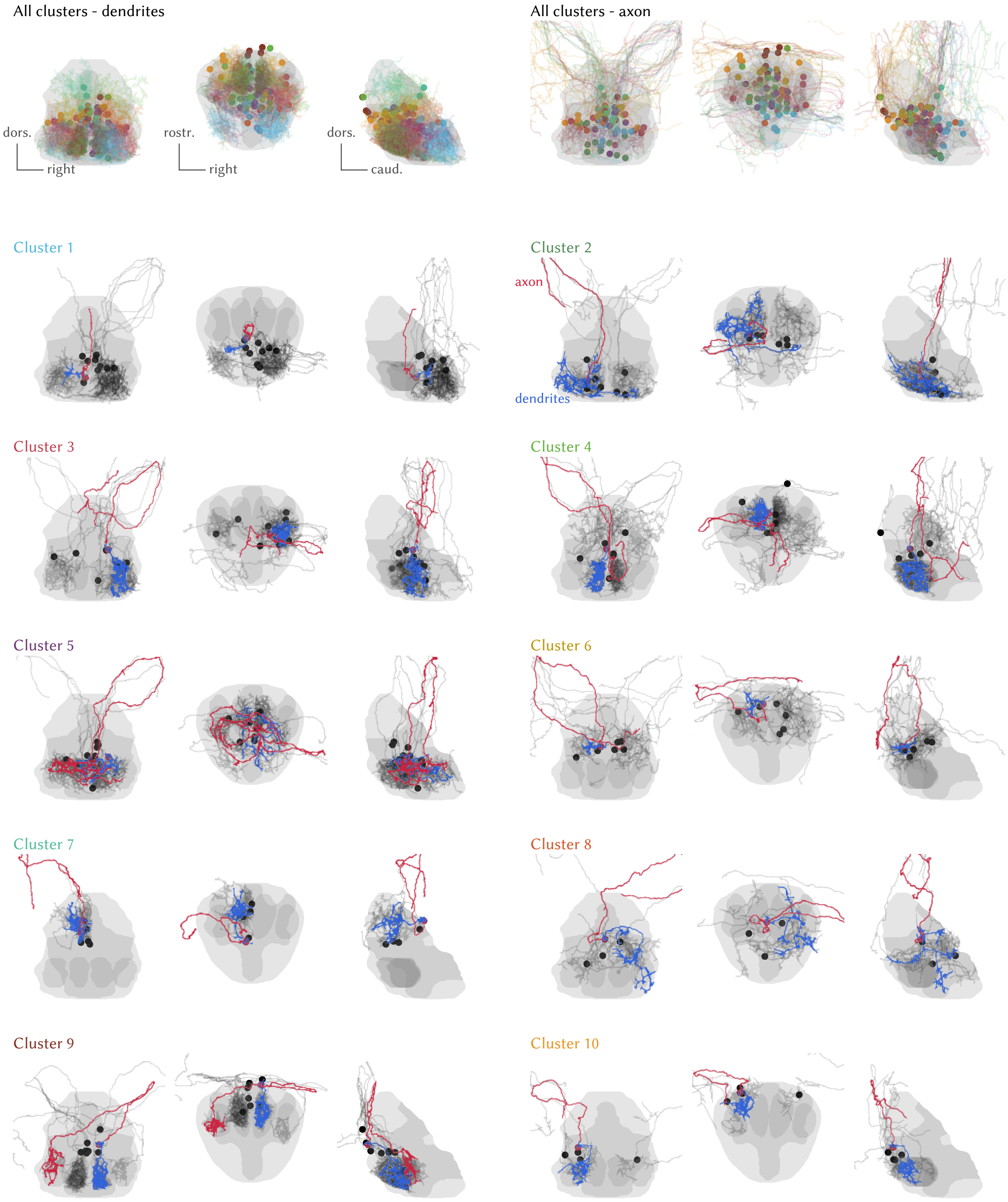

Figure 9: Morphological clusters in EM-reconstructed neurons from the IPN. Top: dendrites (left) and axons (right) from all the neurons, color-coded by cluster. The large circles mark the soma position for each cell. Below: cells from each individual clusters in black, and one representative cell from each cluster is shown in blue (dendrite) and red (axon).

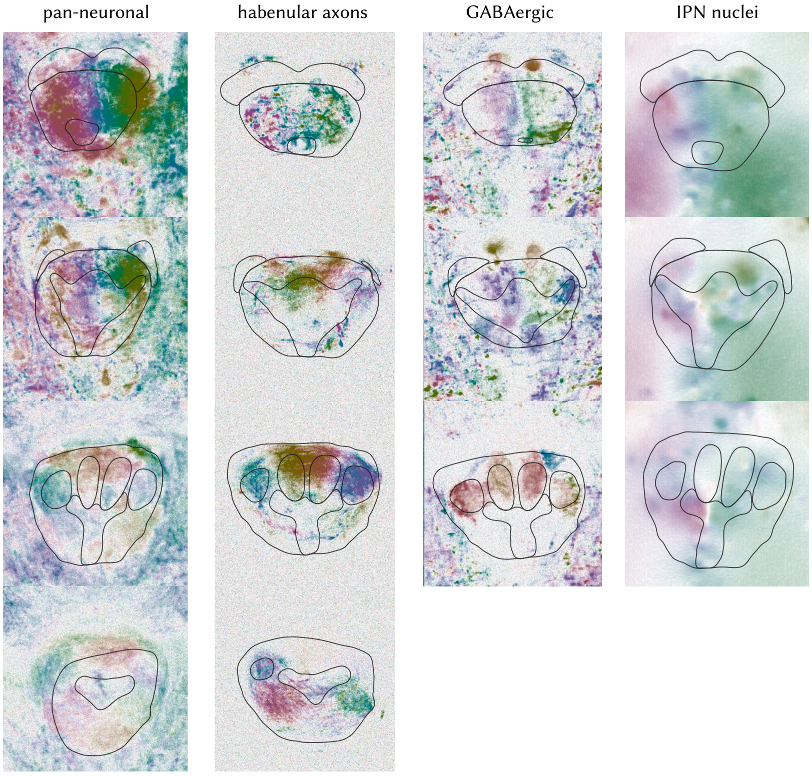

Figure 10: Voxel-wise directional activity tuning in each of the imaged lines, at approximately the same locations as in Figure 8, with the approximate outlines of the structures to help with orientation (the outlines are obtained after a manual affine transform, which is inaccurate in the ventral part due to a lack of landmarks). For the very ventral planes, only the 2-photon pan-neuronal and habenular-axon expressing lines are shown, as there is no expression there of gad1b, and the lightsheet signal quality is too low.

Left-right tuning within the dIPN was overall quite similar to tuning of the surrounding neuropil region (Figure 10). In contrast to the surrounding region, however, the IPN shows clear modulation of activity both above and below the baseline. Figure 11 shows an example plane. Regions adjacent to, but outside of the IPN are also clearly directionally tuned, however the activity is modulated only above baseline. Freely-swimming turn rates also show both direction-dependent increase and suppression, which is a possible indication that this activity might be related to behavior[18].

Next, we imaged the habenular axons that innervate the IPN, using the 16715:Gal4;UAS:GCaMP6s line. Remarkably, we observed a patterning that overlaps quite accurately the structure of the tuning maps observed in the panneuronal imaging, with a smooth left-right transition in the dIPN and alternating patches of different tuning in the vIPN (Figure 10). The presence of direction-selective patterning in the habenular axons projections is surprising because the fibers come from an habenular cells that are of various direction selectivity, and they intermingle together while wrapping around the entire IPN. Nevertheless, their activity still seems to be organized in specific direction-selective patches: the multitude of intermingled fibers from heterogeneously tuned neurons in the habenula display locally coherent directional tuning.

We then turned to imaging gad1b:Gal4;UAS:GCaMP6s larvae, where GCaMP6s was expressed selectively in a sparse fraction of GABAergic neurons. Because of the sparseness of the indicator expression, it was harder to find consistent activity patterns in the dIPN. In the vIPN, how-

[18] Dragomir, Štih, and Portugues, "Evidence Accumulation during a Sensorimotor Decision Task Revealed by Whole-Brain Imaging".

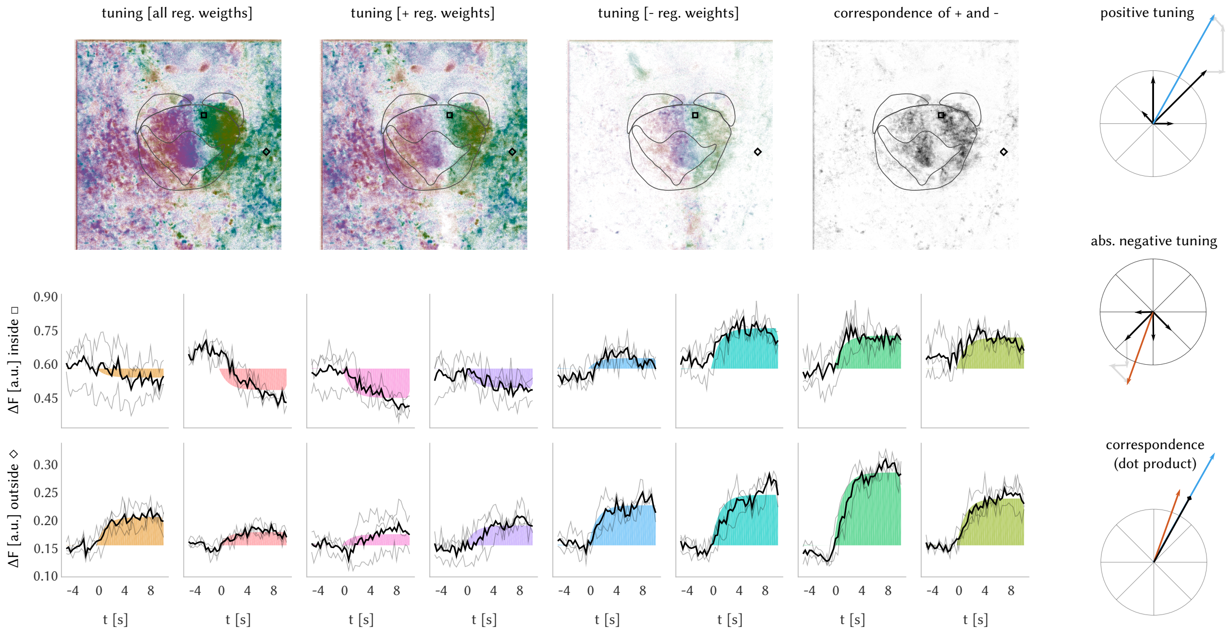

Figure 11: Bidirectional modulation inside the IPN. The voxel-wise tuning is depicted as in previous figures, and additionally computed separately for regression coefficients with positive and negative weights. The grayscale heatmap depicts the alignment of positive and negative contributions to the tuning: it is the relative length of the projection of the negative tuning vector on the positive tuning one (in this plane maximally 0.2). In the schematic diagram the signed inhibitory tuning actually points in a similar direction to the positive tuning (bottom right panel). Given a smooth tuning curve and our multivariate regression analysis this projection cannot be negative. The bottom rows show per-stimulus responses in a region highlighted by □ inside of the IPN in top row of traces, and by ◇ outside of the IPN in the bottom row of the traces. The colored areas are the weighted regressors fitted to the trace.

ever, the four patches of dense neuropil we previously described (Figure 8) displayed a consistent activation pattern: activity in each medial column highly correlated with the activity in the controlateral lateral column (Figure 10). In particular, the left medial column and the right medial column where tuned to backward-right motion, and the right medial column and the left lateral column were tuned to backward-left motion. This patterning was consistent across fish (Figure 12).

To clarify the interesting activity pattern we observed in the GABAergic line imaging, we turned back at the EM reconstruction of IPN neurons. We noticed that cells in Cluster 9 (Figure 9) were remarkably consistent with the observed functional correlations. Cells in cluster 9 featured a dendritic tree in the medial patches, and an axon that extended in the contralateral lateral patch. We therefore concluded that cells of Cluster 9 (two example cells are shown in Figure 12, top right) are putative gad1b neurons, very likely to produce the activity observed, assuming that the same calcium signal is visible and highly correlated throughout the cell's processes.

Finally, we inspected more closely the directional tuning in the habenular axons and compared it to the tuning of the gad1b columns. Even though around the midline the axons and the medial columns share very similar backward-left and backward-right orientation, in the lateral columns the habenular axons activity seems to be completely reversed. This prompted us to hypothesize that the axons from the gad1b neurons could sculpt the activity of the habenular axons by pre-synaptic inhibition.

To address this question, we sent to traces the two selected cells shown in Figure 12, with instructions to annotate all the forward synapses that

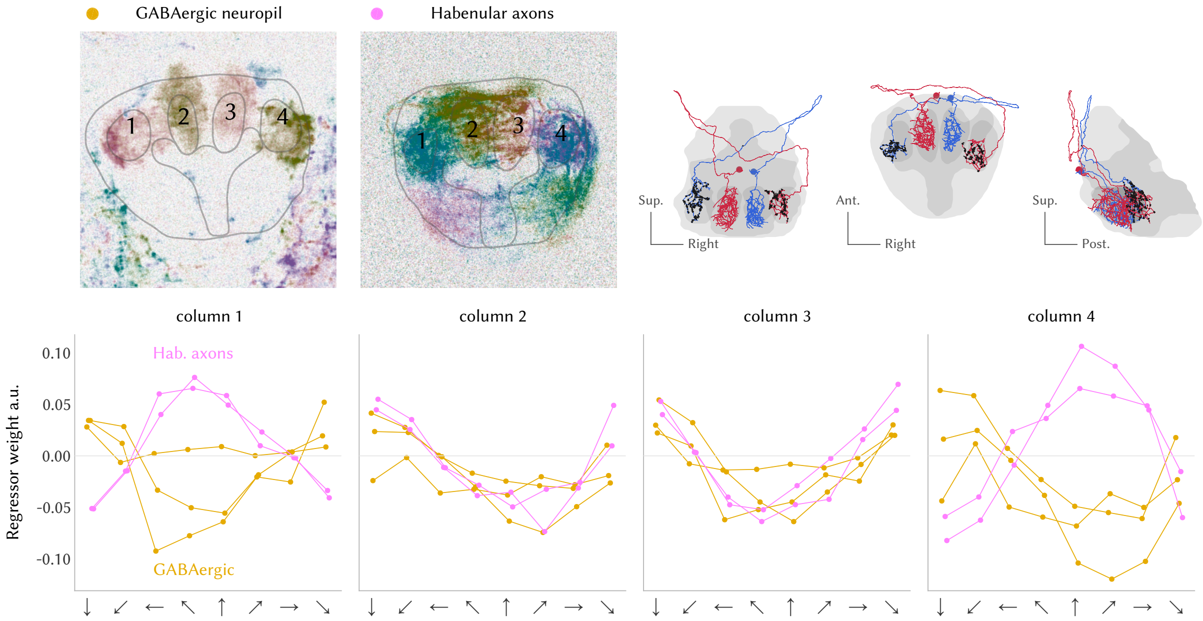

Figure 12: Top row: voxel-wise tuning in an example fish expressing GCaMP6s in GABAergic cells (left) and habenular axons (right). The color encoding is the same as in Figure 4. The bottom panels show average regressor weights for sensory regressors in the 8 different direction per each of the 4 columns. Each tuning curve comes from different animals. The expression in the GABAergic neuron-expressing fish was highly variable: some animals had GCaMP expressed in no or just one pair of columns (as for example in the one flat tuning line in columns 1 and 3).

the gad1b cell axon was establishing (without on our side selecting on the basis of distribution, nature and function of the cells). Black marks on cells in Figure 12 highlight the position where all synapses were found. Annotators reported that large fraction of the annotated synapses were indeed axo-axonal contacts, substantiating more strongly the hypothesis that gad1b neurons modulate activity of the habenular axons though pre-synaptic inhibition (Figure fig:axoaxonal). Still, for this argument to be complete, the nature of such axo-axonal contact would have to be completely characterized and proven to be, at least in part, onto unambiguously identified habenular axons.

Activity of cells within the IPN

The cell bodies inside of the IPN are mainly tuned to the forward half of motion directions. Left and right tuning is most prominent, though there are cell bodies with the activity tuned to forward and backward motion in the ventral part of the IPN.

There are a few cells which show inhibition to the opposite of the tuned direction, but they are predominantly only excited (although it is possible that inhibitory responses are missed due to the responses of the nuclear-localized calcium indicator). Also, a large part of the response variance is not explained by the stimulus (as can be seen in the faint traces at the bottom of Figure 14 on the facing page, which reflects the possible multimodal role of these cells.

Finally, we have found no strong acute motor component in the activity inside the IPN: in all functional experiments the multivariate regression included putative regressors for the different swim directions, but their weights were close to noise levels. For the longer lightsheet experiment, a cross validated regression revealed only 5 cells where the motor

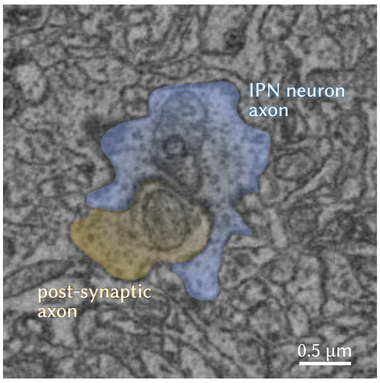

Figure 13: Example of a contact between the blue neuron of Figure 12 and a post-synaptic axon, as imaged in the EM stack.

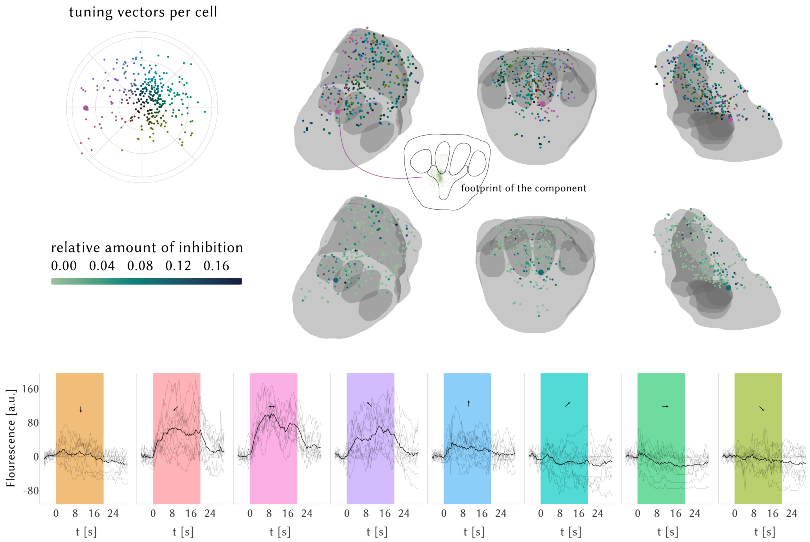

Figure 14: Characterization of responses of cells within the IPN. In top row, the cells are colored according to their preferred tuning direction, in the next row by the projection of the inhibitory component (as the 4th panel in Figure 14). In the last row example traces are shown for the highlighted cell (larger point in the previous scatter plots), for 12 trials individually (faint gray lines) and the average (thick black line).

regressors consistently decreased the unexplained variance, in line with the expected false positive rate of the procedure, and those cells also had very small regressor weights assigned to the motor components. This lack of acute motor responses is in line with the evidence discussed in the introduction, suggesting that the IPN mediates longer-term state changes and biases behavioral outcomes, rather than directly causing them.

Discussion

The striking pattering of motion-tuned parts of the interpeduncular nucleus comes about from unusual and precise neuroanatomical arrangements. We could explain, although not conclusively determine, the possible neural structures underlying these patterns: localized patches of dendritic trees spanning exactly regions with similar tuning, axo-axonal synapses likely modulating activity in different regions and symmetric arrangements of the processes of GABAergic cells selectively inhibiting responses to certain directions.

The space of optomotor stimuli is larger than explored in this study, with other aspects: uncertainty, speed and texture being kept fixed. It remains to be investigated whether the responses in the IPN are sensitive to these dimensions, and if these differences corresponds to the modulations in behavior that these changes in stimuli introduce, or allow for a nuanced representation of displacement.

In this work we explored the representation of visual information in the IPN that is conveyed to the IPN mostly by the left habenula. However, the IPN, and the vIPN in particular, receive abundant innervation from the right habenulae as well. The right habenula has been shown to be a prominently olfactory structure, whose neurons exhibit robust responses when odorants such as food-related amino acids are added in the fish water. Therefore, the interesting axo-axonal modulation that we hypothesize might also take place on fibers that carry olfactory information. This raises the possibility that the IPN is the locus on multimodal integration of directional information and goal-related evidence. Although we could find no signatures of motor responses, we note that optic flow alone, exp. backward motion (the most salient orientation for the gad1b columns) might be used as a sensory proxy for motor activity. Moreover, the responses are sustained for longer time frames, indicating that the IPN could capture information about direction and location. Exploring the recently published traced cell atlas[19] we also found many neurons from the nuclei raphe that might arborize in the IPN area, which remains an important source of inputs to explore.

Due to limitations of two-photon imaging we analyzed the responses inside the IPN only as independent signals, however the information from large parts of the structure are likely to be used together in guiding behavior, and analyzing the population activity might uncover additional properties of the representations.

Finally, it is completely unknown which regions are downstream of the IPN in the larval zebrafish. None of the nuclei traced have projections that extend far out of the structure, except the axon loops into the raphe. The representations in the IPN could be relevant for other behaviors as well, perhaps even more sophisticated ones present only in older fish. While the larval zebrafish do not display any distant-goal related behavior, the availability of tuned directional-motion signals, and potentially other position-specific information, such as chemical gradients, would enable more sophisticated navigational behaviors, as such inputs are a key component of the enotrhinal-hippocampal navigation system of mammals.

Methods

Stimulus

To study the correlates of optic flow in the zebrafish, we developed a optomotor stimulation paradigm which avoids multiple issues of grating stimuli: vertical distance dependence and the abrupt transitions when changing the direction of motion. The tiled pink-noise stimulus has been generated to have structure on all scales up to the projector resolution, be isotropic and tile the plane without discontinuities (Figure 15). Therefore, the motion direction can change without any sharp transitions, and differences in height and resolution of the displayed stimulus do not impact the image statistics. In all experiments except those with the nuclear-localised sensor (elavl-H2B line) the stimulus and pause durations were 10s, for the nuclear-localised sensor experiment the durations were 20s.

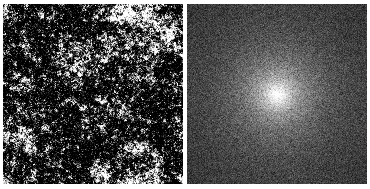
Figure 15: The seamlessly-tiling texture stimulus used in all experiments (left) and its 2D Fourier spectrum

Behavior

Behavior in embedded fish was tracked and stimuli were presented using Stytra Štih, Petrucco, et al., “Stytra: An Open-Source, Integrated System for Stimulation, Tracking and Closed-Loop Behavioral Experiments”, synchronized to microscopes. All the behavioral data presented was acquired during imaging experiments. Discrete swimming events (bouts) were extracted using the Bouter package, to obtain per-experiment summaries (of when bouts occurred and their properties) for use in further analysis.

---

[19] Kunst et al., “A Cellular-Resolution Atlas of the Larval Zebrafish Brain”.

Bouts were classified into left, right and forward turns by fitting a normal distribution to the turn biases and determining the optimal decision boundary for each fish.

Confocal microscopy

To image GABAergic neurons in the IPN we obtained confocal stacks from gad1b/GAD67-GFP × 16715:gal4; UAS:NTtr-mCherry zebrafish larvae (6-7 dpf). In these fish all GABAergic neurons express GFP and most habenular axons express mCherry. The mCherry signal is used to detect the outline of the IPN. Larvae were embedded in 1.5% agarose and anesthetized with Tricaine. Confocal stacks of the IPN were obtained with a Zeiss LSM700 microscope (20× / 1.0 NA water immersion objective) with a voxel resolution of 0.267 × 0.267 × 0.5µm.

Electron microscopy

Neuron morphologies were reconstructed from a SBEM dataset containing the full volume of a 5-dpf old larvae brain was imaged with a voxel resolution of $14x14x25nm$. The IPN was easily located in the stack thanks to its characteristic distribution of somas surrounded by dense neuropil. First, all somas enclosed within the IPN were manually annotated, for a total count of 170 somas (the total number is between 120 and 170 in the whole IPN, depending on the inclusion of somas at the edge of the neuropil region). Then, 70 seeds were chosen for reconstruction from all the regions of the IPN plus 15 additional seeds that were selected in the medial-rostral part of the IPN, for a total of 85 neurons sent to professional annotators (ariadne-service, http://www.ariadne-service.ch). Skeletons were firstly reconstructed without redundancy by one annotator, and then underwent multiple expert revision and proofreading iterations. The skeletons were later browsed using the Knossos software (https://knossostool.org), and the axon was annotated in cells where it could be unambiguously identified. Axon was defined as the exit point of the cell with small diameter (around 0.3 um); in all the cases where such process could be identified, it showed a constantly small diameter and very little branching in the proximity of the soma, confirming the assumption that it corresponds the cell axon. For cells that were later sent for synapse annotation the process identified by the annotators as the axon always matched with our identification, confirming the reliability of our criteria. For subsequent analyses, we included only neurons for which we could reliably identify an axon (74/85). Forward synapse annotation on a selected subset of neurons was outsourced to the same tracing company. For the clustering analysis, we used a Julia implementation (https://github.com/seung-lab/RealNeuralNetworks.jl) of the NBLAST algorithm Hong et al., "Cholinergic Left-Right Asymmetry in the Habenulo-Interpeduncular Pathway", using the table defined there for zebrafish neuron morphologies to build the distance matrix. Then hierarchical clustering with the Ward method was applied on the distance matrix from NBLAST, and the tree was cut with a threshold chosen to produce the minimum number of clusters that captured the variability observed by manual inspection.

Lightsheet microscopy

We used a custom-built two-beam digitally-scanned lightsheet microscope with line diffusors, previously described in Markov et al., "A Cerebellar Internal Model Calibrates a Feedback Controller Involved in Sensorimotor Control". The microscope was controlled and imaging data acquired with the Sashimi programAC, Štih, and Petrucco, *Portugueslab/Sashimi*. Whole-brain imaging data was acquired with both the frontal and lateral beam at 2Hz with 30 planes spaced 7μm apart, while IPN imaging was done only with the lateral beam. The acquired data was aligned with the VolumeRegistration package, an extension of the Suite2p algorithm Pachitariu et al., "Suite2p" for volumetric data.

Two-photon microscopy

The two-photon microscope was also custom-built and was run using Brunoise Štih, EmanPaoli, and AC, *Portugueslab/Brunoise*, a 2-photon acquisition program developed in the lab. Brunoise automatically determines the resolution of the stack given the desired framerate and the limitations of the microscope. The data was aligned using our standard python tools from the scikit-image library as well as VolumeRegistration.

Imaging analysis

Local low-rank decomposition of calcium imaging signals for patches of whole-brain data was performed with the partial SVD implemented in the LowRankApprox Julia package Ho et al., *JuliaMatrices/LowRankApprox.Jl*. The stimuli were decoding from these decompositions with the LightGBM gradient boosting dectision tree classifier Ke et al., "LightGBM" through the MLJ machine learning framework interface Blaom et al., *MLJ*. Voxelwise multivariate regression (for both whole-brain and IPN only datasets) was performed with the GLM.jl Bates et al., *JuliaStats/GLM.Jl* Julia package.

Registration to references

For whole-brain registration we used the ANTS package through the ANTSpy wrapper. To compare experiments, function imaging data was warped into the reference coordinates. For all whole-brain and most IPN-only experiments an initial manual estimation of the affine transform was necessary. This was done by finding corresponding anatomical points in the reference and the imaging stacks, and computing a least-squares fit of the 12-parameter affine transform matrix.

Signal extraction

To extract and demix signals belonging to individual cells in the lightsheet dataset, we used a variant of non-negative matrix factorization.

The factorization was performed in patches to maintain spatial continuity and make the processing computationally tractable. As clear ground truth for regions of interest in this structure is difficult to establish manually, we used a cross-validation procedure to decide on initial parameters for the factorization (number of components per patch and spatial sparsity). The cross-validation was done with an imputation procedure: a randomly-selected amount of elements of the full spatiotemporal matrix was imputed (computed from the low-rank components of the current factorization step), and compared with the true values. This is repeated several times, and the regularization - increasing spatial sparsity and decreasing number of components - was adjusted until the validation error started increasing. As the cross-validation is computationally expensive, and the optimal parameters changing slowly across space, it was applied in a subsampled grid of the actual patches. In the final factorization procedure the parameters were interpolated from those found via cross-validation in the subsampled grid.

Author contributions

V.Š. and R.P. conceived of the project. The experiments were designed by V.Š., L.P. and H.L. The functional imaging data was acquired by H.L., V.Š., L.P., E.D., E.P. and Y.W. V.Š. analyzed the imaging and behavioral data. The EM dataset was collected and prepared by F.S., while the analysis of the IPN neuron anatomy was done by L.P. V.Š. and L.P. wrote the manuscript with input from all the authors.

References

AC, Diego, Vilim Štih, and Luigi Petrucco. *Portugueslab/Sashimi: Alpha.* Zenodo, Oct. 23, 2020. DOI: `10.5281/zenodo.4122062`. URL: `https://zenodo.org/record/4122062` (visited on 10/23/2020) (cit. on p. 14).

Aizawa, Hidenori et al. “Laterotopic Representation of Left-Right Information onto the Dorso-Ventral Axis of a Zebrafish Midbrain Target Nucleus”. In: *Current Biology* 15.3 (Feb. 8, 2005), pp. 238–243. ISSN: 0960-9822. DOI: `10.1016/j.cub.2005.01.014`. URL: `http://www.sciencedirect.com/science/article/pii/S0960982205000400` (visited on 09/14/2020) (cit. on p. 4).

Bates, Douglas et al. *JuliaStats/GLM.Jl: V1.3.10.* Zenodo, Aug. 6, 2020. DOI: `10.5281/zenodo.3974173`. URL: `https://zenodo.org/record/3974173` (visited on 10/11/2020) (cit. on p. 14).

Bianco, Isaac H et al. “Brain Asymmetry Is Encoded at the Level of Axon Terminal Morphology”. In: *Neural Development* 3.1 (2008), p. 9. ISSN: 1749-8104. DOI: `10.1186/1749-8104-3-9`. URL: `http://neuraldevelopment.biomedcentral.com/articles/10.1186/1749-8104-3-9` (visited on 11/17/2020) (cit. on p. 5).

Blaom, Anthony D. et al. *MLJ: A Julia Package for Composable Machine Learning.* July 23, 2020. arXiv: `2007.12285 [cs, stat]`. URL: `http://arxiv.org/abs/2007.12285` (visited on 10/11/2020) (cit. on p. 14).

Cherng, Bor-Wei et al. “The Dorsal Lateral Habenula-Interpeduncular Nucleus Pathway Is Essential for Left-Right-Dependent Decision Making in Zebrafish”. In: *Cell Reports* 32.11 (Sept. 2020), p. 108143. ISSN: 22111247. DOI: 10.1016/j.celrep.2020.108143. URL: https://linkinghub.elsevier.com/retrieve/pii/S2211124720311323 (visited on 09/20/2020) (cit. on p. 2).

Costa, Marta et al. “NBLAST: Rapid, Sensitive Comparison of Neuronal Structure and Construction of Neuron Family Databases”. In: *Neuron* 91.2 (July 2016), pp. 293–311. ISSN: 08966273. DOI: 10.1016/j.neuron.2016.06.012. URL: https://linkinghub.elsevier.com/retrieve/pii/S0896627316302653 (visited on 11/17/2020) (cit. on p. 5).

Dragomir, Elena I., Vilim Štih, and Ruben Portugues. “Evidence Accumulation during a Sensorimotor Decision Task Revealed by Whole-Brain Imaging”. In: *Nature Neuroscience* 23.1 (1 Jan. 2020), pp. 85–93. ISSN: 1546-1726. DOI: 10.1038/s41593-019-0535-8. URL: https://www.nature.com/articles/s41593-019-0535-8 (visited on 10/11/2020) (cit. on pp. 1, 3, 8).

Dunn, Timothy W et al. “Brain-Wide Mapping of Neural Activity Controlling Zebrafish Exploratory Locomotion”. In: *eLife* 5 (Mar. 22, 2016). Ed. by Ronald L Calabrese, e12741. ISSN: 2050-084X. DOI: 10.7554/eLife.12741. URL: https://doi.org/10.7554/eLife.12741 (visited on 11/21/2020) (cit. on p. 1).

Ho, Ken et al. *JuliaMatrices/LowRankApprox.Jl: V0.4.1.* Zenodo, Aug. 17, 2020. DOI: 10.5281/zenodo.3988109. URL: https://zenodo.org/record/3988109 (visited on 10/13/2020) (cit. on p. 14).

Hong, E. et al. “Cholinergic Left-Right Asymmetry in the Habenulo-Interpeduncular Pathway”. In: *Proceedings of the National Academy of Sciences* 110.52 (Dec. 24, 2013), pp. 21171–21176. ISSN: 0027-8424, 1091-6490. DOI: 10.1073/pnas.1319566110. URL: http://www.pnas.org/cgi/doi/10.1073/pnas.1319566110 (visited on 11/20/2020) (cit. on pp. 4, 13).

Ke, Guolin et al. “LightGBM: A Highly Efficient Gradient Boosting Decision Tree”. In: *Proceedings of the 31st International Conference on Neural Information Processing Systems*. NIPS’17. Red Hook, NY, USA: Curran Associates Inc., Dec. 4, 2017, pp. 3149–3157. ISBN: 978-1-5108-6096-4 (cit. on pp. 3, 14).

Kunst, Michael et al. “A Cellular-Resolution Atlas of the Larval Zebrafish Brain”. In: *Neuron* 103.1 (July 3, 2019), 21–38.e5. ISSN: 0896-6273. DOI: 10.1016/j.neuron.2019.04.034. URL: http://www.sciencedirect.com/science/article/pii/S0896627319303915 (visited on 10/13/2020) (cit. on pp. 3, 12).

Markov, Daniil A. et al. “A Cerebellar Internal Model Calibrates a Feedback Controller Involved in Sensorimotor Control”. In: *bioRxiv* (Sept. 14, 2020), p. 2020.02.12.945956. DOI: 10.1101/2020.02.12.945956. URL: https://www.biorxiv.org/content/10.1101/2020.02.12.945956v2 (visited on 11/22/2020) (cit. on p. 14).

Morley, Barbara J. “The Interpeduncular Nucleus”. In: *International Review of Neurobiology*. Vol. 28. Elsevier, 1986, pp. 157–182. ISBN: 978-0-12-366828-8. DOI: 10.1016/S0074-7742(08)60108-7. URL: https:

//linkinghub.elsevier.com/retrieve/pii/S0074774208601087 (visited on 09/14/2020) (cit. on p. 4).

Naumann, Eva A. et al. "From Whole-Brain Data to Functional Circuit Models: The Zebrafish Optomotor Response". In: *Cell* 167.4 (Nov. 3, 2016), 947–960.e20. ISSN: 0092-8674. DOI: 10.1016/j.cell.2016.10.019. URL: http://www.sciencedirect.com/science/article/pii/S0092867416314027 (visited on 10/16/2020) (cit. on pp. 1, 3).

Orger, Michael B. et al. "Control of Visually Guided Behavior by Distinct Populations of Spinal Projection Neurons". In: *Nature Neuroscience* 11.3 (3 Mar. 2008), pp. 327–333. ISSN: 1546-1726. DOI: 10.1038/nn2048. URL: https://www.nature.com/articles/nn2048 (visited on 10/24/2020) (cit. on pp. 1, 2).

Pachitariu, Marius et al. "Suite2p: Beyond 10,000 Neurons with Standard Two-Photon Microscopy". In: *bioRxiv* (July 20, 2017), p. 061507. DOI: 10.1101/061507. URL: https://www.biorxiv.org/content/10.1101/061507v2 (visited on 11/22/2020) (cit. on p. 14).

Štih, Vilim, EmanPaoli, and Diego AC. *Portugueslab/Brunoise: Alpha.* Zenodo, Oct. 23, 2020. DOI: 10.5281/zenodo.4122064. URL: https://zenodo.org/record/4122064 (visited on 10/23/2020) (cit. on p. 14).

Štih, Vilim, Luigi Petrucco, et al. "Stytra: An Open-Source, Integrated System for Stimulation, Tracking and Closed-Loop Behavioral Experiments". In: *PLOS Computational Biology* 15.4 (Apr. 2019), pp. 1–20. DOI: 10.1371/journal.pcbi.1006699. URL: https://doi.org/10.1371/journal.pcbi.1006699 (cit. on p. 12).

Wolf, Sébastien et al. "Sensorimotor Computation Underlying Phototaxis in Zebrafish". In: *Nature Communications* 8.1 (1 Sept. 21, 2017), p. 651. ISSN: 2041-1723. DOI: 10.1038/s41467-017-00310-3. URL: https://www.nature.com/articles/s41467-017-00310-3 (visited on 11/21/2020) (cit. on p. 1).

Yildizoglu, Tugce et al. "A Neural Representation of Naturalistic Motion-Guided Behavior in the Zebrafish Brain". In: *Current Biology* 30.12 (June 22, 2020), 2321–2333.e6. ISSN: 0960-9822. DOI: 10.1016/j.cub.2020.04.043. pmid: 32386533. URL: https://www.cell.com/current-biology/abstract/S0960-9822(20)30557-1 (visited on 10/26/2020) (cit. on p. 1).

Acknowledgements

We thank Thomas Frank and Herwig Baier for providing two fish lines (gad1b:GFP and gad1b:gal4 ; UAS:GCaMP6s respectively)

Supplementary information

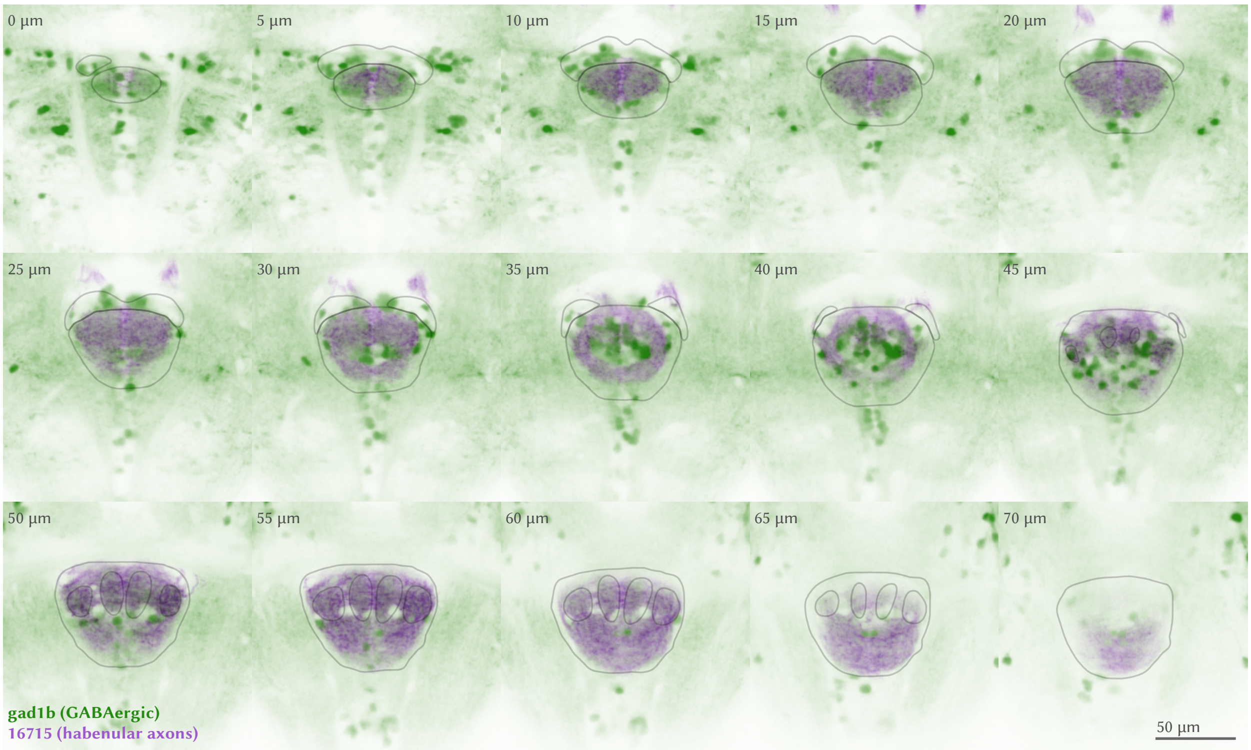

Figure S1: Confocal image of a fish co-expressing gad1b:Gal4-UAS:GFP and mCherry through the 16517 direct driver line. The outlines of the IPN, the cell wall and the arborization columns are approximate to help with orientation within the structure.

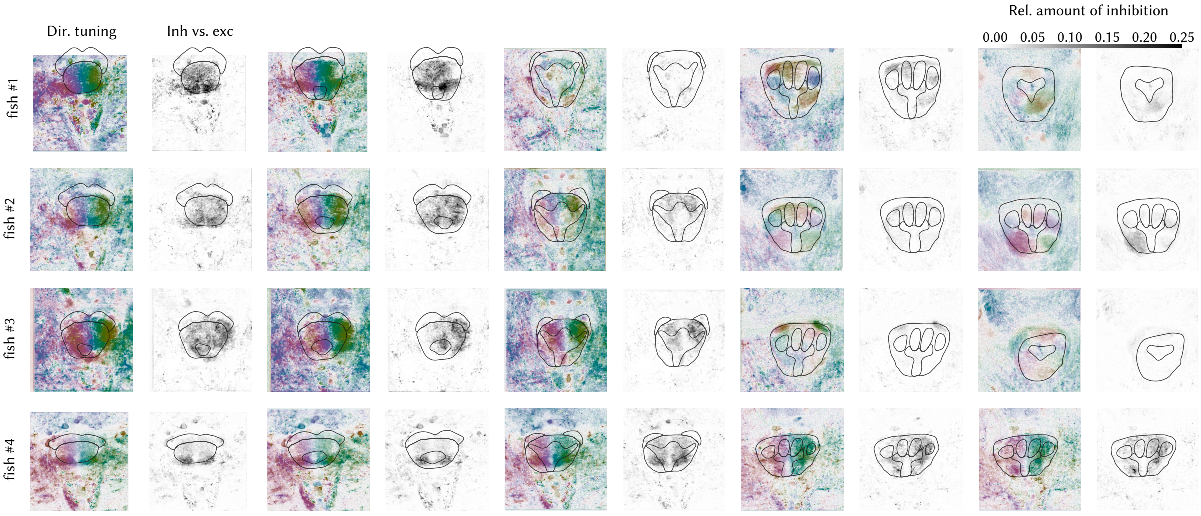

Figure S2: The relationship of excitatory and inhibitory tuning across 4 different fish in different planes (manually selected to be at equivalent positions within the structure), the coloring schema is the same as in Fig. 11

Manuscript 4: Stytra: An open-source, integrated system for stimulation, tracking and closed-loop behavioral experiments

Vilim Štih[1], Luigi Petrucco[1], Andreas M. Kist, Ruben Portugues
[1]equal contribution

Published in: PLOS Computational Biology - 8. April 2019

PLOS | COMPUTATIONAL BIOLOGY

RESEARCH ARTICLE

Stytra: An open-source, integrated system for stimulation, tracking and closed-loop behavioral experiments

Vilim Štih☯, Luigi Petrucco☯, Andreas M. Kist¤, Ruben Portugues*

Research Group of Sensorimotor Control, Max Planck Institute of Neurobiology, Martinsried, Germany

☯ These authors contributed equally to this work.
¤ Current address: Department of Phoniatrics and Pediatric Audiology, University Hospital Erlangen, Medical School, Friedrich-Alexander-University Erlangen-Nürnberg, Germany
* rportugues@neuro.mpg.de

Abstract

We present Stytra, a flexible, open-source software package, written in Python and designed to cover all the general requirements involved in larval zebrafish behavioral experiments. It provides timed stimulus presentation, interfacing with external devices and simultaneous real-time tracking of behavioral parameters such as position, orientation, tail and eye motion in both freely-swimming and head-restrained preparations. Stytra logs all recorded quantities, metadata, and code version in standardized formats to allow full provenance tracking, from data acquisition through analysis to publication. The package is modular and expandable for different experimental protocols and setups. Current releases can be found at https://github.com/portugueslab/stytra. We also provide complete documentation with examples for extending the package to new stimuli and hardware, as well as a schema and parts list for behavioral setups. We showcase Stytra by reproducing previously published behavioral protocols in both head-restrained and freely-swimming larvae. We also demonstrate the use of the software in the context of a calcium imaging experiment, where it interfaces with other acquisition devices. Our aims are to enable more laboratories to easily implement behavioral experiments, as well as to provide a platform for sharing stimulus protocols that permits easy reproduction of experiments and straightforward validation. Finally, we demonstrate how Stytra can serve as a platform to design behavioral experiments involving tracking or visual stimulation with other animals and provide an example integration with the DeepLabCut neural network-based tracking method.

This is a *PLOS Computational Biology* Software paper.

Introduction

The central goal of systems neuroscience is to explain the neural underpinnings of behavior. To investigate the link between sensory input, brain activity and animal behavior, relevant

Citation: Štih V, Petrucco L, Kist AM, Portugues R (2019) Stytra: An open-source, integrated system for stimulation, tracking and closed-loop behavioral experiments. PLoS Comput Biol 15(4): e1006699. https://doi.org/10.1371/journal.pcbi.1006699

Editor: Francesco P. Battaglia, Radboud Universiteit Nijmegen, NETHERLANDS

Received: November 29, 2018

Accepted: March 15, 2019

Published: April 8, 2019

Data Availability Statement: All data can be found at Zenodo: https://zenodo.org/record/1692080#.XAAST9VKi6I doi 10.5281/zenodo.1692080.

Funding: RP was funded through the Human Frontier Science Program (http://www.hfsp.org/) grant RPG0027/2016 and through the Max Planck Gesellschaft (http://www.mpg.de/) (PSY 825). The funders had no role in study design, data collection and analysis, decision to publish, or preparation of the manuscript.

Competing interests: The authors have declared that no competing interests exist.

behavioral variables have to be recorded and quantified. Therefore, the same experimental paradigm has to be replicated in different experimental setups in order to combine it with different recording or stimulation techniques, and it needs to be reproducible across different laboratories. However, the setups generally rely on heterogeneous hardware and custom-made software tailored to the specific requirements of one experimental apparatus. Often, the code used is based on expensive software packages (such as LabView or Matlab), with open-source options for hardware control generally limited to one particular type or brand of devices. As a consequence, the same experimental protocol has to be implemented many times, thus wasting time and increasing potential sources of error. This makes sharing the code for replicating a scientific finding under the same experimental conditions very difficult.

To address these problems, we developed Stytra, a package that encompasses all the requirements of hardware control, stimulation and behavioral tracking that we encounter in our everyday experimental work. Our system, completely written in Python, provides a framework to assemble an experiment combining different input and output hardware and algorithms for online behavioral tracking and closed-loop stimulation. It is highly modular and can be extended to support new hardware devices or tracking algorithms. It facilitates reuse of different components of the package, encourages building upon existing work and enforces consistent data management. The definition of experimental protocols in high-level Python scripts makes it very suitable for version control and code sharing across laboratories, facilitating reproducibility and collaboration between scientists. Finally, it runs on all common desktop operating systems (Windows, MacOS and Linux), therefore incurring no additional costs on the software side. Similar approaches have already been made available for real-time tracking of zebrafish larvae [1, 2]. Still, to our knowledge, none of these solutions implement tracking functions for both head-restrained and freely-swimming larvae, they do not allow the use of custom tracking algorithms, and they do not provide a generic framework to design open- and closed-loop stimulation paradigms.

Stytra was developed primarily in the context of a laboratory working with larval zebrafish, and it fulfills the common requirements of behavioral paradigms used with this animal [3]: video tracking, visual stimulation and triggering of external devices. The tracking functions (for freely swimming and head-restrained fish) include both efficient re-implementations of published algorithms and newly-developed methods. Nevertheless, custom methods can easily be added. Common visual stimuli and methods for combining them and presenting them in different ways are provided. Our experimental setups are open-source as well [4]: hardware designs provided along with the documentation describe the apparatus required for performing common behavioral experiments in zebrafish in detail. The library provides many elements useful for designing behavioral experiments in Python, potentially offering a unified platform to build and share experiments in zebrafish neuroscience and behavioral research. We welcome and will support community contributions to expand the capabilities of the package to other paradigms and animals, although our development efforts will remain focused on zebrafish applications.

Design and implementation

Overview and library structure

We developed Stytra using the Python programming language. We endeavored to follow best practices in software engineering: separation of user interface and data processing code, modularity and consistent programming interfaces. In Stytra, new experiments can be designed using very simple Python syntax, allowing even beginners in programming to develop their own stimulation paradigms. Once defined, the experiment is controlled through a graphical

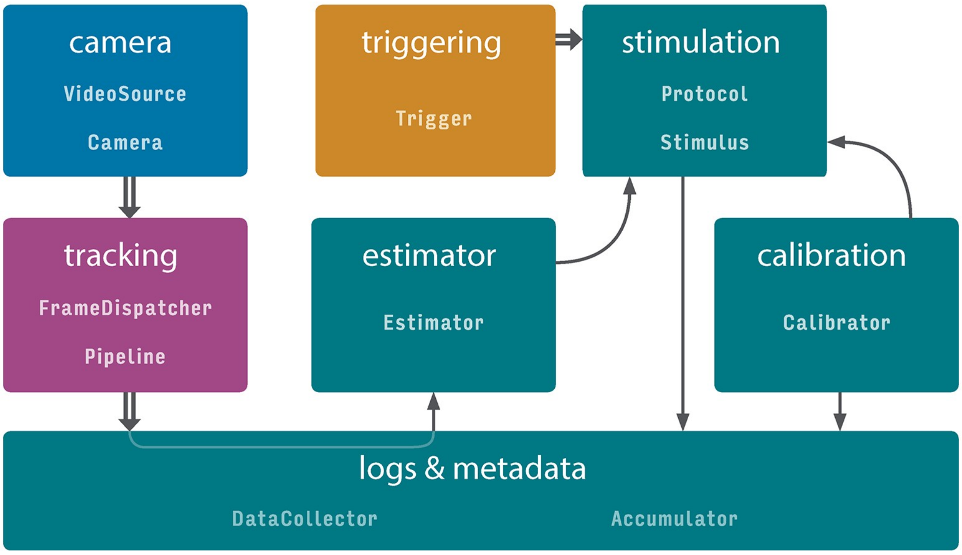

Fig 1. Data flow in Stytra. Communication between different parts of a Stytra experiment. Each color represents a separate process in which the module(s) are running. Data flow between modules within one process is depicted by arrows, and between processes as double arrows. The classes belonging to the data flow elements are displayed in `monospace`. A more comprehensive diagram of the classes is provided in S1 Fig. The user interface, the stimulus update and related functions such as the screen calibration and data saving are performed in the main process, colored in green. The stimulation can be triggered by a triggering process (in orange) that listens for an external triggering signal. Frames can be acquired from a camera process (in blue), analyzed by a tracking function (in purple), and the result can be streamed to the main process for data saving and used in closed-loop experiments via the estimator.

https://doi.org/10.1371/journal.pcbi.1006699.g001

user interface which can be used with no knowledge of Python. At the core of the Stytra package lies the `Experiment` object, which links all components that may be used in an experiment: stimulus presentation, camera, animal tracking, metadata and logging (S1 Fig).

This organization enables composing different experimental paradigms with full code reuse. Improvement of different modules (e.g. the user interface, plotting or tracking) is therefore reflected in all experimental setups, and support for a new piece of hardware or tracking function can be added with minimal effort and interference with other parts of the project. Online image processing is organized along a sequence of steps: first, images are acquired from the camera, then the image is filtered and tracked, and the tracking results are saved. Acquisition, tracking and data saving occur in separate processes (depicted in blue, purple, and green in Fig 1). This approach improves the reliability and the performance of online behavioral tracking, and exploits the advantages of multi-core processors. After processing, streaming numerical data (such as tracking results and dynamic parameters of stimuli) is passed into data accumulators in the main thread, and a user-selected subset can be plotted in real time and saved in one of the several supported formats. Moreover, for every experimental session all changeable properties impacting the execution of the experiment are recorded and saved. Finally, as the software package is version-controlled, the version (commit hash) of the software in use is saved as well, ensuring the complete reproducibility of every experiment.

Building and running an experiment in Stytra

The `Experiment` object binds all the different components required to run an experiment. The most basic `Experiment` object performs the presentation of a succession of stimuli, saving the experiment metadata and the stimulation log. For experiments including video

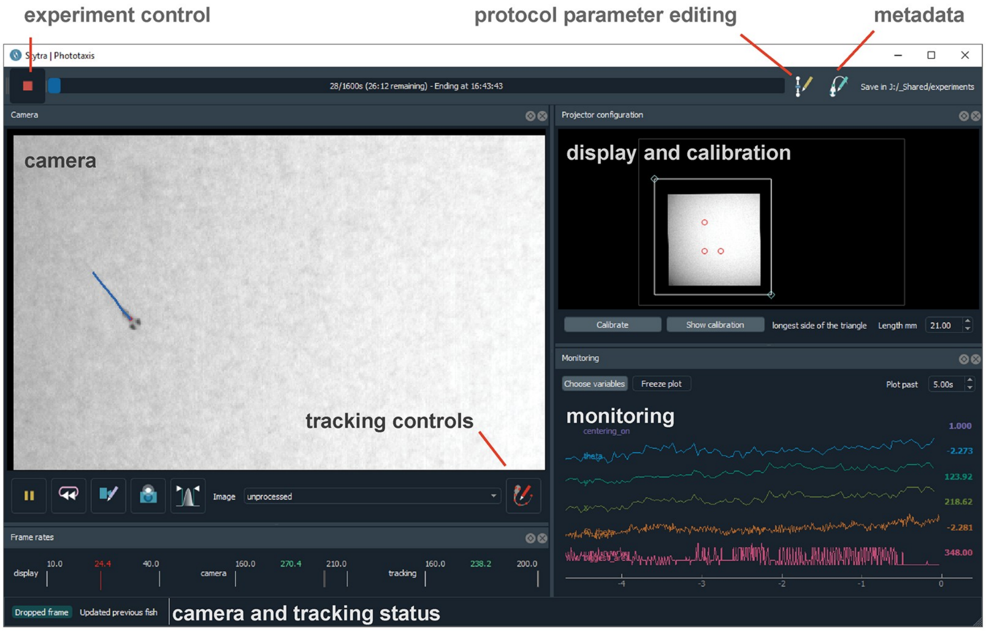

28/1600s (26:12 remaining) - Ending at 16:43:43

Save in J:/_Shared/experiments

Fig 2. Screen capture of the software in use. The various behavioral paradigms supported by Stytra provide the user with a consistent interface to control experiments. The toolbar on top controls aspects of running the experiment, a camera panel shows the tracking results superimposed on the camera image, a calibration panel enables quick positioning and calibration of the stimulus display and a monitoring panel plots a user-selected subset of experimental variables.

https://doi.org/10.1371/journal.pcbi.1006699.g002

tracking, the `TrackingExperiment` object augments the basic `Experiment` with features such as camera frame acquisitions and online image analysis. The image analysis pipeline can be one of the zebrafish specific pipelines supplied with Stytra, or a custom tracking pipeline. The `Experiment` is linked to the user interface for controlling the running of stimulation protocols, inserting metadata, controlling parameters, and calibrating the stimulus display (Fig 2). In general, the users do not need to define new types of `Experiment` objects for every new experimental paradigm. Instead, paradigms are implemented by defining a `Protocol` object which contains the stimulus sequence (as described below) and a configuration dictionary with information about the camera, tracking pipeline, and triggering. The appropriate `Experiment` object can be automatically instantiated from the configuration dictionary using the Stytra constructor. Alternatively, an `Experiment` can be instantiated and run from the experiment script, as described in the documentation examples. Ideally, the provided `Experiment` objects should cover most of the requirements of zebrafish behavioral experiments, and redefining the `Experiment` is required only if one needs to modify the graphical user interface (GUI), add more nodes in the data pipeline (screens or cameras) or implement more specific customizations. A more detailed depiction of the connections and versions of different objects is depicted in S1 Fig. For examples of how to create a `Protocol` and run experiments in Stytra, see the Usage examples box and the more detailed examples gallery in the documentation.

Stimulus design

Experimental protocols in Stytra are defined as sequences of timed stimuli presented to the animal through a projector or external actuators. A sequence of stimuli, defined as a Python list of `Stimulus` objects, is defined in a `Protocol` object (see Usage examples box). This structure enables straightforward design of new experimental protocols, requiring very little knowledge of the general structure of the library and only basic Python syntax. A dedicated class coordinates the timed execution of the protocol relying on a `QTimer` from the PyQt5 library, ensuring a temporal resolution in the order of 15-20 ms (around the response time of a normal monitor, see S2 Fig). Drawing very complex stimuli consisting of many polygons or requiring online computation of large arrays can decrease the stimulus display performance. The stimulus display framerate can be monitored online from the user interface when the protocol is running (see the lower left corner of the window in Fig 2). Milli- or microsecond precision, which might be required for optogenetic experiments, for example, is currently not supported. Each `Stimulus` has methods which are called at starting time or at every subsequent time step while it is set. In this way one can generate dynamically changing stimuli, or trigger external devices. New `Stimulus` types can be easily added to the library just by subclassing `Stimulus` and re-defining the `Stimulus.start()` and `Stimulus.update()` methods.

A large number of stimuli is included in the package. In particular, a library of visual stimuli has been implemented as `VisualStimulus` objects using the `QPainter` object, a part of the Qt GUI library, enabling efficient drawing with OpenGL. Relying on a set of high-level drawing primitives makes the code very readable and maintainable. Stytra already includes common stimuli used in visual neuroscience, such as moving bars, dots, whole-field translation or rotations of patterns on a screen, and additional features such as movie playback and the presentation of images from a file (which can be generated by packages such as Imagen [5]). The classes describing visual stimuli can be combined, and new stimuli where these patterns are moved or masked can be quickly defined by combining the appropriate `Stimulus` types. Finally, new stimuli can be easily created by redefining the `paint()` method in a new `VisualStimulus` object. Multiple stimuli can be presented simultaneously using `StimulusCombiner`. Presenting different stimuli depending on animal behavior or external signals can be achieved using the `ConditionalStimulus` container, or with similarly designed custom objects. Visual stimuli are usually displayed on a secondary screen, therefore Stytra provides a convenient interface for positioning and calibrating the stimulation window (visible in Fig 2 on the right-hand side). Although in our experiments we are using a single stimulation monitor, displaying stimuli on multiple screens can be achieved with virtual desktop technology or screen-splitting hardware boards. Importantly, all stimulus parameters are specified in physical units and are therefore independent of the display hardware. Finally, the timed execution of code inside `Stimulus` objects can be used to control hardware via I/O boards or serial communication with micro-controllers such as Arduino or MicroPython PyBoard. For example, in this way one may deliver odors or temperature stimuli or optogenetic stimulation. Examples for all these kinds of stimuli are provided in the main repository.

Usage examples

Here we present the main parts of simple scripts that can be used to run a Stytra experiment. The complete scripts can be found in the Stytra repository under `stytra/examples`. Stytra is run in most cases by defining a stimulus sequence in a `Protocol` object. This custom protocol is passed to the `Stytra` constructor, which creates an appropriate `Experiment` object. The subclass of `Experiment` is selected depending on the configuration passed through either the Stytra constructor or the `stytra_config` attribute of the `Protocol`. The online documentation contains an example of how to use a custom `Experiment` class.

Creating and running a protocol. To create an experiment, a `Protocol` class has to be defined. The `Protocol.get_stim_sequence()` method returns the sequence of stimuli that will be presented in the experiment. A `Protocol` object is then passed as an argument to the instance of `Stytra` that will run it.

Example:

```
from stytra import Stytra, Protocol
from stytra.stimulation.stimuli import Pause, FullFieldVisualStimulus
class FlashProtocol(Protocol):
  name = “flash protocol” # protocol name
  def get_stim_sequence(self):
    stimuli = [Pause(duration = 9), # black screen, 9 sec FullFieldVisualStimulus
             (duration = 1, # flash, 1 sec color = (255, 255, 255))]
    return stimuli
Stytra(protocol = FlashProtocol())
```

Creating a new stimulus. In an experiment it might be necessary to use a stimulus type not available in the existing library. To design a new stimulus, a `Stimulus` subclass has to be created and its `Stimulus.start()` and `Stimulus.update()` methods should be overwritten. In the following piece of code, we create a closed-loop stimulus which turns the screen red when the fish is swimming. To achieve this, we redefine the `Stimulus.update()` to change the color attribute, and the `Stimulus.paint()` to paint the screen red. The `stytra_config` attribute defines the video source (a Ximea camera), and the tracking functions (tail tracking with vigor as a velocity estimator):

```
from stytra import Stytra, Protocol
from stytra.stimulation.stimuli import VisualStimulus
from PyQt5.QtCore import QRect
from PyQt5.QtGui import QBrush, QColor
class NewStimulus(VisualStimulus):
  def _ _init_ _(self, *args, **kwargs):
    super()._ _init_ _(*args, **kwargs)
    self.color = (255, 255, 255)
  def paint(self, painter, w, h):
    # painter, w and h come from the Qt library drawing functions.
    # painter: QPainter object;
    # w, h: width and height of the window
    painter.setBrush(QBrush(QColor(*self.color))) # Use chosen color
    painter.drawRect(QRect(0, 0, w, h)) # draw full field rectangle
  def update(self):
    fish_vel = self._experiment.estimator.get_velocity()
    # change color if speed of the fish is higher than threshold:
    if fish_vel < -15:
      self.color = (255, 0, 0)
    else:
      self.color = (255, 255, 255)
class CustomProtocol(Protocol):
  name = “custom protocol” # protocol name
  # Here we define tracking method, vigor estimator, and add a camera:
  stytra_config = dict(tracking = dict(method = “tail”, estimator = “vigor”),
  camera = “ximea”)
```

```
  def get_stim_sequence(self):
    return [NewStimulus(duration = 10)]
Stytra(protocol = CustomProtocol())
```

Image acquisition and tracking

Image acquisition. A key feature of Stytra is the extraction of relevant behavioral features in real time from video inputs. The `Camera` object provides an interface for grabbing frames and setting parameters for a range of different camera types. Currently supported models include those by XIMEA, AVT, PointGray/FLIR, and Mikrotron, as well as webcams supported by OpenCV [6]. Support for other cameras can be added as long as a Python or C API exists. In addition, previously-recorded videos can also be processed, allowing for offline tracking. Frames are acquired from the original source in a process separated from the user interface and stimulus display. This ensures that the acquisition and tracking frame rate are independent of the stimulus display, which, depending on the complexity of the stimulus and output resolution, can be between 30 and 60 Hz.

Tracking pipelines. The tracking process receives acquired frames and handles animal tracking (represented in Fig 1). Image processing and tracking are defined in subclasses of `Pipeline` objects and contain a tree of processing nodes, starting from input images and ending with tracking nodes that take images as input and give tracking results as output. This structure allows for multiple tracking functions to be applied on the same input image(s). Currently implemented image processing nodes include image filtering (down-sampling, inversion and low-pass filtering) and background subtraction. The outputs of the tracking nodes are assembled together and streamed to the main process, where the data is saved and visualized. The `Pipeline` object also allows specifying a custom camera overlay to display the results of the tracking and an additional plotting widget for an alternative visualization of data. This modular structure allows easy expansion of the library: new functions for pre-filtering or tracking can be incorporated into the pipeline with minimal effort. Pipelines to track tail and eye position in head-restrained fish, as well as fish position and orientation in an open arena, are included in Stytra. Parts of the tracking functions use the OpenCV computer vision library. Time-critical functions are compiled with the Numba library to increase their performance.

Behavior tracking in head-restrained fish. ***Tail tracking***. Zebrafish larvae swim in discrete units called bouts, and different types of swim bouts, from startle responses to forward swimming are caused by different tail motion patterns [7]. The tail of the larvae can be easily skeletonized and described as a curve discretized into 7-10 segments [8] (Fig 3A). The tail tracking functions work by finding the angle of a tail segment given the position and the orientation of the previous one. The starting position of the tail, as well as a rough tail orientation and length need to be specified beforehand using start and end points, movable over the camera image displayed in the user interface (as can be seen in Fig 3A).

To find the tail segments, two different functions are implemented. The first one looks at pixels along an arc to find their maximum (or minimum, if the image is inverted) where the current segment would end (as already described in e.g. [8]). The second method, introduced here, is based on centers of mass of sampling windows (Fig 3), and provides a more reliable and smoother estimate over a wider range of resolutions and illumination methods. The image contrast and tail segment numbers have to be adjusted for each setup, which can be easily accomplished through the live view of the filtering and tracking results. In the documentation we provide guidelines on choosing these parameters. To compare results across different

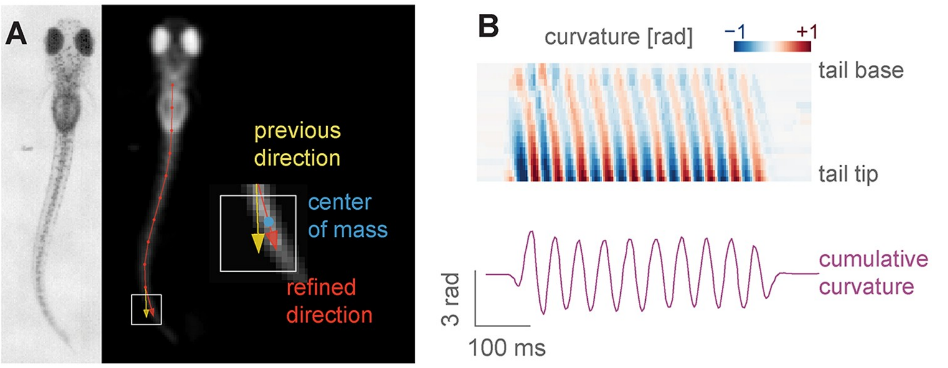

Fig 3. Head-restrained tail tracking in Stytra. A) The image is first pre-processed by inverting, down-scaling, blurring and clipping, resulting in the image on the right, where the fish is the only object brighter than the background. Then, tail tracing starts from a user-defined point, and in the direction determined by another user-defined point at the end of the tail at rest. For each segment, a square (outlined in white) in the direction of the previous segment (yellow) is sampled, and the direction for the next segment is chosen as the vector (red) connecting the previous segment end and the center of mass of the sampled square (blue). B) A heatmap showing the angles of the tail segments from the start to the end of the tail during a bout, and a trace representing the cumulative curvature sum from a behaving animal. The total curvature is just the difference in angle between the first and last tail segment (adding up angle differences between all segments, only these two terms remain).

https://doi.org/10.1371/journal.pcbi.1006699.g003

setups which might have different camera resolutions, the resulting tail shape can be interpolated to a fixed number of segments regardless of the number of traced points.

Eye tracking. Zebrafish larvae move their eyes to stabilize their gaze in response to whole field motion, perform re-positioning saccades, and converge their eyes to follow a potential prey in hunting maneuvers [9]. Naso-temporal eye movements can be described by the eye orientation with respect to the fish axis. Given the ellipsoidal shape of the eyes when seen from above, to find their orientation it is sufficient to fit an ellipse to the eye pixels and determine the angle of the major axis [9]. In Stytra, a movable and scalable rectangular region can be used to select the area of the camera view containing the eyes. As eyes are usually much darker than the background, with proper illumination conditions it is sufficient to binarize the image with an adjustable threshold which selects the pixels belonging to the eyes. Then, functions from the OpenCV library are used to find the two largest connected components of the binarized region and fits an ellipse to them. The absolute angle of the major axis of the ellipse is recorded as the eye angle (Fig 4). A live preview of the binarized image and the extracted ellipses helps the user to adjust the parameters.

Freely-swimming fish tracking. To support different kinds of paradigms where fish are not head-restrained, we provide functions for freely-swimming fish tracking. The range of behavioral paradigms include investigating movement evoked by different kinds of stimuli, characterizing motion kinematics and assessing consequences of pharmacological or genetic interventions. To track the fish in an open arena, the first required step is background subtraction. The background is modelled with a mean image taken from multiple frames averaged in time, and slowly updated with an adjustable time constant. The subsequently processed image is the negative difference between the current frame and the threshold (pixels that are darker than the background are active). This image is first thresholded and regions within the right area range are found. Both eyes and the swim bladder are found as darker parts inside of these regions, and the center of mass of the three objects (two eyes and swim bladder) is taken as the center of the fish head. The direction of the tail is found by searching for the point with the largest difference from the background on a circle of half-tail radius. This direction is

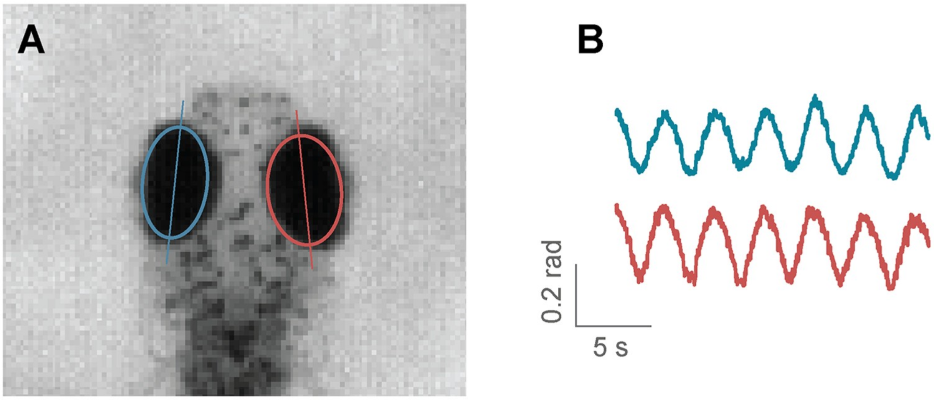

Fig 4. Eye tracking in Stytra. A) Eyes are detected by fitting an ellipse to the connected components of the image of the fish head after thresholding. B) Example trace of eye motion in response to a full-field rotating background.

https://doi.org/10.1371/journal.pcbi.1006699.g004

subsequently refined in the course of tail tracking, as described in the tail tracking section. The kinematic parameters are smoothed by Kalman filtering. An example resulting from tracking multiple fish simultaneously is shown in Fig 5. Fish identities are maintained constant while they are in the field of view and not overlapping, by keeping track of the previous positions and orientations. The number of fish does not significantly impact performance, however the resolution of the camera does, so we recommend a well-configured modern computer (7th generation and above Intel Core i7 processors or AMD Ryzen) for tracking multiple fish in a 90 mm dish. In our experiments not more than 3 fish are usually present, and a tracking framerate of 300 Hz can be reached reliably. We have also tracked individual fish in a 24-well plate, which presented no performance issues at 100 Hz with a mid-range CPU. Simpler tracking scenarios for screening, where the exact position, orientation and tail curvature of individuals are not of interest, can work with even higher numbers of animals.

For closed-loop experiments, the camera view and the projected area need to be aligned to lock the stimulus to the fish position. To this end, a calibration module inside of Stytra finds the mapping between the area covered by the camera and the area illuminated by the screen. During calibration, three points are projected on the screen and detected as local maxima on

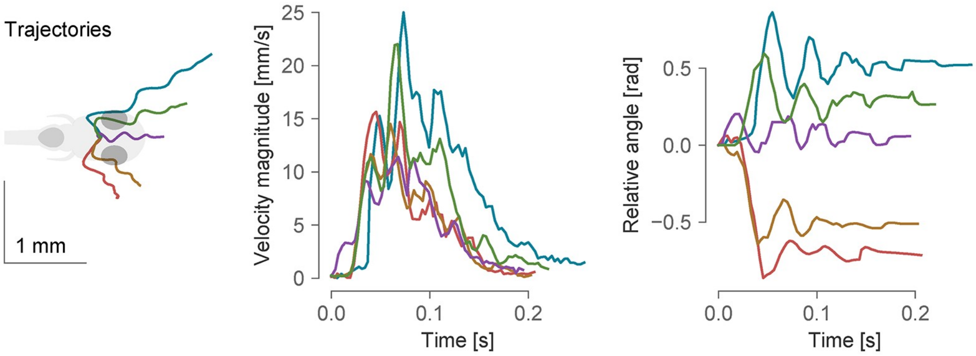

Fig 5. Example bouts tracked from freely-swimming fish. From left to right: trajectories of bouts in different directions, the velocity magnitude and the total angle change during the course of the bouts. In the left-most panel, all trajectories were realigned such that the initial position and orientation of the fish were the same. The data was sampled at 300 Hz.

https://doi.org/10.1371/journal.pcbi.1006699.g005

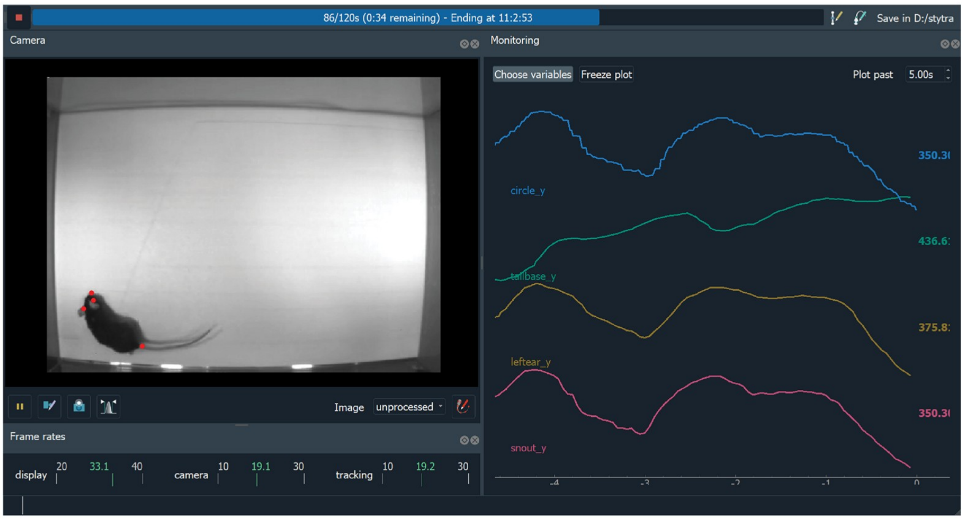

Fig 6. Screenshot of DeepLabCut-based rat tracking in Stytra. On the left, the 4 detected keypoints (snout, two ears and tail base) in red are superimposed on the video. On the right, traces tracking the coordinates of the animal are displayed, along with a parameter of of a closed-loop stimulus (a circle that would be tracking a rat). The video displayed was provided with the DeepLabCut repository [10].

https://doi.org/10.1371/journal.pcbi.1006699.g006

the camera image. Then, a transformation matrix is computed to align the projected and recorded points. If the setup elements are kept firmly in place, the calibration has to be done only once, although regular checking of the calibration on a regular basis is encouraged.

Custom tracking functions. Stytra is designed in an extensible fashion and video tracking algorithms for other animals can be easily added. To demonstrate this, we provide a small example of DeepLabCut-based tracking, which can be integrated with very few lines of code and immediately used with closed-loop stimuli. DeepLabCut is a convolutional neural network-based pose estimation toolbox [10] built on top of the DeeperCut architecture [11]. We incorporated an open-field recording example with the video and parameters provided in the original repository (see Fig 6). The code for this example is in a separate GitHub repository, listed at the end of the manuscript. The tracking performance of DeepLabCut mainly depends on video resolution and CPU and GPU performance. We managed to obtain a tracking speed of 20 Hz (resulting in a tracking latency of 50 ms) for a 640x480 px video on a computer equipped with a nVidia GeForce GTX Titan X GPU and Intel Xeon E5-2687W v3 CPU. For a detailed investigation of DeepLabCut performance see [12].

Closed-loop stimuli design

Stimuli whose state depends on the behavior of the fish (position and orientation for freely swimming fish, and tail or eye motion for head-restrained fish) are controlled by linking the behavioral state logs to the stimulus display via `Estimator` objects (see Fig 1). An `Estimator` receives a data stream from a tracking function (such as tail angles), and uses it together with calibration parameters to estimate some quantity online. For example, a good proxy for fish velocity is the standard deviation of the tail curvature over a window of 50 ms [13], which we refer to as vigor. Fig 7 shows an example of how vigor can be used in a closed-loop optomotor assay. When presented with a global motion of the visual field in the caudal-rostral direction, the fish tend to swim in the direction of perceived motion to minimize the visual flow, a reflex known as the optomotor response [3, 14]. The visual feedback during the

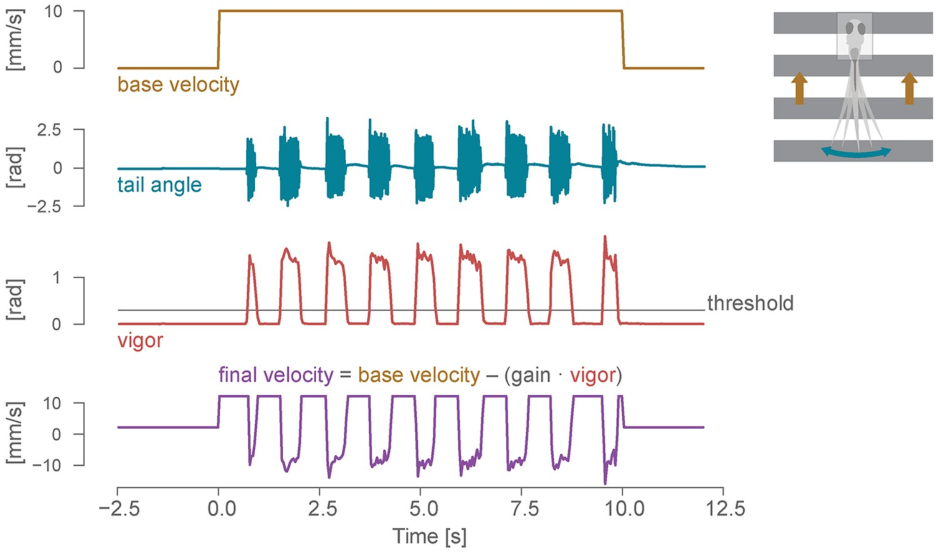

Fig 7. Closed-loop optomotor assay. Dynamic update of the stimulus in a closed-loop assay for the optomotor response. From top: open-loop velocity of the gratings moving caudo-rostrally below the fish; cumulative tail angle (see the tail tracking section and Fig 3 for details); bout vigor, estimated by calculating the instantaneous standard deviation of the angle sum in a 50 ms window; final closed-loop velocity of the gratings, with backward movements induced by the fish swimming.

https://doi.org/10.1371/journal.pcbi.1006699.g007

swimming bout is a crucial cue that the larvae use to control their movements. In this closed-loop experiment, we use the vigor-based estimation of fish forward velocity, together with a gain factor, to dynamically adjust the velocity of the gratings to match the visual flow expected by a forward swimming fish. The gain parameter can be changed to experimentally manipulate the speed of the visual feedback received by the larvae [13] (see below).

Closed-loop stimuli may be important for freely swimming fish as well, for example to display patterns or motion which always maintain the same spatial relationship to the swimming fish by matching the stimulus location and orientation to that of the fish.

Synchronization with external devices

Stytra is designed to support the presentation of stimuli that need to be synchronized with a separate acquisition program, e.g. for calcium imaging or electrophysiology. To this end, the `Trigger` object enables communication with external devices and different computers to synchronize the beginning of the experiment. The `Trigger` object runs in a separate process, ensuring that the interface is not blocked while waiting for trigger signals, and it can be used to either trigger the beginning of the experiment, or to trigger arbitrary parts of the protocol using the existing `TriggerStimulus` object or similar custom stimuli. Two ways of receiving the triggering signal are already supported in the library: TTL pulse triggering via a LabJack board, and communication over a local network employing the ZeroMQ library. Messages exchanged through ZeroMQ can also contain data, such as the microscope configuration, that will be saved together with the rest of the experiment metadata. The triggering module is designed to be easily expandable, and we provide instructions for writing custom trigger objects. In our lab the two-photon microscope is controlled by custom LabView software, which we extended to include ZeroMQ communication with Stytra. An example LabView program that can be used to trigger Stytra is illustrated in the triggering section of the documentation. In Results, we describe an example experiment using this triggering configuration to link behavioral and stimulus quantities and the recorded calcium responses. Proprietary scanning programs where this cannot be achieved can still trigger Stytra using TTL pulses.

Data collection

The design of Stytra encourages automatic data management. A dedicated `DataCollector` object is used to log the metadata about the experiment. Parameters from the entire program are appended to a single hierarchical parameter tree, which is saved at the end of the experiment. Quantities in the tree can come from different sources. Firstly, parameters can be added at any point in the code. For example, at every run the current version number of Stytra and git commit are detected and saved, together with the versions of the dependencies. Secondly, many of the key objects of Stytra (tracking nodes, display and camera controllers. . .) are parametrized though a custom parameters package (lightparam). When constructing them, one needs to pass the parameter tree that collects the data. This ensures that all quantities needed to replicate the experiment are collected within the metadata file. Finally, dedicated parametrized objects can be used to manually input metadata concerning the animal (age, genotype, etc.) or the experiment (setup, session, etc.). These classes can be customized to automatically include lab-specific metadata options, such as setup identifiers or animal lines (examples for this customization are provided in the documentation). Various logs accompanying the experiment run (state of the stimuli, the raw tracking variables and the estimated state of the fish) are saved as tabular data. The supported data formats are CSV, HDF5 and Feather, but others could be added as long as they provide an interface to the Pandas library. To demonstrate the convenience of the data and metadata saving methods of Stytra, we made example data available together with Jupyter notebooks for the analyses that can reproduce the figures in this paper. Finally, a central experiment database can be connected to keep track of all the experiments in a lab or institute. The documentation provides an example of a MongoDB database connection.

Setup hardware

In our effort to make experiments as open and reproducible as possible, we documented example setups that can be used together with the Stytra software for performing behavioral experiments in head-restrained and freely swimming fish (Fig 8). In general, the minimal setup for tracking the fish larvae requires a high-speed camera (a minimum of 100 Hz is required to capture the most common tail beats which have a frequency up to 50 Hz, but we recommend at least 300 Hz to describe the details of the tail kinematics). The camera must be equipped with a suitable objective: a macro lens for the head-restrained tail tracking or a normal lens for the freely swimming recordings, where a smaller magnification and a larger field of view are required. More detailed camera and lens guidelines can be found in the documentation. Infrared illumination is then used to provide contrast without interfering with the animal's visual perception. Since fish strongly rely on vision and many of their reflexes can be triggered by visual stimulation, the setup is usually equipped with a projector or screen to present the visual stimulus to the fish. Although in our setups stimuli are projected below the fish, a lateral projector would be fully compatible with Stytra. Most of our rig frames consist of optomechanical parts commonly used for building microscopes. These parts are convenient but not strictly necessary to build a well-functioning rig. Replacing them with simple hardware-store and laser-cut components can significantly reduce the costs. Therefore, we also provide instructions for a head-restrained setup built inside a cardboard box, where the most expensive item is the high-speed camera, bringing the price of the whole setup without the computer below

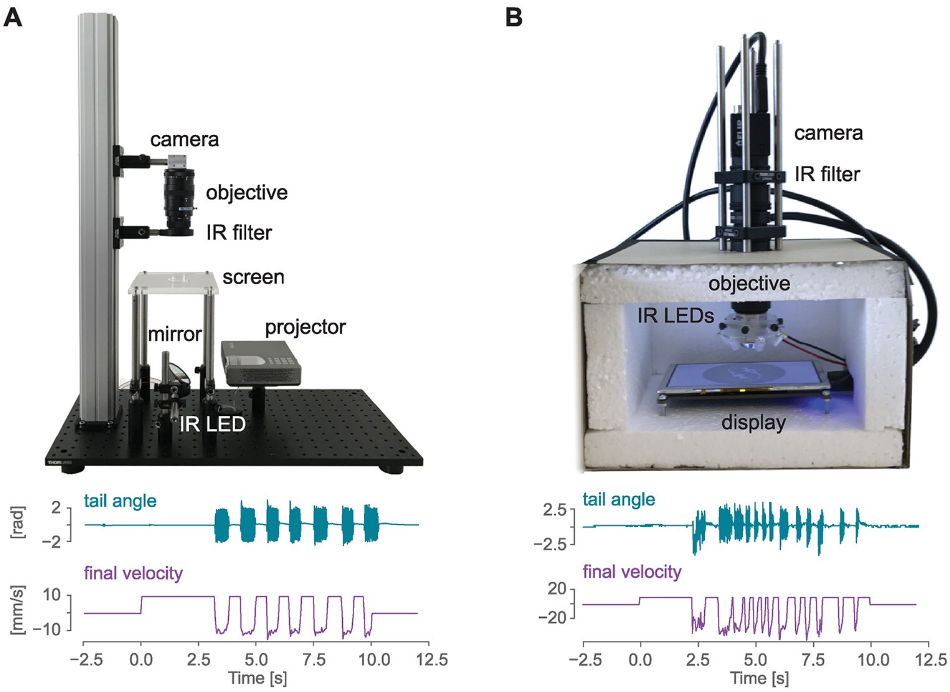

Fig 8. Hardware for zebrafish behavior experiments. A) Above: sample image of a behavioral setup that can be used to track head-restrained zebrafish tail end eyes (the opaque enclosure has been removed for visualization purposes). Below: sample traces for tail angle and grating velocity obtained from this setup with the closed-loop experiment described in Fig 7. B) A low-cost version of the setup presented in A) that can be used to investigate behavior in the head-restrained fish, and sample traces from this setup. A detailed description of the setup together with a complete list of parts can be found at www.portugueslab.com/stytra/hardware_list.

https://doi.org/10.1371/journal.pcbi.1006699.g008

700 euros. We built and documented such a setup, where we were able to elicit and record reliable optomotor responses in larval zebrafish (Fig 8).

A complete description of all the above-mentioned versions of the setup along with an itemized list of parts is included within the Stytra hardware documentation.

Comparison with existing software packages

Many general-purpose systems have been proposed over the years to present visual and other kinds of stimuli and control behavioral experiments, each with its own strengths and limitations. Below we sum up some of the systems which are currently maintained, and we present how they compare to Stytra.

Bonsai. Bonsai [15] is a visual programming language built on top of the language C# with a reactive, dataflow-based paradigm. In Bonsai, users with little experience in programming can implement their own tracking pipelines and basic stimuli. By default Bonsai offers visualization of any data processing node, and custom visualizers. In principle, due to the generality of Bonsai, all functions of Stytra could be implemented within it. Still, implementing many features would require using a programming language uncommon in science (C#). Also, the use of several Python libraries, such as DeepLabCut, is in many cases not possible, as only a subset of Python is supported in C# through the IronPython interpreter.

Psychophysics toolbox. Psychophysics Toolbox [16] offers a large toolbox to build visual stimuli and stimulation protocols. The toolbox has been developed with human psychophysics in mind, in particular visual and auditory psychophysics. It provides large control over display and sound hardware, and many tools for acquiring responses from the subject through the mouse and keyboard. Still, its application is restricted to the stimulus design, as it does not offer any camera integration or animal tracking modules. This makes the toolbox ill-suited for developing closed-loop stimuli where behavior and responses of the animal need to be fed back to the stimulus control software. Moreover, it relies on the proprietary software package Matlab.

Psychopy. Psychopy [17] is a library similar to the Psychophysics Toolbox, written in Python. It provides precise control over displaying visual and auditory stimuli (not currently implemented in Stytra), and a set of tools for recording responses through standard computer inputs (mouse and keyboard). Due to its wide use in human psychophysics experiments, it has a larger library of stimuli than Stytra. However, it is also purely a stimulation library without video or other data acquisition support. Moreover, it does not provide a system for easy online control of stimulus parameters, an essential feature for closed-loop experiments.

MWorks. MWorks is a C/C++ library to control neurophysiological experiments, developed mostly for (visual) neurophysiology in primates and rodents. It provides support for building complex tasks involving trials with different possible outcomes, and contains a dedicated library for handling visual stimuli. Due to being implemented in a compiled language, higher and more consistent performance can be obtained than with our package, which is Python based. However, it is not designed for online video analysis of behavior, which is essential for behaviorally-controlled closed-loop experiments. Furthermore, while scripting and expanding Stytra requires pure Python syntax, experiments in MWorks are coded in custom high-level scripting language based on C++. Most importantly, it runs only on MacOS, which depends on Apple hardware, available only in a minority of laboratories.

ZebEyeTrack. The software solution described in [2] covers a small subset of Stytra functionality—eye tracking and eye-motion related stimulus presentation. It is implemented in LabView and Matlab, which adds two expensive proprietary software dependencies. Running an experiment requires launching separate programs and many manual steps as described in the publication. The tracking frame rate is limited to 30 Hz in real-time while Stytra can perform online eye tracking at 500 Hz, and Stytra's performance is mainly limited by the camera frame rate.

Results

Triggering Stytra from a scanning two-photon microscope

We demonstrate the communication with a custom-built two-photon microscope. We performed two-photon calcium imaging in a seven days post fertilization (dpf), head-restrained fish larva pan-neuronally expressing the calcium indicator GCaMP6f (Tg(*elavl3*:GCaMP6f), [18]). For a complete description of the calcium imaging protocol see [19]. These and following experiments were performed in accordance with approved protocols set by the Max Planck Society and the Regierung von Oberbayern.

We designed a simple protocol in Stytra consisting of either open- or closed-loop forward-moving gratings, similar to the optomotor assay described in the closed-loop section, with the gain set to either 0 or 1. At the beginning of the experiment, the microscope sends a ZeroMQ message to Stytra, as described in the previous section. This triggers the beginning of the visual stimulation protocol, as well as the online tracking of the fish tail, with a 10-20 ms delay. To match behavioral quantities and stimulus features with their evoked neuronal correlates, we used the data saved by Stytra to build regressors for grating speed and tail motion (for a description of regressor-based analysis of calcium signals, see [8]). Then, we computed pixel-wise correlation coefficients of calcium activity and the two regressors. Fig 9 reports the results

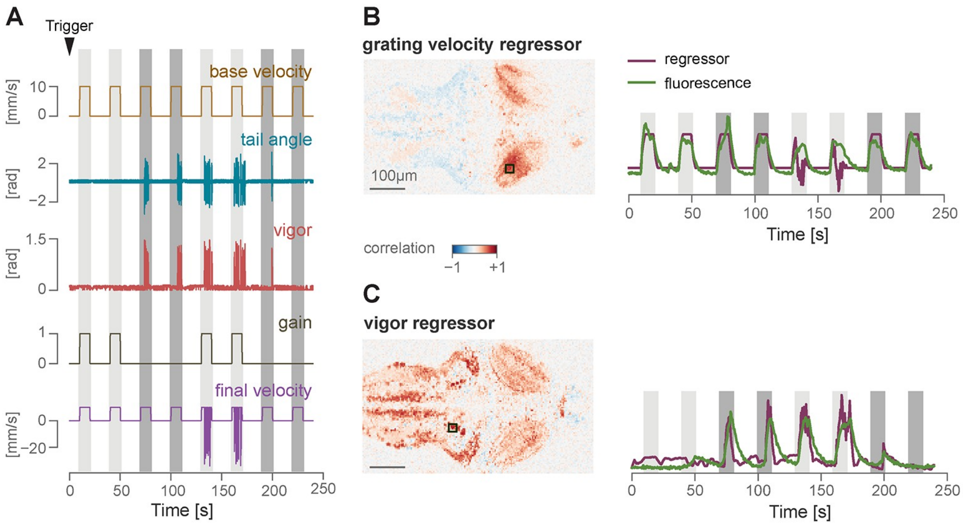

Fig 9. Closed-loop protocol and simultaneous whole-brain calcium imaging. A) A protocol consisting of either open- or closed-loop forward-moving gratings was presented to a seven day old Tg(*elavl3*:GCaMP6f) zebrafish larvae during two-photon imaging. The arrowhead points to the timepoint of receiving the trigger signal from the microscope. Colored stripes indicate periods when the gratings were moving: dark gray represents open loop trials (gain 0) and light gray represents closed-loop trials (gain 1). B) Left: Pixel-wise correlation coefficients with the grating velocity regressor. The square on the regressor map reports the position of the area that was used to compute the calcium trace displayed on the right. Right: z-scored fluorescence trace from the selected area, imposed over the regressor trace. C) Same as B, for the vigor regressor.

https://doi.org/10.1371/journal.pcbi.1006699.g009

obtained by imaging a large area of the fish brain, covering all regions from the rhombencephalon to the optic tectum. As expected, calcium signals in the region of the optic tectum are highly correlated with motion in the visual field, while events in more caudal regions of the reticular formation are highly correlated with swimming bouts. The Stytra script used for this experiment is available at `stytra/example/imaging_exp.py`.

Experiment replication

One of the main strengths of Stytra is the possibility of sharing the experimental paradigms described in a publication as scripts that can be run on different platforms and experimental hardware. To prove the validity of this approach, we decided to showcase the software reproducing the results from two publications that investigated different behaviors of the larval zebrafish. This allowed us to verify the performance of our package in producing and monitoring reliable behavioral responses, and showed how the Stytra platform can be used to share the code underlying an experimental paradigm. The scripts used for designing these experiments are available in our repository, together with a full list of parts and description of the hardware. In this way, everyone can independently replicate the experiments simply by installing and running Stytra on a suitable behavioral setup.

Closed-loop motor adaptation. To demonstrate the effectiveness of the closed-loop stimulation software for head-restrained larvae, we re-implemented in Stytra one of the paradigms described in [13]. This paper addresses the importance of instantaneous visual feedback in the control of the optomotor response in seven dpf zebrafish larvae.

In [13], a closed-loop paradigm was used to have real-time control over the visual feedback that the animal receives upon swimming. After triggering motor activity with forward-moving black and white gratings (10 mm/s, 0.1 cycles/mm), online tail tracking was used to estimate

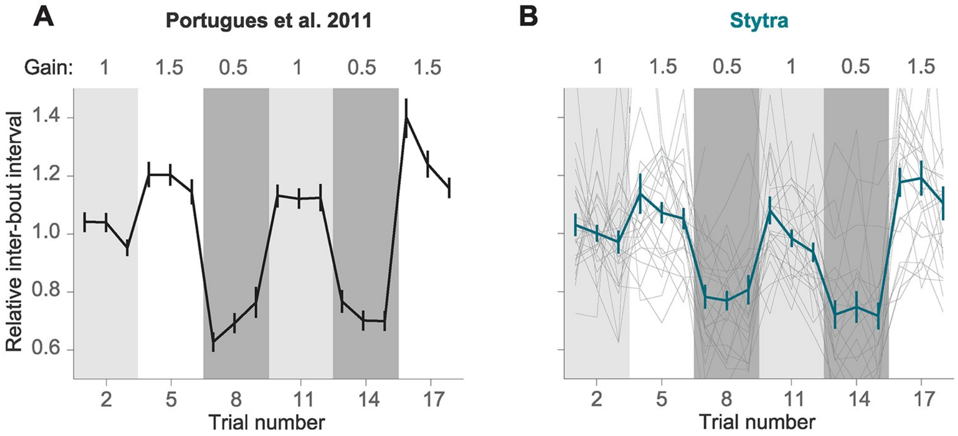

Fig 10. Visual feedback changes inter-bout interval in a head-restrained optomotor assay. Replication within Stytra of results published in [13]. A) Changing the gain that is used to convert the fish's swimming vigor to relative velocity with respect to the grating affects the inter-bout interval. The line represents the average normalized inter-bout time, and bars represent standard error of the mean from n = 28 larvae (adapted from [13]). B) Replication in Stytra of the same experimental protocol (n = 24 larvae). Individual fish traces are shown in gray.

https://doi.org/10.1371/journal.pcbi.1006699.g010

the expected velocity of the fish based on freely-moving observations, and a backward velocity proportional to the expected forward velocity was imposed over the forward grating speed. In one crucial experiment (Fig 3 of [13]) the authors demonstrated that reducing or increasing the magnitude of this velocity by a factor of 1.5 (high gain) or 0.5 (low gain) resulted in modifications of the bout parameters such as bout length and inter-bout interval (time between two consecutive bouts). Fig 10A shows the inter-bout interval along the protocol, where the three gain conditions were presented in a sequence that tested all possible gain transitions. When the gain increased the fish was consistently swimming less (higher inter-bout interval), while the opposite was observed when the gain decreased. Therefore, as expected, fish adapted the swimming parameters to compensate for changes in visual feedback.

We reproduced exactly the same protocol within Stytra, and we used Stytra modules for closed-loop control of a visual stimulus to compare whether it could replicate the findings from [13]. The cumulative angle of the extracted tail segments was used with a gain factor to estimate the fish velocity and the gain factor was changed in a sequence matching the protocol in [13]. The replication with Stytra yielded the same result (Fig 10B), that inter-bout interval decreased in low gain conditions and increased in high gain conditions.

Closed-loop phototaxis assay. To test the freely swimming closed-loop performance, we replicated a protocol from [20]. The fish is induced to perform phototaxis by keeping half of its visual field (the left or the right side) bright while the other is dark. The fish is more likely to turn to the bright side. The stimulus is constantly updated so that the light-dark boundary is always along the mid-line of the fish. We replicated the qualitative trends observed in [20], however the ratios of forward swims to turns are notably different (Fig 11). The variability of fish responses and differences in the stimulus presentation setup (e.g. projector brightness) could account for these differences. Also, to reduce duration of the experiments, we included a radially-inward moving stimulus that brings the fish back into the field of view.

Discussion

We have developed Stytra, a Python-based software package that can perform online behavioral analysis and stimulation and can be interfaced with existing solutions to combine these

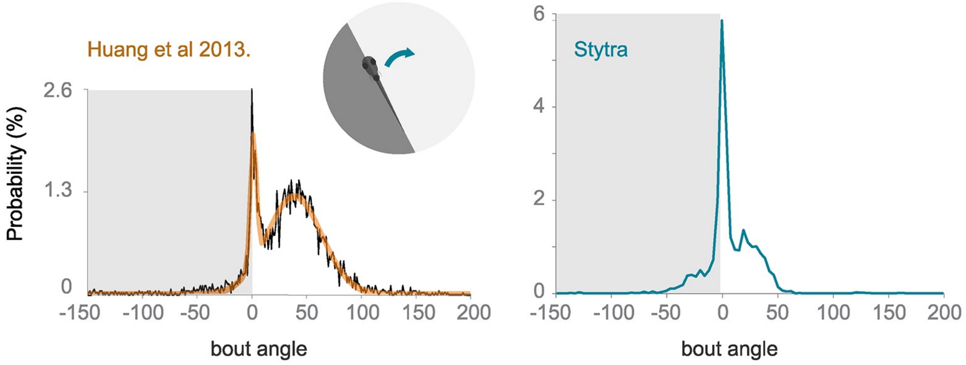

Fig 11. Comparison of turning angle distribution in a closed-loop freely-swimming phototaxis experiment. Left: a histogram of the angle turned per bout, redrawn from [20]. Right: the equivalent panel, with n = 10 fish and the protocol run with Stytra. The dark shading on the plot represents the dark side of the visual field.

https://doi.org/10.1371/journal.pcbi.1006699.g011

with physiological experiments. This demonstrates its suitability as a framework for coding and running experiments in systems neuroscience. In addition to the open-source software, we are contributing to the nascent open hardware movement [4] and are providing a complete description of the hardware used for conducting behavioral experiments. Finally, we provide a set of example analysis scripts for the experiments described in this manuscript, which can be easily modified for other experimental questions. We believe that the simplicity of the implementation of an experiment within Stytra facilitates the collaboration between laboratories, since complex experimental paradigms can be run and shared with Python scripts whose reproducibility can be ensured using version control.

The current version of the software supports all experimental paradigms currently running in our lab. Support for different hardware would require some extensions in the architecture. Simultaneous use of multiple cameras is currently not supported either, but this requires a minor rewriting of the frame dispatching module. We will both continue to extend Stytra's capabilities and support any contributions that expand the library to cover a wider range of experimental conditions. Finally, it is important to note that the choice of Python as a language would make it difficult to obtain millisecond-level or higher temporal precision (e.g. for closed-loop electrophysiology). To this aim, existing solutions based on compiled languages should be employed, such as [21] (a system for closed-loop electrophysiology in C++). Another possibility would be to combine Open Ephys and Bonsai, as in [22].

The modular and open-source nature of the package (licensed under the GNU GPL v3.0 licence) facilitates contributions from the community to support an increasing number of hardware devices and experimental conditions. Although the current implementation deals with typical zebrafish experiments, the package contains many modules that can be used in other contexts, for example: Qt-based design and timed execution of stimuli, support for different cameras models and accumulators to save data streamed from different processes that can be used for closed-loop stimuli. Although the adaptation to very different experimental conditions requires familiarity with Stytra internals, scientists interested in developing behavioral paradigms using pure Python could use many modules of Stytra as a starting point. We will make use of the community features of Github to provide assistance to any interested developers, and to support adopting the package in other labs. In conclusion, we hope that Stytra can be a resource for the neuroscience community, providing a common framework to create shareable and reproducible behavioral experiments.

Online resources

- Stytra repository: https://github.com/portugueslab/stytra DOI:10.5281/zenodo.2548534
- Stytra documentation: http://www.portugueslab.com/stytra/
- data analysis notebooks: https://github.com/portugueslab/example_stytra_analysis
- example data from Stytra: https://zenodo.org/record/1692080
- example extension of Stytra to rat experiments: https://github.com/portugueslab/Stytra-with-DeepLabCut

Supporting information

S1 Fig. Software architecture of Stytra. A partial diagram of classes and the links between them.
(TIF)

S2 Fig. Temporal jitter of a flickering stimulus. The distribution of time differences between bright-dark transitions of a stimulus set to flip between full luminosity on the red channel and darkness on every stimulus. Pure red was flashed in order to avoid artifacts of LED DLP projector color multiplexing. The brightness of a small area of the display was recorded with a Ximea camera with a OnSemi PYTHON 1300 sensor at 2000 Hz.
(TIF)

Acknowledgments

We thank Marco Albanesi for testing the software and the first pull requests, and Virginia Palieri, Elena I. Dragomir, Ot Prat and Daniil Markov for being the first users of Stytra in the lab. We thank the Python open-source community on whose work this package is based on, especially Luke Campagnola for developing the invaluable PyQtGraph package.

Author Contributions

Conceptualization: Vilim Štih, Luigi Petrucco, Ruben Portugues.

Data curation: Vilim Štih, Luigi Petrucco.

Formal analysis: Vilim Štih, Luigi Petrucco.

Funding acquisition: Ruben Portugues.

Investigation: Vilim Štih, Luigi Petrucco.

Methodology: Vilim Štih, Luigi Petrucco, Andreas M. Kist.

Project administration: Ruben Portugues.

Software: Vilim Štih, Luigi Petrucco, Andreas M. Kist.

Supervision: Ruben Portugues.

Validation: Vilim Štih, Luigi Petrucco.

Visualization: Vilim Štih, Luigi Petrucco.

Writing – original draft: Vilim Štih, Luigi Petrucco, Ruben Portugues.

Writing – review & editing: Andreas M. Kist.

References

1. Haesemeyer M. haesemeyer/ZebraTrack: Initial release; 2019. Available from: https://doi.org/10.5281/zenodo.2539837.
2. Dehmelt FA, von Daranyi A, Leyden C, Arrenberg AB. Evoking and tracking zebrafish eye movement in multiple larvae with ZebEyeTrack. Nature protocols. 2018; p. 1.
3. Portugues R, Engert F. The neural basis of visual behaviors in the larval zebrafish. Current opinion in neurobiology. 2009; 19(6):644–647. https://doi.org/10.1016/j.conb.2009.10.007 PMID: 19896836
4. Chagas AM. Haves and have nots must find a better way: The case for open scientific hardware. PLoS biology. 2018; 16(9):e3000014. https://doi.org/10.1371/journal.pbio.3000014
5. Imagen;. https://imagen.pyviz.org.
6. Bradski G. The OpenCV Library. Dr Dobb's Journal of Software Tools. 2000.
7. Budick SA, O'Malley DM. Locomotor repertoire of the larval zebrafish: swimming, turning and prey capture. Journal of Experimental Biology. 2000; 203(17):2565–2579. PMID: 10934000
8. Portugues R, Feierstein CE, Engert F, Orger MB. Whole-brain activity maps reveal stereotyped, distributed networks for visuomotor behavior. Neuron. 2014; 81(6):1328–1343. https://doi.org/10.1016/j.neuron.2014.01.019 PMID: 24656252
9. Beck JC, Gilland E, Tank DW, Baker R. Quantifying the ontogeny of optokinetic and vestibuloocular behaviors in zebrafish, medaka, and goldfish. Journal of neurophysiology. 2004; 92(6):3546–3561. https://doi.org/10.1152/jn.00311.2004 PMID: 15269231
10. Mathis A, Mamidanna P, Cury KM, Abe T, Murthy VN, Mathis MW, et al. DeepLabCut: markerless pose estimation of user-defined body parts with deep learning. Nature Neuroscience. 2018. https://doi.org/10.1038/s41593-018-0209-y PMID: 30127430
11. Insafutdinov E, Pishchulin L, Andres B, Andriluka M, Schiele B. DeeperCut: A Deeper, Stronger, and Faster Multi-Person Pose Estimation Model.
12. Mathis A, Warren RA. On the inference speed and video-compression robustness of DeepLabCut. bioRxiv. 2018. https://doi.org/10.1101/457242
13. Portugues R, Engert F. Adaptive locomotor behavior in larval zebrafish. Frontiers in systems neuroscience. 2011; 5:72. https://doi.org/10.3389/fnsys.2011.00072 PMID: 21909325
14. Orger MB, Kampff AR, Severi KE, Bollmann JH, Engert F. Control of visually guided behavior by distinct populations of spinal projection neurons. Nature neuroscience. 2008; 11(3):327. https://doi.org/10.1038/nn2048 PMID: 18264094
15. Lopes G, Bonacchi N, Frazão J, Neto JP, Atallah BV, Soares S, et al. Bonsai: an event-based framework for processing and controlling data streams. Frontiers in neuroinformatics. 2015; 9:7. https://doi.org/10.3389/fninf.2015.00007 PMID: 25904861
16. Brainard DH, Vision S. The psychophysics toolbox. Spatial vision. 1997; 10:433–436. https://doi.org/10.1163/156856897X00357 PMID: 9176952
17. Peirce JW. PsychoPy—psychophysics software in Python. Journal of neuroscience methods. 2007; 162(1-2):8–13. https://doi.org/10.1016/j.jneumeth.2006.11.017 PMID: 17254636
18. Wolf S, Dubreuil AM, Bertoni T, Böhm UL, Bormuth V, Candelier R, et al. Sensorimotor computation underlying phototaxis in zebrafish. Nature Communications. 2017; 8(1):651. https://doi.org/10.1038/s41467-017-00310-3 PMID: 28935857
19. Kist AM, Knogler LD, Markov DA, Yildizoglu T, Portugues R. Whole-Brain Imaging Using Genetically Encoded Activity Sensors in Vertebrates. In: Decoding Neural Circuit Structure and Function. Springer; 2017. p. 321–341.
20. Huang KH, Ahrens MB, Dunn TW, Engert F. Spinal projection neurons control turning behaviors in zebrafish. Current Biology. 2013; 23(16):1566–1573. https://doi.org/10.1016/j.cub.2013.06.044 PMID: 23910662
21. Ciliberti D, Kloosterman F. Falcon: a highly flexible open-source software for closed-loop neuroscience. Journal of neural engineering. 2017; 14(4):045004. https://doi.org/10.1088/1741-2552/aa7526 PMID: 28548044
22. Buccino AP, Lepperod ME, Dragly SA, Hafliger PD, Fyhn M, Hafting T. Open source modules for tracking animal behavior and closed-loop stimulation based on Open Ephys and Bonsai. bioRxiv. 2018; p. 340141.

Discussion

Larval zebrafish as a model for cerebellar research

In the same year as the publication of *Manuscript 1*, two studies in mice, imaging larger populations of granule cells, have been published [48,49]. In addition to changes in the granule cell activity patterns during learning, the studies shared similar observation in terms of the absence of sparsity. Even though a far smaller proportion of granule cells have been imaged in lobule VI (around 50 - 100 were sampled from tens of millions granule cells in ice), the majority showed task dependent modulation. These studies prompted theoretical reevaluation of the relevance of sparsity for cerebellar coding[50] and pointed to how many assumptions underlying dominant theories of cerebellar function still need to be tested.

A subsequent paper from our lab focused on analysing the responses of Purkinje cells[51]. Knogler et al. have found that the simple spikes, caused by signalling from the granule cells, are driven majorly by motor-related activity. The Purkinje cell activity has been found to be segmented in areas responding to different types of visual stimuli and correlated with motor activity. Finally, in the most recent publication from the lab[52] Markov et al. show that without cerebellar Purkinje cells, long term adaptation to a closed-loop feedback manipulation does not occur.

The major issue that remains with cerebellar studies in larval zebrafish is that behavioral effect sizes after manipulations are very small, even with ablation of large parts of the populations of specific cell types. Sill, a large part of the larval zebrafish behavioral repertoire remains to be explored in the context of the cerebellum, where it could play a more prominent role than in the optomotor response.

A fuller picture of the optomotor response

The work presented in this thesis fills several gaps left by previous studies of the optomotor response: first, focusing on cerebellar representations, secondly, investigating long-term evidence integration as a trigger for behavior, and looking in detail into the representation of motion in all cardinal directions, focusing on an under-studied area, the IPN. A common property of most studies on the optomotor response is that either they investigate only the forward swimming or turning part of the behavior. Even in studies combining both, such as Naumann et al.[53] an incomplete subset of stimuli is used (of the space of 25 stimuli - 4 motion directions and no motion, per eye - only 9 were used, and no predictions were made for the behavior of the remaining combinations, even though it would be possible within the framework developed in the publication.

While the OMR is a versatile behavior to study in zebrafish, it has several limitations compared to other adaptive motor control paradigms: it is highly variable both across individuals and within individuals over longer time spans (see Figure 5). In theory, this variation could be quantitatively described by inferring per-fish and between-fish latent variables, however their dynamics would be impossible to estimate with achievable durations of experiments. The OMR is also rather inaccurate if the goal is considered to be to counteracting the relative visual

[48] Giovannucci et al., "Cerebellar Granule Cells Acquire a Widespread Predictive Feedback Signal during Motor Learning".

[49] Wagner et al., "Cerebellar Granule Cells Encode the Expectation of Reward".

[50] Gilmer and Person, "Theoretically Sparse, Empirically Dense".

[51] Knogler, Andreas M Kist, and Portugues, "Motor Context Dominates Output from Purkinje Cell Functional Regions during Reflexive Visuomotor Behaviours".

[52] Markov et al., "A Cerebellar Internal Model Calibrates a Feedback Controller Involved in Sensorimotor Control".

[53] Naumann et al., "From Whole-Brain Data to Functional Circuit Models".

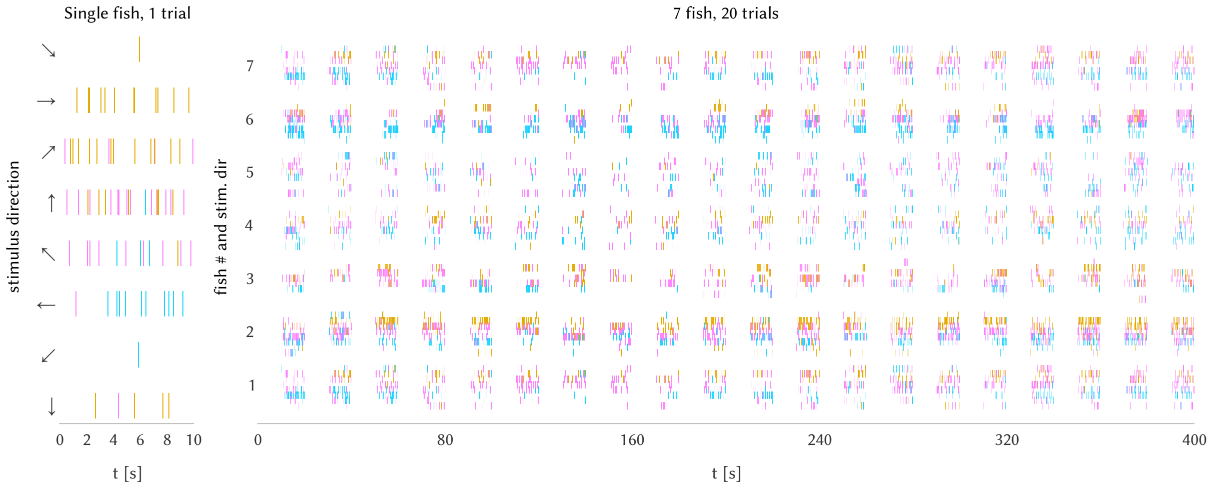

Figure 5: The variability of the optomotor response when presented with 8 different directions, in embedded fish within an animal and across animals. Each line is a bout, and the color is the inferred direction, with left, forward and right bouts. The left panel is an example trial for one fish, with the y axis splitting across the stimuli, whereas the right panel shows 20 trials across 7 fish, each represented analogously to the left panel.

motion by swimming, especially when moving in two dimensions (as opposed to one). This effect is visible only in aggregate, over many bouts and for a part of animals in specific time frames, while the fish remain far from the original position. Other tasks common in behavioral experiments, such as eye reflexes, reaching and various trained paradigms in rodents and primates, can be executed with high reliability and precision[54,55,56], and may be better suited for questions on motor control circuits.

Limitations of embedded experiments

Embedded behavior is a poor proxy of freely-swimming behavior: both the physics are different, as the head cannot swing, and both vestibular and lateral line sensory feedback is absent. In the case of the OMR, the fish employ a different behavioral strategy to deal with the variety of grating speeds[57]. We have attempted to improve the head-embedded virtual reality setup to support simulated both forward swimming and turning. The approach was based on modeling the effects of tail motion on fish velocities using recurrent neural networks trained on freely-swimming data. Even though the models worked well on freely-swimming cases, they did not generalize to head-embedded fish (see example in Figure 6). The tail shape timeseries in the embedded case turned out to be out of the distribution of the freely-swimming ones, so the networks did not generalize well, even for different parameterizations of the tail shape. These observations together show limitations of studying head-embedded larval zebrafish as a proxy for freely-swimming behavior. However, the embedded behavior can be legitimately studied in it's own right, and recently there has been rapid progress in imaging freely-swimming animals[58,59].

Internal states as modulators of behavior

The interpeduncular nucleus and the above-lying nuclei raphe appear in studies showing longer-term modulation of behavior [60,61,62] as long as they are imaged. The IPN is frequently missed even in whole-brain studies due to it's depth. In the absence of a stimulus, the fish have a tendency to repeat previous movements [63], and in phototaxis, there is a clear bias coming from longer-period oscillations[64]. From our studies, presented in Manuscripts 2 and 3, we hypothesize that the IPN is likely to be a part of these circuits acting on a 1-10s timescale in biasing the behavior. As the representations investigated relate to the optic flow, the

[54] Gallego, Perich, Chowdhury, et al., "Long-Term Stability of Cortical Population Dynamics Underlying Consistent Behavior".

[55] Roy et al., "Extracting the Dynamics of Behavior in Decision-Making Experiments".

[56] Laboratory et al., "Standardized and Reproducible Measurement of Decision-Making in Mice".

[57] Severi et al., "Neural Control and Modulation of Swimming Speed in the Larval Zebrafish".

[58] Kim et al., "Pan-Neuronal Calcium Imaging with Cellular Resolution in Freely Swimming Zebrafish".

[59] Zhang et al., "Capturing Volumetric Dynamics at High Speed in the Brain by Confocal Light Field Microscopy".

[60] Yokogawa, Hannan, and Burgess, "The Dorsal Raphe Modulates Sensory Responsiveness during Arousal in Zebrafish".

[61] Pantoja et al., "Rapid Effects of Selection on Brain-Wide Activity and Behavior".

[62] Cherng et al., "The Dorsal Lateral Habenula-Interpeduncular Nucleus Pathway Is Essential for Left-Right-Dependent Decision Making in Zebrafish".

[63] Dunn et al., "Brain-Wide Mapping of Neural Activity Controlling Zebrafish Exploratory Locomotion".

[64] Wolf et al., "Sensorimotor Computation Underlying Phototaxis in Zebrafish".

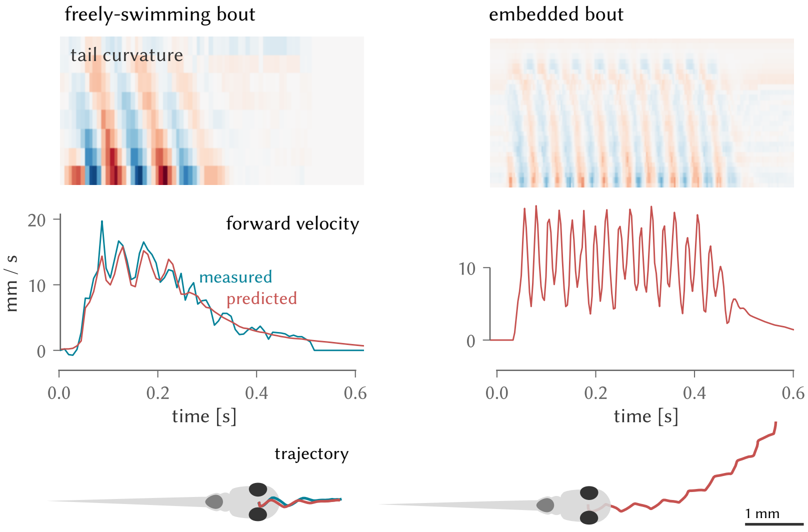

Figure 6: Tail curvature and predicted (for freely-swimming and embedded) and measured (for freeely-swimming) velocity and trajectory for two example bouts.

structure could support more sophisticated functions in adult animals where motion estimation is needed. The IPN could also be a nexus of multisensory spatial information, which will be investigated in further studies in the lab.

Opportunities and challenges with whole-brain imaging

Whole-brain imaging opens an unprecedented window into studying sensorimotor control. All potentially involved areas can be imaged allowing us to overcome preconceptions about what regions of the brain should be involved in which aspects of sensory processing, representing animal state and causing motor outputs. In the context of evidence-accumulation, recent work in mammals also showed that these signals are also widely distributed[65,66], expanding on the traditional conceptions of area involvement in e.g. the primate random dot kinematogram tasks (area MT, lateral interparietal cortex the frontal eye fields)[67].

An important consideration when analyzing whole-brain pan-neuronal calcium imaging data is that different cell types, and even cells of the same type, can have very different links between action potentials and fluorescence changes. These differences can arise, among others, from different baseline firing rates, dynamics of calcium within the cell and the physical dimensions of the cells. The question of timing, i.e. time constants of responses to stimuli, is therefore especially fraught. To make sure that the temporal dynamics of firing rates imputed through calcium imaging e.g. ramping indeed truly behave this way, concurrent electrophysiology is necessary[68,69,70].

The lightsheet and two-photon imaging modalities present different trade-offs. In two-photon experiments, the whole brain can be only imaged plane-by-plane, so in order to cover the whole area the protocol has to be repeated many times, and it is therefore limited in duration. In lightsheet imaging, the optical sectioning from the sheet of light (in our setup at its the narrowest 6.5µm), is imperfect, and there is significant scattering from the tissue above and below the plane currently in focus. Even though this can be ameliorated by using non-negative matrix factorization approaches, there are no guarantees the decomposed signals are corresponding to the true sources. The strong blue lateral and frontal laser illumination can also affects the behavior of the animal, even if the eyes are shielded.

The most obvious application of whole-brain imaging (in zebrafish as in humans and other animals) is localization of function. While localization in itself answers very few deeply interesting questions [71], it can be of great value to con-

[65] Koay et al., “Amplitude Modulations of Cortical Sensory Responses in Pulsatile Evidence Accumulation”.

[66] Jacobs et al., “Cortical State Fluctuations during Sensory Decision Making”.

[67] Gold and Shadlen, “The Neural Basis of Decision Making”.

[68] Theis et al., “Benchmarking Spike Rate Inference in Population Calcium Imaging”.

[69] Greenberg et al., “Accurate Action Potential Inference from a Calcium Sensor Protein through Biophysical Modeling”.

[70] Wei et al., “A Comparison of Neuronal Population Dynamics Measured with Calcium Imaging and Electrophysiology”.

[71] Fodor, “Why the Brain?”

strain models of separated subsystems. In the case of larval zebrafish, localization of functions and response types can be of even greater value than in mammals, as the anatomy is more differentiated (compared to the relative uniformity of the mammalian cortex), and once a structure is found to be interesting, it can be interrogated with the whole spectrum of systems neuroscience techniques available, and the number of neurons remains manageable. This can range from precise genetic targeting of structures and cell types within the structures for both imaging and optogenetic activation, optical and chemical ablation combined with behavioral studies, to tracing the synaptic-level volumes obtained by electron microscopy.

One of the main limitations of the studies presented in this thesis is that we have made correlative, as opposed to causal statements. Although we can pinpoint signatures of various parts of motion processing through imaging, we cannot tell what exact role they play in the control loop without interventions. The available interventions: ablations and optogenetic activations and inactivations suffer from uncertainties on both the behavioral readout side (since the optomotor response is highly variable). On the interpretation side, disabling or activating parts of the circuit, without mapping the whole activity dynamics, can only lead to very coarse statements in the case the behavior is still performed as expected or completely absent. In the best case, there is a specific impairment, and if there is a model that predicts the nature of the impairment, this gives weak evidence for the model describing the situation correctly. However if our model is not precisely quantitatively formulated, which can be difficult when faced with high variability of behavior, the space of possible outcomes is very large. Even with the advances of all-optical recording and stimulation technologies[72,73], the technical advances do not automatically lead to better understanding. Given the wide range of conceivable models, possible manipulations and the uncertainty of behavior given a model, full stimulus-to-to-behavior neural circuit models appear to be a distant goal.

Development and use of Stytra and other software within one lab and beyond

After the manuscript on Stytra was published and promoted at the FENS 2018 conference and through social media, we started receiving feedback and support requests from several different labs, within our institute and beyond, confirming there was a need and use for such a software package. In addition to zebrafish, Stytra has been used for studies with rats, fruit flies and monkeys (personal communication). We were also happy to receive contributions fixing bugs and adding hardware support, and the process is still continuing. A larger update, decoupling stimulus presentation from the user interface process, is in progress and being worked on by new lab members. Other packages with partly overlapping functionality, such as Bonsai, have been extended in the meantime to cover some features of Stytra, such as support of closed-loop visual stimuli[74], and the integration of deep learning-based markerless tracking [75]. However Stytra still maintains unique features including easy programmatic generation of protocols and data and metadata management, as well as optimized tracking for zebrafish experiments, meriting its continued relevance. It is currently used for all behavioral experiments within our lab, so its continued support and development is secured for the near future.

Due to their earlier stage of development, other packages have not yet been used outside of the lab, however several are close to their release at the time of writing (the behavioral analysis package for Stytra, Bouter and the lightsheet control software, Sashimi). The newest analysis packages (Calcium and VolumeRegistration) have been developed in Julia, a language designed from start to serve the needs of computational sciences. It allows writing fast code (within the range

[72] Yang et al., "Simultaneous Two-Photon Imaging and Two-Photon Optogenetics of Cortical Circuits in Three Dimensions".

[73] Packer et al., "Simultaneous All-Optical Manipulation and Recording of Neural Circuit Activity with Cellular Resolution in Vivo".

[74] Lopes et al., "BonVision – an Open-Source Software to Create and Control Visual Environments".

[75] Kane et al., "Real-Time, Low-Latency Closed-Loop Feedback Using Markerless Posture Tracking".

of writing directly in C) while maintaining high-level constructs. This makes it optimal for our uses, as we can improve performance, essential for algorithms that operate on our large-scale imaging data, while maintaining readability and maintainability. Its rich ecosystem for complex interactive visualizations[76] was integral in the data analysis process for Manuscript 3, where all imaging analyses have been done with Julia.

Open source software as a model for science

Since the work of scientists is mostly publicly funded, there is a responsibility for sharing the tools built for the research, as public funding is meant to further the common good[77]. Multiple labs building on a common set of tools has also many practical advantages, from saving development time, through fostering collaborations to reducing the probability of errors, as there is a higher chance of discovering bugs.

The increased sophistication of behavioral paradigms and data analysis pipelines makes the final findings very dependent on the software stack [78]. Many lessons from the fMRI community are applicable in calcium imaging studies, as similar issues appear: high dimensionality of brain and behavioral data, a practically unlimited number of hypotheses to test and many steps from raw data to signals being explained. Keeping details of the analysis behind (reasonable) request clauses both discourages independent verification, and leads to lower standards in code. Making code public incentivizes cleaner software engineering, which also frequently leads to better quality of analyses. As code has become an integral part of almost all systems neuroscience research, the need for increased transparency becomes more pressing.

More generally, the utopian concept of free and open source software (FOSS) overlaps to a large degree with the ideals of scientific conduct. The principles of free software go further than just open source: not just providing the finished software, but empowering the users to understand and build their own tools without restrictions[79]. In science there is the nominal principle that experiments and analyses can be reproduced from the methods section, but open source usually goes further: all tools to reproduce the same program, as far as it is possible, are provided. Of course, in the physical world the analogy is not fully applicable, yet the principles go beyond software, as repositories of hardware designs such as OpenBehavior or plasmids such as Addgene demonstrate. Free-form collaboration is explicitly encouraged in most open source projects: many projects have contributing guidelines and collaboration depends only on shared interests, without requiring previous acquaintances. In the future, hopefully more complete and granular communication of scientific progress will allow for similar structures to emerge for scientific data, hypotheses, analyses and evaluations.

The existence of software as living entities that need to be maintained and supported in order to retain relevance results in a different set of incentives from scientific publications. Publishing of early versions of software is encouraged with the common understanding that there might be issues (analogously to preprints), however the subsequent steps can also provide ideas for development of scientific communications. For example, public tracking of user issues ensures the deficiencies of the work are clear to all newcomers. Additionally, while the review and acceptance of contributions to the project is usually in hands of maintainers, in case of disagreements, anyone is free to take parts of the code (or in case of science, it would be datasets, models or even lines of reasoning) and continue in new directions. Modern version control, which is nearly ubiquitous in open source software, highlights several additional properties in common with good scientific practice: immutable records and distributed repositories. Immutable records of the project progress can help guard against many pitfalls in complex data analysis situations, such as evaluating statistical tests devised by observing subsets of data after it has been acquired (p-hacking). Distributed repositories enable almost

[76] Simon et al., *JuliaPlots/Makie.Jl.*

[77] Gleeson et al., “A Commitment to Open Source in Neuroscience”.

[78] Botvinik-Nezer et al., “Variability in the Analysis of a Single Neuroimaging Dataset by Many Teams”.

[79] Stallman, “Why ”Open Source” Misses the Point of Free Software”.

universal availability: the code is hosted on public servers and accessible without restrictions, and institutions can host verifiably identical copies. Significant archiving efforts, such as Zenodo, the Internet Archive and the GitHub Arctic Vault, also ensure the continued availability of code artifacts even if the original hosting entities disappear.

The advance of movements in open access publishing, as well as new publishing outlets and organizations embracing digital technologies, give hope that many of these ideas will be realized in mainstream scientific communication in the near future.

Acknowledgements

First of all, I would like to thank my supervisor, Ruben Portugues for being both scientifically and personally a great mentor. He gave me an opportunity to pursue all the threads of research that caught my fancy, and supported my development in many directions that were not part of the main research themes, from software to summer schools. His precise and kind feedback solved many issues that I would otherwise puzzle over for weeks in minutes, and his infectious enthusiasm for science never failed to motivate me.

The Portugues lab was an exceptionally stimulating and fun environment to pursue my PhD, and I would like to thank all the lab members, both past and current, for countless discussions, presentations, meals, games and trips we created and undertook together. In particular, I am grateful to Luigi for being a co-conspirator on many of the endeavours presented here, from the open-source efforts to the IPN, Virginia, for being a patient guinea pig of my attempts at teaching programming, Elena for many deep discussions, and Andreas and Laura for teaching me many fundamentals on working in an experimental lab.

Thanks also to my thesis committee members, past and present - Axel Borst, Andreas Herz, Stefan Glasauer for a lot of helpful input on the various projects.

I would also like to thank my friends in Munich - Álvaro, Anna, Alex, Ksenia, Drago, Judita, Veronika, Jaime and Niko whose company made it an immensely rich and rewarding period of my life.

Finally, the greatest thanks goes to my parents, Alemka and Željko, who continuously supported me on my path, including the way from electrical engineering through neuroscience, and whose advice and love I keep relying on.

References

Albus, James S. “A Theory of Cerebellar Function”. In: *Mathematical Biosciences* 10.1 (Feb. 1, 1971), pp. 25–61. ISSN: 0025-5564. DOI: `10.1016/0025-5564(71)90051-4`. URL: `http://www.sciencedirect.com/science/article/pii/0025556471900514` (visited on 12/08/2020) (cit. on p. 10).

Asua, Diego, Vilim Štih, and Luigi Petrucco. *Portugueslab/Sashimi: Alpha.* Zenodo, Oct. 23, 2020. DOI: `10.5281/zenodo.4122062`. URL: `https://zenodo.org/record/4122062` (visited on 10/23/2020) (cit. on pp. 14, 15).

Bianco, Isaac Henry, Adam R. Kampff, and Florian Engert. “Prey Capture Behavior Evoked by Simple Visual Stimuli in Larval Zebrafish”. In: *Front. Syst. Neurosci.* 5 (2011). ISSN: 1662-5137. DOI: `10.3389/fnsys.2011.00101`. URL: `https://www.frontiersin.org/articles/10.3389/fnsys.2011.00101/full` (visited on 12/04/2020) (cit. on p. 8).

Botvinik-Nezer, Rotem et al. “Variability in the Analysis of a Single Neuroimaging Dataset by Many Teams”. In: *Nature* 582.7810 (7810 June 2020), pp. 84–88. ISSN: 1476-4687. DOI: `10.1038/s41586-020-2314-9`. URL: `https://www.nature.com/articles/s41586-020-2314-9` (visited on 12/13/2020) (cit. on p. 115).

Bouvier, Guy et al. “Cerebellar Learning Using Perturbations”. In: *eLife* 7 (Nov. 12, 2018). Ed. by Jennifer L Raymond and Eve Marder, e31599. ISSN: 2050-084X. DOI: `10.7554/eLife.31599`. URL: `https://doi.org/10.7554/eLife.31599` (visited on 12/08/2020) (cit. on p. 10).

Bruno, Angela M, William N Frost, and Mark D Humphries. “A Spiral Attractor Network Drives Rhythmic Locomotion”. In: *eLife* 6 (Aug. 7, 2017). Ed. by Jan-Marino Ramirez, e27342. ISSN: 2050-084X. DOI: `10.7554/eLife.27342`. URL: `https://doi.org/10.7554/eLife.27342` (visited on 11/22/2020) (cit. on p. 9).

Burgess, Harold A., Hannah Schoch, and Michael Granato. “Distinct Retinal Pathways Drive Spatial Orientation Behaviors in Zebrafish Navigation”. In: *Current Biology* 20.4 (Feb. 23, 2010), pp. 381–386. ISSN: 0960-9822. DOI: `10.1016/j.cub.2010.01.022`. URL: `http://www.sciencedirect.com/science/article/pii/S0960982210000618` (visited on 12/10/2020) (cit. on p. 8).

Cherng, Bor-Wei et al. “The Dorsal Lateral Habenula-Interpeduncular Nucleus Pathway Is Essential for Left-Right-Dependent Decision Making in Zebrafish”. In: *Cell Reports* 32.11 (Sept. 2020), p. 108143. ISSN: 22111247. DOI: `10.1016/j.celrep.2020.108143`. URL: `https:`

//linkinghub.elsevier.com/retrieve/pii/S2211124720311323 (visited on 09/20/2020) (cit. on p. 112).

Denk, W., J. H. Strickler, and W. W. Webb. “Two-Photon Laser Scanning Fluorescence Microscopy”. In: *Science* 248.4951 (Apr. 6, 1990), pp. 73–76. ISSN: 0036-8075, 1095-9203. DOI: 10.1126/science.2321027. pmid: 2321027. URL: https://science.sciencemag.org/content/248/4951/73 (visited on 10/26/2020) (cit. on p. 8).

Dunn, Timothy W et al. “Brain-Wide Mapping of Neural Activity Controlling Zebrafish Exploratory Locomotion”. In: *eLife* 5 (Mar. 22, 2016). Ed. by Ronald L Calabrese, e12741. ISSN: 2050-084X. DOI: 10.7554/eLife.12741. URL: https://doi.org/10.7554/eLife.12741 (visited on 11/21/2020) (cit. on p. 112).

Ehrlich, David E. and David Schoppik. “Control of Movement Initiation Underlies the Development of Balance”. In: *Current Biology* 27.3 (Feb. 6, 2017), pp. 334–344. ISSN: 0960-9822. DOI: 10.1016/j.cub.2016.12.003. URL: http://www.sciencedirect.com/science/article/pii/S096098221631449X (visited on 12/04/2020) (cit. on p. 8).

Engelbrecht, Christoph J. and Ernst H. Stelzer. “Resolution Enhancement in a Light-Sheet-Based Microscope (SPIM)”. In: *Opt. Lett., OL* 31.10 (May 15, 2006), pp. 1477–1479. ISSN: 1539-4794. DOI: 10.1364/OL.31.001477. URL: https://www.osapublishing.org/ol/abstract.cfm?uri=ol-31-10-1477 (visited on 12/12/2020) (cit. on p. 9).

Fodor, Jerry. “Why the Brain?” In: *London Review of Books* 21.19 (Sept. 30, 1999). ISSN: 0260-9592. URL: https://www.lrb.co.uk/the-paper/v21/n19/jerry-fodor/diary (visited on 11/19/2020) (cit. on p. 113).

Gallego, Juan A., Matthew G. Perich, Raeed H. Chowdhury, et al. “Long-Term Stability of Cortical Population Dynamics Underlying Consistent Behavior”. In: *Nature Neuroscience* 23.2 (2 Feb. 2020), pp. 260–270. ISSN: 1546-1726. DOI: 10.1038/s41593-019-0555-4. URL: https://www.nature.com/articles/s41593-019-0555-4 (visited on 12/14/2020) (cit. on p. 112).

Gallego, Juan A., Matthew G. Perich, Stephanie N. Naufel, et al. “Cortical Population Activity within a Preserved Neural Manifold Underlies Multiple Motor Behaviors”. In: *Nature Communications* 9.1 (1 Oct. 12, 2018), p. 4233. ISSN: 2041-1723. DOI: 10.1038/s41467-018-06560-z. URL: https://www.nature.com/articles/s41467-018-06560-z (visited on 11/22/2020) (cit. on p. 9).

Gilmer, Jesse I. and Abigail L. Person. “Theoretically Sparse, Empirically Dense: New Views on Cerebellar Granule Cells”. In: *Trends in Neurosciences* 41.12 (Dec. 1, 2018), pp. 874–877. ISSN: 0166-2236. DOI: 10.1016/j.tins.2018.09.013. URL: http://www.sciencedirect.com/science/article/pii/S0166223618302716 (visited on 12/02/2020) (cit. on p. 111).

Giovannucci, Andrea et al. “Cerebellar Granule Cells Acquire a Widespread Predictive Feedback Signal during Motor Learning”. In: *Nature Neuroscience* 20.5 (5 May 2017), pp. 727–734. ISSN: 1546-1726. DOI: 10.1038/nn.4531. URL: https://www.nature.com/articles/nn.4531 (visited on 12/02/2020) (cit. on p. 111).

Giusti, Chad et al. “Clique Topology Reveals Intrinsic Geometric Structure in Neural Correlations”. In: *PNAS* 112.44 (Nov. 3, 2015), pp. 13455–13460. ISSN: 0027-8424, 1091-6490. DOI: `10.1073/pnas.1506407112`. pmid: 26487684. URL: `https://www.pnas.org/content/112/44/13455` (visited on 11/22/2020) (cit. on p. 9).

Gleeson, Padraig et al. “A Commitment to Open Source in Neuroscience”. In: *Neuron* 96.5 (Dec. 6, 2017), pp. 964–965. ISSN: 0896-6273. DOI: `10.1016/j.neuron.2017.10.013`. URL: `http://www.sciencedirect.com/science/article/pii/S0896627317309819` (visited on 09/16/2020) (cit. on p. 115).

Gold, Joshua I. and Michael N. Shadlen. “The Neural Basis of Decision Making”. In: *Annual Review of Neuroscience* 30.1 (2007), pp. 535–574. DOI: `10.1146/annurev.neuro.29.051605.113038`. pmid: 17600525. URL: `https://doi.org/10.1146/annurev.neuro.29.051605.113038` (visited on 12/13/2020) (cit. on pp. 12, 113).

Greenberg, David S. et al. “Accurate Action Potential Inference from a Calcium Sensor Protein through Biophysical Modeling”. In: *bioRxiv* (Nov. 29, 2018), p. 479055. DOI: `10.1101/479055`. URL: `https://www.biorxiv.org/content/10.1101/479055v1` (visited on 10/19/2020) (cit. on pp. 8, 113).

Haesemeyer, Martin et al. “The Structure and Timescales of Heat Perception in Larval Zebrafish”. In: *Cell Systems* 1.5 (Nov. 25, 2015), pp. 338–348. ISSN: 2405-4712. DOI: `10.1016/j.cels.2015.10.010`. URL: `http://www.sciencedirect.com/science/article/pii/S2405471215001842` (visited on 12/04/2020) (cit. on p. 8).

Herrera, Kristian J. et al. “Larval Zebrafish Use Olfactory Detection of Sodium and Chloride to Avoid Salt-Water”. In: *bioRxiv* (Aug. 20, 2020), p. 2020.08.19.258061. DOI: `10.1101/2020.08.19.258061`. URL: `https://www.biorxiv.org/content/10.1101/2020.08.19.258061v1` (visited on 12/14/2020) (cit. on p. 8).

Ito, Masao. “Cerebellar Circuitry as a Neuronal Machine”. In: *Progress in Neurobiology*. The Contributions of John Carew Eccles to Contemporary Neuroscience 78.3 (Feb. 1, 2006), pp. 272–303. ISSN: 0301-0082. DOI: `10.1016/j.pneurobio.2006.02.006`. URL: `http://www.sciencedirect.com/science/article/pii/S0301008206000232` (visited on 12/08/2020) (cit. on p. 10).

Jacobs, Elina A. K. et al. “Cortical State Fluctuations during Sensory Decision Making”. In: *Current Biology* (Oct. 22, 2020). ISSN: 0960-9822. DOI: `10.1016/j.cub.2020.09.067`. URL: `http://www.sciencedirect.com/science/article/pii/S0960982220314378` (visited on 12/13/2020) (cit. on p. 113).

Kane, Gary et al. “Real-Time, Low-Latency Closed-Loop Feedback Using Markerless Posture Tracking”. In: *bioRxiv* (Aug. 5, 2020), p. 2020.08.04.236422. DOI: `10.1101/2020.08.04.236422`. URL: `https://www.biorxiv.org/content/10.1101/2020.08.04.236422v1` (visited on 12/01/2020) (cit. on p. 114).

Keller, Philipp J. et al. “Reconstruction of Zebrafish Early Embryonic Development by Scanned Light Sheet Microscopy”. In: *Science* 322.5904 (Nov. 14, 2008), pp. 1065–1069. ISSN: 0036-8075, 1095-9203. DOI: `10.`

1126/science.1162493. pmid: 18845710. URL: https://science.sciencemag.org/content/322/5904/1065 (visited on 10/26/2020) (cit. on p. 9).

Kim, Dal Hyung et al. "Pan-Neuronal Calcium Imaging with Cellular Resolution in Freely Swimming Zebrafish". In: *Nature Methods* 14.11 (11 Nov. 2017), pp. 1107–1114. ISSN: 1548-7105. DOI: 10.1038/nmeth.4429. URL: https://www.nature.com/articles/nmeth.4429 (visited on 12/01/2020) (cit. on p. 9).

– "Pan-Neuronal Calcium Imaging with Cellular Resolution in Freely Swimming Zebrafish". In: *Nature Methods* 14.11 (11 Nov. 2017), pp. 1107–1114. ISSN: 1548-7105. DOI: 10.1038/nmeth.4429. URL: https://www.nature.com/articles/nmeth.4429 (visited on 12/14/2020) (cit. on p. 112).

Kist, Andreas M. and Ruben Portugues. "Optomotor Swimming in Larval Zebrafish Is Driven by Global Whole-Field Visual Motion and Local Light-Dark Transitions". In: *Cell Reports* 29.3 (Oct. 15, 2019), 659–670.e3. ISSN: 2211-1247. DOI: 10.1016/j.celrep.2019.09.024. URL: http://www.sciencedirect.com/science/article/pii/S221112471931201X (visited on 12/05/2020) (cit. on p. 12).

Knogler, Laura D, Andreas M Kist, and Ruben Portugues. "Motor Context Dominates Output from Purkinje Cell Functional Regions during Reflexive Visuomotor Behaviours". In: *eLife* 8 (Jan. 25, 2019). Ed. by Indira M Raman et al., e42138. ISSN: 2050-084X. DOI: 10.7554/eLife.42138. URL: https://doi.org/10.7554/eLife.42138 (visited on 03/10/2019) (cit. on p. 111).

Koay, Sue Ann et al. "Amplitude Modulations of Cortical Sensory Responses in Pulsatile Evidence Accumulation". In: *eLife* 9 (Dec. 2, 2020). Ed. by Emilio Salinas, e60628. ISSN: 2050-084X. DOI: 10.7554/eLife.60628. URL: https://doi.org/10.7554/eLife.60628 (visited on 12/13/2020) (cit. on p. 113).

Laboratory, The International Brain et al. "Standardized and Reproducible Measurement of Decision-Making in Mice". In: *bioRxiv* (Oct. 9, 2020), p. 2020.01.17.909838. DOI: 10.1101/2020.01.17.909838. URL: https://www.biorxiv.org/content/10.1101/2020.01.17.909838v5 (visited on 12/14/2020) (cit. on p. 112).

Lopes, Gonçalo et al. "BonVision – an Open-Source Software to Create and Control Visual Environments". In: *bioRxiv* (July 4, 2020), p. 2020.03.09.983775. DOI: 10.1101/2020.03.09.983775. URL: https://www.biorxiv.org/content/10.1101/2020.03.09.983775v2 (visited on 12/01/2020) (cit. on p. 114).

Markov, Daniil A. et al. "A Cerebellar Internal Model Calibrates a Feedback Controller Involved in Sensorimotor Control". In: *bioRxiv* (Sept. 14, 2020), p. 2020.02.12.945956. DOI: 10.1101/2020.02.12.945956. URL: https://www.biorxiv.org/content/10.1101/2020.02.12.945956v2 (visited on 12/05/2020) (cit. on pp. 11, 111).

Marques, João C. et al. "Structure of the Zebrafish Locomotor Repertoire Revealed with Unsupervised Behavioral Clustering". In: *Current Biology* 28.2 (Jan. 22, 2018), 181–195.e5. ISSN: 0960-9822. DOI: 10.1016/j.cub.

2017.12.002. URL: http://www.sciencedirect.com/science/article/pii/S0960982217316044 (visited on 12/04/2020) (cit. on p. 8).

Marr, David and W. Thomas Thach. “A Theory of Cerebellar Cortex”. In: *From the Retina to the Neocortex: Selected Papers of David Marr*. Ed. by Lucia Vaina. Boston, MA: Birkhäuser, 1991, pp. 11–50. ISBN: 978-1-4684-6775-8. DOI: 10.1007/978-1-4684-6775-8_3. URL: https://doi.org/10.1007/978-1-4684-6775-8_3 (visited on 12/08/2020) (cit. on p. 10).

Naumann, Eva A. et al. “From Whole-Brain Data to Functional Circuit Models: The Zebrafish Optomotor Response”. In: *Cell* 167.4 (Nov. 3, 2016), 947–960.e20. ISSN: 0092-8674. DOI: 10.1016/j.cell.2016.10.019. URL: http://www.sciencedirect.com/science/article/pii/S0092867416314027 (visited on 10/17/2020) (cit. on pp. 12, 13, 111).

Orger, Michael B. and Herwig Baier. “Channeling of Red and Green Cone Inputs to the Zebrafish Optomotor Response”. In: *Visual Neuroscience* 22.3 (May 2005), pp. 275–281. ISSN: 1469-8714, 0952-5238. DOI: 10.1017/S0952523805223039. URL: https://www.cambridge.org/core/journals/visual-neuroscience/article/abs/channeling-of-red-and-green-cone-inputs-to-the-zebrafish-optomotor-response/180B0E41BDD8D237586D42D07B9908E0 (visited on 12/05/2020) (cit. on p. 11).

Orger, Michael B., Adam R. Kampff, et al. “Control of Visually Guided Behavior by Distinct Populations of Spinal Projection Neurons”. In: *Nature Neuroscience* 11.3 (Mar. 2008), pp. 327–333. ISSN: 1546-1726. DOI: 10.1038/nn2048. URL: https://www.nature.com/articles/nn2048 (visited on 01/08/2019) (cit. on p. 11).

Orger, Michael B., Matthew C. Smear, et al. “Perception of Fourier and Non-Fourier Motion by Larval Zebrafish”. In: *Nature Neuroscience* 3.11 (11 Nov. 2000), pp. 1128–1133. ISSN: 1546-1726. DOI: 10.1038/80649. URL: https://www.nature.com/articles/nn1100_1128 (visited on 12/08/2020) (cit. on pp. 8, 11).

Oteiza, Pablo et al. “A Novel Mechanism for Mechanosensory-Based Rheotaxis in Larval Zebrafish”. In: *Nature* 547.7664 (7664 July 2017), pp. 445–448. ISSN: 1476-4687. DOI: 10.1038/nature23014. URL: https://www.nature.com/articles/nature23014 (visited on 12/04/2020) (cit. on p. 8).

Pachitariu, Marius et al. “Suite2p: Beyond 10,000 Neurons with Standard Two-Photon Microscopy”. In: *bioRxiv* (July 20, 2017), p. 061507. DOI: 10.1101/061507. URL: https://www.biorxiv.org/content/10.1101/061507v2 (visited on 12/14/2020) (cit. on p. 16).

Packer, Adam M. et al. “Simultaneous All-Optical Manipulation and Recording of Neural Circuit Activity with Cellular Resolution in Vivo”. In: *Nature Methods* 12.2 (2 Feb. 2015), pp. 140–146. ISSN: 1548-7105. DOI: 10.1038/nmeth.3217. URL: https://www.nature.com/articles/nmeth.3217/ (visited on 12/13/2020) (cit. on p. 114).

Pantoja, Carlos et al. “Rapid Effects of Selection on Brain-Wide Activity and Behavior”. In: *Current Biology* 30.18 (Sept. 21, 2020), 3647–3656.e3. ISSN: 0960-9822. DOI: 10.1016/j.cub.2020.06.086. URL: http:

//www.sciencedirect.com/science/article/pii/S0960982220309386 (visited on 12/14/2020) (cit. on p. 112).

Portugues, Ruben and Florian Engert. “Adaptive Locomotor Behavior in Larval Zebrafish”. In: *Frontiers in Systems Neuroscience* 5 (2011). ISSN: 1662-5137. DOI: 10.3389/fnsys.2011.00072. URL: http://journal.frontiersin.org/article/10.3389/fnsys.2011.00072/abstract (visited on 01/13/2016) (cit. on pp. 10, 11).

Portugues, Ruben, Claudia E. Feierstein, et al. “Whole-Brain Activity Maps Reveal Stereotyped, Distributed Networks for Visuomotor Behavior”. In: *Neuron* 81.6 (Mar. 2014), pp. 1328–1343. ISSN: 08966273. DOI: 10.1016/j.neuron.2014.01.019. URL: http://linkinghub.elsevier.com/retrieve/pii/S0896627314000506 (visited on 01/13/2016) (cit. on p. 8).

Portugues, Ruben, Martin Haesemeyer, et al. “Whole-Field Visual Motion Drives Swimming in Larval Zebrafish via a Stochastic Process”. In: *Journal of Experimental Biology* 218.9 (May 1, 2015), pp. 1433–1443. ISSN: 0022-0949, 1477-9145. DOI: 10.1242/jeb.118299. pmid: 25792753. URL: https://jeb.biologists.org/content/218/9/1433 (visited on 12/05/2020) (cit. on p. 11).

Prevedel, Robert et al. “Simultaneous Whole-Animal 3D Imaging of Neuronal Activity Using Light-Field Microscopy”. In: *Nature Methods* 11.7 (7 July 2014), pp. 727–730. ISSN: 1548-7105. DOI: 10.1038/nmeth.2964. URL: https://www.nature.com/articles/nmeth.2964 (visited on 12/01/2020) (cit. on p. 9).

Rose, Tobias et al. “Putting a Finishing Touch on GECIs”. In: *Frontiers in Molecular Neuroscience* 7 (Nov. 18, 2014). ISSN: 1662-5099. DOI: 10.3389/fnmol.2014.00088. URL: http://journal.frontiersin.org/article/10.3389/fnmol.2014.00088/abstract (visited on 01/13/2016) (cit. on p. 7).

Roy, Nicholas A. et al. “Extracting the Dynamics of Behavior in Decision-Making Experiments”. In: *bioRxiv* (May 25, 2020), p. 2020.05.21.109678. DOI: 10.1101/2020.05.21.109678. URL: https://www.biorxiv.org/content/10.1101/2020.05.21.109678v1 (visited on 12/13/2020) (cit. on p. 112).

Schnörr, S. J. et al. “Measuring Thigmotaxis in Larval Zebrafish”. In: *Behav Brain Res* 228.2 (Mar. 17, 2012), pp. 367–374. ISSN: 1872-7549. DOI: 10.1016/j.bbr.2011.12.016. pmid: 22197677 (cit. on p. 8).

Scott, Ethan K. et al. “Targeting Neural Circuitry in Zebrafish Using GAL4 Enhancer Trapping”. In: *Nature Methods* 4.4 (4 Apr. 2007), pp. 323–326. ISSN: 1548-7105. DOI: 10.1038/nmeth1033. URL: https://www.nature.com/articles/nmeth1033 (visited on 10/26/2020) (cit. on p. 7).

Severi, Kristen E. et al. “Neural Control and Modulation of Swimming Speed in the Larval Zebrafish”. In: *Neuron* 83.3 (Aug. 2014), pp. 692–707. ISSN: 08966273. DOI: 10.1016/j.neuron.2014.06.032. URL: http://linkinghub.elsevier.com/retrieve/pii/S0896627314005789 (visited on 01/13/2016) (cit. on pp. 11, 112).

Simon et al. *JuliaPlots/Makie.Jl: V0.11.2.* Zenodo, Dec. 13, 2020. DOI: 10.5281/zenodo.4319718. URL: https://zenodo.org/record/4319718 (visited on 12/13/2020) (cit. on p. 115).

Stallman, Richard. “Why ”Open Source” Misses the Point of Free Software”. In: *Commun. ACM* 52.6 (June 1, 2009), pp. 31–33. ISSN: 0001-0782. DOI: `10.1145/1516046.1516058`. URL: `https://doi.org/10.1145/1516046.1516058` (visited on 10/19/2020) (cit. on p. 115).

Štih, Vilim. *Portugueslab/VolumeRegistration.Jl: Release for Zenodo Tag.* Zenodo, Dec. 14, 2020. DOI: `10.5281/zenodo.4320585`. URL: `https://zenodo.org/record/4320585` (visited on 12/14/2020) (cit. on p. 16).

Štih, Vilim, Emanuele Paoli, and Diego Asua. *Portugueslab/Brunoise: Alpha.* Zenodo, Oct. 23, 2020. DOI: `10.5281/zenodo.4122064`. URL: `https://zenodo.org/record/4122064` (visited on 10/23/2020) (cit. on pp. 14, 15).

Štih, Vilim, Ot Prat, et al. *Portugueslab/Bouter: Release for Zenodo Tag.* Zenodo, Dec. 14, 2020. DOI: `10.5281/zenodo.4320583`. URL: `https://zenodo.org/record/4320583` (visited on 12/14/2020) (cit. on p. 14).

Temizer, Incinur et al. “A Visual Pathway for Looming-Evoked Escape in Larval Zebrafish”. In: *Current Biology* 25.14 (July 20, 2015), pp. 1823–1834. ISSN: 0960-9822. DOI: `10.1016/j.cub.2015.06.002`. URL: `http://www.sciencedirect.com/science/article/pii/S0960982215006673` (visited on 12/04/2020) (cit. on p. 8).

Theis, Lucas et al. “Benchmarking Spike Rate Inference in Population Calcium Imaging”. In: *Neuron* 90.3 (May 4, 2016), pp. 471–482. ISSN: 0896-6273. DOI: `10.1016/j.neuron.2016.04.014`. URL: `http://www.sciencedirect.com/science/article/pii/S0896627316300733` (visited on 12/14/2020) (cit. on p. 113).

Wagner, Mark J. et al. “Cerebellar Granule Cells Encode the Expectation of Reward”. In: *Nature* 544.7648 (7648 Apr. 2017), pp. 96–100. ISSN: 1476-4687. DOI: `10.1038/nature21726`. URL: `https://www.nature.com/articles/nature21726` (visited on 12/02/2020) (cit. on p. 111).

Wei, Ziqiang et al. “A Comparison of Neuronal Population Dynamics Measured with Calcium Imaging and Electrophysiology”. In: *PLOS Computational Biology* 16.9 (Sept. 15, 2020), e1008198. ISSN: 1553-7358. DOI: `10.1371/journal.pcbi.1008198`. URL: `https://journals.plos.org/ploscompbiol/article?id=10.1371/journal.pcbi.1008198` (visited on 12/14/2020) (cit. on p. 113).

Wolf, Sébastien et al. “Sensorimotor Computation Underlying Phototaxis in Zebrafish”. In: *Nature Communications* 8.1 (1 Sept. 21, 2017), p. 651. ISSN: 2041-1723. DOI: `10.1038/s41467-017-00310-3`. URL: `https://www.nature.com/articles/s41467-017-00310-3` (visited on 11/21/2020) (cit. on p. 112).

Yang, Weijian et al. “Simultaneous Two-Photon Imaging and Two-Photon Optogenetics of Cortical Circuits in Three Dimensions”. In: *eLife* 7 (Feb. 7, 2018). Ed. by Karel Svoboda, e32671. ISSN: 2050-084X. DOI: `10.7554/eLife.32671`. URL: `https://doi.org/10.7554/eLife.32671` (visited on 12/13/2020) (cit. on p. 114).

Yildizoglu, Tugce et al. “A Neural Representation of Naturalistic Motion-Guided Behavior in the Zebrafish Brain”. In: *Current Biology* 30.12 (June 22, 2020), 2321–2333.e6. ISSN: 0960-9822. DOI: `10.1016/j.cub.2020.04.043`. pmid: 32386533. URL: `https://www.cell.com/current-`

biology/abstract/S0960-9822(20)30557-1 (visited on 10/26/2020) (cit. on pp. 11, 12).

Yokogawa, Tohei, Markus C. Hannan, and Harold A. Burgess. “The Dorsal Raphe Modulates Sensory Responsiveness during Arousal in Zebrafish”. In: *J. Neurosci.* 32.43 (Oct. 24, 2012), pp. 15205–15215. ISSN: 0270-6474, 1529-2401. DOI: 10.1523/JNEUROSCI.1019-12.2012. pmid: 23100441. URL: https://www.jneurosci.org/content/32/43/15205 (visited on 12/13/2020) (cit. on p. 112).

Zhang, Zhenkun et al. “Capturing Volumetric Dynamics at High Speed in the Brain by Confocal Light Field Microscopy”. In: *bioRxiv* (Jan. 6, 2020), p. 2020.01.04.890624. DOI: 10.1101/2020.01.04.890624. URL: https://www.biorxiv.org/content/10.1101/2020.01.04.890624v1 (visited on 12/14/2020) (cit. on p. 112).

Author contributions

Manuscript 1: Sensorimotor Representations in Cerebellar Granule Cells in Larval Zebrafish Are Dense, Spatially Organized, and Non-temporally Patterned

Authors Laura D. Knogler, Daniil A. Markov, Elena I. Dragomir, **Vilim Štih**, Ruben Portugues

Author Contributions L.D.K. and R.P. designed the study and experiments with help from E.I.D. L.D.K. and E.I.D. performed the imaging experiments. L.D.K. performed the electrophysiology experiments. R.P. wrote the data acquisition and analysis software, with help from L.D.K. and **V.Š.**. L.D.K. and R.P. performed data analysis,with help from E.I.D. and **V.Š.** D.A.M. performed single-cell labeling of granule cells and tracing of dendritic and axonal projections. L.D.K. and R.P. wrote the manuscript with help from all authors.

Manuscript 2: Evidence accumulation during a sensorimotor decision task revealed by whole-brain imaging

Authors Elena I. Dragomir, **Vilim Štih**, Ruben Portugues

Author Contributions E.I.D. and R.P. conceived the project and designed the experiments. E.I.D. performed all experiments. E.I.D. and R.P. analyzed experimental data.**V.Š.** and R.P. designed and implemented the model. E.I.D. and R.P. wrote the manuscript with help from **V.Š.**

Manuscript 3: The interpeduncular nucleus exhibits structured optic flow-dependent activity

Authors **Vilim Štih**, Luigi Petrucco, Hagar Lavian, Elena Dragomir, Emanuele Paoli, You Wu, Fabian Svara, Ruben Portugues

Author Contributions **V.Š.** and R.P. conceived of the project. The experiments were designed by **V.Š.**, L.P. and H.L. The functional imaging data was acquired by H.L., **V.Š.**, L.P., E.D., E.P. and Y.W. **V.Š.** analyzed the imaging and behavioral data. The EM dataset was collected and prepared by F.S., while the analysis of the IPN neuron anatomy was done by L.P. **V.Š.** and L.P. wrote the manuscript with input from all the authors.

Manuscript 4: Stytra: An open-source, integrated system for stimulation, tracking and closed-loop behavioral experiments

Authors **Vilim Štih**, Luigi Petrucco, Andreas M. Kist, Ruben Portugues

Author Contributions Conceptualization; **V.Š.**, L.P.; R.P. Data curation: **V.Š.**, L.P., Formal analysis: **V.Š.**, L.P., Funding acquisition: R.P.; Investigation: **V.Š.**, L.P.; Methodology: **V.Š.**, L.P., A.M.K.; Project administration: R.P. Software: **V.Š.**, L.P., A.M.K. Supervision: R.P.; Validation: **V.Š.**, L.P.; Visualization: **V.Š.**, L.P.; Writing– original draft: **V.Š.**, L.P., R.P.; Writing – review & editing: A.M.K.

List of Publications

Dragomir, Elena I., Vilim Štih, and Ruben Portugues. "Evidence Accumulation during a Sensorimotor Decision Task Revealed by Whole-Brain Imaging." Nature Neuroscience 23, no. 1 (January 2020): 85–93. https://doi.org/10.1038/s41593-019-0535-8.

Štih, Vilim, Luigi Petrucco, Andreas M. Kist, and Ruben Portugues. "Stytra: An Open-Source, Integrated System for Stimulation, Tracking and Closed-Loop Behavioral Experiments." PLOS Computational Biology 15, no. 4 (2019): 1–20. https://doi.org/10.1371/journal.pcbi.1006699.

Knogler, Laura D., Daniil A. Markov, Elena I. Dragomir, Vilim Štih, and Ruben Portugues. "Sensorimotor Representations in Cerebellar Granule Cells in Larval Zebrafish Are Dense, Spatially Organized, and Non-Temporally Patterned." Current Biology 27, no. 9 (May 8, 2017): 1288–1302. https://doi.org/10.1016/j.cub.2017.03.029.

Siju, K. P., Vilim Štih, Sophie Aimon, Julijana Gjorgjieva, Ruben Portugues, and Ilona C. Grunwald Kadow. "Valence and State-Dependent Population Coding in Dopaminergic Neurons in the Fly Mushroom Body." Current Biology 30, no. 11 (June 8, 2020): 2104-2115.e4. https://doi.org/10.1016/j.cub.2020.04.037.

Eidesstattliche Versicherung/Affidavit

Hiermit versichere ich an Eides statt, dass ich die vorliegende Dissertation ”Signatures of motion processing and decisions in the larval zebrafish brain” selbstständig angefertigt habe, mich außer der angegebenen keiner weiteren Hilfsmittel bedient und alle Erkenntnisse, die aus dem Schrifttum ganz oder annähernd übernommen sind, als solche kenntlich gemacht und nach ihrer Herkunft unter Bezeichnung der Fundstelle einzeln nachgewiesen habe. I hereby confirm that the dissertation ”Signatures of motion processing and decisions in the larval zebrafish brain” is the result of my own work and that I have only used sources or materials listed and specified in the dissertation.

Vilim Štih Berlin, 16. 12. 2020

Supervisor Prof. Dr. Ruben Portugues Munich, 16. 12. 2020.